Spectroscopy and modelling of ion charge exchange in energetic discharges used in nuclear fusion

by

Oded Shrier

A thesis submitted in fulfilment
of the requirements for the degree of
Doctor of Philosophy

School of Physics
University of Sydney
July 2007

Declaration of originality

To the best of my knowledge, this thesis contains no copy or paraphrase of work published by another person, except where duly acknowledged in the text. This thesis contains no material which has been presented for a degree at the University of Sydney or any other university.

Oded Shrier
[redacted]

Abstract

Inertial electrostatic confinement (IEC) uses electrostatic fields to confine energetic ions such that nuclear fusion occurs. It basically consists of a concentric anode and cathode arrangement, with a mostly transparent cathode being the inner electrode. The attraction of this device is that it can produce substantial fusion rates in a table-top size chamber. However, current IEC devices are operated in the gaseous discharge regime. Consequently, there is considerable energy loss from inelastic collisions of ions with the predominantly neutral background gas. The most prominent of these collisions is charge exchange. This thesis is about experimental and theoretical investigations of various aspects of charge exchange in IEC devices.

The main aims of this work were to determine ion and neutral energy distributions, confinement times, fusion rates and the way these parameters scale with the size of the device and the electrostatic fields. A secondary aim was to use this knowledge to produce a new device that maximizes the neutron generation rate from the fusion reactions of energetic ions and neutrals with the background gas.

Doppler shift spectroscopy was used as the main diagnostic tool in this work. This enabled ion and neutral energy distributions to be determined. In the course of this work, a previously unreported phenomenon was found. Highly energetic and collimated beams of neutral atoms were found to exit the cathode. A model was proposed to account for this counter-intuitive phenomenon. It was proposed that the source of neutrals originates as ions in the cathode centre at the top of a potential hill. These then accelerate outwards and undergo charge exchange - exiting as neutral atoms from within the cathode. In addition, it was proposed that the substantial flux of these neutrals accounts for most of the fusion that occurs in IEC devices. The model involved the development of a new semi-analytical approach to charge exchange modelling that is similar to Markov chain theory and in contrast to the usual Monte Carlo approach. Computationally, this semi-analytical approach is much faster with no numerical noise. Moreover, this model was used to reproduce all the spectral work in this thesis, and the fusion rates of other IEC devices.

The success of the semi-analytical theory was applied to the design (and subsequent construction) of an ion cyclotron that operated under gaseous discharge conditions. Ions created within the cyclotron undergo charge exchange to produce energetic neutrals. Both an experimental and theoretical study was carried out to maximize the fusion rates from this device.

Acknowledgements

Metaphorically speaking, my life has followed a path resembling the sinusoidal snake track engraved on desert sands. Many kind, friendly, helpful, loving and encouraging people, whom I met along this path, have directly and indirectly helped me to reach this point. I thank them all, and in particular,

I thank my supervisor Dr. Joe Khachan. Words can not express my deep appreciation. He had dedicated much time to solve any experimental or theoretical thesis related problem that arose during the research, revised my writings and took care of bureaucratic issues. He was not only my supervisor but also my teacher and guide, seeing me through the stages of my development as a physicist. Moreover, being open-hearted and sensitive as he is, I could seek his advice on any matter that was not related to physics.

I also thank my first co-supervisor A/Prof. Brian James for his helpful comments and my later co-supervisor Dr. Stephen Bosi for his professional advice, mental support and for expanding my general knowledge on topics such as Italian spelling and grammar. My thanks also go to the plasma group members, whose professional advice was helpful and encouraging. Special thanks go to Dr. Alex Samarian and Dr. Ian Falconer for their useful advice and concern.

Further, I would like to thank Mr. Robert Davies for technical support, for being helpful and inventive. Part of this work could not have been carried out without the assistance of Mr. Michael Paterson and Mr. Terry Pfeiffer from the workshop. I thank them for their patience, professional work and for standing to schedule (they have taught me to use mm units instead of the more commonly used Angstrom units). Most special thanks to Ms Eve Teran from the student support office who helped me through any bureaucratic problem and with such dedication, willingness and kindness.

I would like to express my deep appreciation to the UPA scholarship scheme and many thanks to former Head of School A/Prof. Brian James and present Head of School A/Prof. Anne Green for financial support arrangements.

I take this opportunity to also thank my lecturers, who prepared me for my postgraduate studies and gave me the opportunity to enrol in the doctoral program at the University of Sydney: A/Prof. Tim Bedding, A/Prof. Anne Green, A/Prof. Robert Hewitt, Prof. Richard Hunstead, Dr. Gordon Robertson, Prof. Ross McPhedran, Dr. Kevin Varvell, A/Prof. Lawrence Peak, Prof. Marcela Bilek, Dr. Serdar Kuyucak. Special thanks to A/Prof. Tim Bedding from whom I learned a lot and supported me throughout my study period.

I was also lucky to share a room with my colleagues Michael Fitzgerald, John Kipritidis, Dr. Daniel Andruczyk, Aping Zeng and Nick Parslow. I thank them for their professional advice when needed and for their moral support, not to mention, all the fun times we had. Many thanks to Michael Fitzgerald ("twin brother"), who was both a supporting colleague and a friend to share our mutual interests in piano playing and martial arts.

There are many people out of the school of physics who helped me through this period whom I would like to thank: Aristotle Paipetis made my stay in Australia possible. Sharon and Greg Warren adopted me as a close family member, making my stay in Australia much easier. Without their help and support this work would have not been done in Sydney. My Ji Do Kwan (martial art) students, who had to endure my fists and kicks on bad days and some more on good days, were loving and caring all through. My piano teachers Ms Ella Eizenshtat and Mrs Gillian Selikowitz; the philosophical discussions and lessons were a break from the daily routine, clearing my mind and giving me motivation to continue forwards. Iqbal Syed and Lorraine Ivancic for balancing my emotional state with good food, wine and laughter.

Thanks to my family: Mum, Dad, my two sisters, my brother, and Shoham Shefy for being so supportive and encouraging throughout my entire life.

Last, I would like to thank Carmit Schwartz, my love and twin soul. Some parts of the "sinusoidal snake track" we have walked together. She was always supportive, understanding, helpful and caring. Although she is enrolled in a doctoral program herself, she was constantly there for me. It is for her that I managed to maintain a balancing perspective throughout the doctoral period and especially at the last stages.

I dedicate this thesis to whoever finds it useful.

Author's Publications

Publications

O. Shrier, J. Khachan, S. Bosi, M. Fitzgerald and N. Evans., "Diverging ion motion in an inertial electrostatic confinement discharge", Phys. of Plasmas, **13**, 012703 (2006).

O. Shrier, J. Khachan and S. Bosi, "A Markov chain approach to modelling charge exchange processes of an ion beam in monotonically increasing or decreasing potentials", J. Phys. A: Math. Gen., **39**, 11119–11128 (2006).

Conference

J. Khachan and O. Shrier, "Diverging ion motion in an IEC discharge", 8th U.S.-Japan Workshop on IEC Fusion, Kansai University, Osaka, Japan, May 10-12, 2006.

Contents

List of Figures

List of Tables

List of Tables

Chapter 1

Introduction

1.1 IEC initial concepts and its development

1.1.1 From the invention of television to a portable fusion device

Fusion is the process where two nuclei are brought together while overcoming Coulomb repulsion to be bound to one another by the strong nuclear force. Fusion between nuclei that have less mass than iron will result in the release of energy in the form of energetic protons, neutrons, alpha, and other energetic particles.

Table 1.1 presents the main fusion reactions occurring in fusion reactors and various other fusion devices. The particle energy (in brackets) or the total energy released (no brackets) is stated in MeV units and was calculated for zero energy reactants [1]. It is energetically too costly to produce nuclear fusion for energy generation by overcoming the Coulomb barrier, which is generally greater than 1MeV. For this reason, one relies on quantum tunnelling through the Coulomb barrier. In fact, in some cases the probability of fusion occurring reaches a peak at much lower energies than the maximum Coulomb barrier ($\sim$ 100 keV for D$-$T interactions). Table 1.2 presents the required activation energy corresponding to the maximum fusion cross section for each of the reactions stated in table 1.1.

$\mathrm{D+D\xrightarrow{50\%}T(1.011)+p(3.002)}$
$\mathrm{D+D\xrightarrow{50\%}{}^{3}He\,(0.820)+n(2.449)}$
$\mathrm{p+T\longrightarrow {}^{3}He+n-0.764}$
$\mathrm{D+T\longrightarrow {}^{4}He(3.560)+n(14.029)}$
$\mathrm{T+T\longrightarrow {}^{4}He+2n+11.332}$
$\mathrm{D+{}^{3}He\longrightarrow {}^{4}He(3.713)+p(14.640)}$
$\mathrm{T+{}^{3}He\xrightarrow{59\%}{}^{4}He+n+p+12.096}$
$\mathrm{T+{}^{3}He\xrightarrow{41\%}{}^{4}He\,(4.800)+D(9.520)}$
$\mathrm{{}^{3}He+{}^{3}He\longrightarrow {}^{4}He+2p+12.860}$

Table 1.1: Fusion Reactions

Reaction	Max cross section (barns)	Required energy (MeV)
D+D	$\sim 2 \times 10^{-1}$	~ 3.3
p+T	$\sim 6 \times 10^{-1}$	~ 3
D+T	~ 5	~ 0.11
T+T	$\sim 1.7 \times 10^{-1}$	~ 2
D+^{3}He	$\sim 7 \times 10^{-1}$	~ 0.43
T+^{3}He	$\sim 5 \times 10^{-1}$	~ 5
^{3}He+^{3}He	$\sim 2 \times 10^{-1}$	> 10

Table 1.2: Energies corresponding to maximum fusion cross sections

It has been shown theoretically and experimentally that the probability of a fusion event not only depends on the energies of the nuclei but also on their interaction time. Fusion for practical energy production requires the generation of a fully ionized plasma (10^{20} m^{-3}) so that one need only be concerned with the elastic collisions of Coulomb interactions, which has a much higher cross-section than fusion. Consequently, the fusion rates are determined by the plasma temperature and confinement time. The central theme of this thesis is the study of fusion reactions for the production of energetic neutrons in a weakly ionized plasma, where inelastic atomic collisions must be accounted for.

[1]Inertial electrostatic confinement (IEC) is a fusion method thought to provide the energy and confinement time using a deep electrostatic potential well and therefore, a promising energy source. Since its inception more than 50 years ago, IEC has not received the same level of research effort as magnetic confinement and consequently there was not much progress in its energy gain. However, it has developed to be a potentially useful portable neutron source having many applications in various fields (see section 1.2). During the many years of research the device has taken on many different designs while trying to improve its energy output. At present there are few groups around the world (mainly in Japan, USA and Australia) that are pursuing the IEC concept in the hope of improving the device's operation as a neutron source but ultimately to become an energy source.

The concept of IEC originated in the 1930's from the inventor of electronic television, Philo T. Farnsworth [2]. At 14 years of age Farnsworth sketched his idea of television for his science teacher. After spending several weeks working on the idea it was concluded that it was physically possible. A few years later Farnsworth went to study at Brigham Young University. During this period he spent much of his time learning about vacuum tubes and cathode ray tubes. In 1923 Farnsworth's father died and Farnsworth left college taking a number of jobs related to communication. Nevertheless, Farnsworth kept on trying to make television work and in the process he discovered the "multipactor" vacuum tube, which led to the IEC concept. With the multipactor vacuum tube Farnsworth could focus electrons at some point in space. During the same period plasma fusion was at its initial stages of development. One of the major problems the fusion community faced was heat loss due to

---

[1] Dedicated to the inventor of Television and IEC concept, Philo T. Farnsworth.

ions colliding with the chamber's wall. Farnsworth suggested a device that can confine ions to the centre of the chamber with a central negative space charge, thus preventing the ions from colliding with the chamber's wall. Farnsworth called the central electron density build-up a "virtual electrode", and the entire set-up was named "the fusor". This first design was cylindrical where ions were injected into the vacuum tube and accelerated to the centre by the virtual cathode. Positively charged electrodes were placed around the virtual cathode with the aim of preventing ions from escaping to the wall. Moreover, it was thought that new ions accelerating to the centre would further help confine ions trying to escape from the centre. Farnsworth named this method "Inertial Electrostatic Confinement". Although this relatively simple fusor could produce fusion reactions, the electrodynamics in such a system was far more complex than Farnsworth imagined and the fusor did not fulfill its initial aim of energy generation.

In the early 1960s the cylindrical arrangement became a spherical one although still using the same concepts [3]. During the same period Hirsch [4] simplified the device by replacing the virtual cathode with a real spherical cathode grid surrounded by a larger spherical anode mesh. This design was named the Hirsch-Meeks Fusor and became the standard device, which continues in most of the IEC laboratories to-date. A convergent ion focus was produced at the cathode centre where fusion took place. The means of ion production ranged from external ion guns to the production of a discharge between anode and cathode. The highly transparent cathode allowed multiple passes of ions through the centre thus increasing the confinement time. It was also thought that positive ions collecting on the cathode would further confine ions already at the core [5]. This Fusor was successful since it was simple, compact in size and produced neutrons but not promising enough for the ITT corporation to continue supporting this work (interestingly, the same company had purchased the Farnsworth television labs). In 1967 the company stopped funding fusion research, which led the fusor team to apply for funding from the atomic energy commission (AEC). One anecdotal story concerning the request for funding from the AEC is that Hirsch appeared before a committee with an operating portable IEC device. Although the committee was impressed, due to other priorities the funding was refused. In 1968 Farnsworth's team operated as a new company at Brigham Young University. Due to large debts, in 1971 the IRS seized their assets and in that same year Farnsworth died.

Although IEC started in the USA, in 1963 Lavrent'ev [6] from the USSR came up with similar ideas to standard IEC. For the first time Europeans became interested in the potential of IEC. This concept was soon abandoned for the more popular TOKAMAK concept. In the 1970s most of the experimental IEC research was sparse but increased in the 1980s with Miley and Nadler [7, 8] from the University of Illinois, and Bussard [9] being some of the main groups. In the early 1990s the IEC concept split into two main streams: the grid cathode approach and the virtual cathode approach using magnetic and electric fields to create a dense negative space charge (virtual cathode). The latter is similar to the initial Farnsworth concept and overcomes the main problems arising from the solid grid cathode, which are sputtering and melting due to the high electron-ion currents [9–17]. During the

1990s research groups in Japan became much involved in IEC development and applications (among are Tokyo Inst. Tec., Kyoto University and Kansai University). A collaboration between Japan and the U.S. was established and in 1998 the first U.S.-Japan IEC work shop took place at Los Alamos National Laboratory (LANL) in the U.S.

1.1.2 The grid cathode IEC device

The work presented in this thesis is related to the study of solid cathode IEC systems. Nevertheless, it should be noted that much work has been done in the field of virtual cathodes and it is claimed that these systems can produce net energy gain [18–20]. The major problems concerning these systems are the instability of the virtual cathode and the depth of potential being limited to a fraction of the applied voltage [21–24]. A slab model predicted that in the kinetic limit a constant density of electron cloud becomes unstable when the ratio of the effective Debye length to the plasma radius is smaller than one and that the maximum potential depth is limited to $\sim 14\%$ of the applied voltage [25]. However, in later experiments a potential of $\sim 60\%$ of the applied voltage was measured and the discrepancy is explained with the same model for the electron-electron two-stream stability limit but considering spherical geometry instead of slab geometry (basically, solving in spherical coordinates and in three dimensions the fluid equation of continuity for zero pressure, the dynamic equation for conservation of momentum and Poisson's equation). These calculations predict a potential depth limit of $\sim 90\%$ of the applied potential [21].

Figure 1.1 illustrates a commonly used system for commercial and research purposes. This consists of a concentric spherical anode and cathode arrangement where the cathode is the inner grid. Cathode diameters used in previous IEC studies range between 2 cm and 20 cm, where anode diameters range between 30 cm and 50 cm. This assembly of electrodes is placed in a spherical or cylindrical vacuum chamber with gas pressures from 0.5 mTorr to ~ 30 mTorr. This range enables neutron and optical diagnostics to be applied [26–30]. The cathode voltages are mainly restricted by arcing and most experiments were carried out with voltages up to 70 kV (improvements in technology enables pulsed IEC to operate at 110 kV [31]). Current IEC devices have used D$-$D or D$-$T reactions, both of which produce highly energetic neutrons. The device has also shown promise with the use of D$-^3$He [32–34], which is an aneutronic reaction. The methods used to ionize the gas include glow discharge that may be supplemented with RF breakdown ionization [26, 27, 30] or with an additional third outermost grid. For the latter, hot tungsten filaments placed near the walls emit electrons that accelerate to the positively biased grid while ionizing the plasma via collisions [29].

There are several advantages to the relatively simple set-up shown in Fig. 1.1. The ions are accelerated directly by a central electric field, which leads to a non-Maxwellian ion energy distribution. Ideally, this mono-energetic distribution should be maintained at the cathode's centre. Since the fusion cross sections are largely dependent on the ion energies, beam-beam interactions in the centre of cathode should be significant. However, at present most of the fusion reactions are shown to be a product of beam-background interactions [28]

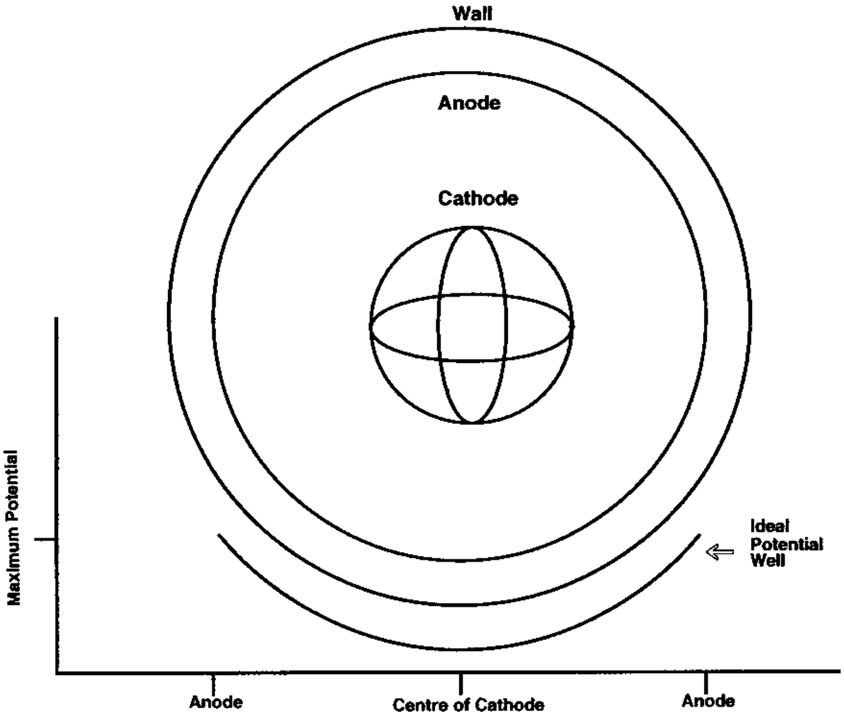

Figure 1.1: The standard IEC system of cathode and anode grids . The ideal potential well is responsible for the confinement.

- several reasons are presented in section 1.2. As a neutron source, gas target fusion (beam-background interactions) has an advantage over solid target fusion since the targets do not deteriorate. The simplicity of the device, which does not exploit magnetic fields (avoiding cyclotron radiation and drifts associated with magnetic fields) enables the use of advanced fuels such as p$-^{11}$B. This is a cheap natural isotope that in the fusion process produces 3 alpha particles for each reaction and a total energy release of 8.7 Mev. The reaction is free from radioactive products and the energy can be directly converted into electric power [34,35]. In the IEC configuration the fusion products are not used to heat the plasma and their energy can be directly converted into the required energy form. Lastly, since the device is compact and portable it can be used as a neutron source for various potential applications (see section 1.2).

1.2 Current state of IEC research

At present the output power of IEC is about $7-8$ orders of magnitude lower than the input power. Although it is far from being an efficient energy source it is improving as a neutron/proton source. The University of Wisconsin have shown results of $\sim 10^6$ and $\sim 10^7$ n/s with D$-$D and D$-^3$He reactions (it is potentially $\sim$ 3 orders of magnitude more for D$-$T reactions) [28,32,33] where as, the University of Illinois at Urbana-Champaign achieved $\sim 10^8$ n/s using the IEC device in the pulsed mode [36]. The applications of a neutron source scale with neutron/proton production rates. In the range of $10^5 - 10^7$ n/s the source can be used for teaching experiments, dosimeter calibration, on-line raw material analysis and research of new applications. With $10^8 - 10^{11}$ n/s the source can be used for air luggage security inspection, portable analysis applications, isotope activation proton source and as a thermal neutron lens. An emitter of $10^{12} - 10^{13}$ n/s can be used for land mine detection, boron neutron capture therapy, sub-critical reactors. The many technological and industrial applications of a portable neutron source strongly promotes IEC research. In Japan IEC research groups are investigating the IEC neutron source with respect to cancer treatment and detection of land mines [37]. The IEC group at the University of Wisconsin are involved in many of the mentioned applications [34, 38, 39].

For the last 50 years knowledge of IEC has been accumulating via experimental and theoretical studies. Hirsch [5] was the first to achieved a maximum count rate of $\sim 10^{10}$ n/s. Models based on beam-beam interactions could not account for these fusion rates where Baxter and Stuart [40] were the first to explain the high reactivity in Hirsch's experiments assuming beam-backround interactions. They developed a model assuming a mixture of ions and fast neutrals having a distribution of energies ranging from zero to the maximum energy gained by the ion gun potential. The combination of highly energetic ions (achieved with the ion guns) and the relatively large corresponding D−T fusion cross sections could account for the reactivity while considering the charge exchange process taking place in the accelerating path of the ion guns. Although their study was applied to the ion guns arrangement, it was later experimentally found that the beam-background interactions dominate also in conventional gridded IEC devices. This is supported by some experimental studies showing that the neutron counts linearly increase with increased ion density and furthermore, claiming that the total reactivity originates mainly from regions outside the cathode [28].

Considering the operational principles of the device it is not surprising that the cathode core has been of major interest. Although ions supposedly converge to the centre of cathode, the beam-beam interactions in the core are a lesser component in the total fusion count. The more significant contributor to the fusion count is the neutral-background fusion interaction, originating from the charge exchange process. This process is dominant in experimental set-ups that operate at pressures higher than ~ 0.5 mTorr where the ion beams are largely attenuated before reaching the cathode core. Equally important is the complex potential that is established in the core that further reduces the beam-beam dominance. Independent and direct experimental measurements show that a virtual anode is established at the centre of the cathode [26, 29]. This give rise to a potential well extending from the anode to the centre of cathode, where the minimum of the potential is found to rest at the cathode's edge (see Fig. 3.2). The maximum potential depth has been measured to be in the range of 20%− 60% of the applied potential. The converging ions should not only be slowed down by the virtual anode but also a deflected current should be established (deflected from the radial direction). Regardless of these experimental measurements, there have been studies of multiple virtual electrodes in the cathode core [5, 41, 42]. Hirsch initially attempted to explained his high neutron count measurements with a model of multiple virtual electrodes

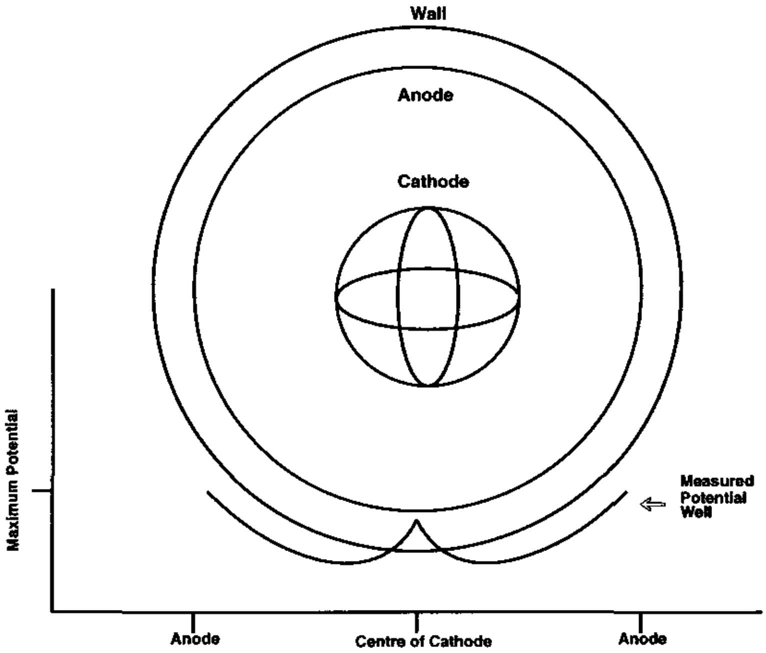

Figure 1.2: A schematic of the measured potential well. The well extends from the anode to the cathode centre and the minimum of the potential is found at the cathode edge.

that would trap a high density of hot plasma in the core. The required density of the hot plasma was found to be orders of magnitude larger than the density of the injected ion beam and Hirsch did not support the model with experimental measurements of the core density. Microwave cavity measurements of electron densities [43] in similar experiments to Hirsch's suggest that Hirsch's model is not responsible for the neutron counts. Although there were other studies and theoretical predictions of multi electrode structure [41,42], there is no conclusive experimental evidence supporting such structures for the neutron producing devices.

Cathode physical parameters were comprehensively and systematically studied by Thorson et al. [28]. The transparency of the spherical grid cathode was varied by changing the thickness of the grid's wire. Transparency ranging between 91% – 96% did not significantly change the neutron production rates. However, increasing the cathode radius did show a slight increase in the neutron production rates. Different cathode materials such as stainless steel, titanium and tungsten showed small variations in the neutron production rates. Other cathode geometries [26, 27, 30] have been used for spectroscopic diagnostics (see chapter 2). A two ring cathode has been used in order to isolate an emission channel thereby creating a one dimensional IEC device. Further, a two coned cathode was used to collimate the hot neutrals comprising the beams and responsible for the emission channels [26, 27, 30]. A two coned cathode is also used in the experiments presented in chapter 5, where the experiments suggest that a maximum potential depth of 60% of the applied voltage is established at the cathode's edge.

Currently there are technical and physical issues that must be resolved before IEC can progress towards a viable fusion energy device. The technical issues mainly concern cathode materials, arcing (limiting the applied voltages) and energy conversion [44]. As for the physical issues, the limited potential depth is of great concern. The established steady state potential depth has been shown to be a fraction of the maximum applied potential, consequently preventing the ions from gaining the maximum possible kinetic energy. To overcome this problem the applied voltage can be increased but this solution is limited by technical problems such as cathode melting and arcing. A theoretical study [45] has shown that non-equilibrium fusion systems, which include IEC, lose energy from Bremsstrahlung radiation at a greater rate than fusion energy gain. However, this is mass dependent and D−T and D−D fuels can still provide a net energy gain. The potential established by ion-electron currents (where a virtual anode is established at the centre of the cathode) changes the ion confinement mechanism. Moreover, calculations show [46] that the ion thermalization time will be much shorter than the ion fusion time. Another physical issue concerns sputtering where energy is lost via collisions and X-rays emission. The heavy ions that are created in the process further reduce the efficiency of the device since they have lower fusion cross sections.

A major energy loss mechanism is charge exchange (and the major focus of the work presented in this thesis). Most IEC devices are operated in the units of mTorr range where charge exchange is dominant. Charge exchange attenuates the ion beams, redistributes ion/neutral energies while reducing the ion energies. Consequently, energy is lost and fusion rates are limited to a maximum that depends on the background gas pressure.

1.3 Aims of this thesis

The major aims of this work include: the explanation of the spectral line resulting from Doppler shift measurements of energetic neutrals in an IEC discharge. A model describing charge exchange was developed and was used for this purpose. In the experimental stage of the work a significant amount of neutral atoms were found to diverge from the cathode. This is contrary to the traditional view of ions converging to the cathode, which has an impact on the confinement mechanism and fusion rate output of the device. When analyzing the spectral line this phenomenon was included and accounted for. The model was further used to predict fusion rates while considering this phenomenon. The results were shown to agree with previous experimental work of others. A systematic experimental study of the scaling of the device with varied parameters was carried out. As a consequence a new neutron producing device was designed and built in the aim of improving the neutron production. Spectroscopic measurements were compared with the model, which was extended to apply to a two dimensional system. Once the model was verified through spectroscopic measurements, predictions of the neutron production rate were carried out.

Specifically, the work presented in this thesis concerns charge exchange collisions, which is the predominant interaction for IEC devices operating in the gaseous discharge regime. Charge exchange represents a major energy loss mechanism since it results in energetic neutrals that can leave the system without any confinement. The process also redistributes the ion/neutral energies while preventing them from having a mono-energetic distribution at the centre of cathode.

The excited energetic neutrals have been used to determine their energies by the emitted Doppler shifted spectrum [26,27]. It has been found that the maximum ion energy was $\sim 25\%$ of the applied potential energy for the device operating in units and tens of mTorr pressure range. It was further shown that this energy corresponds to the maximum potential depth of the potential well that is established between the centre of cathode and anode. This implies that the steady state potential established in the plasma is a significant constraint on the possible maximum ion energies. However, this for itself does not account for the broad ion energy distribution that is suggested by the broad extended Doppler shifted wings observed in the spectra. As will be explained in detail in chapter 2, the Doppler shifted wings are formed by the distribution of wavelength shifts caused by de-exciting hot neutrals having a broad distribution of energies (e.g. see Fig. 2.8). It has been established [26, 27] that the excited hot neutrals are formed via charge exchange, implying that charge exchange is a dominant process that significantly reduces the ion energies.

When using hydrogen gas (for diagnostic purposes) or deuterium gas (for neutron counting experiments), several molecular species form in the plasma. The most dominant species are H^+, H_2^+ and H_3^+ (or D^+, D_2^+ and D_3^+) where the formation of these is largely dependent on charge exchange as well as on other processes [26, 27, 47]. Since heavy molecules gain lower velocities the fusion cross sections per nucleon drops significantly. Furthermore, the charge exchange process is partially responsible for the breaking down of the assumption of a peaked uniform energy distribution at the centre of cathode. As demonstrated in this work, due to significant damping of ion energies only a fractions of the entire ion density gains the maximum possible potential energy. Baxter and Stuart [40] showed that charge exchange could explain the high fusion rates in Hirsch's ion guns experiment. Thorson et al. [28] experimentally demonstrated that charge exchange is dominant in conventional IEC devices. However, there was no specific charge exchange modelling applied to the conventional gridded IEC device. As part of the study of the influence of molecular species on the net resulting energy distribution, a semi-analytical method is developed to model the charge exchange process while accounting for each separate specie [48]. This enables the prediction of the energy distributions resulting from each specie (since the method is easy to compute, flexible in changing input parameters and does not consume much computer operation time, a large number of systems can be studied).

The Doppler shift has been used to measure ion energies, to distinguish between different ion species and to find relative ion densities [26, 27]. This is a non-intrusive diagnostic and is well suited to this type of discharge. Doppler shift diagnostics relies on the emission received from de-exciting fast neutral atoms that are created via charge exchange. Although the properties of the resulting spectra were sufficiently understood for extracting physical information [26,27,30], there was no model to account for the specific details of the spectrum shape. In this work charge exchange models are applied to specific IEC devices and other discharge systems confirming assumptions made in previous work and further detailing the information of the energy distributions responsible for the spectrum shape. Consequently, the diagnostic method is justified and better understood.

The conventional view of the IEC operation is of ions converging from the outer spherical anode to the centre of an inner spherical grid cathode. As a result of charge exchange, the ion energy distribution depends strongly on distance. Changing the path length is simply a matter of changing the distance between electrodes. The ion energy distribution, as a result of charge exchange, is also dependent on gas pressure and cathode voltage. Consequently, one of the aims of this study was to model the dependence of the ion energy distribution on path length, pressure and electric field. This enabled the optimization of these parameters for maximum fusion rates. Moreover, it enabled the prediction of spectroscopic line shapes. Measurements of the line shapes of the hydrogen H_α Balmer line were carried out for many different combinations of path length, pressure and electric field in order to test the predictions of the model and to establish scaling laws. To the author's knowledge, this is the first systematic study of the influence of the anode to cathode distance, pressure and voltage on the ions' energy distribution. Previous studies were mainly concerned with the cathode's physical features [28].

In the course of determining the spectroscopic line shape, it was strongly suggested that a substantial number of energetic neutral atoms originated from the cathode centre while diverging from the cathode. Consequently, an additional aim was the inclusion of this phenomenon in conjunction with earlier work and with the work presented in this thesis. This more accurately accounts for the spectroscopic line shape and for any ion confinement that occurs in a gridded IEC device.

This thesis further extends beyond an IEC device with the aim of producing an efficient neutron device that makes use of the optimization of the three parameters (investigated with the IEC device): ion path length, gas pressure and applied electric field. This is a target based neutron source exploiting charge exchange that is caused by ion cyclotron motion in cold background gas. In the study of the IEC device the charge exchange model was applied to a one dimensional problem of a beam of ions in a hydrogen background gas. In the study of the ICR device the model is extended to solve a two dimensional problem for spiraling ions in a hydrogen background gas. The validation of the model through spectroscopic measurements both on IEC and ICR devices, allows for the extrapolations and predictions of the fusion rates for varied parameters.

1.4 Overall view of the thesis

About three quarters of the volume of this work concerns the study of an IEC device while focussing on charge exchange. As mentioned in section 1.2, in recent years IEC devices have become potentially useful neutron sources with various commercial applications [31, 34, 37–39, 49]. In the remaining quarter of this work, conclusions drawn from the IEC study are further used to investigate a new type of target based neutron source that uses ion cyclotron resonance, hereafter named “ion cyclotron resonance” (ICR) device. The investigation is carried out using modelling and is supplemented with a first experimental prototype.

Chapter 1 has presented a brief discussion of IEC history, principles of operation, current state of research and the contributions of this work. Chapter 2 presents the experimental apparatus of the IEC device and a discussion of the Doppler shift diagnostic method in relation to IEC studies. In chapter 3 a semi-analytical method of modelling charge exchange is developed in the aims of verifying the interpretation of experimental spectra with the resulting ion energy distributions, predicting ion energy distributions for various experimental set-ups operating at various conditions and estimating fusion rates. Chapter 4 presents experimental evidence suggesting that a substantial number of energetic neutral atoms are diverging out from the cathode. Assuming these findings and based on the charge exchange model, the spectrum line shapes are simulated and explained. Other applications of the model concerning high pressure discharge systems and IEC confinement time are also presented. Chapter 5 presents a comprehensive experimental study of the beams (emission channels), which extend from the centre of cathode, through the anodes, to the wall of the chamber. Scaling rules are found for variations in anode to cathode distance, gas pressure and applied voltage. In chapter 6 neutron/proton production rates are estimated and are compared with published experimental data. The calculations consider the new observation presented in chapter 4 and are based on the charge exchange model. Chapter 7 presents the principles of operation of a prototype of the neutron producing ICR device. A two dimensional model is developed to describe the charge exchange in the device. Chapter 8 presents the experimental apparatus of the ICR device. Results of initial experiments that measured neutral hydrogen energies are compared with the model results. Furthermore, the expected neutron production rates of the ICR device are approximated with two methods. In chapter 9 overall conclusions are drawn and suggestions for further work are presented.

Bibliography

[1] G. W. C. Kaye and T. H. Laby, "Tables of Physical and Chemical Constants" (1989).

[2] P. Schatzkin, "Farnsworth Chronicles".

[3] P.T. Farnsworth, Patent #3,258,402, issued 28 June 1966.

[4] R. L. Hirsch et al., Patent #3,530,497, issued 22 Sep 1970.

[5] R. L. Hirsch, J. Appl. Phys., **38**, 4522 (1967).

[6] O. A. Lavrent 'ev, Ukr. Fiz. Zh., **8**, 440 (1963).

[7] J. H. Nadler, G. H. Miley, Y. Gu, T. Hochberg, Fusion Technology, **21**, 1639 (1992).

[8] G. H. Miley, 1991 U.S. - Japan Workshop on Nuclear Fusion in Dense Plasmas, Austin, TX , Oct. 7-9, 1991 (sited by J.H. Nadler).

[9] R. W. Bussad, Fusion Technol., **19**, 273 (1991).

[10] N. A. Krall, Fusion Technol., **22**, 42 (1992).

[11] M. M. Schauer, T. B. Mitchell, M. H. Holtzcheiter and D. C. Barnes, Rev. Sci. Instrum., **68**, 3340 (1997).

[12] T. B. Mitchell, M. M. Schauer and D. C. Barnes, Phys. Rev. Lett., **78**, 58 (1997).

[13] D. C. Barnes, T. B. Mitchell and M. M. Schauer, Phys. Plasmas, **4**, 1745 (1997).

[14] D. C. Barnes and R. A. Nebel, Physics of Plasmas, **5**, 2498 (1998).

[15] R. A. Nebel and D. C. Barnes, Fusion Tech., **38**, 28 (1998).

[16] D. C. Barnes, Phys. Plasmas, **6**, 4472 (1999).

[17] D. C. Barnes, M. M. Schauer, K. R. Umstadter et al., Phys. Plasmas, **7**, 1693 (2000).

[18] R. L. Hirsch, Phys. Fluids, **11**, 2486 (1968).

[19] D. A. Swanson, B. E. Cherrington and J. T. Verdeyen, Phys. Fluids, **16**, 1939 (1973).

[20] R. A. Nebel and J. M. Finn, Phys. Plasmas, **7**, 839 (2000).

[21] R. A. Nebel, S. Stange, J. Park, J. M. Taccetti, S. K. Murali and C. E. Garcia, Phys. of Plasmas, **12**, 012701 (2005).

[22] A. Siebenförcher and R. Schrittwieser, Rev. Sci. Instrum., **67**, 849 (1996).

[23] J. Park, R. A. Nebel, W. G. Rellergert and M. D. Sekora, Phys. Plasmas, **10**, 3841 (2003).

[24] N. A. Krall, M. Coleman, K. Maffei, J. Lovberg, R. Jacobsen and R. W. Bussard, Phys. Plasmas, **2**, 146 (1995).

[25] R. A. Nebel and J. M. Finn, Phys. Plasmas, **8**, 1505 (2001).

[26] J. Khachan, D. Moore and S. Bosi, Phys. of Plasmas, **10**(3), 596 (2003).

[27] J. Khachan and S. Collis, Phys. of Plasmas, **8**(4), 1299 (2001).

[28] T. A. Thorson, R. D. Durst, R. J. Fonck and A. C. Sontag, Nuclear Fusion, **38**(4), 945 (1998).

[29] T. A. Thorson, R. D. Durst, R. J. Fonck and L. P. Wainwright, Phys. Plasmas, **4**(1), 4 (1997).

[30] O. Shrier, J. Khachan, S. Bosi, M. Fitzgerald and N. Evans., Phys. of Plasmas, **13**, 012703 (2006).

[31] G. L. Kulcinski, "Overview of University of Wisconsin IEC Research", 8th U.S.-Japan Workshop on IEC Fusion, Kansai University, Osaka, Japan, May 10-12, 2006.

[32] R. P. Ashley et al., Fusion Tech., **39**, 546 (2001).

[33] R. P. Ashley et al., "Progress in Steady State D ^{3}He Fusion at the University of Wisconsin", Proc. of U.S.-Japan workshop, March 22-23, 2001, Huntsville, AL.

[34] G. L. Kulcinski and J. F. Santarius, Fusion Tech., **39**, 480-485 (2001).

[35] G. L. Kulcinski and J. F. Santarius, "New Horizons for Fusion - Advanced Fuels for the 21st Century," APS Meeting, New Orleans L. A., 19 November 1998.

[36] G. H. Miley, Proc. of 2^{nd} U.S. - Japan workshop on IEC Neutron Source, Osaka, Japan, Feb. 28-29, 2000.

[37] K. Yoshikawa, "Current Status of IEC (Inertial Electrostatic Confinement) Fusion Neutron/Proton Source Study", (available on web).

[38] G. L. Kulcinski, Fusion Tech., **30**, 411 (1996).

[39] G. L. Kulcinski, Fusion Tech., **34**, 477 (1998).

[40] D. C. Baxter and G. W. Stuart, J. Appl. Phys., **53**, 7 (1982).

[41] B. E. Cherrington, J. T. Verdeyen and D. A. Swanson, Ann. (N.Y.) Acad. Sci., **251**, 139 (1975).

[42] J. T. Verdeyen, B. E. Cherrington, D. A. Swanson and D. J. Meeker, Ann. (N.Y.) Acad. Sci., **251**, 126 (1975).

[43] A. L. Gardner, "Studies of Charged-Particle Distributions in an Electrostatic Confinement System", ERDA Tech. Report (1976).

[44] J. H. Nadler, "INERTIAL-ELECTROSTATIC CONFINEMENT (IEC) OF A FUSION PLASMA WITH GRIDS", Nuclear Engineering Department, University of Illinois, Urbana, IL 61801 (available on web).

[45] T. H. Rider, Physics of Plasmas, **2**(6), 1853-1872 (1995).

[46] W. M. Nevins, Phys. Plasmas, **2**, 3804 (1995).

[47] C. Barbeau and J. Jolly, J. Phys. D: Appl. Phys., **23**, 1168 (1990).

[48] O. Shrier, J. Khachan and S. Bosi, J. Phys. A: Math. Gen., **39**, 11119–11128 (2006).

[49] K. Yoshikawa, "A Current Status of Humanitarian Landmine Detection With A Compact Water-Cooled IEC Device", 8th U.S.-Japan Workshop on IEC Fusion, Kansai University, Osaka, Japan, May 10-12, 2006.

Chapter 2

Apparatus and Diagnostic Method

In this chapter the experimental apparatus is presented in detail. This is followed with a presentation of the Doppler shift diagnostic method and a review of the Doppler spectra analysis. A section is dedicated to measurements and spectra analysis related issues that concern the work presented in this thesis.

2.1 Experimental apparatus

2.1.1 Background

In a typical IEC, an approximately spherically symmetric cathode grid is mounted in the center of a larger spherical anode grid within a vacuum chamber (see cathode in Fig. 1.1). In some devices, a spherically symmetric chamber acts as the anode. The chamber may contain H_2 or D_2 gas in the range of units of mTorr pressure, depending on the application. When a sufficiently large dc bias is applied between the anode and cathode, beams of collimated discharge "channels" emanate radially through the apertures in the cathode grid, appearing to intersect at the cathode center ("star mode" [1]).

In earlier work [2], Doppler spectroscopic measurements of channel ion energies on a spherical IEC cathode were confounded by the nearly spherical symmetry of the arrangement of the resulting channels because of the difficulty in separating the optical emission of numerous converging channels from the one under study. This led to two designs for reduced symmetry cathodes, which produced mainly two oppositely directed channels.

The first design consisted of a two parallel ring cathode, where the centers of the two rings were placed on the same axis [3]. The diameter of each ring was 20 mm and the separation of the rings was 20 mm. This enabled Doppler spectra originating within the cathode and those just outside it to be measured. The second design included a cathode that consisted of two hollow stainless-steel cones attached base-to-base (see cathode in Fig. 2.2). The tips of the cones were truncated to produce the two apertures that served to collimate the two channels in the direction of the cone axis. The use of this "biconical" cathode resulted in sharper and better defined spectra than for the spherical and rings IEC cathodes. However, the spectra outside all cathodes were found to be similar in shape and the only difference was

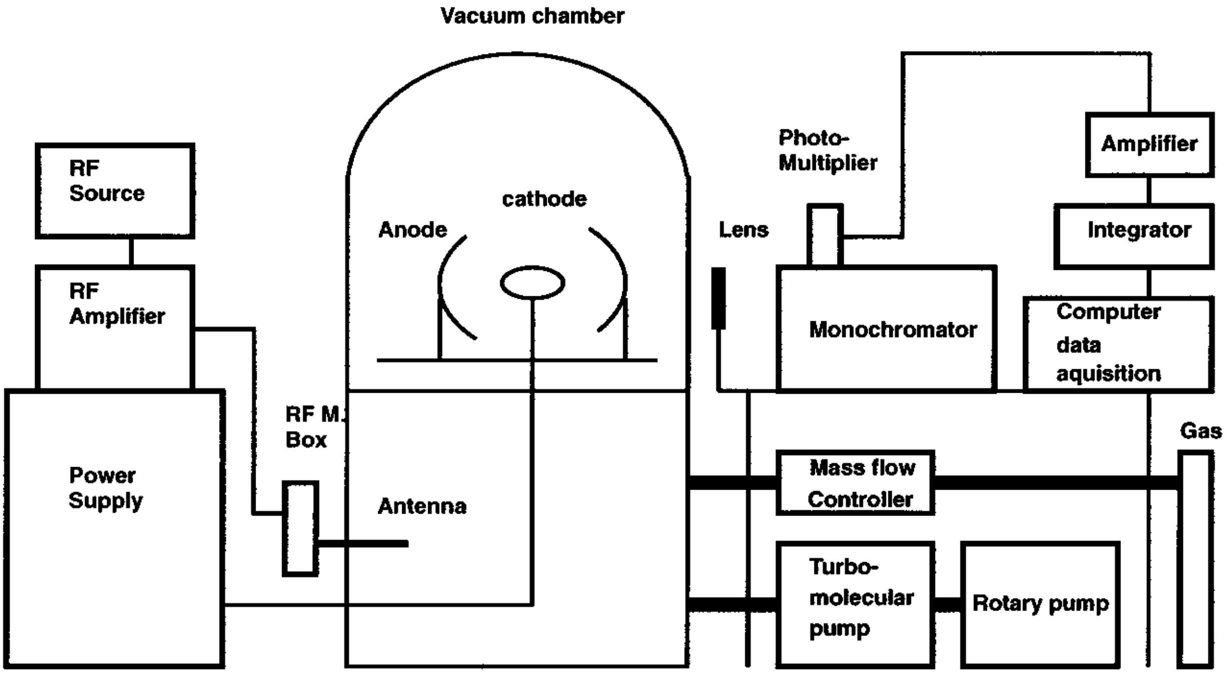

Figure 2.1: The experimental IEC assembly.

the resolution of the structure in the spectra wings.

This work presents experimental results obtained with the biconical cathode. First a description of the apparatus will be given.

2.1.2 The apparatus

In this work Doppler spectroscopy was carried out on the set-up shown in Fig. 2.1. The cathode in the vacuum chamber was negatively biased with a DC voltage ranging between −1 and −10 kV. To ensure a sustained DC discharge when the cathode was DC biased, a low power RF source amplified by an RF amplifier (10 W at 14.2 MHz) was used. The signal was transferred through an RF impedance matching box to a short antenna that was placed well outside the anode grids so that the intensity of the RF excitation did not obscure the intensity of the channel under investigation. Spectroscopic measurements were carried out with and without the external RF discharge, and no difference between the two cases was found. Consequently, it was assumed that the behavior of the species within the discharge, as determined by spectral behavior, was dominated by the effects of the large dc bias. This enabled the pressure and voltage to be varied independently of each other.

The gas pressure was regulated with a mass flow controller. A rotary pump and a turbomolecular pump (500 l/s) were used, enabling a base pressure well below 1 millitorr to be reached.

A red-sensitive photo-multiplier (Hamamatsu R1509) was mounted on a scanning monochromator (2051 GCA/McPherson), having a resolution of 0.07 nm. The signal from the photo-

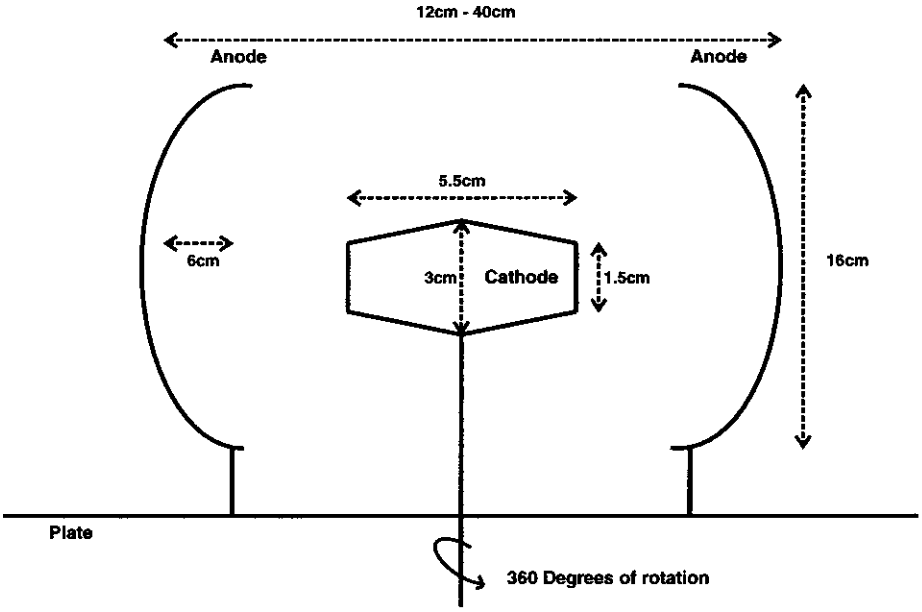

Figure 2.2: The assembly within the vaccum chamber.

multiplier was amplified and averaged using a box-car integrator (Stanford Research System SR 250). In some cases the monochromator's slit was widened from 25 microns to a maximum of 75 microns however, this did not adversely affect any of the results. Increasing the width was needed for lower pressures (<10 mTorr) since the emission intensity was dependent on pressure. A lower pressure in general meant lower intensity. The width was also increased when observing an emission channel at 30° or 90° angle relative to the channel. Resolvable spectra with good signal to noise were obtained for pressures higher than ~ 5 mTorr. The data acquisition system consisted of a PC and a 12 bit, 100 kHz Keithley Instruments DAQ1400 data acquisition card. The software supplied with this card, Easyest AG, was used.

The vacuum chamber consisted of a glass bell jar back-filled with hydrogen gas. Figure 2.2 shows the assembly within the vacuum chamber. The biconical cathode (two hollow stainless steel cones attached with their larger bases) diameter at its two tips was 1.5 cm and at center 3.5 cm. The total length of the cathode was 5.5 cm and it was centered in the chamber above a surface of a long aluminum plate, which was 17 cm from the axis of the cathode (see Fig. 2.2). Two hemispherical stainless steel meshes (diameter of 16 cm) were used as anodes and were mounted on the plate at each side of the cathode. The anodes could be mounted at different distances from the cathode independently in intervals of 2 cm and were held at the same potential as the vacuum chamber. The plate could be turned around its centre axis 360°, allowing Doppler spectroscopy measurements to be taken from different angles with respect to the channels.

The system described above produced two intense collimated beams (channels) spanning the distance between the cathode and anodes (see Fig. 2.3). The spectra from the regions of interest along the channels were sampled by using a glass lens to project a real image of

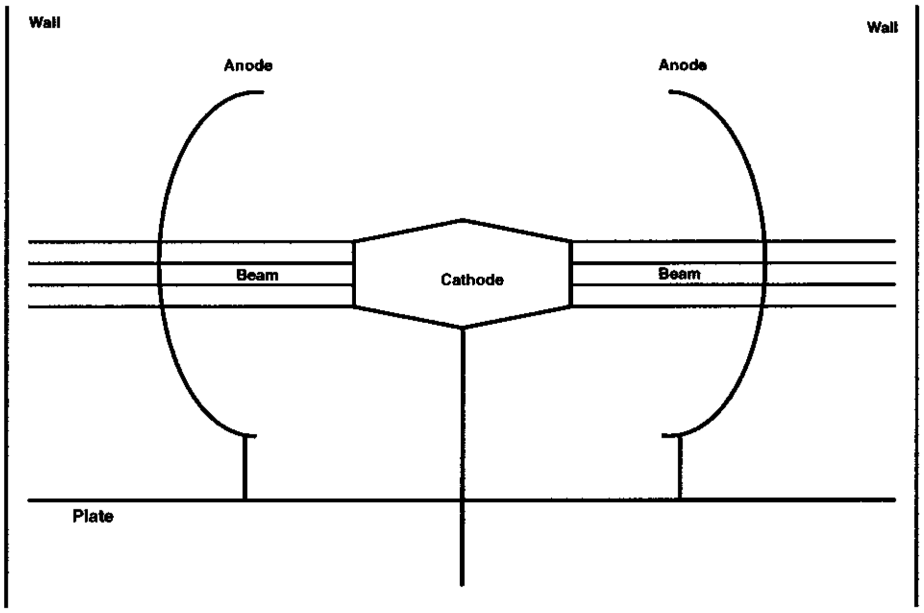

Figure 2.3: A schematic of the two intense collimated beams (channels) spanning the distance between the cathode and anodes. The beams go through the anodes mesh reaching the wall of the chamber.

those regions onto the entrance slit of the monochromator. Alignment of the monochromator was carried out with a helium-neon laser to set the correct entrance angle between the beam and monochromator axes. The 360° rotatibility in the horizontal plane of the aluminum plate (with the cathode and anode) enabled measurements at 0°, 30° and 90° relative to the beam. Spectra were measured for dc cathode bias voltages in the range of -1 to -10 kV and pressures in the range of $5-30$ mTorr.

2.1.3 RF matching unit

In the assembly shown in Fig. 2.1 an RF source was used to enhance the ionization of the gas. An in-house RF impedance matching box was built to couple the RF power to the antenna. The circuit is shown in Fig. 2.4 and will now be described.

In this design two variable capacitors C_1, C_2, and an inductor L were used as shown in Fig. 2.4. The impedance Z of the capacitors, inductor and IEC device were measured in vacuum. Ideally, the capacitors should have only capacitive reactance of $X_c = -1/\omega C$, and the inductor only an inductive reactance of $X_L = \omega L$. In practice high voltage capacitors and inductors were used, which had a resistive component r as well. We found the following impedances for the components used:

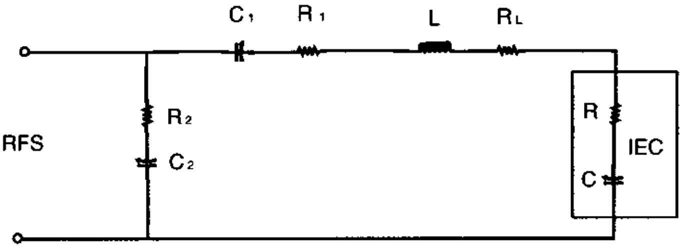

Figure 2.4: The RF matching circuit used in the apparatus of Fig. 2.1.

Component	Amplitude	Phase
C_1	0.358 kΩ	−90°
C_2	12.53 Ω	−80.3°
L	5.35 kΩ	88°
IEC	1 kΩ	−82.7°

Note that C_2, L and the IEC device have a resistive component, which is a resistance equivalent to all the parasitic effects associated with a certain component. The RF source (RFS) was chosen to operate at a frequency of $f = 14.25$ MHz, and analysis was carried out to determine the capacitive or inductive reactance and the resistance of each element (note that $\omega = 2\pi f$).

Variable capacitors were used to compensate for the changing plasma impedance. The forward and reflected power were monitored with a power meter placed in series between the RF amplifier and the matching box. In this case C_1 and C_2 could be varied to maximum capacitances of ~ 35 pF and ~ 750 pF respectively, and the RFS frequency could be varied in the range of units and tens of MHz.

Figure 2.4 shows the RF impedance matching circuit used in this work. The resistive components, indicated by R_1, R_2 and R_L, arise naturally within the components of the systems. Note also that there is a resistance R associated with the discharge.

The objective is to match the input impedance of the circuit to the output impedance of the RF source, which is 50Ω. The input of the circuit consists of two parallel impedances given as:

$$\frac{1}{Z_1} + \frac{1}{Z_2} = \frac{1}{50} \tag{2.1}$$

where:

$$\begin{aligned} Z_1 &= -\frac{j}{\omega C_1} - \frac{j}{\omega C} + R' + j\omega L \\ Z_2 &= R_2 - \frac{j}{\omega C_2} \end{aligned} \tag{2.2}$$

and,

$$R' = R + R_L + R_1 \tag{2.3}$$

When comparing the imaginary and the real elements on one side of eq. 2.1 with the imaginary and real elements on the other, two equations emerge. With some algebraic manipulations it is possible to solve for the variables C_1 and C_2 such that:

$$\begin{aligned} C_1 &= \frac{1}{\left[\omega^2 L - \frac{1}{C} - \sqrt{\frac{\omega(50-R)(50\omega R_2+50\omega R-\omega R R_2)}{(50-R_2)}}\right]} \\ C_2 &= \sqrt{\frac{(50-R)}{\omega\,(50-R_2)\,(50\omega R_2+50\omega R-\omega R R_2)}} \end{aligned} \tag{2.4}$$

Note that C_1 and C_2 are the values of the capacitance calculated for a match while considering the given inductance, resistances and capacitance of the IEC device (the inductance and resistances were measured in atmospheric conditions, where the capacitance of the IEC device was measured in vacuum conditions). If the given variable capacitors C_1, C_2 are not in the matching range it is possible to increase or decrease their capacitance by adding capacitors in series or in parallel. Having the freedom of varying the frequencies and capacitance, the matching circuit had allowed $\sim$ 60% efficiency and was sufficient in maintaining the plasma without destroying the RFS.

2.2 Doppler shift diagnostics

Charge exchange reactions are dominant in energetic (keV energies) glow discharges [5, 10], particularly in hollow cathode [2, 3, 6–10] and plane cathode [11–13] hydrogen discharges operating in the units and tens of mTorr pressure range, which exhibit directional ion beams. As a result, Doppler spectroscopy has been used as a diagnostic tool to infer on the ion energy distributions. Since IEC devices are often operated at this pressure range, similar directional ion beams are formed, which makes Doppler spectroscopy suitable for these devices.

Doppler shift spectra are formed by the emission of de-exciting atoms originating in the charge exchange reactions [11]. A physical interpretation of the spectrum has been found, enabling the determination of ion and neutral energies in the cathode region and along the neutral beam, where the beam is an emission channel extending from the anode, through the cathode, to the other anode on the opposite side. Furthermore, from the specific spectral line shape it is possible to estimate the relative densities of ionic species that are formed in the gas under the experimental conditions [2, 3].

In devices containing hydrogen gas, several physical (chemical) processes are responsible for the formation of H^+, H_2^+ and H_3^+ ionic species in the gas. An applied cathode voltage creates a potential that accelerates these ionic species through the gas while charge exchanging with the background gas. Equations 2.5, 2.6 present possible charge exchange interactions:

$$
\begin{aligned}
H^+ + H &\longrightarrow H^* + H^+ \\
H_2^+ + H &\longrightarrow H^* + H + H^+ \\
H_3^+ + H &\longrightarrow H^* + H_2 + H^+
\end{aligned}
\tag{2.5}
$$

$$
\begin{aligned}
H^+ + H_2 &\longrightarrow H^* + H_2^+ \\
H_2^+ + H_2 &\longrightarrow H^* + H + H_2^+ \\
H_3^+ + H_2 &\longrightarrow H^* + H_2 + H_2^+
\end{aligned}
\tag{2.6}
$$

where H and H_2 are the background gas atoms and H^* is the resulting excited fast neutral. In the range of units and tens of mTorr the H_2 is the major component of the background gas, and therefore, it is sufficient to consider the reactions in eq. 2.6 [2,3,11].

It has been shown that the excited H^* atom's trajectory is in the same direction as that of the initial incident ion's trajectory and any diversion is between 1° and 2°, depending on the energy of the incident ion [14]. The molecular dissociation energy is negligible in comparison to the fragment energy, and in a charge exchange interaction the total energy of all the fragments is approximately equal to the energy of the incident ion. Furthermore, considering that the ion energies are in the order of keV, any energy lost to electronic or vibrational excitation is negligible (in the order of units and tens of eV).

Emission from fast H^* atoms is responsible for a broad Doppler shifted spectrum that is dependent on the incident ion energies. In this work, the hydrogen H_α line was detected since it was most intense and gives the largest Doppler shift in the visible spectrum. This is the Balmer α emission line corresponding to the transition from $n = 3$ to $n = 2$ levels with a wavelength $\lambda = 6563$ Å, emitted by stationary (or low energy) atoms.

The excited H^* atom has approximately the same velocity as the incident ion's velocity but may differ in energy. Referring to the first reaction in eq. 2.6, the H^* atom has the H^+ incident ion's energy. In the case of the second reaction in eq. 2.6, the H^* atom has half of the H_2^+ incident ion's energy. Similarly, the H^* atom in the third reaction of eq. 2.6 has a third of the energy of the incident H_3^+ ion. Measuring the Doppler shift in the emission of the de-exciting atom is a direct measure of the excited H^* atom's energy, and therefore if the reaction is known, the incident ion's energy can be determined. The non-relativistic expression for the Doppler wavelength shift can be expressed as follows:

$$\Delta\lambda \approx \frac{v\lambda_0}{c}\cos\theta \tag{2.7}$$

where λ_0 is the wavelength of the unshifted line, v is the speed of the excited atom, c is the speed of light and θ is the angle between the observation line and the trajectory of the excited atom (note that if the observation is at 90° to the trajectory of the excited atom, the wavelength shift is zero). In eq. 2.7 $\Delta\lambda = \lambda - \lambda_0$, and therefore, a positive $\Delta\lambda$ implies that the excited atom is receding from the monochromator whereas, a negative $\Delta\lambda$ implies that

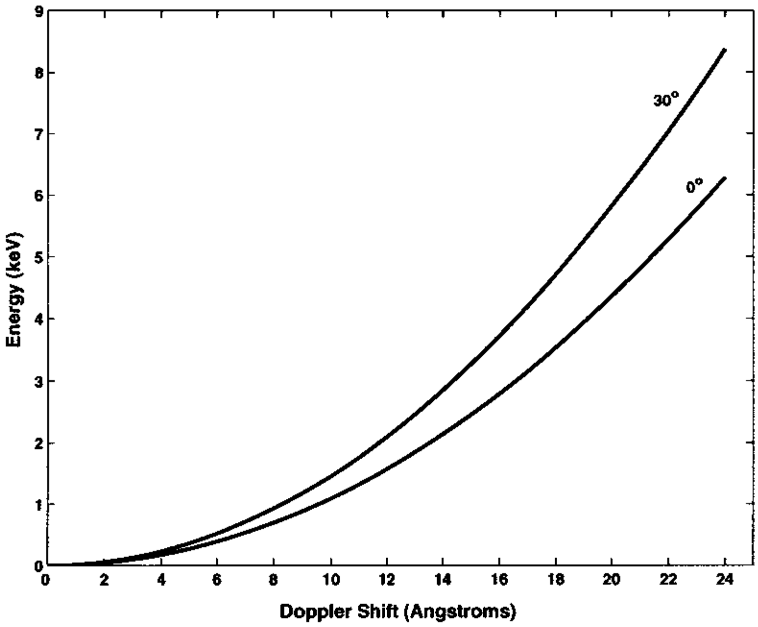

Figure 2.5: The energy of the excited atom as a function of the Doppler shift wavelength for $\theta = 0°$ and $\theta = 30°$. The unshifted λ_0 emission line is 6563 Å.

the excited atom is approaching the monochromator. The angle θ is chosen to be the acute angle between the observation line and the trajectory of the excited atom.

Expressing the velocity in terms of the wavelength shift and substituting in the classical expression for the kinetic energy results in an expression for the H* kinetic energy as a function of the wavelength shift squared:

$$E_k = \frac{m_H c^2 (\Delta\lambda)^2}{2\lambda_0^2 \cos^2\theta} \tag{2.8}$$

where m_H is the mass of the excited atom. Figure 2.5 presents a plot of the energy of the excited atom as a function of the Doppler shift wavelength for $\theta = 0°$ and $\theta = 30°$, and for λ_0 set to be the unshifted H_α emission line (6563 Å).

2.3 Analysis of Doppler spectra

Khachan [2] obtained Doppler shift spectra from a gridded IEC device at the units and tens of mTorr pressure range, where emission channels ("beams") emerge from the spacing in the cathode grid. The resulting spectrum showed a relatively sharp and intense central peak with two broad peaks ("wings") extending on each side of the central peak. Although each of the wings had a nearly smooth envelope shape, they were suspected to have structure. The structure could not be resolved since there was interference of emission from other channels that smeared the structure of the wings. Overcoming this problem, a two ring cathode was used to isolated one of the channels (making the IEC device one dimensional). Consequently,

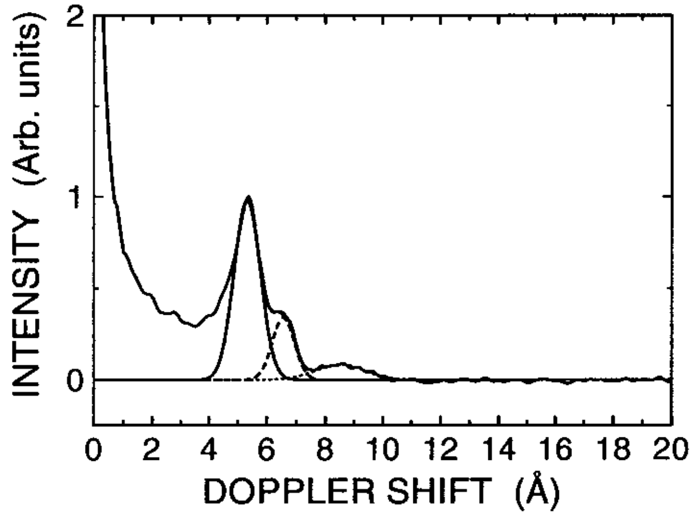

Figure 2.6: A spectrum of the resolved wing structure. The one dimensional IEC device was operated at pressure of 5 mTorr and cathode voltage of −4 kV (taken from J. Khachan and S. Collis, Phys. Plasmas, 8, 1299, 2001).

the structure of the wings was clearly resolved.

Figure 2.6 is taken from Khachan and Collis [2]. This spectrum was taken for an applied cathode voltage of −4 kV and a pressure of 5 mTorr. The line-of-sight of the monochromator was along the beam ($\theta = 0°$) but focusing on the centre of cathode. The central sharp peak corresponds to the unshifted H_α emission line (6563 Å). The peak arises from the excitation of the cold background gas via electron impact and other physical processes [11]. The wing clearly shows three distinct peaks. The two peaks closer to the unshifted peak are relatively intense and narrow, whereas the third smaller peak (most right in the figure) is broadened and is mostly isolated from the others.

It was suspected that the three peaks were the Doppler shift of H_α originating from different ionic species given in eq. 2.6, where the three energy distributions add to give the resultant spectrum. Figure 2.6 presents a three Gaussian fit that was applied to the distribution and clearly shows an overlap of the reconstructed and experimental spectra. Assuming that all three species of ions are accelerating via the same potential while charge exchanging, and since each has a different mass, three distinct distributions of wavelengths shifts are expected (see section 2.2: although the initial ions might have the same energy, the resulting fast neutral energies will differ). The Gaussian distribution implies that the energy corresponding to the average wavelength shift of each of the three ionic distributions is the most intense.

Other spectra were obtained for voltages between 2 kV and 10 kV at a pressure of 5 mTorr. Gaussian fits were carried out for each spectrum and the wavelength shift of the peaks were plotted against the square root of the applied voltage. It was found that there

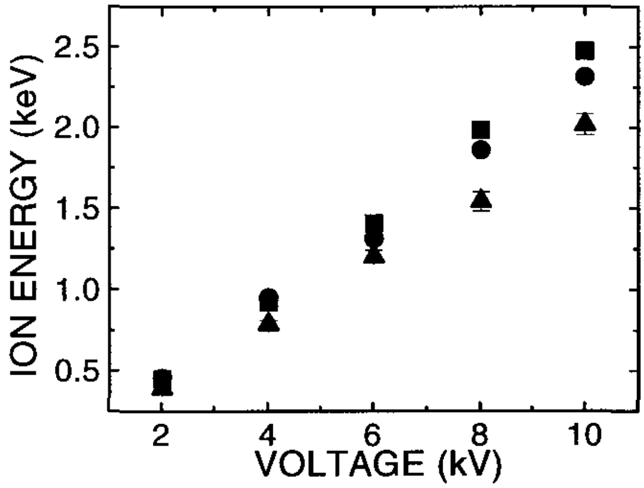

Figure 2.7: For each spectrum the three energies corresponding to the three Gaussian peaks are plotted. The energy corresponding to the first peak (closest to the unshifted peak) was multiplied by three (□) and the energy corresponding to the second peak was multiplied by two (○). The energies are plotted against the varied voltage (taken from J. Khachan and S. Collis, Phys. of Plasmas, 8(4), 1299, 2001).

is a linear relationship between the Doppler wavelength shift and the square root of the applied voltage for each of the three peaks respectively [2]. The wavelength shift squared is proportional to the kinetic energy (see eq. 2.8), and therefore, the ions' kinetic energy is linear with the applied voltage (this had to be verified since there are various ion energy loss mechanisms).

Figure 2.7, taken from Khachan and Collis [2], suggests that each of the three peaks can be identified with one of the reactions presented in eq. 2.6. For each spectrum (taken at different voltages) the three wavelength shifts corresponding to the three Gaussian peaks were converted into energies (see eq. 2.8). The energy corresponding to the first peak (closest to the unshifted peak) was then multiplied by three, the energy corresponding to the second peak was multiplied by two and were all plotted against the applied voltages. It is clear that for each of the voltages the three energies nearly overlap and since the multiplication factors are the mass ratios of H_3^+ to H^+ and of H_2^+ to H^+ respectively, it is strongly implied that the three peaks correspond to each of the processes described in eq. 2.6. The first peak represents the initial H_3^+ incident ion, the second peak represents the initial H_2^+ incident ion and the third peak represents the initial H^+ incident ion for each of the reactions (this is based on the principle of equal energy partition between the resulting fragments). This finding enabled the determination of the energies of each of the three incident ionic species and to predict relative ion densities [2,3].

2.4 Further discussion and related issues

Although the diagnostic method has been found to be successful in estimating ion energies and densities, there are some related issues to consider. These further contribute to the understanding of the diagnostic method and the spectral profiles.

Line integration of emission

The spectrum in Fig. 2.6 represents a typical spectrum taken while the line-of-sight of the monochromator is aligned along the beam ($\theta = 0°$). This was obtained with a lens, which focused emission from the centre of cathode onto the slit of the monochromator. However, it is not clear whether the spectrum was constructed from localized emission focused from the centre of cathode or from emission in the entire cathode region, around the central point.

It has been established that a potential well extends from the cathode centre to the anode [3, 15] and therefore, the ions should have increasing energies while approaching the cathode edge, where there is a minimum in the potential. If the lens images a very small region of the beam onto the slit of the monochromator, imaging different points along the potential well should result in different maximum wavelength shifts. As energy decreases the extended wings in the spectrum should approach the unshifted peak. Using the experimental set-up presented in this chapter, it has been found that when imaging points along the beam, within the cathode region, the spectra do not change significantly (note that the monochromator is aligned at $\theta = 0°$ relative to the beam). A trial and error experiment was carried out with the focus of the lens whereby an object was placed at the centre of cathode and focused onto the slit of the monochromator. The object was then moved from the centre towards the entrance of the cathode. At a distance of $\sim \pm 3$ cm there was still a blurry image formed on the slit of the monochromator. That implies that emission at $\sim \pm 3$ cm from the centre of cathode reaches the slit. This all suggests that emission in the entire cathode reaches the slit of the monochromator and also that this emission enters the instrument acceptance cone. Therefore, it can be concluded that the emission in the entire cathode contributes to the final signal, where it is line integrated along the cathode.

This conclusion is further supported by the experimental work of Khachan et al. [3] showing that when the monochromator was aligned at $\theta = 30°$ relative to the beam, the energies (spectrum wings) vary when moving out from the cathode centre to the cathode's edge. In this case the monochromator receives emission from a very short length cylinder (a small interval of the beam) that is projected by the lens on the slit. The depth-of-focus does not affect the wings of the spectrum since the background emission does not contribute to the wings' structure.

The Gaussian distribution assumption

As demonstrated in Fig. 2.6, the Gaussian fit can explain the experimental spectrum line shape while implying that the Doppler shift distribution resulting from each ionic specie is Gaussian. However, there are a few inconsistencies with the Gaussian approach:

1. It is clear that there is a significant distribution of ion wavelength shifts in the gap between the unshifted peak and the first peak (representing the H_3^+ specie). The three Gaussian fits do not account for the distribution in the gap.
2. When fitting three Gaussians for the wing, in many cases there is some variability in the amplitudes of the three Gaussians, which result in a good fit to the experimental spectrum. However, the positions of the three Gaussian peaks do not change significantly.
3. In the work of Khachan et al. [2,3], it was found that the Gaussian peaks represent the maximum energy that the ions gained for a given applied cathode potential. However, if the distribution of a specie is Gaussian, the peak should reflect the average energy of the ions.

In chapter 3 the distributions of each specie are modeled based on charge exchange, enabling the explanation and reconstruction of the observed spectra. This will also set limitations to the Gaussian approach.

Overlapping distributions

The energy distribution shapes of the three ionic species largely depend on cross sections, the distance the electrostatic potential extends to (hereafter will be defined as the pathlength of the potential) and pressure. For combinations of relatively high pressures (above 10 mTorr), voltages in the range of 3-10 kV and cylindrically hollow cathodes longer than 4 cm, the creation of many low energy ions was observed. These ions are responsible for an additional broad peak that is created between the unshifted peak and the peak representing the heavy H_3^+ specie (see discussion in section 2.2). Moreover, the peak representing the H_3^+ specie significantly overlaps with the peak representing the H_2^+ specie and both can not be resolved.

Figure 2.8 presents a spectrum taken with the experimental set-up detailed in section 2.1, where the monochromator was set at 0° relative to the beam and focussing on the cathode centre. The anodes were placed 16 cm apart from the center of cathode, pressure was set to 15 mTorr and a cathode voltage of -6 kV was applied. Note that the spectrum is symmetric around the main unshifted peak. This is a result of the depth-of-focus, which enables light from both sides of the centre of cathode to reach the monochromator's slit.

The figure presents a three Gaussian fit. However, the first Gaussian (closer to the unshifted peak) does not represent the H_3^+ specie but rather a peak caused by many low energy ions that are created under the specific experimental conditions. This peak can only be accounted for with an appropriate model, which is presented in chapter 3. The second Gaussian represents the H_3^+ and the H_2^+ species' overlapping distributions. In chapter 4 it will be shown that it is reasonable to consider the position of the Gausssian peak as the average of the positions of the two ionic distributions peaks. Since the H^+ specie has the maximum

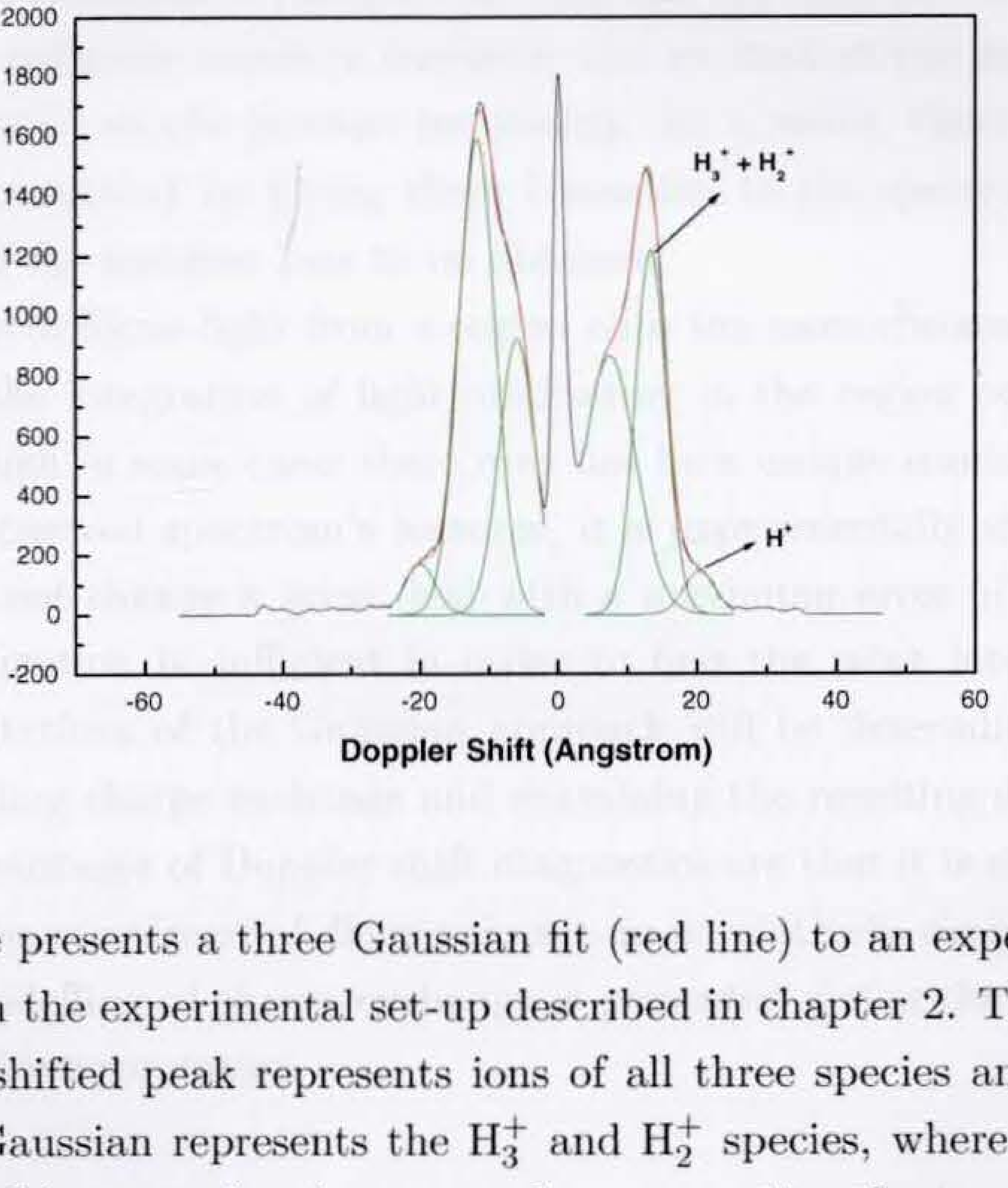

Figure 2.8: The figure presents a three Gaussian fit (red line) to an experimental spectrum (black line) taken with the experimental set-up described in chapter 2. The Gaussian (green line) closer to the unshifted peak represents ions of all three species and of relatively low energy. The second Gaussian represents the H_3^+ and H_2^+ species, where their distributions overlap. It is not possible to resolve the two peaks representing the two species. The third peak represents the well resolved H^+ ionic specie.

wavelength shift[1], it is well out of the low energy range and therefore, in most cases the third peak is well resolved.

2.5 Summary

The experimental apparatus described in section 2.1 enabled the study of two emission channels (beams), spanned between the cathode and anodes. The apparatus allowed for spectroscopic measurements to be done at different angles relative to the beam, and for spectra to be obtained for dc cathode bias voltages in the range of -1 to -10 kV and pressures in the range of $5 - 30$ mTorr.

The diagnostic tool used in this work is Doppler shift spectroscopy, which is made possible due to charge exchange collisions of energetic H^+, H_2^+ and H_3^+ with the background hydrogen gas, H_2. These three collisions result in energetic and excited atomic hydrogen, H^*, which have energies that depend on the incident ion energy. As a result, there is a convolution of peaks that can be deconvolved by fitting three Gaussians to the spectra. This enables the energy distributions of the incident ions to be obtained.

When using a lens to focus light from a region onto the monochromator's slit, the spectra are formed from the integration of light originating in the region corresponding to the depth-of-focus. Although in some cases there may not be a unique combination of Gaussian intensities to fit the observed spectrum's features, it is experimentally shown that the positions of the peaks do not change a great deal with a maximum error of ~ 5 %. Therefore, the Gaussian approximation is sufficient in order to find the most intense ion energy for each specie. The limitations of the Gaussian approach will be determined in the following chapters, while modelling charge exchange and examining the resulting distributions.

The two main advantages of Doppler shift diagnostics are that it is a non-intrusive diagnostic method, and the experimental diagnostic set-up is relatively simple. In the following chapter theoretical modelling of charge exchange is presented giving the background for the spectrum analysis and interpretation.

---

[1] This is a shorthand usage that will be used throughout this thesis meaning that the emission resulting from the H^+ charge exchange interaction has the maximum wavelength shift.

Bibliography

[1] G. H. Miley, Y. Gu, J. M. DeMora, R. A. Stubbers, T. A. Hochberg, J. H. Nadler and R. A. Anderl, IEEE Trans. Plasma Sci., **25**, 733 (1997).

[2] J. Khachan and S. Collis, Phys. of Plasmas, **8**(4), 1299 (2001).

[3] J. Khachan, D. Moore and S. Bosi, Phys. of Plasmas, **10**(3), 596 (2003).

[4] S. C. Haydon, "Discharge and Plasma Physics", p. 480 (1964).

[5] A. V. Phelps, J. Phys. Chem. Ref. Data, **19**, 653 (1990).

[6] O. Shrier, J. Khachan, S. Bosi, M. Fitzgerald and N. Evans, Phys. of Plasmas, **13**, 12703 (2006).

[7] W. Benesch and E. Li, Opt. Lett., **9**, 338 (1984).

[8] E. Ayers and W. Benesch, Phys. Rev., A **37**, 194 (1988).

[9] N. M. Šišović, G. Lj. Majstorović and N. Konjević, Eur. Phys. J., D **32**, 347 (2005).

[10] N. Konjević, G. Lj. Majstorović and N. M. Šišović, Appl. Phys. Lett., **86**, 251502 (2005).

[11] C. Barbeau and J. Jolly, J. Phys. D: Appl. Phys., **23**, 1168 (1990).

[12] M. Kuraica and N. Konjević, Phys. Rev., A **46**, 4429 (1992).

[13] M. R. Gemišić Adamov, B. M. Obradović, M. M. Kuraica and N. Konjević, IEEE Trans. Plasma Sci., **31**, 444 (2003).

[14] G. W. McClure, Phys. Rev., **140**, A769 (1965).

[15] T. A. Thorson, R. D. Durst, R. J. Fonck and L. P. Wainwright, Phys. Plasmas, **4**(1), 4 (1997).

Chapter 3

Charge Exchange Modelling

In this chapter, a semi-analytical method is developed, which enables the rapid determination of spatial ion energy distributions for discharges such as described in the previous chapter. This method will be shown to be a special case of Markov Chain theory and will be compared with the results of Monte Carlo simulations.

3.1 Motivation and previous work

Charge exchange has been recognized to be dominant in IEC devices (in the units of mTorr range) and has been modeled, mostly in an attempt to explain fusion rates. From the early 1960's to the late 1990's D–D and D–T fusion rates were measured while operating IEC devices at gas pressures of units of mTorr (including devices based on ion guns, where ions are accelerated through cold background gas into a vacuum chamber) [1–4]. Models based on beam-beam interactions that incorporated various processes in the cathode region failed to explain the experimental high fusion reactivity measured in these devices [1]. Baxter and Stuart [5] developed a model based on charge exchange that clearly agreed with some experimental results. The model assumed that the neutron production rate was mainly due to ion beam-background and neutral-background interactions. The modelling method was based on simplifying the Boltzmann equation and solving it numerically. However, the modelling was done for Hirsch's ion guns arrangement and not for the most commonly used gridded IEC device.

Thorson et al. [6] reported fusion rate measurements from a gridded IEC device and concluded that the major contribution was from ions and fast neutrals interacting with background gas. They supplemented their experiments with a collisionless flow model that did not account for the measured neutron production rates and for the dependence of the neutron production rate on gas pressure.

Børve et al. [7] reported investigations of kinetic instabilities associated with an injection of a plasma beam into background gas while assuming that the charge exchange process is the major contributor to the velocity distribution of the ions. In their model they approximated the charge exchange cross sections with an analytical expression and used the Monte Carlo method, which was shown to converge to the analytical solution of the linear Boltzmann equation [8]. Although this study was not specifically related to IEC, it is relevant to gridded IEC systems since ion beams are accelerated in background gas.

Here a general method of modelling is developed and specifically applied to linear and parabolic potentials, enabling the determination of energy distributions that will explain spectra obtained in this work.

3.2 The charge exchange process

The dominant charge exchange reactions in a hydrogen discharge are the ones given in eq. 2.6 (see chapter 2). The resulting fast neutrals (H^*) have trajectories that are in the same direction as the incident ("parent") ions and the total energy of the resulting fragments from the reaction is approximately equal to the energy of the incident ion. If the parent ion is H_2^+, each of the H fragments will have half the energy. Similarly, for the parent ion H_3^+, each fragment has a third of the parent's energy [9]. In addition, note that a cold ion H_2^+ is created with each reaction. These cold ions can subsequently accelerate in the discharges via the potential, and in turn can undergo a charge exchange collision.

Two distinct chain processes can take place: the ion specie interacting with the same background specie (e.g. H_2^+ interacting with H_2 background gas), and the ion specie interacting with a different background specie (e.g. H_3^+ interacting with H_2 background gas). In the latter case, the newly created cold ion is of a different specie to the initial interacting energetic ion. As a result, this process ends when all the initial ion densities starting the process have charge exchanged. The latter case is shown to be a sub-set of the former case and modelling the first case incorporates both.

In this chapter, this chain of charge exchange reactions is modeled in order to determine the spatial distribution of ion energies along a hydrogen ion beam in an H_2 background gas, which is a one dimensional problem. The method is generalized for all monotonically increasing (or decreasing) potentials, where the linear and parabolic potentials are special cases of this set. Note that Monte Carlo modelling can easily be used to model these chain reactions except it suffers from numerical noise or long computing times. The method presented here overcomes both of these limitations. Next, the semi-analytical method, which is an intuitive approach to this modelling, is presented for both linear and parabolic potentials (as mentioned, the method is generalized for monotonically increasing/decreasing potentials and can account for the estimated potential in an IEC device, which is presented in Fig. 4.4). The results for the linear potential are also derived by applying a Markov Chain approach.

3.3 Semi-analytical method for linear potential

This section will focus on the H_2^+-H_2 (same specie interaction) charge exchange reaction given in eq. 2.6 since the density of H_2^+ is greatest in hydrogen discharges operating in the units and tens of mTorr, which is our region of interest. The model will be shown equally to apply to the other two interactions (different specie interaction).

After the incident ion undergoes charge exchange, it becomes an energetic neutral and will be regarded as being lost from the system. Consequently, the newly created cold ion will then move along the beam and go through the same charge exchange process. The charge exchange cross-sections are greatly dependent on the incident ion energies. Since we are dealing with energies that range from zero to the order of 10 keV, the energy distributions are heavily dependent on the spatial electrostatic potential profile and the background gas pressure.

Let us assume a total beam length that consists of k segments each with a length of Δx. The beam consists of an arbitrary discrete distribution of ions, n_i, placed at the beginning of each segment. The normalized distribution can be defined as follows:

$$\mathbf{F_0} = \begin{bmatrix} f_1 & f_2 & \cdots & f_k \end{bmatrix} \tag{3.1}$$

where:

$$f_i = \frac{n_i}{\sum_{i=1}^{k} n_i} \tag{3.2}$$

In order to simplify further explanations, we define the positions X_n^B and X_m^E to be the positions along the ion beam before and after a segment respectively (e.g. $X_{n=1}^B$ is the position at the beginning of the first segment whereas, $X_{m=1}^E$ is the position at the end of the first segment). The indexes n and m refer to the segments along the beam and since there are k segments they get the values 1 to k.

The ions comprising the f_i densities accelerate from their positions and charge exchange at different segments along the path. Assuming very small segments, the energy of each ion undergoing charge exchange in a segment can be approximated to be constant throughout the segment in which it underwent charge exchange. This energy is defined to be the energy acquired when accelerating from position X_n^B to position X_m^E and is associated with a charge exchange event in the m segment. It is possible to construct a matrix containing all possible energies E_{nm} such that each element represents the energy acquired when accelerating from position X_n^B to position X_m^E:

$$\mathbf{E} = \begin{bmatrix} E_{11} & E_{12} & E_{13} & \cdots & E_{1k} \\ 0 & E_{22} & E_{23} & & E_{2k} \\ 0 & 0 & E_{33} & & E_{3k} \\ \vdots & & & \ddots & \vdots \\ 0 & \cdots & & & E_{kk} \end{bmatrix} \tag{3.3}$$

Note that in each j column (when referring to a matrix, the indexes i and j will be used to represent the rows and columns respectively) of matrix $\mathbf{E}$ there are all possible E_{nm} energies for $m = j$ and for $n = 1, ..., j$, which are associated with ions that have undergone charge exchange in the j segment along the beam. In each row there are possible energies for ions that started accelerating at an $X^B_{n=i}$ position and undergone charge exchange at an $m = j$ segment along the beam.

Next, the fraction of ions charge exchanging in each segment along the path has to be found. Generally, the fraction of ions (out of an initial density starting the process) charge exchanging along a path x is given by the expression [10]:

$$R = \frac{N}{N_0} = 1 - \exp\left(-nx\sigma\left(E\right)\right) \tag{3.4}$$

where N_0 is the initial density of ions, N is the density of ions charge exchanging along the path x, n is the background gas density and $\sigma\left(E\right)$ is the charge exchange cross section corresponding to energy E. In the case discussed here the cross-section is energy dependent and therefore changes as the ion energy changes in successive segments.

The explicit expression for eq. 3.4 can be found by following the path of the first density f_1 starting at position X^B_1 and ending at position X^E_k. When going through the first segment the fraction of ions surviving charge exchange is:

$$M_1 = \exp\left(-n\Delta x_1\sigma_{11}\right) \tag{3.5}$$

where σ_{11} corresponds to the energy E_{11}. After the surviving M_1 fraction passes the second segment, the fraction of ions surviving charge exchange becomes:

$$M_2 = M_1 \exp\left(-n\Delta x_2\sigma_{12}\right) \tag{3.6}$$

where σ_{12} corresponds to the energy E_{12}. Proceeding in this manner, it is possible to define M_k fractions of ions, which are the surviving fractions of f_1 after each segment:

$$\begin{aligned} M_3 &= M_2 \exp\left(-n\Delta x_3\sigma_{13}\right) \\ &\vdots \\ M_k &= M_{k-1} \exp\left(-n\Delta x_k\sigma_{1k}\right) \end{aligned} \tag{3.7}$$

Note that each M_i (for $i > 1$) is dependent on the previous fraction M_j, which leads to the following expression for the surviving fractions of f_1 at the end of each segment:

$$M_g = \exp\left(-n\sum_{j=1}^{g}\Delta x_j\sigma_{1j}\right) \tag{3.8}$$

where g is the current segment number with a range from 1 to k. Consequently, the fraction of ions out of the initial source f_1 that charge exchange along the path is given by the expression:

$$R_g = 1 - M_g \tag{3.9}$$

It is now possible to generalize the above result for the entire $\mathbf{F_0}$ distribution of sources spread along the beam, and for each source express the fraction of ions charge exchanging while passing any given number of segments in the following expression:

$$R_{ij} = 1 - \exp\left(-n\Delta x \sum_{h=i}^{j} \sigma_{ih}\right) \tag{3.10}$$

The index i refers to the f_i density comprising the $\mathbf{F_0}$ distribution, where $j \geq i$. The charge exchange cross section σ_{ih} corresponds to the energy E_{ih} and Δx is outside the summation since the segments are of the same length.

From eq. 3.10 the fraction of ions charge exchanging in each segment is expressed as follows:

$$\begin{aligned} P_{ij} &= R_{ij} - R_{i,j-1} & |j > i \\ P_{ij} &= R_{ij} & |j = i \\ P_{ij} &= 0 & |j < i \end{aligned} \tag{3.11}$$

The P_{ij} densities correspond to the E_{ij} energies in eq. 3.3 and hence, the P_{ij} elements can be ordered in matrix $\mathbf{P}$ as follows:

$$\mathbf{P} = \begin{bmatrix} P_{11} & P_{12} & P_{13} & \cdots & P_{1k} \\ 0 & P_{22} & P_{23} & & P_{2k} \\ 0 & 0 & P_{33} & & P_{3k} \\ \vdots & & & \ddots & \vdots \\ 0 & \cdots & & & P_{kk} \end{bmatrix} \tag{3.12}$$

Matrix $\mathbf{P}$ contains all the fractions of ions charge exchanging out of the initial $\mathbf{F_0}$ distribution. Each row i presents the fractions charge exchanging out of an f_i source. The total fraction of ions charge exchanging in each segment is the sum of each column of the following matrix:

$$\mathbf{P}' = \begin{bmatrix} f_1P_{11} & f_1P_{12} & f_1P_{13} & \cdots & f_1P_{1k} \\ 0 & f_2P_{22} & f_2P_{23} & & f_2P_{2k} \\ 0 & 0 & f_3P_{33} & & f_3P_{3k} \\ \vdots & & & \ddots & \vdots \\ 0 & \cdots & & & f_kP_{kk} \end{bmatrix} \tag{3.13}$$

Since the charge exchanging ions produce the same amount of new cold ions, the fractions in eq. 3.13 are also the first generation of new sources of cold ions that can follow the potential and further charge exchange. Considering that each column in matrix $\mathbf{P}'$ represents a segment along the beam, the sum of elements in each column represents a new source of ions accelerating forwards. Starting with the source produced in the first column: $S_1 = \sum_{q=1}^{1} P'_{q1}$, this source will create new sources $S_1\mathbf{P}_{2j}$ in each segment along the beam (in this notation

$\mathbf{P}_{2j}$ is the second row of matrix $\mathbf{P}$). The source produced in the second column is now: $S_2 = \sum_{q=1}^{2} P'_{q2} + S_1 P_{22}$ (the first term is the sum of the second column of matrix $\mathbf{P}'$ and the second term is the additional source created by the previous source S_1). The source S_2 creates new sources $S_2\mathbf{P}_{3j}$ along the beam. The source produced in the third column is: $S_3 = \sum_{q=1}^{3} P'_{q3} + S_1 P_{23} + S_2 P_{33}$ (S_3 includes the new sources created by the sources S_1 and S_2). This source will create new sources $S_3\mathbf{P}_{4j}$. This chain can be developed to the last segment, where the following matrix is obtained:

$$\mathbf{D} = \begin{bmatrix} f_1 P_{11} & f_1 P_{12} & f_1 P_{13} & \cdots & f_1 P_{1k} \\ 0 & (f_2 + S_1) P_{22} & (f_2 + S_1) P_{23} & \cdots & (f_2 + S_1) P_{2k} \\ 0 & 0 & (f_3 + S_2) P_{33} & \cdots & (f_3 + S_2) P_{3k} \\ \vdots & & & \ddots & \vdots \\ 0 & & \cdots & 0 & (f_k + S_{k-1}) P_{kk} \end{bmatrix} \tag{3.14}$$

In this matrix each row contains the fraction of ions charge exchanging out of the initial source, which is $f_n\ \mathbf{P}_{nj}$, and the sources resulting from the chain $S_{n-1}\mathbf{P}_{nj}$. Therefore, the elements of the matrix can also be expressed as: $D_{ij} = P_{ij}\,(f_i + S_{i-1})$, where $S_{i-1} = \sum_{q=1}^{i-1} D_{q,i-1}$ (for $i = 1$ it is defined that $S_0 = 0$).

The columns of matrix $\mathbf{D}$ store the information of the total fractions of ions charge exchanging in each segment along the beam. The matrix keeps track of the energy of each fraction of ions when charge exchanging such that each fraction D_{ij} has an associated energy E_{ij}. It is possible to derive cumulative and statistical quantities such as the total amount of ions charge exchanging in each segment and the average ion energy along the beam. Let us define, $N_0 = \sum_{i=1}^{k} n_i$, to be the total initial amount of ions starting the process. The total amount of ions charge exchanging in each segment is then:

$$N_j = N_0 \sum_{i=1}^{j} D_{ij} \tag{3.15}$$

Using the densities of ions as probability weights, the expression for the average energy of the ions charge exchanging in each segment can be defined as follows:

$$\overline{E}_j = \frac{\sum_{i=1}^{j} E_{ij} D_{ij}}{\sum_{i=1}^{j} D_{ij}} \tag{3.16}$$

In section 3.2 it was mentioned that the solution for an $\mathbf{F_0}$ distribution of ion densities charge exchanging with the background gas of another specie (two different species interaction) can be obtained from the solution of the one specie interaction, presented above. In the case of a two different species interaction the newly created ion is of a different specie to the initial charge exchanging ion (e.g. if an H^+ ion specie charge exchanges with H_2 background gas, the newly created specie will be an H_2^+ ion). Therefore, once the initial ions starting the process have charge exchanged the process ends for this specific ion specie. We do not further consider the newly created ions of the background gas specie in this chain. Each row i in matrix **P** represents the fraction of ions, out of an initial ion density accelerating from the beginning of the i segment, that underwent charge exchange in each segment. Consequently, matrix **P** is the solution of the two different species interaction, where it replaces matrix **D**. Therefore, P_{ij} replaces D_{ij} in eqs. 3.15 and 3.16.

3.4 Markov chains method for a linear potential

It is clear from the previous section that the number of charge exchange events in any particular segment along a beam path greatly depends on the number of charge exchange reactions in preceding segments. This is a typical example of a Markov chain, where the outcome of a particular result is weighted by the previous results. Since Markov chain theory is based on probabilities (named "transition probabilities"), our problem has to be defined in terms of these probabilities. Noting that the sum of the elements of a row in matrix **P** (eq. 3.12) represents the total fraction of ions that charge exchanged out of an initial ion source f_i, for an infinite path it follows that:

$$\sum_{j=1}^{\infty} P_{ij} = 1$$

Although matrix **P** is finite, the P_{ij} elements form subsets of normalized sets of probabilities and can be interpreted as the appropriate probabilities for the problem.

In this approach a new generation of ion sources that are distributed along the beam results from a previous generation of sources that had charge exchanged. The initial source distribution $\mathbf{F_0}$ is the first generation of sources in our current problem (defined in eq. 3.1 and formally referred to as the "probability state vector"). Once the sources go through charge exchange they create the second generation of sources along the beam:

$$\mathbf{F_1} = \mathbf{F_0}\mathbf{P}$$

Note that $\mathbf{F_1}$ is a vector containing the sum of the columns of matrix $\mathbf{P}'$ (matrix $\mathbf{P}'$ is defined in eq. 3.13). Matrix **P** defines the Markov chain process (formally referred to as the "transition matrix", where the elements P_{ij} are referred to as the "one step transition probabilities").

The first source of ions in the distribution $\mathbf{F_1}$ starts the charge exchange process at position X_2^B (beginning of second segment) where the second source of ions in the distribution $\mathbf{F_1}$ starts the charge exchange process at position X_3^B, etc. The matrix of fractions describing this process is a sub matrix of **P**, which takes the form:

$$\mathbf{TP} = \begin{bmatrix} 0 & P_{22} & P_{23} & & P_{2k} \\ 0 & 0 & P_{33} & & P_{3k} \\ \vdots & & & \ddots & \vdots \\ 0 & \cdots & & & P_{kk} \\ 0 & \cdots & & & 0 \end{bmatrix}$$

where, $\mathbf{T}$ is a shifting matrix that, in general, selects the sub matrices describing the charge exchange process of each successive $\mathbf{F_i}$ distribution and is defined as:

$$\mathbf{T} = \begin{bmatrix} 0 & 1 & 0 & \cdots & 0 \\ 0 & 0 & 1 & \cdots & 0 \\ \vdots & & \ddots & \ddots & \vdots \\ 0 & \cdots & & 0 & 1 \\ 0 & \cdots & & & 0 \end{bmatrix} \tag{3.17}$$

The $\mathbf{F_N}$ distribution (the N'th generation of new sources or equivalently, the total fraction of ions charge exchanging in each segment along the beam resulting from the $N-1$ generation of sources) can be described as follows:

$$\mathbf{F_N} = \mathbf{F_0 P} \left(\mathbf{TP}\right)^{N-1} \tag{3.18}$$

The total fractions of ions produced in each segment for k maximum possible number of generations, where k is also the number of segments, is:

$$\mathbf{F} = \sum_{\mathbf{N=1}}^{k} \mathbf{F_N} \tag{3.19}$$

Note that $N_0\mathbf{F}$ is the same result obtained by the semi-analytical method in eq. 3.15 and the two methods converge in their results. As opposed to the semi-analytical method the expression for the average energy is not straight forwards since the energy variables in eq. 3.3 have to be inserted into eq. 3.18, where eq. 3.18 includes matrix operations. In order to simplify the notation, a normalizing vector is defined as follows:

$$\mathbf{F'} = \begin{bmatrix} \frac{1}{F_1} & \frac{1}{F_2} & \cdots & \frac{1}{F_k} \end{bmatrix} \tag{3.20}$$

where the F_i's are the elements of $\mathbf{F}$. The expression for the average energy in each segment becomes:

$$\overline{\mathbf{E}} = \left[\mathbf{F_0} \sum_{\mathbf{N=1}}^{k} \mathbf{P} \left(\mathbf{TP}\right)^{\mathbf{N-1}} \circ \left(\mathbf{T^{N-1}E}\right)\right] \circ \mathbf{F'} = \left[\sum_{\mathbf{N=1}}^{k} \mathbf{F_N} \circ \left(\mathbf{T^{N-1}E}\right)\right] \circ \mathbf{F'} \tag{3.21}$$

In this notation "$\circ$" represents the Hadamard product of two matrices or two vectors, which is the multiplication of the corresponding elements in the matrices or vectors (e.g. $\mathbf{V} \circ \mathbf{W} = \begin{bmatrix} v_1w_1 & v_2w_2 & \cdots & v_kw_k \end{bmatrix}$). The result of eq. 3.21 is identical to the result of the semi-analytical method in eq. 3.16.

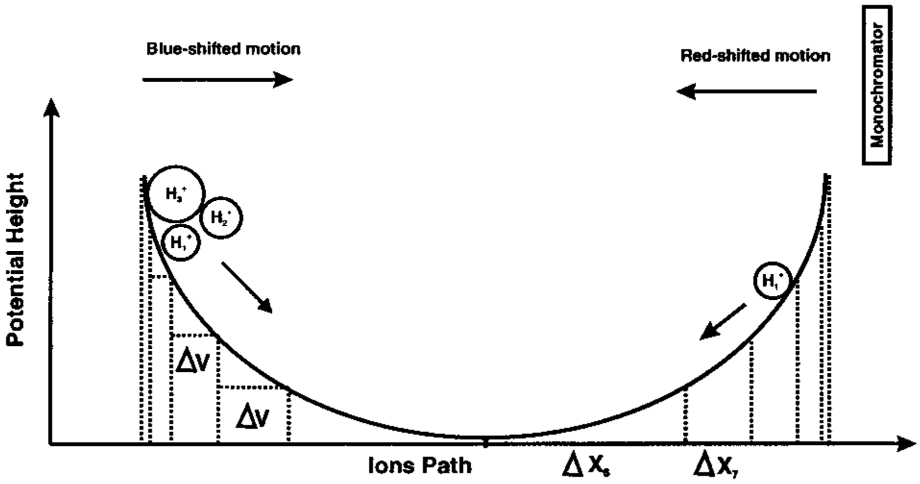

Figure 3.1: An illustration of ions going down the potential well in both directions. The potential height is divided into equal intervals whereas, the segments along the ions path are unequal. The figure also shows blue-shifted ions moving towards the monochromator and red-shifted ions moving away from the monochromator.

3.5 Semi-analytical method for a potential well

3.5.1 Charge exchange in a well

The charge exchange process detailed in section 3.2 is general and equally applies to the potential well case. The main difference between the linear case and the well case is that in the latter, one has to consider oscillations of the ions in the well (see illustration in Fig. 3.1). Ions charge exchange in the well while creating new sources along the path in the well. The sources will follow the potential in one of two directions, depending on their position of creation along the path. Not all ions will undergo charge exchange on their first pass of the well. As a result, they will oscillate along the path-length of the well until they eventually all undergo charge exchange.

For the Doppler shift measurements presented in this work the monochromator was positioned on one side of the cathode. This gives rise to a blue and red shifted spectrum referring to ions approaching and receding from the monochromator respectively (see Fig. 3.1). Throughout this section ions travelling towards the monochromator will be referred to as blue shifted and ions travelling in the opposite direction will be referred to as red shifted. This will allow a direct comparison of the model results to the experimental results.

There are two modelling approaches to consider: the first is to divide the path-length along the potential into small unequal segments by dividing the potential height into equal intervals (equal energy segments). The second is to divide the path-length into small equal segments, which might force the potential height intervals to be unequal. The former approach was found to simplify the modelling and therefore is chosen here. The potential height is divided into k segments having the same ΔV intervals (here V stands for potential). The aim of the modelling is to find the spatial distribution of ion and neutral atom energies for any given number of oscillations and for any arbitrary ion distribution along the well.

3.5.2 Matrix representation for ion charge exchange

The modelling presented in section 3.3 is now extended for the case of a potential well and the inclusion of all three charge exchange interactions presented in eq. 2.6. This model refers to a one dimensional potential well and therefore, the ions will follow the potential in both directions. Note that the modelling is general and encompasses all functions representing potentials that monotonically decrease to a minimum and then monotonically increase.

Let us define two matrices: the first contains all possible ions energies (the same as matrix **E** in section 3.3), and the second contains all possible fractions of ions (out of the initial sources placed at the beginning of each segment) that charge exchanged in each segment along the path of the potential (the same as matrix **P** in section 3.3).

The potential axis (y-axis in Fig. 3.1) is divided into t intervals of ΔV increments such that $t \times \Delta V$ is the maximum potential depth. Consequently, the position axis (x-axis in Fig. 3.1) is divided into $k = 2 \times t$ segments of Δx_j length each (note that the Δx_j segments may be of different lengths). As in section 3.3, X_n^{Bb} and X_m^{Eb} (or X_n^{Br}, X_m^{Er}) refer to a position at the beginning and at the end of each segment respectively. Since ions accelerate in opposite directions in the well, the superscripts b and r will be used to refer to an ion motion in one direction and in the other respectively. For example, from Fig. 3.1, the position axis was divided into 10 segments. The positions of the ions when traveling in the blue-shifted direction and passing the beginning of each segment are: X_1^{Bb}, X_2^{Bb}, ..., X_{10}^{Bb}, whereas, the positions of the ions when traveling in the red-shifted direction and passing the beginning of each segment are: X_1^{Br}, X_2^{Br}, ..., X_{10}^{Br}. Note that for the motion of the ions in the red-shifted direction we count the segments starting from the monochromator's side and vice versa, therefore, $X_1^{Bb} = X_{10}^{Br}$, $X_2^{Bb} = X_9^{Br}$ etc.

Starting with the blue-shifted ion motion, constant energies, E_{nm}, are assigned to each Δx_j segment. These are defined to be the energies gained when accelerating from the beginning of a segment, Δx_i, to the mid point of a segment, Δx_j, for $i \leq j$. The energies are ordered in the following matrix:

$$\mathbf{E}_b = \begin{bmatrix} E_{11} & E_{12} & \cdots & E_{1t} & E_{1t} & \cdots & E_{12} & E_{11} \\ 0 & E_{22} & \cdots & E_{2t} & E_{2t} & \cdots & E_{22} & 0 \\ 0 & 0 & \cdots & E_{3t} & E_{3t} & \cdots & 0 & 0 \\ \vdots & & & \vdots & \vdots & & & \vdots \\ & & & E_{tt} & E_{tt} & & & \\ 0 & \cdots & & & & & & \\ 0 & \cdots & & & & & & 0 \end{bmatrix} \tag{3.22}$$

The indexes of the elements in matrix $\mathbf{E}_b$ refer to n, m respectively (e.g. the energy E_{1t} is the energy gained by accelerating from the beginning of Δx_1 segment to the mid of Δx_t segment, where $n = 1$ and $m = t$ respectively). As in the linear potential case, each j column contains all possible energies for a j segment along the path and each i row contains the energies along the path of ions that start to accelerate from the i segment.

It is now possible to define a matrix containing all fractions of ions charge exchanging in each segment out of an initial density source of ions starting the process at the beginning of each segment and that will accelerate in the blue-shifted direction. This matrix has the same structure as matrix $\mathbf{E}_b$,

$$\mathbf{P}_b = \begin{bmatrix} P_{11} & P_{12} & \cdots & P_{1t} & P_{1t+1} & \cdots & P_{1k-1} & P_{1k} \\ 0 & P_{22} & \cdots & P_{2t} & P_{2t+1} & \cdots & P_{2k-1} & 0 \\ 0 & 0 & \cdots & P_{3t} & P_{3t+1} & \cdots & 0 & 0 \\ \vdots & & & \vdots & \vdots & & & \vdots \\ & & & P_{tt} & P_{tt+1} & & & \\ 0 & \cdots & & & & & & \\ 0 & \cdots & & & & & & 0 \end{bmatrix} \qquad (3.23)$$

Note that the i'th row in the matrix corresponds to ions accelerating from the X_i^{Bb} position. The quantities P_{nm} are found in a similar way to the ones in eq. 3.12. Note that since the Δx_j segments are not necessarily of the same length, they have to be included in the summation in eq. 3.10, resulting in the following:

$$R_{nm} = (1 - \exp\left(n_B \sum_{j=1}^{m} \Delta x_j \sigma_{nj}\right) \qquad (3.24)$$

where n_B is the number density of the background gas and σ_{nj} is the charge exchange cross section corresponding to the energy E_{nj} (note that for $E_{nj} = 0$, $\sigma_{nj} = 0$). The P_{nm} elements are defined to be:

$$P_{nm} = R_{nm} - R_{n,m-1} \qquad (3.25)$$

where for $m = 1$, $R_{n,m-1} = 0$.

The same procedure is repeated to find the matrices that correspond to the red-shifted motion of the ions, $\mathbf{E}_r$ and $\mathbf{P}_r$. Note that for ion motion in the red-shifted direction we number the segments starting from the last to the beginning (e.g. referring to Fig. 3.1, $X_1^{Br} = X_{10}^{Bb}$, $X_2^{Br} = X_9^{Bb}$ etc.). In this case $\mathbf{E}_r = \mathbf{E}_b$ and $\mathbf{P}_r$ has the same form as $\mathbf{P}_b$ but not necessarily equals $\mathbf{P}_b$. There is a clear physical interpretation of matrices $\mathbf{P}_b$ and $\mathbf{P}_r$: for a source of ions starting at X_i^{Bb} or X_i^{Br} position, each element in the i'th row of the matrices represents the fraction of ions charge exchanging in the j'th segment. The sum of the elements in each row i is the total fraction of ions charge exchanging out of the ion source starting at position X_i^{Bb} or X_i^{Br}. Matrices $\mathbf{P}_b$ and $\mathbf{P}_r$ are also the Markov transition matrices used when formalizing the model with the Markov chain method for a potential well (see section 3.4).

3.5.3 Distribution matrices

As in section 3.3, the distribution matrices that account for the charge exchange chain process have to be found (this is matrix **D** in section 3.3). Since the ions can oscillate back and forth, a calculation is required for the fraction of ions charge exchanging in each segment along the path in the potential well for each half oscillation.

After each half oscillation a new spatial distribution of ion sources, $\mathbf{U}_b^p$ or $\mathbf{U}_r^p$, is created along the path (the index p refers to the number of half oscillations). The ions of the $\mathbf{U}_b^p$ distribution travel in the blue-shifted direction. These ions were initially created: first, from the ions that had traveled in the red-shifted direction, underwent charge exchange and produced ions that can return in the blue-shifted direction. Second, from the ions that did not undergo charge exchange at the end of the potential well, which then return in the blue-shifted direction. Similarly, ions of the $\mathbf{U}_r^p$ distribution travel in the red-shifted direction and result from the ions that had previously traveled in the blue-shifted direction.

Let us assume an arbitrary discrete distribution, $\mathbf{U}_b^p$, along the position axis (x-axis in Fig. 3.1). We are interested in modelling the chain process in the blue shifted direction. Following the same procedure described in section 3.3, matrix $\mathbf{D}_b^p$ is derived as follows: for all integers $j = 1$ to $j = k$, starting with integers $i = 1$ and running to $i = k$, $\left(D_b^p\right)_{ij} = (P_b)_{ij}\left(\left(U_b^p\right)_i + S_{i-1}\right)$, where $S_{i-1} = \sum_{q=1}^{i-1}\left(D_b^p\right)_{q,i-1}$ ($S_0 = 0$ for $i = 1$). The first few columns of matrix $\mathbf{D}_b^p$ take the form:

$$\mathbf{D}_b^p = \begin{bmatrix} \left(U_b^p\right)_1 P_{11} & \left(U_b^p\right)_1 P_{12} & \left(U_b^p\right)_1 P_{13} & \cdots \\ 0 & \left(\left(U_b^p\right)_2 + S_1\right) P_{22} & \left(\left(U_b^p\right)_2 + S_1\right) P_{23} & \cdots \\ 0 & 0 & \left(\left(U_b^p\right)_3 + S_2\right) P_{33} & \cdots \\ \vdots & & & \\ 0 & \cdots & & \\ 0 & \cdots & & \end{bmatrix} \tag{3.26}$$

Note that the P_{nm} elements are the elements of matrix $\mathbf{P}_b$. Matrix $\mathbf{D}_b^p$ stores the fractions of ions charge exchanging in each segment along the path due to an initial ion distribution $\mathbf{U}_b^p$. The matrix also keeps track of the energy of each fraction of ions when charge exchanging such that each fraction $\left(D_b^p\right)_{ij}$ has an associated energy $(E_b)_{ij}$.

As an explicit example of the chain process, the first and second rows of matrix $\mathbf{D}_b^p$ are developed as follows: all sources placed at X_n^{Bb}, for $n \leq t$ (sources that are placed from the beginning of the first segment to the minimum of the potential), can charge exchange along the path in the blue shifted direction. Matrix $\mathbf{P}_b$ describes the fractions of ions out of the initial sources $\mathbf{U}_b^p$ that charge exchange along the path. Therefore, we insert into matrix $\mathbf{D}_b^p$ the fractions $\left(U_b^p\right)_i (\mathbf{P}_b)_i$, which are now new sources of cold ions ready to accelerate. In this notation $\left(U_b^p\right)_i$ is the i element of $\mathbf{U}_b^p$ and $(\mathbf{P}_b)_i$ is a vector representing the i row of matrix $\mathbf{P}_b$. The new source of ions produced at the first segment (the first column of matrix $\mathbf{D}_b^p$) will start accelerating while charge exchanging further along the path. The fraction of ions charge exchanging out of this source is described in the second row of matrix $\mathbf{P}_b$. We add to the second row of matrix $\mathbf{D}_b^p$ the resulting new sources $S_1\left(\mathbf{P}_b\right)_{i=2}$, where $S_1 = \sum_{i=1}^{1}\left(D_b^p\right)_{i,1}$ $\left((\mathbf{P}_b)_{i=2}\right.$ is a vector representing the second row of matrix $\mathbf{P}_b)$. In the same manner, the source of ions produced at the second segment (sum of the second column) can further charge exchange, etc. (see section 3.3).

For an arbitrary discrete distribution ,$\mathbf{U}_r^p$, along the position axis (x-axis in Fig. 3.1), the $\mathbf{D}_r^p$ matrices are similarly constructed and take the form:

$$\mathbf{D}_r^p = \begin{bmatrix} (U_r^p)_1 P_{11} & (U_r^p)_1 P_{12} & (U_r^p)_1 P_{13} & \cdots \\ 0 & ((U_r^p)_2 + S_1) P_{22} & ((U_r^p)_2 + S_1) P_{23} & \cdots \\ 0 & 0 & ((U_r^p)_3 + S_2) P_{33} & \cdots \\ \vdots & & & \\ 0 & \cdots & & \\ 0 & \cdots & & \end{bmatrix} \tag{3.27}$$

Note that the P_{nm} elements are the elements of matrix $\mathbf{P}_r$. Each matrix $\mathbf{D}_r^p$ stores the fractions of ions that underwent charge exchange in each segment along the path due to an initial ion distribution $\mathbf{U}_r^p$. Similar to the linear potential case, if the interaction is a two specie interaction (e.g. $H^+ - H_2$ interaction), matrices $\mathbf{D}_b^p$, $\mathbf{D}_r^p$ take the same form as in eqs. 3.26 and 3.27 respectively, but setting $S_j = 0$.

Next, the ion source distribution vectors $\mathbf{U}_r^p$ and $\mathbf{U}_b^p$, resulting from each blue-shifted and red-shifted half oscillation respectively, are explicitly found.

3.5.4 Spatial ion source distributions

For the $p = 1$ half oscillation, an initial $\mathbf{U}_b^{p=1}$ distribution of ion sources has to be defined. Similar to the linear potential case, $\mathbf{U}_b^{p=1}$ is defined such that each density of ions n_i is placed at the beginning of each segment:

$$\mathbf{U}_b^{p=1} = \begin{bmatrix} f_1 & f_2 & \cdots & f_k \end{bmatrix} \tag{3.28}$$

where:

$$f_i = \frac{n_i}{\sum_{i=1}^{k} n_i} \tag{3.29}$$

For $p > 1$, as a result of the $p-1$ half oscillation a new distribution of ion sources $\mathbf{U}_r^p$ or $\mathbf{U}_b^p$ is produced along the path and will undergo the p half oscillation. The spatial distribution of ions in $\mathbf{U}_r^p$ contain contributions from three different sources, all of which result from the previous blue-shifted half oscillation. Explicitly, the initial $\mathbf{U}_b^{p-1}$ ion distribution might have had ion sources placed at positions X_j^{Bb}, for $j > t$ (X_{t+1}^{Bb} is the position of the minimum of the potential). These ions could not have traveled in the blue-shifted direction, however, they can now travel in the red-shifted direction. Therefore, these ion sources are placed in vector $\mathbf{U}^p_{r1}$ in reverse order such that:

$$\mathbf{U}^p_{r1} = \left[\left(U^{p-1}_b\right)_k \quad \left(U^{p-1}_b\right)_{(k-1)} \quad \dots \quad \left(U^{p-1}_b\right)_{(t+1)} \quad 0 \quad \dots \quad 0 \right] \tag{3.30}$$

The second distribution of ion sources that can travel in the red-shifted direction results from ions that traveled in the blue-shifted direction but did not charge exchange. These are simply a fraction of the first ion source in $\mathbf{U}^{p-1}_b$ (the first element of $\mathbf{U}^{p-1}_b$) and fractions of each of the S_j sources of matrix $\mathbf{D}^{p-1}_b$ for $1 \leq j < t$ (S_j are the sum of columns of matrix $\mathbf{D}^{p-1}_b$, defined in section 3.5.3). More explicitly, the fractions of ions that had charge exchanged along the path (out of the $\mathbf{U}^{p-1}_b$ ion sources) are the sum of each row in matrix $\mathbf{P}_b$. Denoting the sum of each row as $v_1 = \sum_{j=1}^{k} \mathbf{P}_{b(1,j)}$, $v_2 = \sum_{j=1}^{k} \mathbf{P}_{b(2,j)}$, ..., $v_t = \sum_{j=1}^{k} \mathbf{P}_{b(t,j)}$, the fraction of ions that had survived charge exchange is: $S_{j-1}\left(1 - v_j\right)$. In this notation S_0 is defined to be the first element of the distribution $\mathbf{U}^{p-1}_b$, which is $\left(U^{p-1}_b\right)_{i=1}$. The results are inserted in a row vector,

$$\mathbf{U}^p_{r2} = \left[S_0\left(1 - v_1\right) \quad S_1\left(1 - v_2\right) \quad \dots \quad S_{(t-1)}\left(1 - v_t\right) \quad 0 \quad \dots \quad 0 \right] \tag{3.31}$$

The third distribution of ion sources that can travel in the red-shifted direction results from the ions that have charge exchanged along the path. These are the S_j elements of matrix $\mathbf{D}^{p-1}_b$, for $t \leq j < k$. The S_j elements are inserted into vector $\mathbf{U}^p_{r3}$ in reverse order, starting from the S_k element:

$$\mathbf{U}^p_{r3} = \left[S_k \quad S_{(k-1)} \quad \dots \quad S_{(t+1)} \quad 0 \quad \dots \quad 0 \right] \tag{3.32}$$

The new $\mathbf{U}^p_r$ spatial ion distribution is the sum of the three distributions:

$$\mathbf{U}^p_r = \mathbf{U}^p_{r1} + \mathbf{U}^p_{r2} + \mathbf{U}^p_{r3} \tag{3.33}$$

If the interaction is a two specie interaction (e.g. $H^+ - H_2$ interaction), the new cold ions produced due to charge exchange are not of the same specie, and therefore, when constructing $\mathbf{U}^p_{r2}$ the expression $S_{(j-1)}\left(1 - v_j\right)$ should be replaced by the expression $\left(U^{p-1}_b\right)_j \left(1 - v_j\right)$ for $j = 1$ to $j = t$, and $\mathbf{U}^p_r = \mathbf{U}^p_{r1} + \mathbf{U}^p_{r2}$.

In the same way the new distributions $\mathbf{U}^p_b$ (resulting from each previous red shift half oscillation) are found while using the distribution $\mathbf{U}^{p-1}_r$, matrix $\mathbf{P}_r$ and matrix $\mathbf{D}^{p-1}_r$:

$$\mathbf{U}^p_b = \mathbf{U}^p_{b1} + \mathbf{U}^p_{b2} + \mathbf{U}^p_{b3} \tag{3.34}$$

Note that for $p > 1$ oscillations, the vectors $\mathbf{U}^p_{r1}$, $\mathbf{U}^p_{b1}$ become zero vectors and do not contribute to $\mathbf{U}^p_r$ and $\mathbf{U}^p_b$ respectively.

3.5.5 Cumulative and statistical properties

Each of the $\mathbf{D}_b^p$ and $\mathbf{D}_r^p$ matrices contain the fraction of ions that underwent charge exchange in the well for each half oscillation, where the columns of the matrices store the fraction of ions that underwent charge exchange in each segment along the path. Moreover, each fraction of ions in matrices $\mathbf{D}_b^p$ and $\mathbf{D}_r^p$ has a corresponding energy in matrices $\mathbf{E}_b$ and $\mathbf{E}_r$ respectively.

The distribution of the total fraction of ions that underwent charge exchange along the path for the blue-shift motion and for a q number of half oscillations is:

$$\mathbf{D}_{bT}^q = \sum_{p=odd}^{q} \mathbf{D}_b^p \tag{3.35}$$

whereas, the distribution of the total fraction of ions that underwent charge exchange along the path for the red-shifted motion and for a q number of half oscillations is:

$$\mathbf{D}_{rT}^q = \sum_{p=even}^{q} \mathbf{D}_r^p \tag{3.36}$$

The average energy of the ions in each segment along the path for the blue-shifted or red-shifted motions is:

$$\left(\overline{E}_{b/r}\right)_j = \frac{\sum_{i=1}^{k} \left(D_{b/rT}^q\right)_{ij} \left(E_{b/r}\right)_{ij}}{\sum_{i=1}^{k} \left(D_{b/rT}^q\right)_{ij}} \tag{3.37}$$

where the indexes b/r refer to the blue-shifted or red-shifted motions, respectively. We also define an expression for the total average energy of the blue-shifted and red-shifted directions in each segment:

$$\left(\overline{E}_{b+r}\right)_j = \frac{\sum_{i=1}^{k} \left[\left(D_{bT}^q\right)_{ij} \left(E_b\right)_{ij} + \left(D_{rT}^q\right)_{i,k-j+1} \left(E_r\right)_{i,k-j+1}\right]}{\sum_{i=1}^{k} \left[\left(D_{bT}^q\right)_{ij} + \left(D_{rT}^q\right)_{i,k-j+1}\right]} \tag{3.38}$$

where in this expression we consider that the numbering of the Δx_j segments in matrix $\mathbf{D}_r^q$ is reversed in relation to the segments of matrix $\mathbf{D}_b^q$.

3.6 Model based programs

3.6.1 Programs

The semi-analytical approach was used for charge exchange modelling, where the electric field is uniform along the beam path and will be compared to Monte Carlo modelling. Programs based on the semi-analytical approach were constructed also for the potential well case.

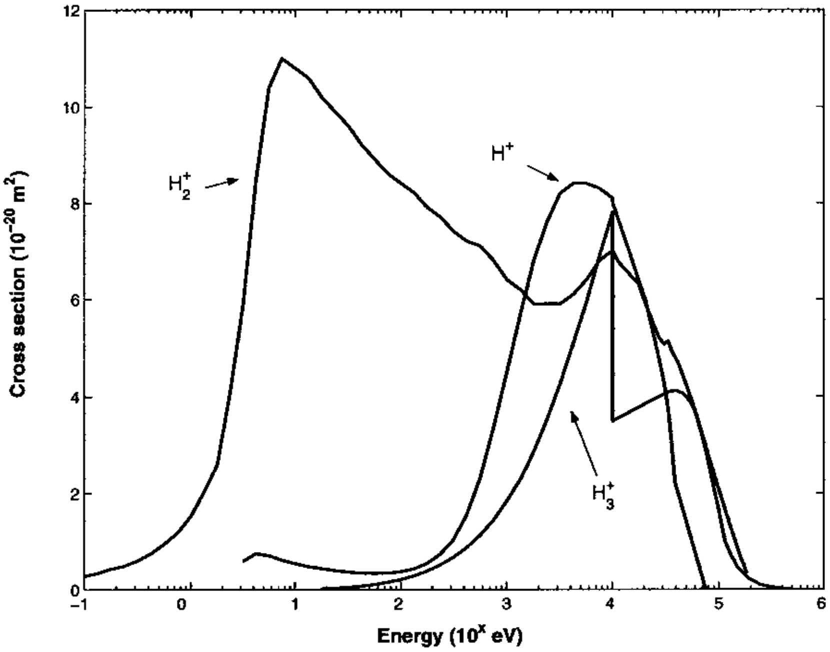

Figure 3.2: The charge exchange cross sections as a function of energy for the three ionic species H^+, H_2^+ and H_3^+. The data was taken from two independent sources [11, 12], where one source of data is for energies in the range of $10^{-4} - 10$ keV and the other is for energies larger than 10 keV.

Six programs, one for each of the three charge exchange reactions (see eq. 2.6) and for the two cases of the linear potential and potential well, were structured using MATLAB. Each program included the appropriate mass, charge and charge exchange cross sections. The variable parameters were background gas pressure, shape of the potential and ion source distribution.

The numerical results of the programs strongly depend on the charge exchange cross sections. Figure 3.2 presents the experimental charge exchange cross sections used for the three dominant ionic species H^+, H_2^+ and H_3^+ [11,12]. The plot shows a log-linear relationship between the cross section and energy. The x axis was logarithmically scaled so that every value on the x axis corresponds to an energy of 10 to the power of that value, in units of eV. Note that the data in the plot was taken from two independent sources. One source of data is for energies in the range of $10^{-4} - 10$ keV and the other is for energies larger than 10 keV. this accounts for the sudden jump of the cross section at 10 keV for the H_3^+ specie.

Verification of the reliability of the programs was carried out by using different computational approaches given in the following section.

3.6.2 The semi-analytical method in comparison to Monte Carlo simulations

Monte Carlo simulations are considered a standard approach when modelling the charge exchange process. Khachan [13] had used the Monte Carlo approach to model charge exchange for an H_2^+ hydrogen ion beam accelerating in a hydrogen background gas due to a linear potential. Similar to the semi-analytical method, the beam length was divided into segments and all ions were started at the beginning of the first segment. A potential difference was applied between the start and end points of the beam. As a result, the electric field across these two points was constant. Although the theory presented above can address much more complex spatial potential distributions with arbitrary ion starting positions, the simplest case is explored where ions start in the first segment since it applies to certain types of hollow cathode glow discharges that produce hydrogen ion beams (including the IEC device presented in Figs. 2.1, 2.2). Moreover, the acceleration region between the anode and cathode can be approximated to have a constant electric field. H_2^+ is the most abundant specie in these discharges [14, 15], therefore, this discussion focuses on the $H_2^+ - H_2$ charge exchange interaction.

The basic procedure for the Monte Carlo modelling was to accelerate the ions starting from the first segment, one at a time. The ion energy was calculated from the change in potential, which enabled the charge exchange cross-sections to be determined from tables given by Phelps [11] and have been reproduced in Fig. 3.2. The charge exchange probability, P, was then determined from $P = 1 - \exp(-n\sigma\Delta x)$, where n is the number density of the background gas, σ is the charge exchange cross-section, and Δx is the length of a segment. A random number is then generated and if it falls within this probability, then charge exchange is considered to have taken place. As a result, the energy of the resulting neutral is stored for that segment, and a new ion is started from rest at that position. This ion is again followed along the remainder of the beam and the whole process is repeated until the end of the beam length is reached. This process is repeated for another ion starting from the first segment. With increasing number of ions, a tally is obtained of the average energy of ions that have undergone charge exchange in each segment. This enabled a comparison to be made with $\overline{E}_j$ given in eq. 3.16.

The results of the Monte Carlo modelling are presenting in Fig. 3.3, where a beam path of 10 cm was used for background H_2 gas pressures of 1, 5, 10, 20 and 30 mTorr. A voltage of 10 kV was applied across the beam path length.

The same conditions were used for the semi-analytical modelling, presented in Fig. 3.4. Clearly the results of the two methods are identical, notwithstanding the numerical noise in the Monte Carlo results, where 10^4 ions were used. There was a stark difference in computational time for each of these results, where the semi-analytical results took in the order of seconds to complete for 100 segments, whereas the Monte Carlo approach required in the order of 10 minutes for 50 segments for the same microprocessor (Pentium 4) and computing language (MATLAB).

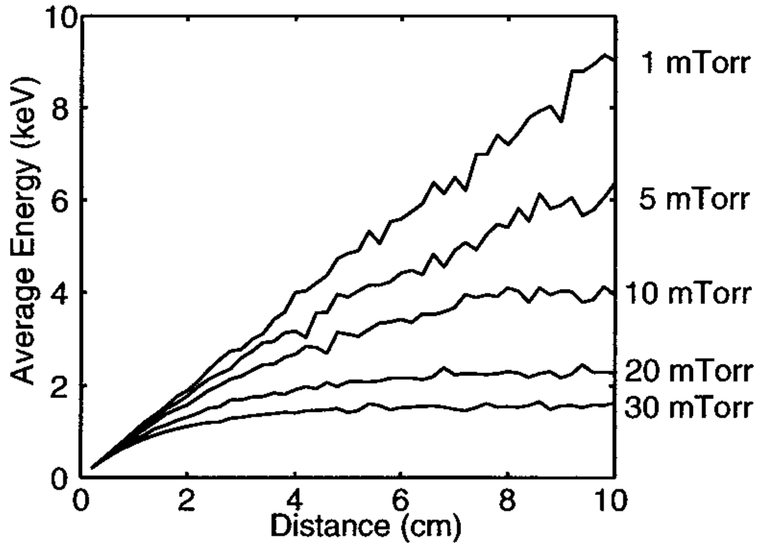

Figure 3.3: Monte Carlo simulations for an $H_2^+ + H_2$ charge exchange interaction and for a linear potential. The average energy is given as a function of distance from an anode. The voltage across the 10 cm beam was set to 10 kV while varying the pressures between 1 mTorr and 30 mTorr.

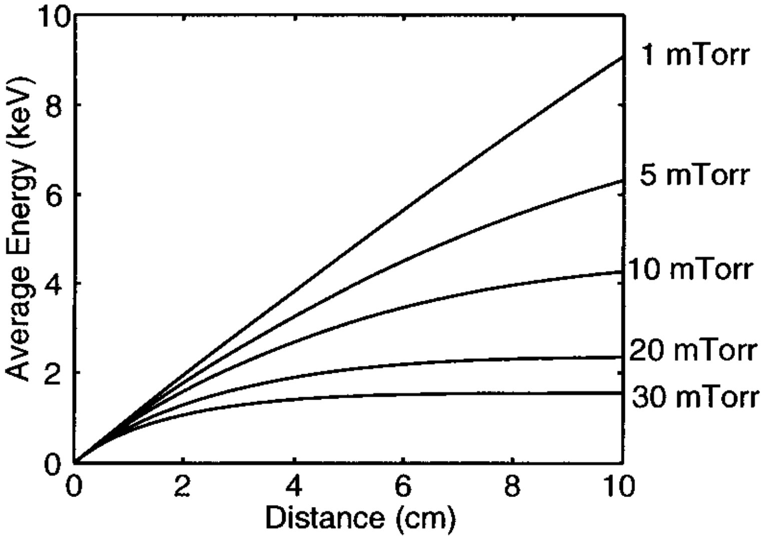

Figure 3.4: Average ion energy versus distance from the anode using the semi-analytical approach for the same conditions as in Fig. 3.3.

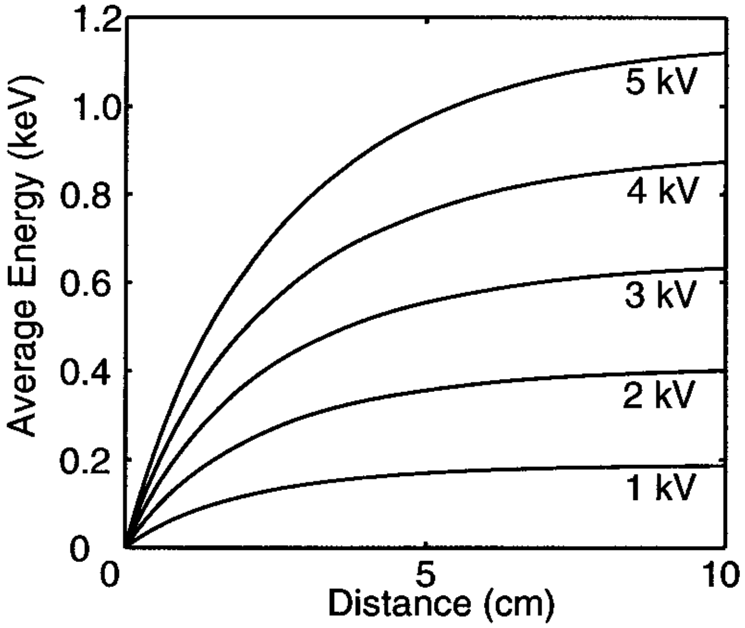

Figure 3.5: Average ion energy versus distance from the anode at a pressure of 20 mTorr for 1, 2, 3, 4 and 5 kV across 10 cm of beam length.

The computing superiority of the semi-analytical approach aside, note that the average ion energy reaches a limiting value with increasing pressure. It is shown in Fig. 4.8 that the value of this average energy limit is roughly at the same percentage of the applied potential for the same pressure.

3.7 Summary

An intuitive method ("semi-analytical") for modelling the charge exchange process of hydrogen ion beams has bean developed as an alternative to a Monte Carlo method. Moreover, a Markov chain approach was used and was shown to agree with the semi-analytical method. The modelling was carried out for the general cases of monotonic increasing (or decreasing) potentials, which include the linear potential and potential well. The semi-analytical method was applied to hydrogen ions accelerating in a linear potential in a background H_2 gas and compared with a Monte Carlo simulation. It was found that the advantage of the semi-analytical method was the rapid computing time without any numerical noise. The method can easily be applied to many systems where charge exchange is dominant, and further applied to other processes providing they have similar chain properties.

This chapter, in addition to the second chapter, present all the necessary experimental and theoretical background material for the analysis of spectroscopic measurements presented in the following chapters. The models are used to predict spatial energy distributions, reconstruct spectra, estimate confinement time and neutron production rates for IEC systems operating in the units of mTorr region.

Bibliography

[1] R. L. Hirsch, J. Appl. Phys., **38**, 4522 (1967).

[2] G. H. Miley, J. Nadler, T. Hochberg, Y. Gu, O. Barnouin and J. Lovberg, Fusion Technol., **19**, 840 (1991).

[3] J. Nadler, G. H. Miley, Y. Gu and T. Hochberg, Fusion Technol., **20**, 850 (1991).

[4] T. A. Thorson, R. D. Durst, R. J. Fonck and L. P. Wainwright, Phys. Plasmas, **4**(1), 4 (1997).

[5] D. C. Baxter and G. W. Stuart, J. Appl. Phys., **53**, 7 (1982).

[6] T. A. Thorson, R. D. Durst, R. J. Fonck and A. C. Sontag, Nuclear Fusion, **38**(4), 495 (1998).

[7] S. Børve, H. L. Pécseli, J. Trulsen and S. Longo, Phys. Scr. T122, 125-128 (2006).

[8] S. Longo and P. Diomede, Eur. Phys. J. Appl. Phys., **26**, 85-177 (2004).

[9] G. W. McClure, Phys. Rev., **140**, A769 (1965).

[10] S. C. Haydon, "Discharge and Plasma Physics" (1964).

[11] A. V. Phelps, J. Phys. Chem. Ref. Data, **19**, 653 (1990).

[12] C. F. Barnett, J. A. Ray, E. Ricci, M. I. Wilker, E. W. McDaniel, E. W. Thomas, H. B. Gilbody, Atomic Data for Controlled Fusion Research Volume I., ORNL-5206 (1977).

[13] O. Shrier, J. Khachan and S. Bosi, J. Phys. A: Math. Gen., **39**, 11119–11128 (2006).

[14] J. Khachan and S. Collis, Phys. of Plasmas, **8**(4), 1299 (2001).

[15] M. Fitzgerald, J. Khachan and S. Bosi, Eur. Phys. J. D, **39**, 35–39 (2006).

Chapter 4

Spectrum Analysis and Model Applications

In this chapter the charge exchange model is used to explain the observed Doppler shift spectral broadening. Furthermore, other applications of the model are presented. The chapter opens with the presentation of a new phenomenon, which is the divergence of neutral atoms from the cathode. This phenomenon is responsible for the dominant blue-shifted wing observed in the spectra, where the wing was simulated with the charge exchange model. Since the spectra also show a less significant red-shifted wing, the model was then used also to account for this. Last, two other applications of the model are presented relating to high pressure discharge systems and to IEC confinement time estimations.

4.1 Motivation

An experimental result has been found and gives rise to an hypothesis that challenges the conventional view of the operation of IEC (when operating in the mTorr regime). The conventional view of operation is of ions converging to the cathode centre. High fluxes of neutral atoms were found to diverge from the cathode, where the hypothesis states that the ions originate in the cathode centre [1–3]. The semi-analytical method (described in chapter 3) has been applied to a potential well while accounting for the charge exchange process in the entire well region. The model, together with the application of the experimental result, was used to reconstruct the blue-shifted distribution in spectra taken with IEC devices operating in the units and tens of mTorr pressure range.

The spectra also show a fainter red-shfited component implying that smaller densities of neutral atoms converge to the cathode. Since a discharge exists between the cathode and anode, ions are produced along the cathode to anode path. The model is used to reconstruct the red-shifted distribution in the spectra while approximating the potential between the anode and cathode to be linear (the potential extends to a longer distance than the maximum collision pathlength for the experimental conditions).

In addition, energy distributions resulting from the model were used to demonstrate

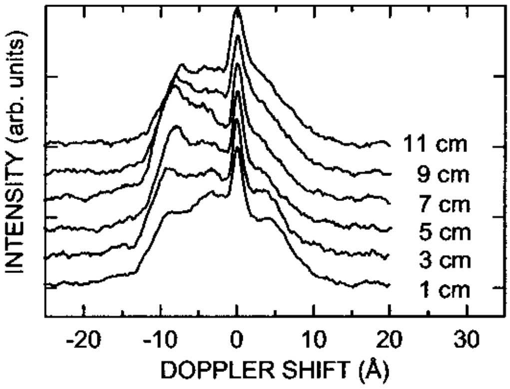

Figure 4.1: Measurements taken along the channel, at 30° relative to the monochromator, in intervals of 2 cm, starting from 1 cm from the cathode's edge. The spectra are displaced vertically with respect to each other, showing the dominance of the blue-shifted wing.

spectrum reconstruction for high pressure discharge systems (hundreds of mTorr). As a last application, the model was used to estimate confinement time in IEC devices operating in the units and tens of mTorr pressure range.

4.2 The "blue shift" phenomenon

4.2.1 Neutral atom divergence from the cathode

The main principles of IEC are convergence of ions to the cathode centre and confinement of the ions in a potential well. Figure 2.8 (chapter 2) presents a typical spectrum, observed at 0° relative to the beam (channel), where the lens imaged the cathode centre onto the monochromator's slit. Considering line integration effects, the spectrum was found to reflect the distribution of wavelength shifts in the entire cathode region. The blue shifted side (negative wavelength shifts) and the red shifted side (positive wavelength shifts) were found to be symmetric around the unshifted peak. These results can be explained with the above-mentioned principles, where ions converging to the cathode undergo charge exchange, resulting in emission from excited neutrals in the cathode region. The symmetry of the apparatus gives rise to the symmetry in the Doppler shift (the wings on both sides of the unshifted peak).

Measurements of ion energies along the beam (from the cathode edge to anode) were carried out at an observation angle of 30° relative to the beam. As a result of the $\cos\theta$ factor (see eq. 2.7, chapter 2), the wings moved towards the unshifted peak. Nevertheless, in most cases it was clearly possible to identify the positions of the second and third peaks (representing the H_2^+ and H^+ species respectively). Figure 4.1 presents measurements taken along the beam in intervals of 2 cm, starting 1 cm from the cathode edge and moving towards the anode. The measurements were taken for an applied cathode voltage of -7 kV and for

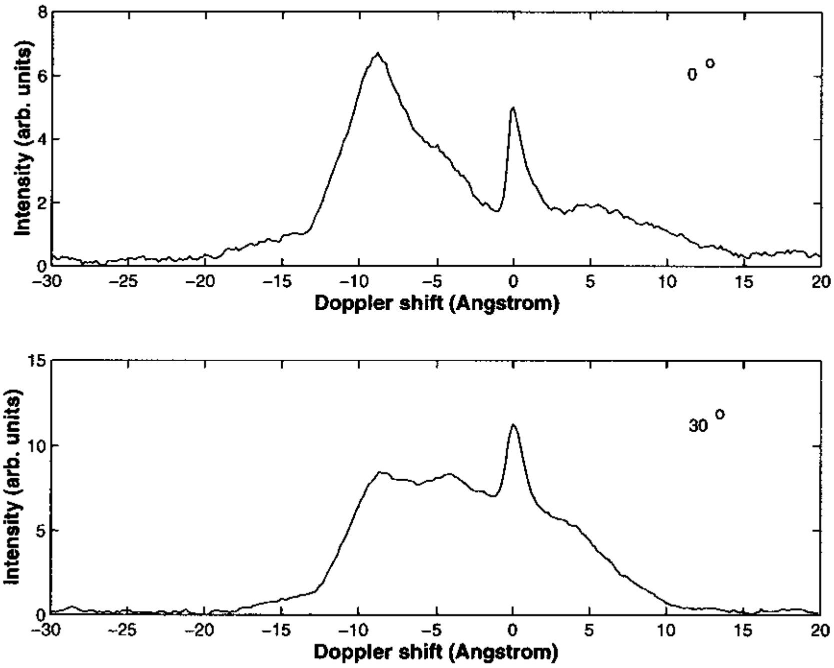

Figure 4.2: Two spectra taken 8 cm away from the centre of cathode showing the dominance of the blue-shifted wing. The upper and lower spectra were obtained at 0° and 30° angles, respectively, relative to the beam.

a pressure of 15 mTorr. For comparison, the spectra are displaced vertically with respect to each other.

It is clear that the blue-shifted wing now dominates the spectra, with a great reduction in the intensity of the red-shifted wing. Since the scan is outside of the cathode region, it is assumed that a higher density of neutrals are streaming in one direction. The cathode is tilted at 30° relative to the monochromator, such that the beam on the one side of the cathode is closer to the monochromator than the other. The spectra were recorded from the beam closer to the monochromator, which implies that neutral atoms are streaming towards the monochromator, away from the cathode (blue-shifted neutrals).

Figure 4.2 further supports the phenomenon. The two spectra were taken 8 cm from the cathode centre, along the beam. In both cases the anode-to-cathode distance was set to 16 cm and pressure was 20 mTorr. The upper spectrum was taken when the beam was aligned at 0° relative to the monochromator while applying a cathode voltage of -4.2 kV. The lower spectrum was recorded at 30° relative to the beam and for a cathode voltage of -5 kV. The upper spectrum was obtained by ensuring that the region in focus on the monochromator's slit was 8 cm from the cathode centre. As a result it was expected to be asymmetric (as opposed to the spectra taken while focussing on the centre of cathode), which is clearly seen in the figure.

The apparatus is symmetric about the cathode. Therefore, if a spectrum is taken at 30° angle relative to the beam but from the opposite beam (the beam further away from the

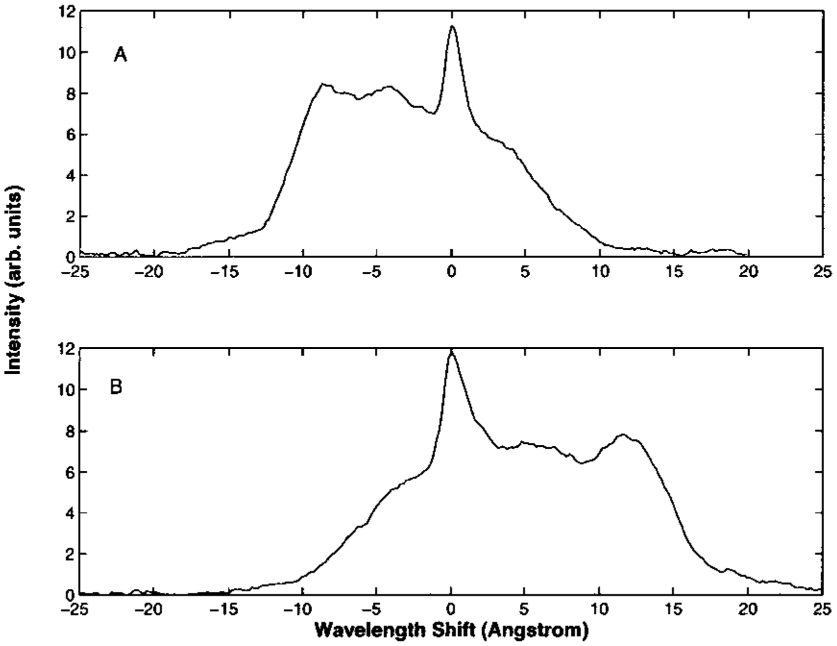

Figure 4.3: Two spectra taken 8 cm away from the centre of cathode showing the dominance of the blue-shifted wing. The upper and lower spectra were obtained at 0° and 30° angles, respectively, relative to the beam.

monochromator), the red-shifted wing should be the dominant. Figure 4.3 shows two spectra taken while focusing on the two beams, 5 cm from each edge of the cathode. The upper plot represents the beam closer to the monochromator and vice versa. The anodes were each placed 16 cm from the cathode center, pressure was set to 20 mTorr and a cathode voltage of -5 kV was applied. Clearly, the two spectra imply that neutrals are diverging from the cathode towards the anodes.

4.2.2 Hypothesis: ions originating in the cathode centre

The basic principle of IEC is to produce a cylindrically or spherically symmetric electrostatic potential well that accelerates and converges ballistic positive ions to produce fusion reactions. While this concept may be valid for high vacuum conditions [4–9], in reality many contemporary IEC machines are operated in the units to tens of mTorr pressure range [10] where gaseous discharge physics is dominant. Nevertheless, it has been demonstrated that nuclear fusion reaction rates in deuterium are typically $\sim 10^7$ s^{-1} for input powers of several hundred Watts (a factor of 100 higher for a 50% tritium mixture) [10]. Moreover, it has also been shown that this is due to the collision of deuterium beams with the background gas [11] rather than beam-beam collisions. A possible explanation for the blue shift could be that ions approaching the cathode from the other side of the cathode undergo charge exchange become excited neutrals. These pass through the cathode and de-excite while approaching the monochromator, thereby producing the dominant blue shifted wing in the spectrum. The

H_α line results from several transitions. The slowest transition is from the $3s-2p$ states and is ~ 0.5 μs while the fastest transition is from the $3d-2p$ states and is $\sim$ 16 ns. Assuming an energy of 1 kV, some of the excited H^* will de-excite through the $3s-2p$ transition along a 20 cm path [1]. Therefore, when focusing on some part of the beam closer to the monochromator it is possible to receive the emission of these excited atoms.

However, it has been found that a potential well is established between the cathode center and anode, where a minimum is found at the cathode edge (a virtual anode is established in the cathode) [12,13]. This gives rise to a steep potential drop extending between the cathode center and edge (see Fig. 4.4). An hypothesis, challenging the conventional view of IEC device operation, suggests that a significant density of ions originate at the cathode center and diverge outwards. The ions charge exchange and become energetic neutral atoms that exit the cathode interior and travel toward the anode. It is suggested that this is due to electron emission from the inner surface of the cathode which converges to the center, where a plasma is generated and a space charge produces an electric field that is directed away from the center ([14–16]). Therefore, IEC devices operating in the gaseous discharge regime could be considered a type of hollow cathode discharge. This is also suggested in the qualitative measurements presented in Fig. 4.1, where the red-shifted wavelength distribution does not vary much along the beam. This implies that most of the neutral energy distribution is established in the cathode region (note that the potential has a minimum at the cathode edge such that ions within the cathode must accelerate out of the cathode and vice versa).

Attempts were made to verify the hypothesis, by trying to eliminate one of the beams by blocking one cathode entrance with glass. The glass became an anode and a short beam was formed between the cathode center and the glass. Removing one anode from the system did not block the beam either, since the wall of the chamber became an anode and a beam was formed between the cathode center and the wall.

A non-intrusive measurement was carried out with the aim of tracing the origin of the neutral atoms by determining their energy distribution for different ion path-lengths. The anodes were placed at different distances from the cathode, where spectra were obtained at 0° relative to the beam while focusing on the cathode center. It was assumed that the neutral energy distribution of the ions that charge exchanged should change for different ion path-lengths. If the ions were to travel from the anode to the cathode centre, the spectrum should reflect different distributions for different anode-to-cathode distances. However, if the ions diverge from the centre of cathode outwards, no changes in the spectrum shape is expected (since the potential has a minimum at the cathode's edge and the cathode size is a constant, which does not depend on the anodes placement). The spectra did not show any change for different anode-to-cathode distances (these measurements are presented in chapter 5 in relation to scaling laws). This evidence by itself is not conclusive and is not sufficient, however, other work was found to strongly support this hypothesis; these include measurements of dusty plasma [2], a thruster that was build on the basis of the hypothesis [3] and other spectroscopic measurements carried out on IEC devices [1].

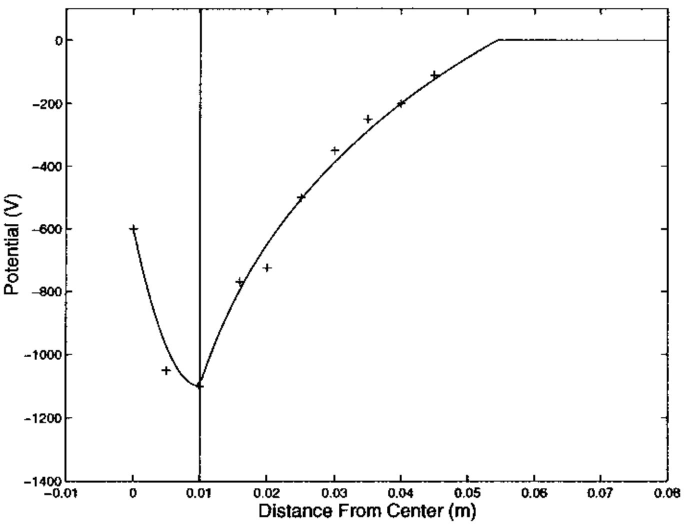

Figure 4.4: Measurements of the potential from Khachan et al. [12] (marked with "+"). The x axis represents distances measured from the cathode centre. The cathode was 2 cm long (the cathode edge is marked with a vertical line), the applied cathode voltage was −2 kV and pressure was 5 mTorr. The analytical function that was fitted to the data is represented by the continuous line.

4.3 The blue-shifted distribution in the spectrum

4.3.1 Ion and neutral energy distributions in the potential well

Energy distributions for ions and neutrals in a potential well were calculated for both spatially uniform and non-uniform ion distributions. These distributions were used to reconstruct the blue-shifted part of the spectra. The energy distributions were obtained from matrices $\mathbf{E}_b$, $\mathbf{D}^q_{bT}$ and $\mathbf{E}_r$, $\mathbf{D}^q_{rT}$ (see chapter 3), where the fractions of ions having the same energies were summed to give the intensities. Note that matrices $\mathbf{E}_b$ and $\mathbf{E}_r$ contain the energies of the parent ions, which had charge exchanged. The energies of the neutral H atoms can easily be obtained by dividing the ion energies by the ratio of the mass of the parent ion to the mass of the neutral atom, as mentioned in chapter 2. Furthermore, the distributions of ion energies are for the entire well and not for different positions along the well.

In gridded IEC devices independent experiments suggest that a potential well is established between the cathode centre and the anode [12,13]. The shape of the potential measured by Khachan et al. [12] was fitted to an analytical function and used in the simulations described in chapter 3. The measurement was obtained for an applied cathode voltage of −2 kV and for a pressure of 5 mTorr, where the measured potential (marked with "+") and the analytical function (continuous line) are presented in Fig. 4.4. It is clear that the potential reaches zero at $\sim$ 0.68 of the total path and that the potential has a minimum at the cathode edge. Similar results were independently obtained in other work [13] and therefore, the potential depth and the position of the minimum of the potential were made to vary while

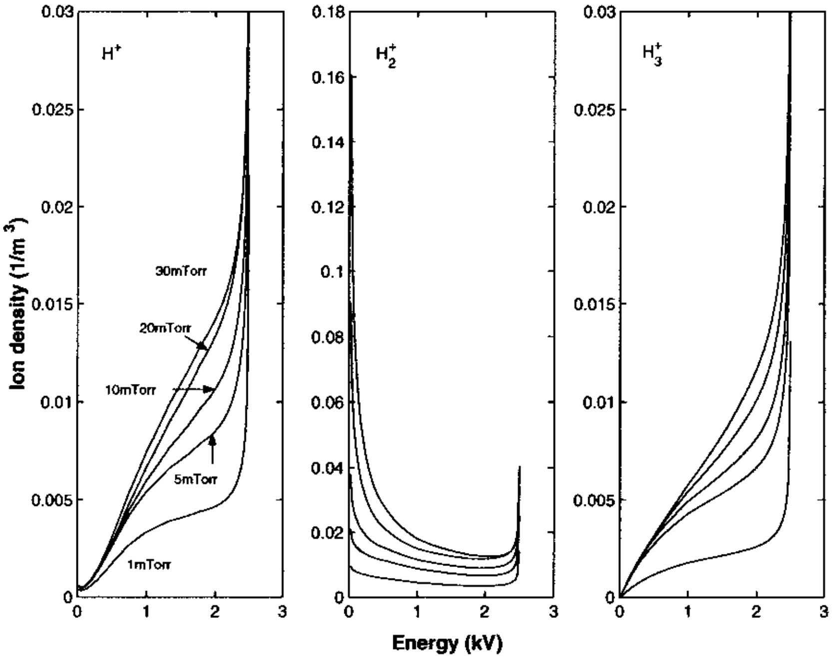

Figure 4.5: A local ion source used in the simulation resulting in energy distributions for the H^+, H_2^+ and H_3^+ species and for pressures of 1, 5, 10, 20 and 30 mTorr. The total width of the potential well (having the shape of the well in Fig. 4.4) was set to 16 cm. The potential depth was set to −2.5 kV and the minimum in the potential was positioned at 2.5 cm of the width of the potential. Note that the distributions are for the blue-shifted motions only.

maintaining these conditions. In the experimental set-up presented in Fig. 2.2 the cathode half length was ~ 2.5 cm and therefore, the potential minimum was set at that distance in the simulation. The experimental result, presented in Fig. 4.4, shows that the depth of the potential is ~ 25 % of the total applied cathode voltage with respect to the potential at the cathode centre. Following this experimental result, the depth of the potential used in the simulation was −2.5 kV (that is for −10 kV applied on the cathode). Hereafter, we define the maximum potential depth to be the potential difference between the cathode centre and the potential well minimum.

Figure 4.5 presents results of energy distributions for a potential well and for a local ion density positioned at the top of the well, which is at the centre of cathode. The ions were started at the beginning of the first segment, which in this case represents the position of the centre of cathode. The local ion density starting the process was normalized to $1/m^3$. For each specie (marked in the figure) there are 5 distributions corresponding to input pressures of 1, 5, 10, 20 and 30 mTorr. The simulation was stopped after 10 oscillations (the process damps after ~ 4 oscillations and the distributions do not change). However, the distributions are constructed from matrices $\mathbf{E}_b$ and $\mathbf{D}^q_{bT}$, representing only the blue-shifted motion in the well.

From Fig. 4.5, it is clear that the intensities are higher for the higher ion energies.

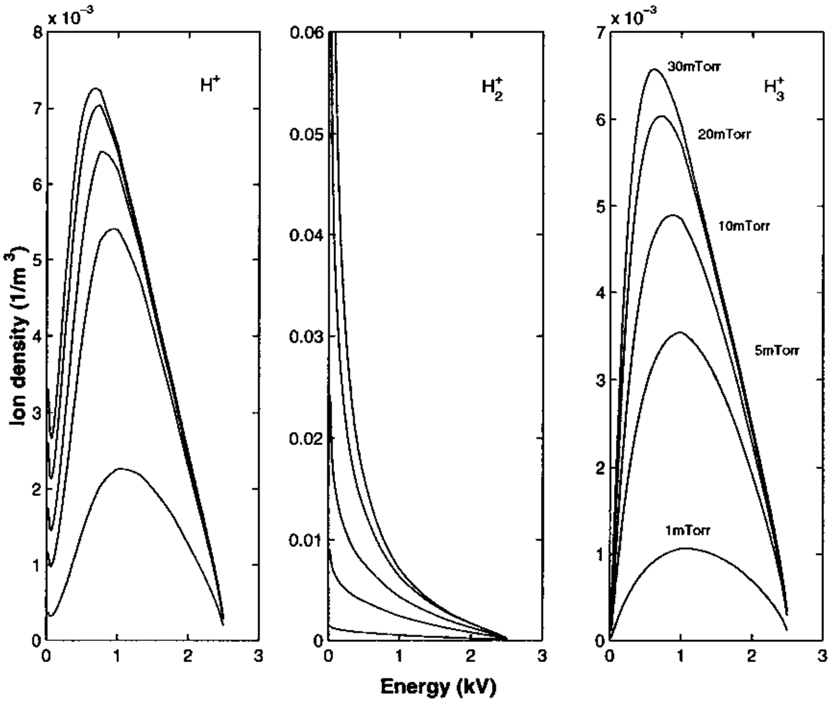

Figure 4.6: Ion energy distributions for H^+, H_2^+ and H_3^+ for the same pressure ranges as those in Fig. 4.5 but using a uniform ion source distribution within the potential well region (having the shape of the well presented in Fig. 4.4).

However, note that the H_2^+ specie distributions differ from the H^+, H_3^+ species distributions. This is due to the many low energy neutral atoms produced in the H_2^++H_2 interaction. Consequently, the intensity of the lower energies is enhanced.

The distributions presented in Fig. 4.5 result from an ion source placed at the top of the potential, at the cathode centre. Consequently, it is assumed that the highest ion density is localized at the centre, which has been supported by experiment. Another scenario is where the ion density is not sharply peaked at the centre or the discharge along the path is dominant and a distribution of ion sources is created along the path. As a first approximation, a uniform distribution of ion sources along the path was assumed.

Figure 4.6 presents the resulting distributions for the same conditions as of Fig. 4.5, but for a spatially uniform ion source distribution along the path (as seen in Fig. 4.4, the ion path ranges from the cathode centre to the minimum in the well and out to a radial distance at which the potential equals the central potential). Note that the distributions of the three species in Fig. 4.6 are different to those of Fig. 4.5. In contrast to the results in Fig. 4.5, the maximum intensities now occur at the lower energy range for H^+ and H_3^+. In particular, the intensity peak occurs at $\sim 40\%$ of the maximum possible energy that can be gained from the potential well depth. However, the intensity for the H_2^+ reaction decreases monotonically with increasing energies.

As a second order approximation for the discharge, a linearly increasing density distribution of ion sources along the path was used, which showed similar results to the uniform distribution (the peaks slightly shifted to lower energies).

4.3.2 Spectrum reconstruction

The blue-shifted spectrum (such as the blue-shifted wing presented in Fig. 4.2) has been simulated by modelling the ion motion in a potential well.

The spectrum presented in Fig. 2.6 (chapter 2) was obtained with the same IEC device used for the measurements of the potential presented in Fig. 4.4, where the measurements were taken by Khachan et al. [12, 17]. The apparatus produced two colinear and opposing beams, similar to the beams produced by the apparatus shown in Fig. 2.1. The modelling was carried out for the three interactions ($H^+ + H_2$, $H_2^+ + H_2$, $H_3^+ + H_2$) for conditions that were also used experimentally. The cathode to anode distance was 8 cm. The minimum of the potential was set at 1 cm distance since the potential has a minimum at the cathode entrance (cathode was 2 cm long). The potential was set to approach zero at ~ 0.68 of the total anode-to-cathode distance (see Fig. 4.4). The neutral atoms maximum energy was found to be 25% of the applied cathode voltage [12, 17]. Therefore, the potential depth (with respect to the potential at the cathode centre) was set to -0.5 kV, which is 25% of the applied cathode voltage. Pressure was set to 5 mTorr and an initial density of N_0 ions was placed at the top of the potential, at the cathode centre. Note that the spectrum in Fig. 2.6 was obtained for a cathode voltage of -4 kV, whereas the potential used for the modelling was the measured potential presented in Fig. 4.4, which was obtained for a cathode voltage of -2 kV. This does not affect the spectrum line shape, which was experimentally found to be similar for applied cathode voltages in the range of $1 - 10$ kV [12, 17]. However, the peaks of the wing shift further away from the unshifted peak for increasing voltages.

The three resulting energy distributions (for each specie) were found to be similar in shape to the distributions presented in Fig. 4.5. The reconstruction of the spectrum is based on the resulting energy and density distributions obtained in matrices $\mathbf{E}_b$, $\mathbf{D}_{bT}^{q}$ respectively (see chapter 3), where the energies were converted to wavelength shifts. The wavelength scale in the simulations was divided at most into 0.5 Å segments (in most case the segments were made smaller than 0.5 Å), which was also the resolution of the monochromator. These segments shall be referred to as "bins". The densities in each bin were accumulated to give the total density for a bin. We regard this density as the density of neutrals at an average wavelength shift represented by the position of the bin. A Lorentzian was used to approximate the central unshifted peak, where the half-width was set equal to the experimental half-width.

Figure 4.5 shows that the total density of charge exchanging ions is largest for the H_2^+ specie and smallest for the H_3^+ specie (this is for the same initial ion density starting the process). However, for the range of energies of units of keV the H_α excitation cross-sections are largest for the H_3^+ specie and smallest for the H^+ specie [18]. Moreover, the density of the H_2^+ specie was estimated to be larger than the densities of the other two species [17]. This accounts for the relative intensities of the peaks of the spectrum presented in Fig. 2.6.

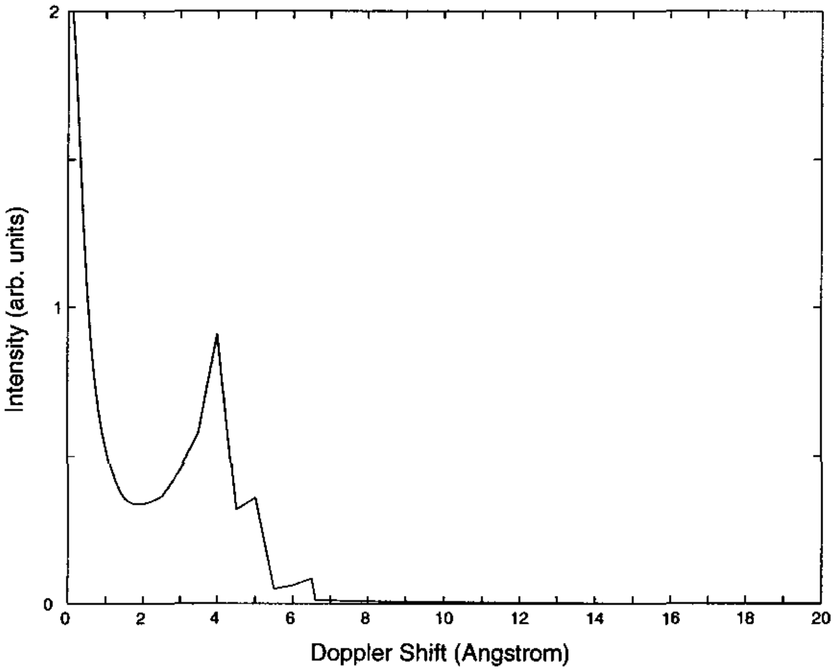

Figure 4.7: A simulation of the spectrum shown in Fig. 2.6.

Since we do not have information of the initial relative densities of the three ionic species starting the process, in the reconstruction the densities were scaled so that the three peaks (representing the three ionic species) had the same ratio as the experimental relative intensity of the peaks.

The results are presented in Fig. 4.7. The shape of the theoretical spectrum is found to be in good agreement with the experimental spectrum shown in Fig. 2.6. The H_2^+ distributions given in Fig. 4.5 have the shape of a flat well where the intensity steeply increases at low and high energies. Consequently, this distribution fills the gap between the unshifted and first peak and is also responsible for the second peak. The H^+ and H_3^+ distributions are most intense at the highest energy and are responsible for the third and first peaks, respectively.

In previous work it has been found that the energy of all three species is the same and corresponds to the maximum potential depth [12, 17]. The distributions presented in Fig. 4.5 illustrate these experimental findings, where it is evident that the energies corresponding to the three peaks are equal and are also the maximum energies allowed by the depth of the potential well. Any inconsistencies that appear between the simulated and experimental spectra can be attributed to simplifying assumptions; In practice the ion source distribution is not a point like source, the beam might have a slight angular spread, ions are accelerated in the cathode region towards the cathode surface in all directions via the sheath, and there are neutral atoms coming through from the well on the other side of the cathode. These can be responsible for peak broadening.

Next is a spectrum reconstruction that further considers the complexity of the spectrum, which results from the ion oscillation motion in the well. The spectra shown in Fig. 4.2 were

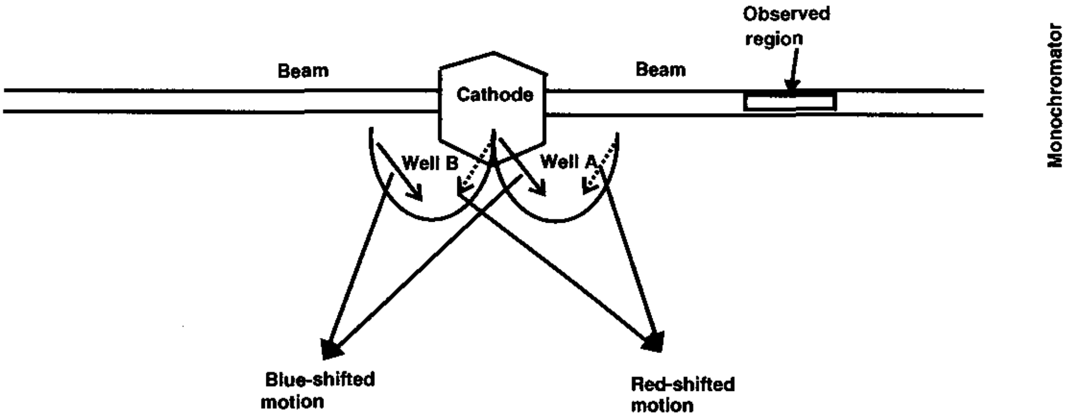

Figure 4.8: An illustration of the blue and red shifted motions in the two wells. The blue-shifted distribution in the experimental spectrum results from the blue-shifted motion of the ions in both wells A and B. Furthermore, the blue-shifted neutral atom distribution resulting from well B is the same as the red-shifted neutral atom distribution resulting from well A.

obtained with the experimental set-up described in chapter 2 (the experimental conditions are detailed in section 4.2.1). Here we refer to the upper spectrum in the figure, where the beam was aligned at 0° relative to the monochromator while focussing a region of the beam on the monochromator's slit, 8 cm away from the cathode center. Energy measurements show that the ions gained a maximum energy equivalent to $\sim$ 60% of the applied cathode voltage (the detailed analysis is presented in chapter 5). Therefore, a potential depth of 60% of the applied cathode voltage was used in the simulation. Since the cathode was 5.5 cm long and the minimum in the potential is assumed to be found near the cathode edge, the minimum in the potential was set at a distance of 2.5 cm.

Each of the two wells in the cathode is $\sim$ 5 cm long and the neutral atom energy distribution is established within this range. The ions are trapped in the wells until they charge exchange and escape the cathode as neutral atoms, either towards or away from the monochromator. Fig. 4.8 illustrates the blue and red shifted ion motion in the two wells (the closer well to the monochromator is marked "A" and the other is marked "B"). The observed region on the beam was out of the cathode, far from the minimum of the potential position. Therefore, the red-shifted distribution in the spectrum does not result from the emission of neutral atoms escaping the wells from the cathode region. However, the blue-shifted distribution originates from neutral atoms escaping both wells A and B in the monochromator's direction (see Fig. 4.8). Furthermore, the blue-shifted neutral atom distribution resulting from well "B" is identical to the red-shifted neutral atom distribution resulting from well "A". This allows for the use of one well for the reconstruction, where the blue-shifted and red-shifted energy distributions are superposed.

The reconstruction follows the same procedure previously described, however, in this case, matrices $\mathbf{E}_b$, $\mathbf{D}^q_{bT}$, $\mathbf{E}_r$ and $\mathbf{D}^q_{rT}$ were used. The results are presented in the upper plot of Fig. 4.9, where the simulated spectrum illustrates the superposition of the blue-shifted

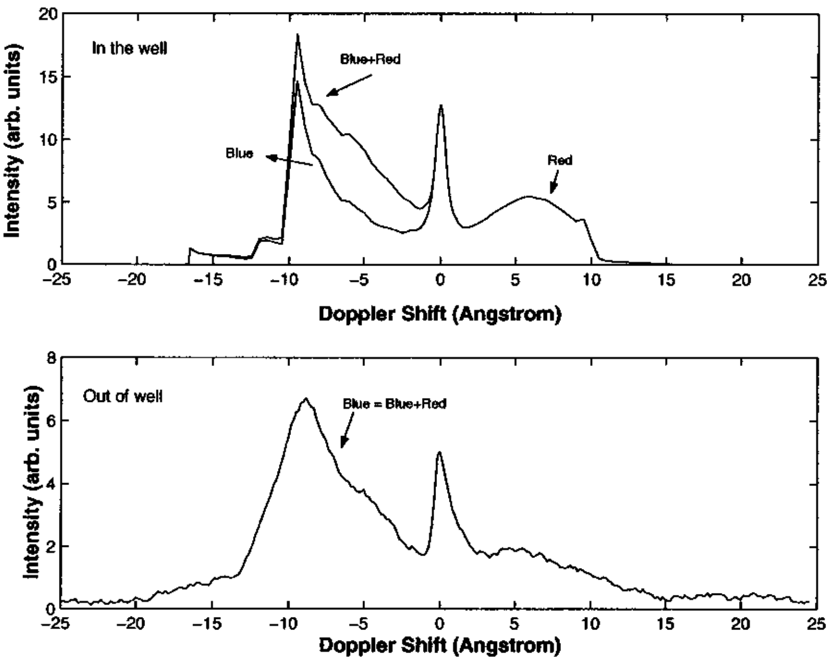

Figure 4.9: The upper plot presents the simulated spectrum for the experimental conditions used to obtain the experimental spectrum shown in the lower plot. The plot illustrates the superposition of the blue-shifted and red-shifted distributions in the potential well.

and red-shifted energy distributions. The lower plot presents the experimental spectrum.

The blue-shifted and red-shifted wings in the reconstruction are the accumulated distributions in the well for 10 oscillations (assuming a steady state). They refer to the blue and red shifted ion motion in the well, respectively (note that the red-shifted distribution in the reconstruction is for well "A" and is the same as the blue-shifted neutral atom distribution resulting from well "B". This distribution is not the red-shifted distribution of the experimental spectrum). The asymmetry between the two distributions is a consequence of the point ion source being placed at the cathode centre (it is expected that the two resulting distributions will be relatively symmetric for a uniform ion source distribution in the well).

The superposition of the two distributions (marked in the figure as "Blue+Red") clearly agrees with the experimental blue-shifted side of the spectrum shown in Fig. 4.9. An additional peak appears in the gap between the unshifted and the peak representing the H_3^+ specie. The gas pressure is relatively high (20 mTorr), where Fig. 4.5 shows that with increasing pressure the low energies resulting from the $H_2^+ + H_2$ interaction become more dominant in intensity. Furthermore, the potential pathlength is relatively long (5 cm), and consequently, many lower energy neutral atoms are created. It is also evident that the red-shifted distribution (representing neutral atoms drifting towards the monochromator from well B), when superposed on the blue-shifted distribution, increases the total intensity of the lower energy range.

Note that the three species distributions are broadened and difficult to resolve from one another in the experimental spectrum. As mentioned in the previous case, this might result from the complexity of the system, where the ion source distribution is not a point like source, the beam might have a slight angular spread and ions are accelerated in the cathode region towards the cathode surface in all directions via the sheath.

4.4 The red-shifted distribution in the spectrum

4.4.1 Linear potential approximation and ion energy distributions

Although the blue-shifted distribution was found to be dominant (implying that high densities of neutral atoms are diverging from the cathode), spectra taken out of the cathode region (between the cathode and anode) also show a fainter red-shifted distribution (see Fig. 4.2). This distribution results from neutral atoms converging to the cathode. It is possible to explain the experimental findings while assuming a discharge along the anode-to-cathode path. This can be approximated in the model with a distribution of ion sources placed along the anode-to-cathode path. Moreover, as seen in Fig. 4.4 the potential drop from the anode to the edge of the cathode can be approximated to be linear. Ions that are created between the cathode and anode will follow the potential in the cathodes direction.

Here energy distributions for a linear potential are presented while considering a uniform distribution along the path and a local ion density distribution near the anode. Following the same procedure described in section 4.3.1, the energy distributions were obtained from matrices **E** and **D** (see chapter 3).

Figure 4.10 presents energy distributions resulting from the programs for a linear potential and for a local ion density distribution. The ions were made to start accelerating from the beginning of the first segment. For each specie (marked in the figure) there are 5 distributions, corresponding to input pressures of 1, 5, 10, 20 and 30 mTorr. The total ion path was set to 16 cm and the potential was set to -10 kV across the entire path (this is an accelerating electric field of $10,000/0.16$ V/m due to a cathode voltage of -10 kV).

Since the initial ion density distribution is normalized, all densities in the energy distribution are expressed as a fraction of the initial ion density distribution (e.g. if there are N_0 ions starting the process, a density of 0.5 suggests that half of the N_0 ions have some corresponding energy). Moreover, it is possible to have density values larger than one. The initial ions starting the process might have all undergone charge exchange while creating the same amount of cold ions along the ions path. These ions undergo charge exchange and create more cold ions, etc. The process ends when ions are created only in the last segment. In this case, the total amount of ions that undergone charge exchange exceeds the number of ions starting the process. An increase in pressure increases the collision frequency and as a result the peak density rises with pressure for all three species. The H_2^+ specie distributions monotonically decrease in density with increasing energies. This is caused by the "one specie interaction": the initial charge exchanging H_2^+ ions produce the same amount of cold H_2^+ ions along the path. These further undergo charge exchange and create more ions along the

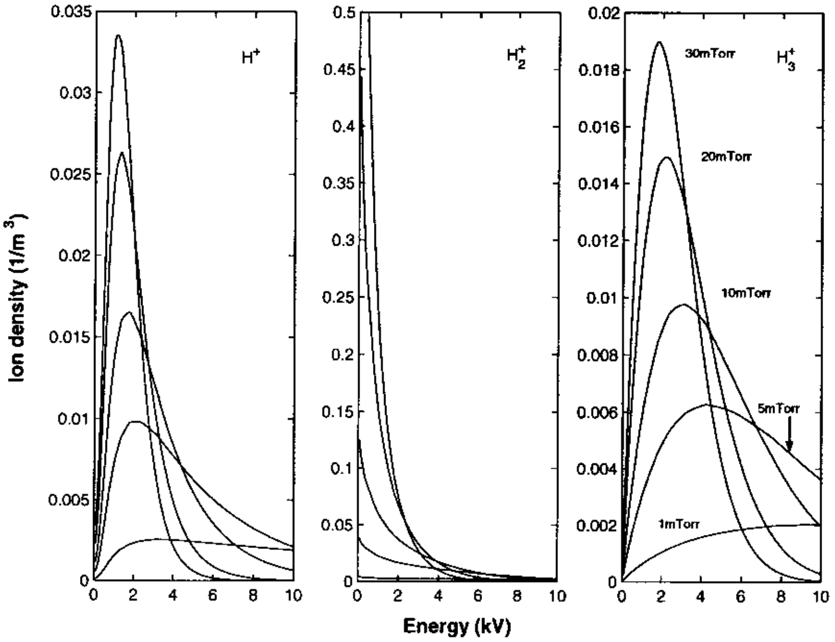

Figure 4.10: Energy distributions resulting from the simulations for a point ion density distribution placed at the beginning of the first increment for a linear potential. 5 energy distributions are shown for each of the H^+, H_2^+ and H_3^+ species and for pressures of 1, 5, 10, 20 and 30 mTorr. The total ion path was set to 16 cm, where −10 kV were applied on the total path.

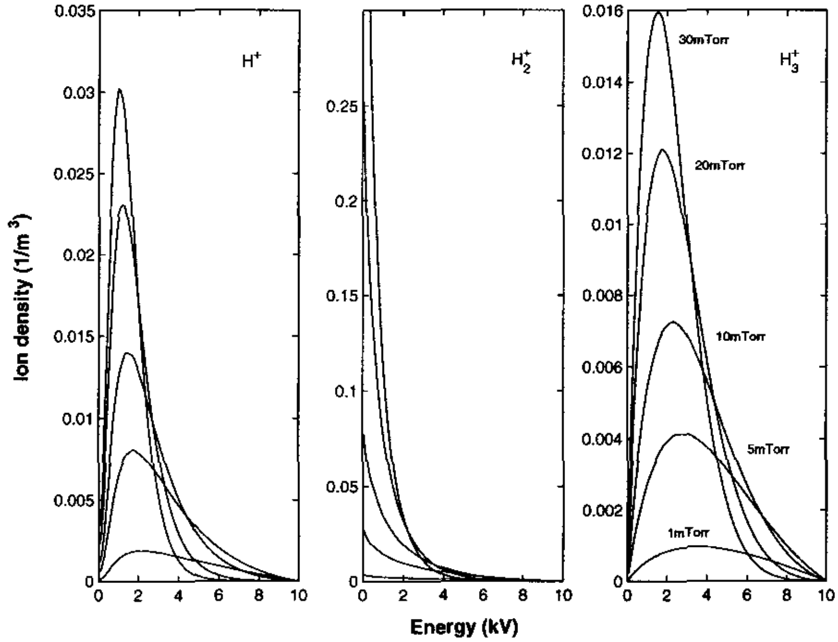

Figure 4.11: Energy distributions for the same ionic species and for the same conditions as in Fig. 4.10 (for a linear potential), but for a uniform ion density distribution along the ion path-length.

path, etc. However, each new generation of cold ions is created closer to the last segment, and therefore, the total number of low energy neutral atoms is greater than the number of high energy neutral atoms. The differences between the H^+ and H_3^+ species distributions are mainly due to the differences in the charge exchange cross sections.

Figure 4.11 presents the distributions for the same parameters of those in Fig. 4.10, but for a uniform spatial ion density distribution along the path. The energy distributions shown in Fig. 4.11 are similar in shape to the energy distributions presented in Fig. 4.10. In this case more ions of lower energies are created along the path and the total number of neutral atoms that is created in the process is smaller. Consequently, in Fig. 4.11 the density peaks slightly drop and slightly shift to the lower energy range, in comparison to Fig. 4.10.

4.4.2 Spectrum reconstruction

Figure 4.12 shows measured spectra at several positions along the beam, outside the cathode region, at 30° angle relative to the beam. The measurements were taken with the experimental set-up presented in Fig. 2.1, where the cathode voltage was set to −6 kV, pressure to 20 mTorr and anode-to-cathode distance to 16 cm (these are similar measurements to those presented in Fig. 4.1 but for different pressure and voltage). The distances stated in the figure were measured from the cathode edge. The unshifted peaks in the spectra were normalized based on experimental results obtained by John Kipritidis [1] and taken with the same experimental

---

[1] The author thanks John Kipritidis for supplying these results.

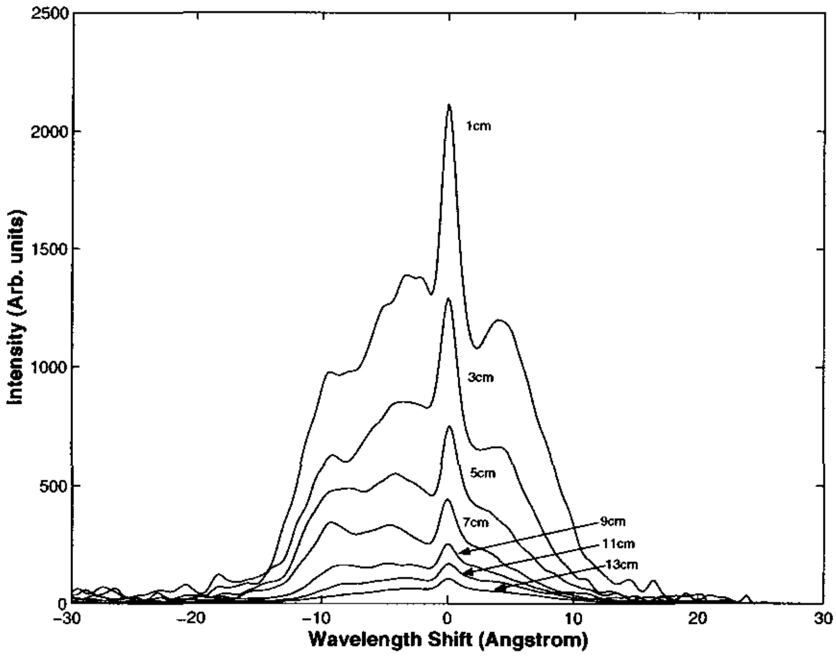

Figure 4.12: Measured spectra along the beam at 30° relative to the beam out of the cathode region. Cathode voltage was set to −6 kV, pressure to 20 mTorr and anode-to-cathode distance to 16 cm. The distances stated in the figure are measured from the cathode edge.

apparatus. For these measurements the device was operated at a cathode voltage of −9 kV, at pressure of 10 mTorr, at anode-to-cathode distance of 11 cm and for an observation angle of 90° relative to the beam. Figure 4.13 shows the intensity of the unshifted peak for Balmer α and β emissions as a function of distance, starting from the cathode edge to approximately half the anode-to-cathode distance. The experimental results were estimated with an analytical function, allowing for an extrapolation to the entire anode-to-cathode distance. The intensities of the main unshifted peaks of the spectra shown in Fig. 4.12 were scaled with the analytical function. Note that the normalization only scales the spectra relative to one another and does not affect the reconstruction in any way.

Here we refer to the red-shifted wings in the spectra, which implies that neutral atoms are moving towards the cathode. This could partially be explained by blue-shifted neutral atoms that are reflected from the chamber's wall in the opposite direction. However, the red-shifted wing resulting from the reflection should decrease in intensity when moving from the anode towards the cathode, which is counter to the experimental results presented in Fig. 4.12. Considering that electrons accelerate out of the cathode, towards the anode, a discharge is formed between the cathode and anode (this is also suggested by the appearance of the unshifted peak along the path, which implies that background gas excitation and ionization take place). Since the potential has a minimum at the cathode edge, the ions created outside the cathode accelerate towards the cathode edge resulting in an observed red-shifted distribution.

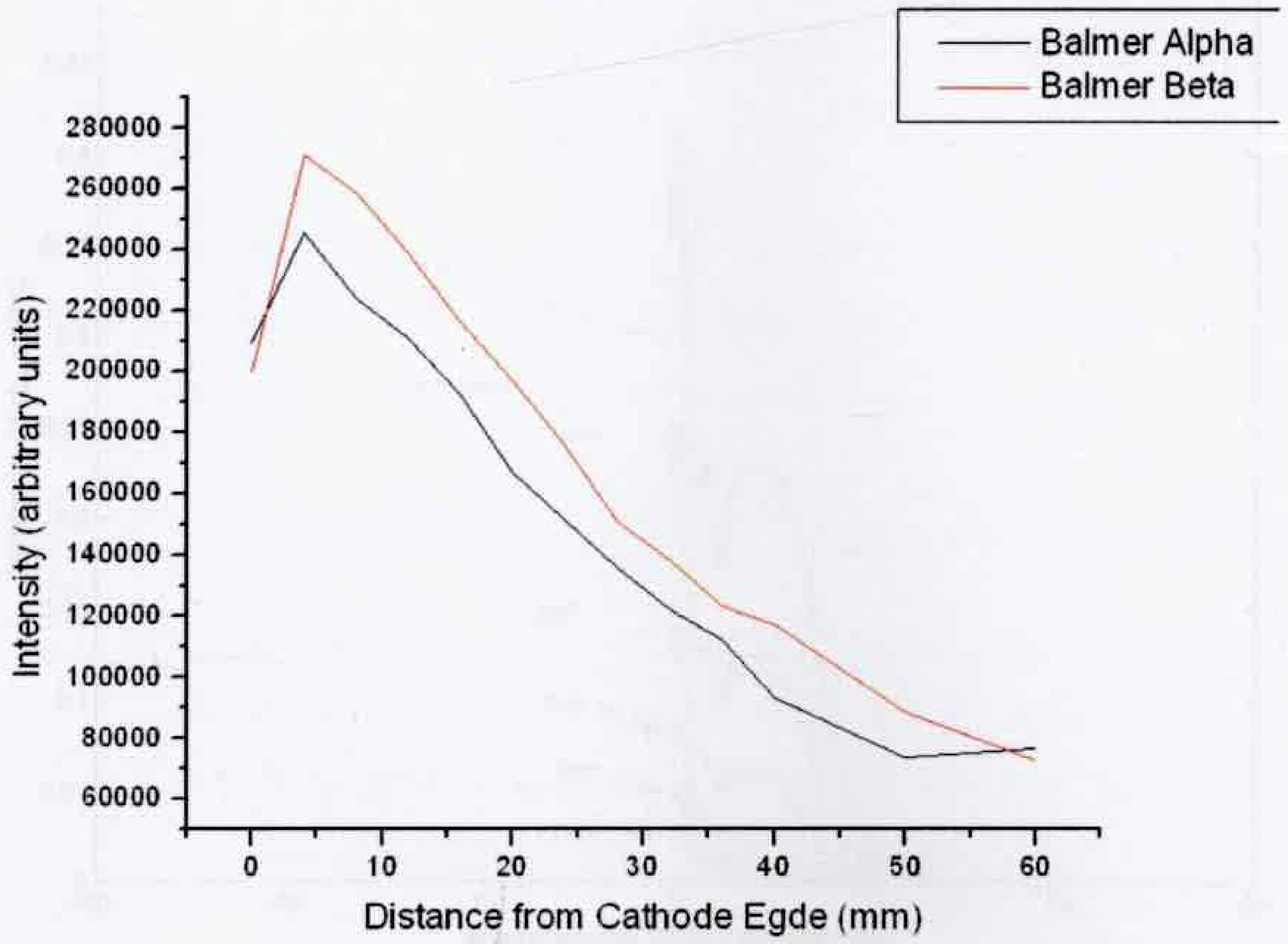

Figure 4.13: Intensity measurements of the unshifted main peak for Balmer α (bottom line) and β (top line) emissions as a function of distance, starting from the cathode edge to approximately half the anode-to-cathode distance. The observation angle was 90° to the beam axis.

The red-shifted distribution has been reconstructed with the semi-analytical model while assuming a discharge between the anode and cathode, and approximating the potential to be linear in this region. The approximation is based on the fact that the potential extends over a distance longer than the maximum collision path length for the experimental conditions (see the potential in the anode-cathode region in Fig. 4.4). Moreover, the approximation is justified by the results of the charge exchange modelling, where the energy distributions resulting from a uniform ion density distribution along the potential well (Fig. 4.6) were found to be similar in shape to the distributions resulting from a uniform ion density distribution along a linear potential (Fig. 4.11). The discharge was approximated with a uniform ion density distribution along the path (a linearly increasing density distribution does not change the results significantly).

The experimental conditions of Fig. 4.12 were included in the simulations for the three ionic species (H^+, H_2^+, H_3^+) mentioned in chapter 3. Note that a factor of $\cos 30$ had to be included in the Doppler shift equation since the spectra were measured at 30° relative to the beam (see eq. 2.8). Moreover, the potential was estimated to be $\sim 60\%$ of the applied cathode voltage (this was found to be equivalent to the maximum energy of the neutral atoms). The resulting energy distributions for all species were similar in shape to the distributions presented in Fig. 4.11. The reconstruction follows the procedure described in section 4.3.2, where the energies (matrix $\mathbf{E}$ in eq. 3.3) were converted to wavelength shifts. The densities (matrix $\mathbf{D}$ in eq. 3.14) of wavelength shifts, corresponding to wavelength

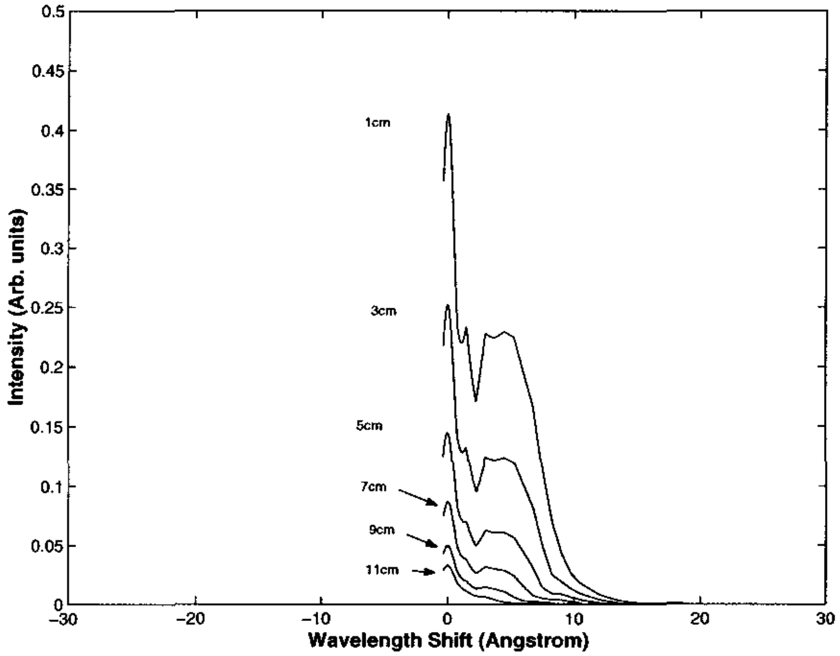

Figure 4.14: The 6 simulated spectra of the red shifted wings shown in Fig. 4.12.

shifts in intervals smaller than 0.5 Å, were placed in bins and the densities in each bin were accumulated to give the total density representing the density of the average wavelength shift of the bin. The spectra shown in Fig. 4.12 were recorded at various distances from the anode thus representing different acceleration lengths. Therefore, the spectrum reconstruction was carried out for the distance between the anode and the observation point.

Fig. 4.14 presents the results of the reconstructed red-shifted wings (positive wavelength shifts), after scaling according to the experimental spectra presented in Fig. 4.12. Clearly the simulation results are in good agreement with the experimental results. Starting closer to the anode (11 cm from the cathode edge), the intensity of the wing is relatively low and the wing is flat. Considering that ions are accelerating from the anode towards the cathode, at that position not many neutral atoms have been accumulated. The broadening of the experimental spectrum at the base of the unshifted peak, due primarily to energetic neutrals, might be caused by wall reflection of fast neutrals (this is supported with experimental results presented in chapter 5). The intensity of the wing increases at each observation point closer to the cathode. This results from a cumulative effect, where the spectrum at each point closer to the cathode edge includes emission from the de-exciting neutral atoms that were produced along the path between the anode and the observation point (the neutrals do not decay instantaneously). The peak in the distribution is a result of the charge exchange of the initial uniform spatial ion distribution. This is seen in Fig. 4.11, where the intensity of relatively low energy neutral atoms is enhanced.

In many measurements the unshifted peak shows a slight asymmetry, where the red-shifted side of the peak is slightly broader than its blue-shifted side. Although atomic and electronic processes are responsible for the broadening of the Lorentzian peak, these should not cause an asymmetry in the broadening. The reconstructed spectra show a small spike near the Lorentzian. This spike is a component of the H_2^+ specie distribution that broadens the red-shifted side of the Lorentzian (see H_2^+ energy distribution in Fig. 4.11) and might be responsible for this asymmetry. The broadening of the Lorentzian peak due to other processes overlaps with the H_2^+ energy distribution while smoothing the spike, as seen in the spectra of Fig. 4.12.

4.5 Energy distributions and the "blue shift" phenomenon

The experimental apparatus shown in Fig. 2.1 creates a discharge between the cathode and anode, where ions accelerate towards the cathode edge. In section 4.4.1 it was shown that the energy distributions resulting from such a discharge account for the red-shifted wing and therefore, do not account for the blue-shifted wing in the spectrum. If the neutral atoms produced on one side of the cathode had to drift to the other, the observed blue-shifted wing should have resembled the red-shifted distribution, which it does not.

Moreover, measurements taken by Khachan et al. [12, 17] suggest that the three peaks representing the three ionic species in a spectrum are of the same energy, where the energy is equivalent to the maximum potential depth. Referring to Figs. 4.6, 4.10 and 4.11, the H_2^+ energy distribution steeply declines in intensity with increasing energies. The only set of distributions that can account for the experimental findings are the ones presented in Fig. 4.5. These represent a system, where a local ion distribution is placed at the centre of cathode. The ions are accelerated via a steep potential drop (extending from the cathode center to the edge of the cathode), undergo charge exchange and escape the cathode as neutral atoms.

4.6 Other applications: high pressure discharge systems

The charge exchange models were applied to a high pressure discharge system, where charge exchange was dominant. A similar Doppler shift diagnostic method was used to study hollow cathode and plane cathode discharge devices while operating at hundreds and thousands of mTorr [19]. Fig. 4.15 refers to Doppler shift measurements taken by Barbeau and Jolly [19]. These were obtained at an observation angle of 0° relative to the beam (see the schematics of the apparatus in Fig. 4.16).

In their experiments an iron cathode of 3 cm in diameter was used, where the distance between the plane anode and cathode was set to 3 cm. The pressure of the hydrogen gas was varied in the range of 0.14 - 1 Torr. The potential between the anode and cathode was not measured however, it is reasonable to estimate the sheath to be a narrow well, having a minimum at $\sim$ 1 cm from the cathode surface (the total length of the potential is 3 cm). A discharge was created between the anode and cathode. Therefore, the ion density distribution was estimated to be linearly increasing. The potential depth was estimated to be 1 kV, corresponding to the maximum experimental wavelength shift of $\sim$ 10 Å (see Fig.

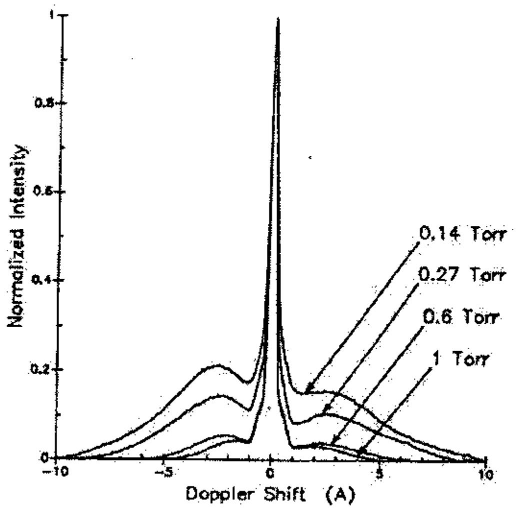

Figure 4.15: Doppler shift measurements obtained at an observation angle of 0° relative to the beam. A plane cathode discharge device was used, operating at pressures of $0.14-1$ Torr (taken from C. Barbeau and J. Jolly [19]).

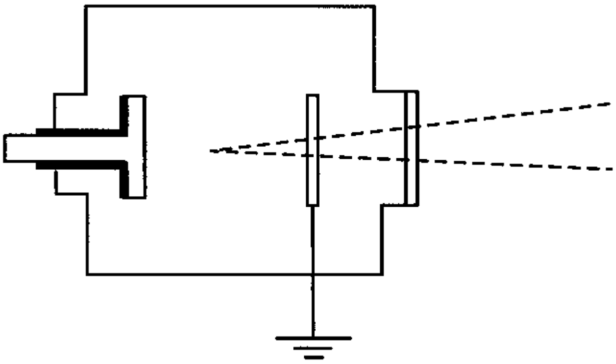

Figure 4.16: Reconstructed schematic illustrating the apparatus in the vacuum chamber and the angle of observation. The observation was carried out along the optical axis, where the optical emission is integrated along the discharge axis (reconstructed from C. Barbeau and J. Jolly [19]).

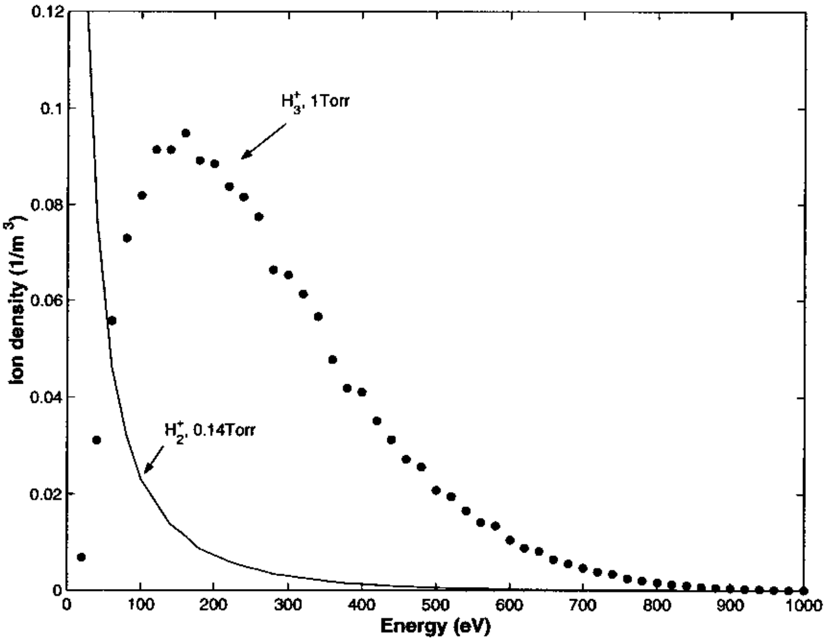

Figure 4.17: Modelled energy distributions for the H_2^+ and H_3^+ species at pressures of 0.14 and 1 Torr respectively. The parameters used in the model are the same as the operational conditions of Barbeau and Jolly [19].

4.15).

Figure 4.17 presents the energy distributions in the potential well for the H_2^+, H_3^+ species, for pressures of 0.14 and 1 mTorr, respectively. The H_2^+ specie density decreases rapidly with increasing energies and cuts off at ~ 60 % of the applied voltage. The H_3^+ and H^+ (H^+ not shown in the figure) spectra are skewed like a Poisson distribution. The maximum intensity occurs at an energy equivalent to ~ 20 % of the applied voltage. The peaks of the H_3^+ and H^+ energy distributions are dependent on the initial ion density distribution. The maximum intensity slightly shifts to higher energies for a uniform distribution along the path (not shown in the figure).

The reconstruction of the spectra is presented in Fig. 4.18 by following the same procedure mentioned in section 4.3.2. The figure shows two reconstructions calculated for pressures of 0.14 and 1 Torr. The reconstructions are in good agreement with the experimental spectra shown in Fig. 4.15. The reconstruction for the 0.14 Torr has a peak at ~ 3.5 Å, which is in good agreement with the corresponding experimental spectrum. This can be explained by the dominance of the H_3^+ specie at that region. The H^+ specie is responsible for the "tail" of the spectrum, which reaches as far as ~ 10 Å. The H^+ and H_3^+ species combine to a gradual decline of the spectral line, starting from the H_3^+ peak to the outer part of the spectrum. The H_2^+ specie is mainly responsible for filling the gap between the H_3^+ peak and the unshifted peak, where it also slightly broadens the unshifted peak at its base. Referring to the reconstructed 1 Torr spectrum in the figure, the H_3^+ and H^+ peaks are shifted towards the

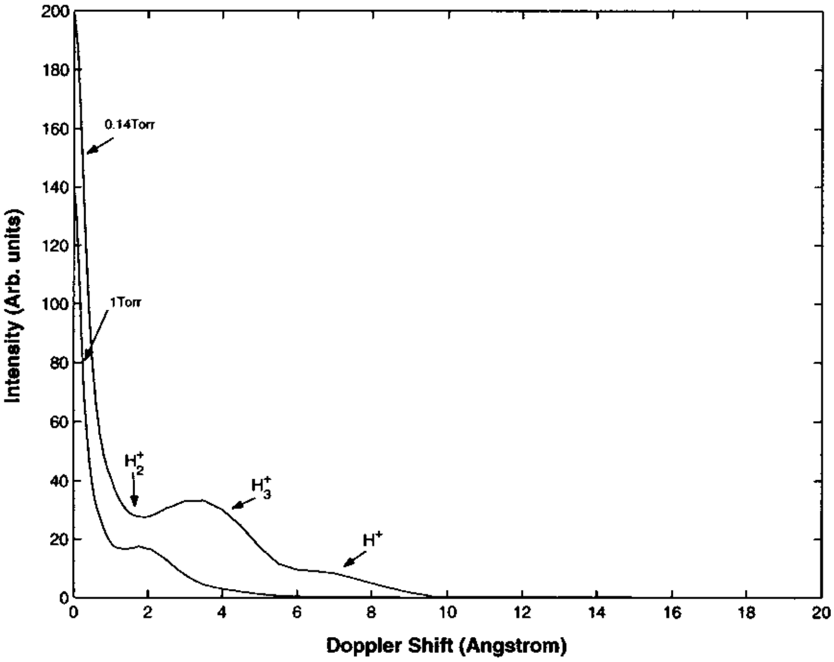

Figure 4.18: The reconstructed spectra resulting from the energy distributions of the three species for pressures of 0.14 and 1 Torr.

unshifted peak and the cutoff point of the spectral line is at ~ 5.5 Å. Note that an increase in pressure significantly reduces the energies.

4.7 Other applications: IEC confinement time estimations

The charge exchange model was used to estimate confinement times for IEC devices operating in the range of units of mTorr. The Lawson criterion for D-D confinement time is $\sim \frac{5\times10^{15}}{n}$ seconds, where n is the ion density in units of cm^{-3}. As a result, the minimum confinement time for energy gain and for devices operating in the range of 1 to 10 mTorr is in the order of 10's of seconds.

Here, a procedure has been developed to estimate the existing confinement time for these conditions. The three ionic species oscillate in the potential well and after gaining some kinetic energy they could be lost from the system via charge exchange. Since the fusion rates significantly depend on the ion energies, we consider only ions having energies greater than 80 % of the maximum possible energy. The ions, while oscillating in the well, acquire this range of energies for a defined interval of time. The total confinement time was calculated by estimating the longest interval of time for a single oscillation and multiplying by the total number of oscillations. For N_0 density of ions starting at the top of the potential well, a fraction of them undergo charge exchange and are lost to the background gas. The calculation was stopped when the surviving ion density was 0.1% of their initial value, N_0.

The charge exchange programs (presented in chapter 3) were modified for the calculation

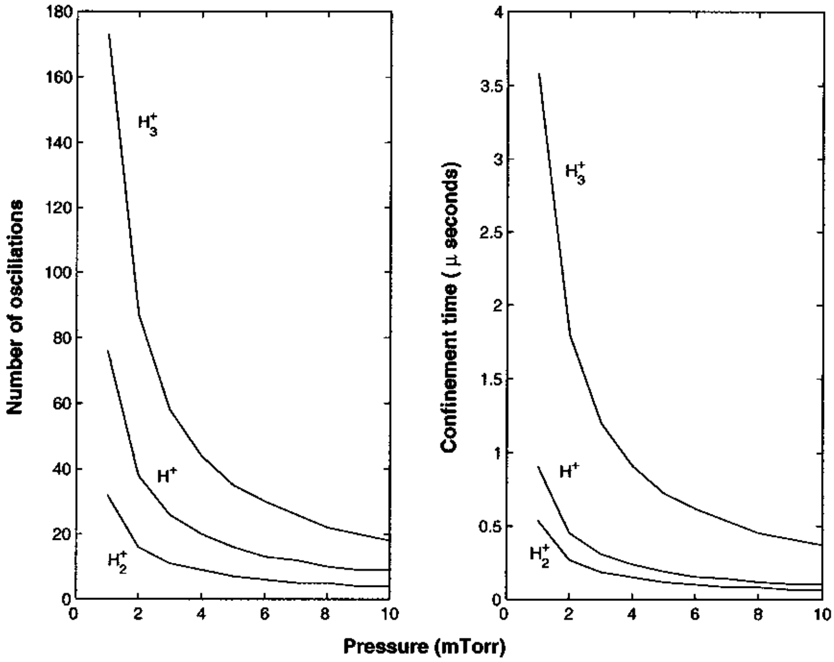

Figure 4.19: The left plot shows the number of oscillations the ions have gone through for pressures between 1 and 10 mTorr. The right plot shows the estimated total confinement time as a function of the same range of pressures. This is for the experimental set-up of Khachan et al. [12]and for the three ionic species, as marked in the figure.

of the confinement time. The experimental conditions of the potential measurement presented in Fig. 4.4 and the potential shape were used in the simulation. Specifically, the potential depth was set to −2.5 kV (equivalent to a cathode voltage of ∼ −10 kV), the position of the potential minimum was at 0.01 m (the cathode entrance), the cathode to anode distance was 0.08 m and the gas was set to be 10 % ionized. Results of the calculations are shown in Fig. 4.19.

The left plot presents the number of oscillations the ions have gone through for pressures between 1 and 10 mTorr. The right plot presents the estimated total confinement time as a function of the same range of pressures. The confinement time is in the order of microseconds, which is ∼ 7 orders of magnitude smaller than the Lawson criterion for D-D fusion interactions at these pressures. Although the confinement time for the three species is of the same order of magnitude, it is evident that the H_3^+ specie is confined the longest. However, the H_3^+ specie is also the heaviest and since the fusion rate production is proportional to relative velocity, the H_3^+ specie is expected to be less efficient. In most studies the H_2^+ specie is the most abundant specie out of the three, but it is lost to the background gas after fewer oscillations and its confinement time is the shortest (this is a result of the "same specie interaction" mentioned in chapter 3).

Figure 4.20 presents a similar calculation for a conventional IEC device such as the one used in Wisconsin [13]. In this case the potential depth was set to −20 kV (that is

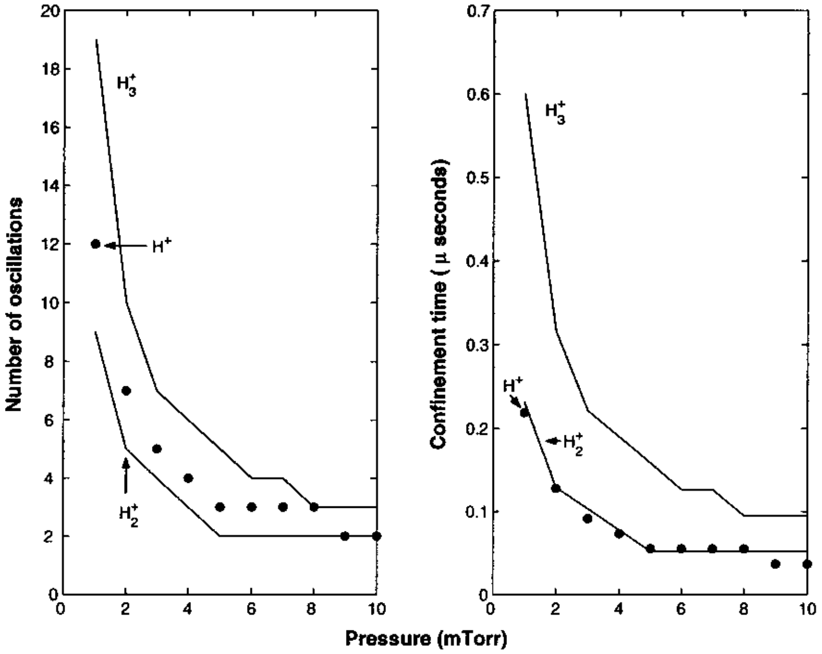

Figure 4.20: The left plot shows the number of oscillations the ions have gone through for pressures between 1 and 10 mTorr. The right plot shows the estimated total confinement time as a function of the same range of pressures. This is for the experimental set-up of Thorson et al. [13] and for the three ionic species, as marked in the figure.

for a cathode voltage of −60 kV), the potential minimum was set at 0.05 m (the cathode edge), the cathode to anode distance was set to 0.2 m and the gas was set to be $\sim$ 0.01 % ionized. For these experimental conditions the charge exchange becomes more dominant and rapidly damps the oscillations while decreasing the confinement time for all species. The confinement time in IEC devices operating in the mTorr range is suggested to be in the order of microseconds or 10^{-1} microseconds. The ions go through very few oscillations, which implies that the charge exchange process is dominant and is responsible for the damping of the oscillations.

4.8 Summary and discussion

Doppler shift measurements, taken with the apparatus described in Fig. 2.1, show that high fluxes of neutral atoms are diverging from the cathode. It was suggested that the neutral atoms originate within the two potential wells via charge exchange of ions that are created in the cathode centre. This was strongly supported by other work [1–3] and further supported with the charge exchange models. Energy distributions, calculated based on this hypothesis, were found to be in good agreement with previous experimental findings, where the neutral atoms energy of the three species (represented by the Gaussian peaks) were found to be equal and gained the maximum possible energy. Furthermore, it was possible to reconstruct the blue-shifted wing of the spectrum with these distributions.

Energy distributions were obtained for the H^+, H_2^+ and H_3^+ species for discharge conditions between the anode and cathode. It was shown that these distributions can account for the fainter red-shifted wing in the spectra. This implies that the blue-shifted wing does not result solely from neutral atoms drifting from the other side of the cathode (the conventional view). If that had been the case, the blue-shifted wing should have resembled the red-shifted wing (at least near the cathode).

The charge exchange model was further applied to a high pressure (hundreds of mTorr) discharge system, where spectra were reconstructed for an approximation of the discharge conditions. This further validates the reliability of the modelling method and shows the generality of the model, where it can be applied to various systems.

Estimates of the confinement time was given for IEC devices operating in the mTorr region (where charge exchange is dominant). It was found that the confinement time is 7-8 orders of magnitude smaller than the Lawson criterion for D-D confinement (note that although the calculation was carried out for hydrogen, since the charge exchange cross sections are similar for deuterium, the results are valid for deuterium as well).

Chapter 2 introduced the Gaussian method of analysis for obtaining the three ionic species energies. The charge exchange models explain the physical interpretation and the limitations of the method. The distributions presented in Fig. 4.5 clearly show that the Gaussian peaks do not represent the average neutral atoms energy but rather the maximum energy gained in the well (this agrees with previous experimental findings, where the neutral atoms energy, represented by the Gaussian peaks for the three species, were found to be equal and have the maximum possible energy). This interpretation is valid for distributions having similar shapes to the ones presented in Fig. 4.5. This also justifies the use of this method of analysis in the next chapter, where an experimental study of the neutral beam is presented.

Bibliography

[1] O. Shrier, J. Khachan, S. Bosi, M. Fitzgerald and N. Evans, Phys. of Plasmas, **13**, 12703 (2006).

[2] J. Khachan and A. Samarian, Physics Letters A 363, 297–301 (2007).

[3] L. Blackhall and J. Khachan, J. Phys. D: Appl. Phys., **40**, 2491–2494 (2007)

[4] W. C. Elmore, J. L. Tuck and K. M. Watson, Phys. Fluids, **2**, 239 (1959).

[5] O. A. Lavrent'ev, Ukr. Fiz. Zh., **8**, 440 (1963).

[6] T. Farnsworth, U.S. Patent No. 3,258,402 (1966).

[7] P. T. Farnsworth, U.S. Patent No. 3,386,883 (1968).

[8] R. L. Hirsch, J. Appl. Phys., **38**, 4522 (1967).

[9] R. L. Hirsch, Phys. Fluids, **11**, 2486 (1968).

[10] The 4th U.S.–Japan workshop on Intertial Electrostatic Confinement Neutron Sources, March 25-26 Kyoto University, Kyoto, 2002.

[11] H. Miley, Y. Gu, J. DeMora and M. Ohnishi, Fusion Eng. Des., **41**, 461 (1998).

[12] J. Khachan, D. Moore and S. Bosi, Phys. of Plasmas, **10**(3), 596 (2003).

[13] T. A. Thorson, R. D. Durst, R. J. Fonck and L. P. Wainwright, Phys. Plasmas, **4**(1), 4-15 (1997).

[14] O. Lloyd, J. Phys. D **4**, 1291 (1971).

[15] F. Sigeneger and R. Winkler, Plasma Chem. Plasma Process, **25**, 147 (2005).

[16] J. E. Foster and M. J. Patterson, 39th Joint Propultion Conference and Exhibit cosponsored by the AIAA, ASME, SAE, and ASEE Huntsville, Alabama, July 20-23 (2003).

[17] J. Khachan and S. Collis, Phys. Plasmas, **8**, 1299 (2001).

[18] A. V. Phelps, J. Phys. Chem. Ref. Data, **19**, 653 (1990).

[19] C. Barbeau and J. Jolly, J. Phys. D: Appl. Phys., **23**, 1168 (1990).

Chapter 5

Spectroscopic Studies of the Beam

In this chapter a comprehensive study of the neutral beam is presented. First, spectrum measurements in the cathode region are presented. Second, spectrum measurements in the cathode-to-anode region are presented. Third, spectrum measurements in the anode-to-wall region are presented. Last, the radial component to the beam is studied.

5.1 Aim

The experimental apparatus described in chapter 2 (figures 2.1, 2.2) was used for a systematic study of the beam of neutral atoms, extending from cathode to anode (and through the anode mesh spacing to the wall of the chamber).

In previous work, spectroscopic measurements were carried out on conventional IEC devices (multi emission channels) and one dimensional devices (two emission channels) [1–3]. Ion energies were obtained for the three dominant ionic species (H^+, H_2^+ and H_3^+) within the cathode region and relative ion densities were estimated. However, there was no systematic study of the entire beam. In chapter 4 it was suggested that a large number of neutral atoms are diverging from the cathode. Assuming a source of ions placed at the centre of cathode, modelling showed that the blue-shifted distribution observed in the spectra was established in the cathode region. A less significant red-shifted wing observed in the spectra suggests that there were some neutral atoms converging to the cathode. This was explained with a model assuming a discharge along the anode-to-cathode distance. However, a red-shifted wing was observed also between the wall and the anode. A study of the entire beam would further enforce the "blue shift effect" hypothesis and modelling presented in chapter 4 and will coherently explain the observed spectral line of the spectra, taken at different angles to the beam and at different parts of the beam. Furthermore, in this study scaling rules were found for the dependence of ion energy on pressure, voltage and system size. The latter was varied simply by changing the distance between the cathode and anode.

Spectroscopic measurements are presented for the full length of the beam in order to obtain the ion energies. The beam was divided into there regions for this study: the cathode, cathode edge to anode and anode-to-wall regions. Spectra were obtained at observation

Size (cm)	Voltage range (−kV)	Pressures (mTorr)	No. of spectra
12	1 - 9	15, 20, 25, 30	30
16	1 - 9	15, 20, 25, 30	37
20	1 - 9	15, 20, 25, 30	29

Table 5.1: Cathode 0 degrees measurements: details of the symmetric measurements.

Anode A - B (cm)	Voltage range (−kV)	Pressure (mTorr)	No. of spectra
8/12 - 12/8	1 - 7	15	12
8/16 - 16/8	1 - 7	15	12
8/20 - 20/8	1 - 7	15	12
12/16 - 16/12	1 - 7	15	12
12/20 - 20/12	1 - 7	15	12
16/20 - 20/16	1 - 7	15	12

Table 5.2: Cathode 0 degrees measurements: details of the asymmetric measurements.

angles of 0°, 30° and 90° relative to the beam.

5.2 Spectrum measurements in the cathode region

5.2.1 0° measurements in the cathode region

In this section energy distributions of neutral atoms in the cathode region were analyzed with the aim of finding scaling rules for variations in pressure and size. For these measurements the beam was aligned at 0° relative to the monochromator (this was done by changing the orientation of the aluminium plate shown in Fig. 2.2), observing the central part of the cathode.

This set of measurements included two sub-sets: symmetric and asymmetric distances between the cathode and the two anodes. In the symmetric case both anodes were placed equidistant on both sides of the cathode. The experimental details are given in table 5.1, where "Size" represents the distance between the anode and cathode centre, "Voltage range" is the range of applied cathode voltages, "Pressures" is the pressures under which the voltage was varied and "No. of spectra" is the total number of spectra taken for a given "Size".

In the asymmetric case the distances between anodes and cathode were unequal. The experimental conditions of the asymmetric measurements are given in table 5.2, where each row in the first column represents two sets of measurements having the two anodes, A and B, at different distances from the cathode and later reversing the distances for A and B (e.g. for "8/12 - 12/8", anodes A, B were placed 8 and 12 cm from the cathode centre respectively and then reversed to be placed at 12 and 8 cm from the cathode centre respectively). Note that changing the distances of the anodes or the beam orientation requires opening the chamber and later re-stabilizing the system to the required conditions.

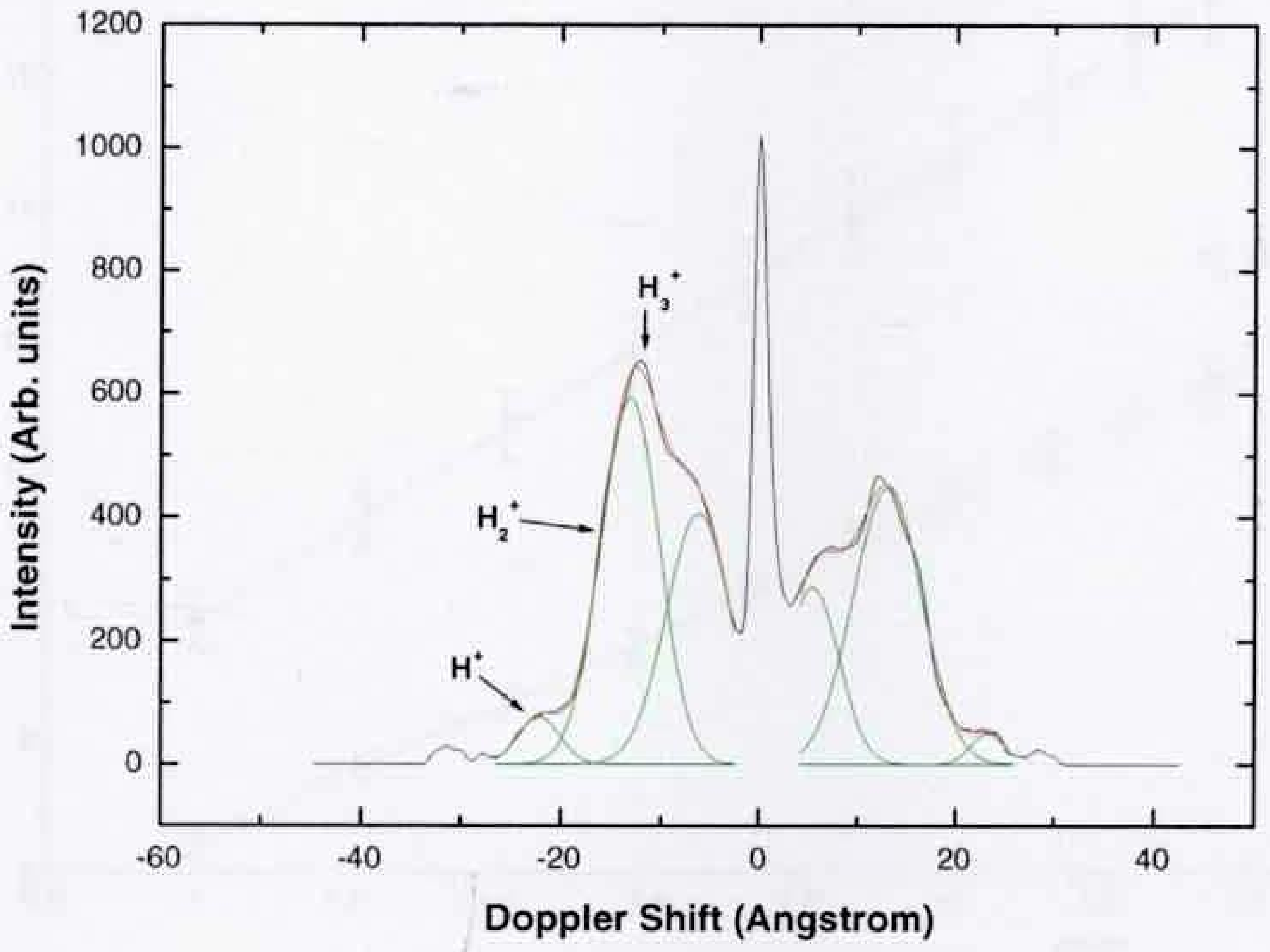

Figure 5.1: Three Gaussians fit (red line) were carried out for each of the blue-shifted (negative wavelength shifts) and red-shifted (positive wavelength shifts) wings. The three Gaussians and the experimental spectrum are presented with the green and black lines, respectively.

5.2.2 Analysis procedure

The convolution of the emission with the instrumental (monochromator's) response function made it necessary to carry out a deconvolution procedure based on the maximum entropy method [4–6][1]. Before deconvolving the spectrum, noise was reduced by smoothing the data with the 3 point averaging method (the code was written by the author in MATLAB). It was found that the deconvolution process did not significantly change the resolution of the original spectra.

A three Gaussian fit was generated for each spectrum's blue-shifted and red-shifted wings (see discussion in chapter 2). This was done with the ORIGIN program. A spectrum with its three Gaussian fit is presented in Fig. 5.1. The spectrum was obtained for a pressure of 10 mTorr, cathode voltage of −7 kV and 20 cm distance between the anode and cathode centre. Note that the Gaussian fit of the peak closest to the unshifted peak is due to the superposition of the three ionic distributions (see spectrum reconstruction in section 4.3.2). The H_2^+ and H_3^+ distributions strongly overlap and they are both represented by the single second Gaussian peak in Fig. 5.1. The third Gaussian (furthest away from the unshifted peak) in Fig. 5.1 is well resolved and represents the H^+ distribution.

In previous work a linear relationship between the position of the Gaussian peaks (wave-

---

[1] The author thanks Dr. Steven Bosi for supplying the deconvolution program.

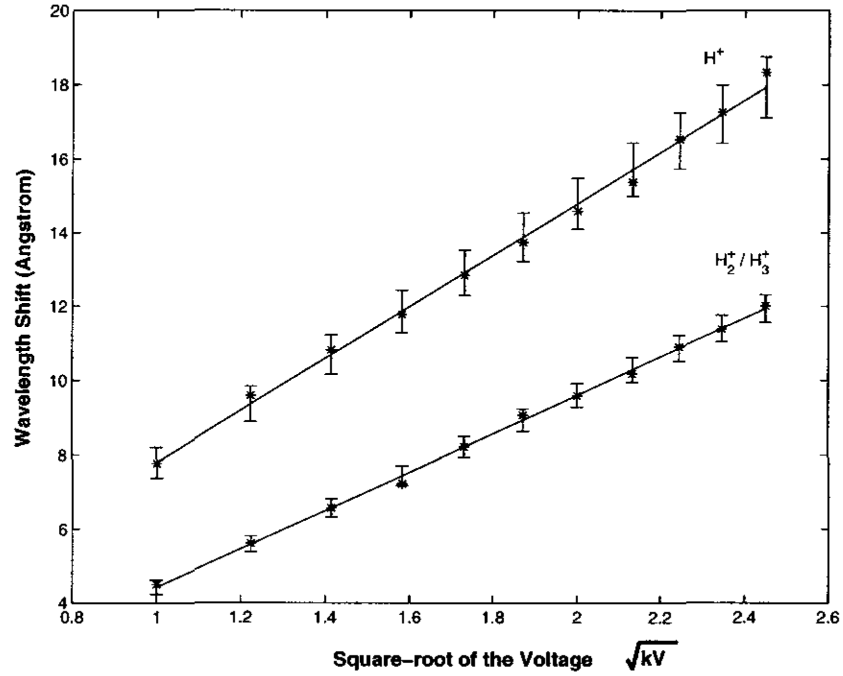

Figure 5.2: A linear fit for Doppler shift versus square root of the applied voltage. The spectra were taken for a pressure of 25 mTorr and a cathode voltage range of −1 to −6 kV. The lower line represents the linear fit for the H_2^++H_3^+ ion species (these are represented with the second Gaussian peak in Fig. 5.1). The upper line represents the linear fit for the H^+ (represented with the outer Gaussian peak in Fig. 5.1). The original experimental set of data and the maximum error of the fit at each data point are shown in the figure.

length shift) and the square-root of the voltage was established [1]. This suggests a linear relationship between the ion energy and the applied voltage (see eq. 2.8 in chapters 2). Based on the "Maximum Likelihood" method (the code was written by the author in MATLAB [7]), a linear fit was carried out on data obtained from measurements at various pressures and voltages. Figure 5.2 presents an example of this procedure. The measurements in the figure were taken for a pressure of 25 mTorr, where the voltage was varied between −1 and −6 kV. The distance between the anode and cathode centre was set to 16 cm. The continuous lower line represents the linear fit to the data of the H_2^+ and H_3^+ ionic species (corresponding to the second Gaussian in Fig. 5.1) and the upper continuous line represents the linear fit to the data of the H^+ ion (corresponding to the third (outermost) Gaussian in Fig. 5.1). The original experimental data and the maximum error of the fit at each data point are noted in Fig. 5.2.

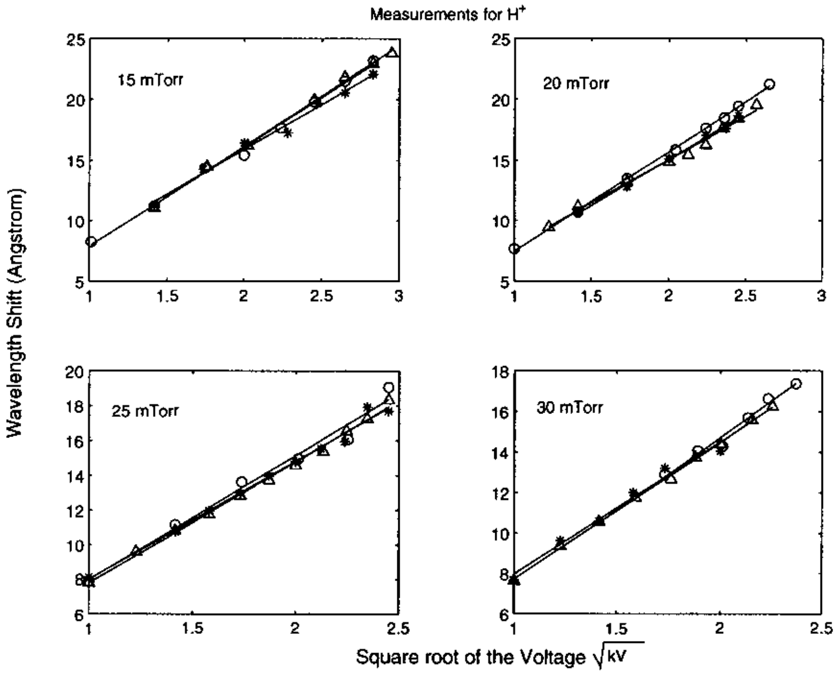

Figure 5.3: The dependence of the Doppler shift on the square root of the applied voltage of atomic hydrogen arising from charge exchange by H^+ with the background gas at pressures of 15, 20, 25 and 30 mTorr, where each plot represents measurements taken for cathode to anode distances of 12, 16 and 20 cm. The data points are over plotted, where the measurements for 12, 16 and 20 cm are denoted with stars, triangles and circles, respectively.

5.2.3 Scaling: energy dependence on size and pressure

Symmetric measurements

From the symmetric measurements (anodes placed at the same distance from the cathode) scaling rules were found in relation to the ion energy dependence on anode-to-cathode distance and background gas pressure. Figures 5.3 and 5.4, each present 4 plots of Doppler shift versus square root of the applied voltage that were taken for pressures of 15, 20, 25 and 30 mTorr. Each plot contains the results for cathode to anode distances of 12, 16 and 20 cm. Figure 5.3 shows the results for the H^+ specie (third Gaussian peak), and Fig 5.4 shows results for the $H^+_{2/3}$ species (second Gaussian peak). Note that each set of data in Fig. 5.3(denoted as stars, triangles and circles) is positioned close to its line of fit, where the maximum error is smaller than the experimental random error (can reach ±200 eV). It is clear that the 3 lines in each plot overlap, which strongly suggests that the energy of the ions is independent of the cathode-to-anode distance for the experimental conditions presented in this work.

The position of the minimum of the potential well and the potential depth were found to be dependent on the cathode's geometry and material [2,8]. Furthermore, the energies of the three species were found to be the maximum possible that can be gained from the potential well (see chapter 4). Considering that the same cathode was used for all measurements, the

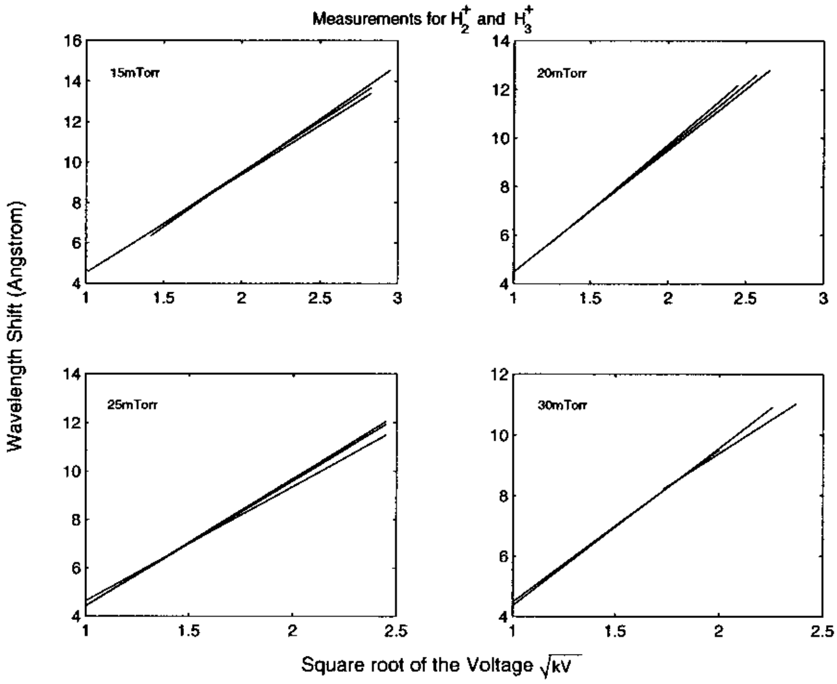

Figure 5.4: The dependence of the Doppler shift on the square root of applied voltage for excited atomic hydrogen resulting from the charge exchange of H_2^+ and H_3^+ with the background gas at pressures of 15, 20, 25 and 30 mTorr, where each plot represents measurements taken for 3 cathode to anode distances of 12, 16 and 20 cm.

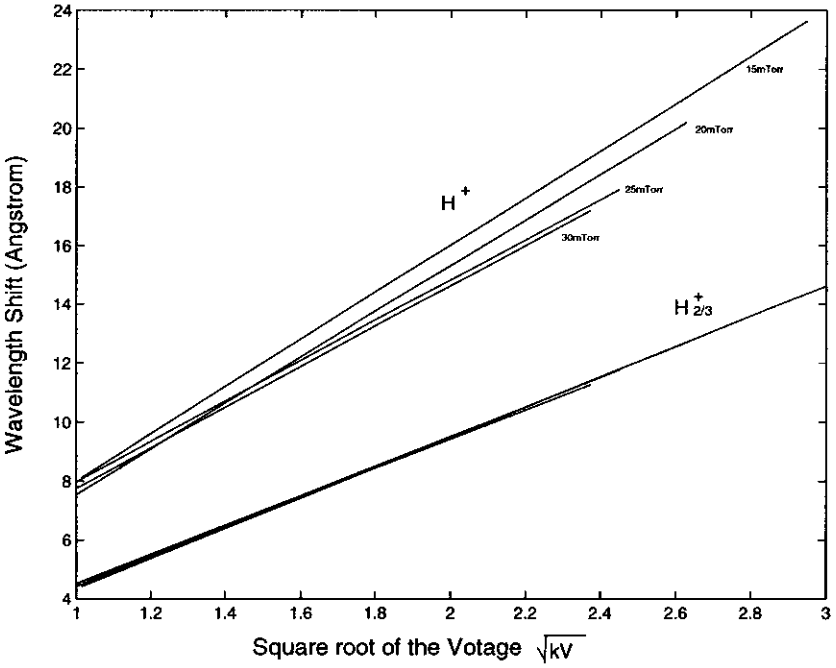

Figure 5.5: A linear fit was carried out for Doppler shifts versus square root of the applied voltage for 3 cathode-to-anode distances. Consequently, there are 8 lines representing the 4 pressures and the $H^+_{2/3}$, H^+ species in the bottom and top groups, respectively.

independence of the energy from the cathode-to-anode distance is expected.

Since it has been established that the energies are independent of different cathode-to-anode distances, a linear fit was carried out for all data points of the 3 cathode-to-anode distances in Figs. 5.3 and 5.4 (for each of the species and 4 pressures). The resulting linear lines for each pressure are plotted in Fig. 5.5, where the lower group of lines represent the $H^+_{2/3}$ species and the upper group of lines represent the H^+ specie. Clearly there is considerable overlap of the lines representing the $H^+_{2/3}$ species, implying that the energy is independent of pressure. The lines representing the H^+ specie cross one another, where the deviation of the lines from one another is random. This is a result of the linear fitting procedure. The deviation of adjacent lines is smaller than ~ 0.5 Å, which can be accounted for in the initial Gaussians fit error (there are a number of Gaussian combinations that can construct the spectrum line shape and the position of the peak representing the H^+ specie can vary to ± 0.2 Å around some average value. See also chapter 2). Reinforced by the $H^+_{2/3}$ species results, it is strongly suggested that the ion energies are independent of pressure (in the range of $5 - 30$ mTorr and given the instrumental uncertainties, any small variation in pressure can be neglected).

The distributions presented in Fig. 4.5 can explain these findings; The distributions show that the energies represented by the Gaussian peaks are equivalent to the maximum potential energy. If the maximum potential depth does not vary much with pressure (in

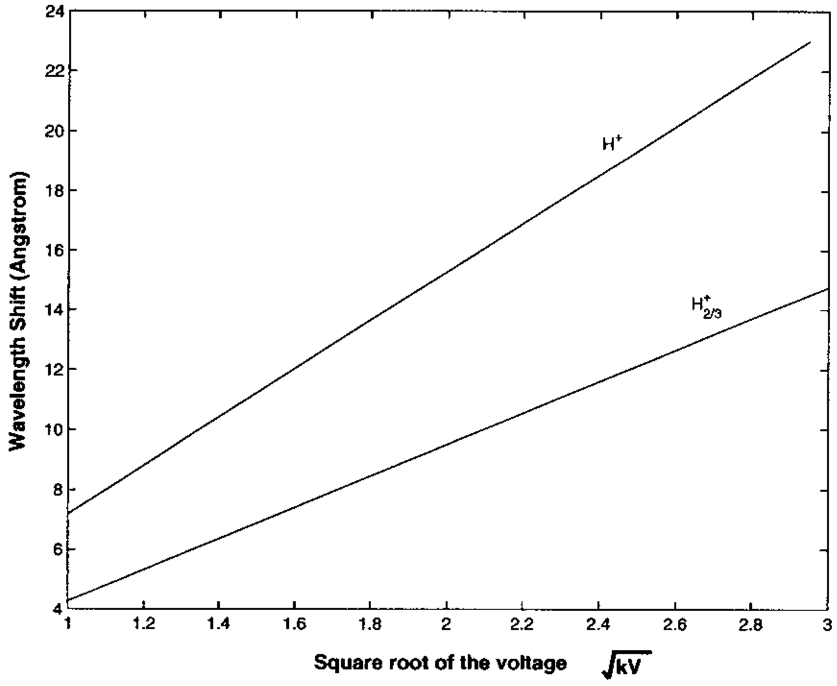

Figure 5.6: For each of the 2 species a linear fit was carried out for the data at the 4 different pressures that were presented in Fig. 5.5. The top and bottom lines represent the H^+ and $H^+_{2/3}$ species, respectively.

the experimental range presented in this work), the energies associated with the Gaussian peaks should be independent of pressure. Consequently, neutral atom energies obtained from spectra are a measure of the maximum potential depth. Khachan et al. [1, 2] measured maximum neutral atom energies that were ~ 25% of the applied voltage for a double ring cathode. Independent potential measurements for the same system showed that the maximum potential depth of the well (as defined in section 4.3.1) was also ~ 25% of the applied voltage. Fig. 5.5 (also Figs. 5.6 and 5.7) shows that in this work the maximum energy gained by atomic hydrogen was ~ 60% of the applied voltage, which implies that for this experimental set-up the maximum potential depth of the well was ~ 60% of the applied voltage.

A linear fit of the dependence of Doppler shift on the square root of the applied potential is given in Fig. 5.6 at 4 different pressures and for each of the 2 species. The straight lines given in the figure were best fits to 96 points for each fit. The lower and upper lines represent the $H^+_{2/3}$ and H^+ species, respectively. The relationship between the $H^+_{2/3}$ species and the H^+ specie becomes evident if the linear relation between the wavelength shift and the square-root of the applied voltage is converted to an energy versus voltage plot (see eq. 2.8 in chapter 2). The result is presented in Fig. 5.7. Multiplying the lower line by a factor of 2.5 results in the upper line (marked $H^+_{2/3}$), which clearly overlaps with the line representing the H^+ specie.

In chapters 2 and 4 it was shown that the energies of the three species (represented by the three Gaussian peaks) were found to be the same [1]. It was also shown that the energy

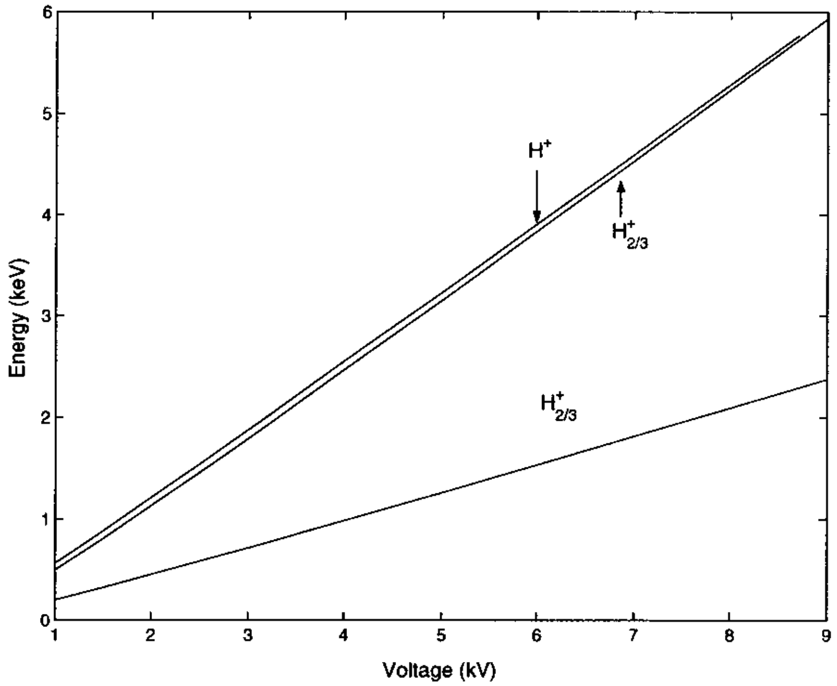

Figure 5.7: A plot of energy versus voltage showing that the upper line, representing the H^+ specie, is a factor of 2.5 larger than the line representing the $H^+_{2/3}$ species.

of the H_i^+ specie (where $i = 1, 2, 3$) partitions between the resulting fragments such that the resulting excited H^* fast neutral atom has the energy of the H_i^+ specie divided by i. Since the lower line (stated as $H^+_{2/3}$) represents a merger of the H_2^+ and H_3^+ species, it is expected that the multiplication factor will be between 2 and 3. In this case the energies of the lower line (representing the $H^+_{2/3}$) are $\sim$ 0.40 of the energies of the upper line (representing the H^+ and also the total energy of the two other species), which is the average energy of the excited H^* neutral atom energies resulting from the H_2^+ and H_3^+ species (the exact average energy is 0.416 of the total energy).

Asymmetric measurements

Although the results for the symmetric systems (anodes placed at the same distance from the cathode) showed no dependence on anode-to-cathode distance, this was verified for the asymmetric case (anodes are placed at different distances from the cathode). The details of the asymmetric measurements are given in table 5.2.

Qualitatively, the blue and red shifted wings (representing different sides of the cathode) were found to be similar in shape, implying that the energies are independent of asymmetry. Figure 5.8.B presents the results of the analysis of the 20/12 asymmetric measurements (see details in the fifth row of table 5.2). The anode closer to the monochromator was placed at 20 cm from the cathode centre and the other at 12 cm from the cathode centre (the results for the 12/20 asymmetric experiments were found to be identical and are not shown here.

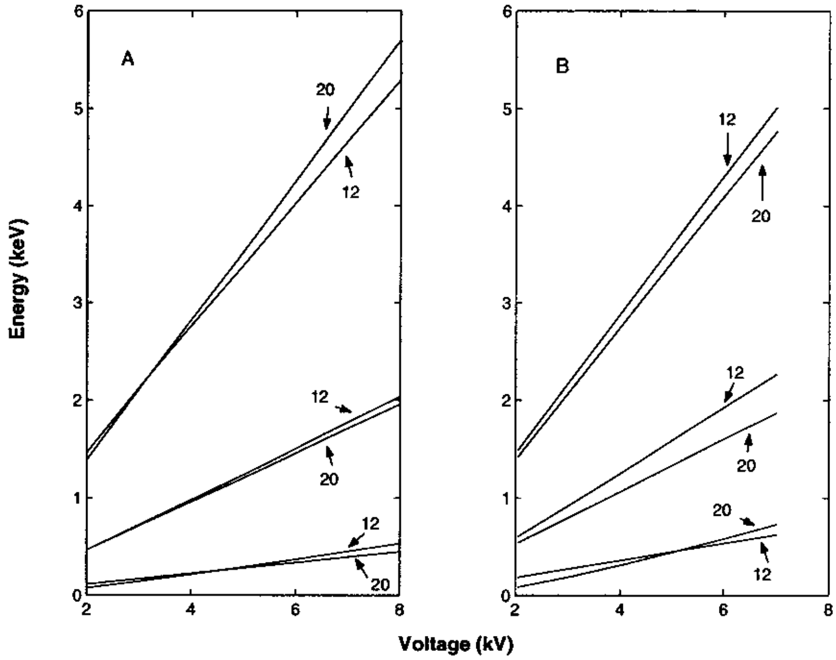

Figure 5.8: Plot A presents the results for the symmetric system , where both anodes were placed once at 20 cm from the cathode centre (marked "20") and again at 12 cm from the cathode centre (marked "12"). Plot B presents the results of the 20/12 asymmetric experiments (fifth row in table 5.2). The measurements for the symmetric and asymmetric systems were carried out for the same operating conditions, mentioned in table 5.2. The three sets of lines represent the analysis of the three Gaussian fit for each voltage measurement, where the lower, mid and upper sets of lines are the results of the first, second and third peak analysis respectively.

This is expected, since the set-up is symmetric about the cathode). The three sets of lines (note that there are two lines in each set) represent the analysis of the three Gaussian fit for each voltage measurement, where the lower, mid and upper sets of lines are the results of the first, second and third peak analysis respectively.

The upper most set of lines represents the H^+ specie, the middle set represents the $H^+_{2/3}$ species, and the lowest represents the peak caused mostly by the energy distributions of the H_2^+ and H_3^+ species, and neutral atoms drifting from the other side of the cathode (see discussion chapter 4.3). In each set of two lines, one line represents the analysis of the blue-shifted wing (for 20 cm anode-to-cathode distance and marked "20" in the figure) and the other line represents the analysis of the red-shifted wing (for 12 cm anode-to-cathode distance and marked "12" in the figure). It is clear that the two lines of each set in Fig. 5.8.B overlap, implying that asymmetry does not affect the energy independence from the cathode-to-anode distance.

Figure 5.8.A presents the results for the symmetric system and for the same operating conditions, where both anodes were placed once at 20 cm from the cathode centre and again

Distances (cm)	Voltages (−kV)	Pressure (mTorr)	No. of spectra
4, 6, ..., 16	6	5	7
4, 6, ..., 16	5, 6	10	14
4, 6, ..., 16	3.5, 4, 5, 6	15	28
4, 6, ..., 16	3, 4, 5, 6	20	28
4, 6, ..., 16	3, 4, 5, 6	25	28

Table 5.3: 30 degrees measurements along the beam, between the cathode and anode.

at 12 cm from the cathode centre (two experiments were carried out). Also in this case the three sets of lines (two lines in each set) represent the analysis of the three Gaussian fit for each voltage measurement, where the lower, mid and upper sets of lines are the results of the first, second and third peak analysis respectively. However, the results are for the blue-shifted wing in both experiments (note that in the symmetric case the blue and red shifted wings are symmetrical and yield the same results). In each set of two lines, one line represents the analysis of the experiment for 20 cm anode-to-cathode distance (marked "20" in the figure), and the other line represents the analysis of the experiment for 12 cm anode-to-cathode distance (marked "12" in the figure). A comparison of Fig. 5.8.A with Fig. 5.8.B shows that the two systems are equivalent and the asymmetric system does not affect the energies in relation to the symmetric system.

The first peak in the spectrum (represented by the Gaussian closest to the unshifted peak) does not change its position with cathode-to-anode distance and with asymmetry of the system (seen in the overlap of the lower lines in Fig. 5.8). This implies that the total energy distribution does not change significantly (the spectra are all similar in shape) and reinforces the fact that the cathode geometry and material are the most dominant influence on the energy distribution of the neutral atoms (it is suggested that the ions are accelerating from the centre of the cathode outwards and the minimum of the potential is established at the cathode edge. Considering that the same cathode is used for all measurements, the anode-to-cathode distance should not affect the energy distribution of the neutral atoms).

5.3 Spectrum measurements in the cathode-to-anode region

5.3.1 30° cathode-to-anode measurements

Energies of the fast neutral atoms were measured between the cathode edge and the anode. Assuming the energy distribution of the neutral atoms is established mostly within the cathode region, it is expected that the energy distribution will not change along the cathode-to-anode region (neglecting de-excitation processes that affect the spectra line shape). For these measurements the beam was set at 30° angle relative to the monochromator, and spectra were obtained at 2 cm intervals along the beam. The cathode-to-anode distance was set to 16 cm and measurements were taken for a pressure range of 5 to 25 mTorr and for a voltage range of 3 to 6 kV. Table 5.3 presents the experimental details. Note that the distances were

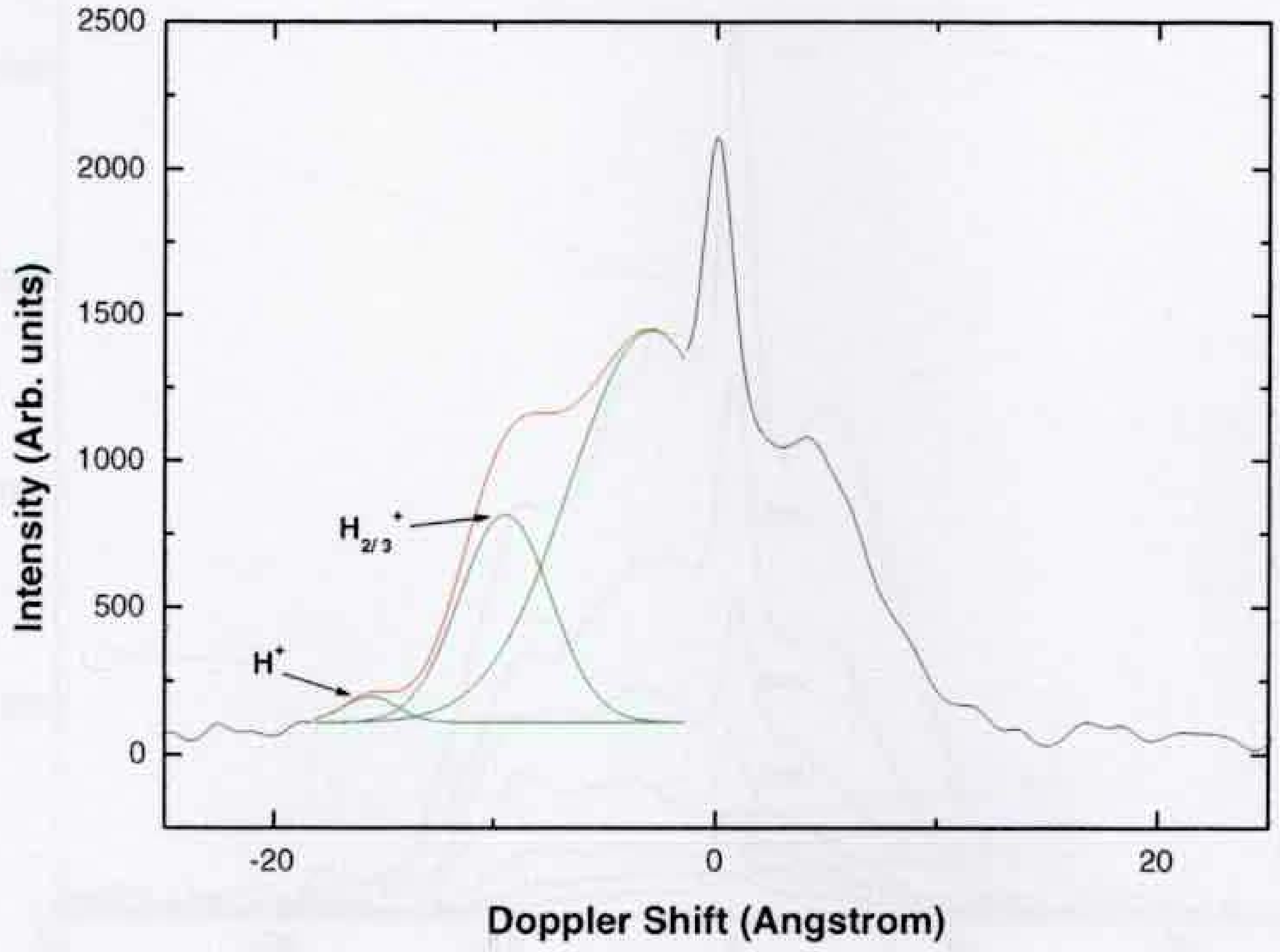

Figure 5.9: Spectrum taken at 30° relative to the beam showing a squashed profile of the spectrum (black line) obtained at 0° relative to the beam and for the same experimental conditions. The spectrum also shows a three Gaussian fit to the blue-shifted wing (red line, where the three Gaussians are presented with the green line).

measured from the cathode centre. Next, analysis and results are presented.

5.3.2 Spectrum profile, Gaussian fit and the alternative approximation method

Measurements of neutral atom energies along the beam were taken at 30° relative to the beam. Therefore, the resulting spectra are a 30° component of the spectra observed at 0° relative to the beam. Figure 5.9 presents a spectrum that was taken 1 cm from the cathode edge, for a cathode voltage of -5 kV and a pressure of 15 mTorr. Referring to the blue-shifted distribution, it is clear that there are three significant peaks that correspond to the three peaks of the spectra taken at 0° angle relative to the beam, however, there is no gap between the unshifted peak and the first peak (see 0° spectrum in Fig. 5.1). This is explained by eq. 2.7 (chapter 2), where a 30° observation decreases the wavelength shifts by a factor of cos(30°). Consequently, the blue-shifted wing moves closer to the main unshifted peak. Following the analysis procedure discussed in chapter 2, it is possible to fit 3 Gaussians to the wing. This is shown in Fig. 5.9, where the second peak from the unshifted peak is at -9.59 Å and the third peak from the unshifted peak is at -15.82 Å. Dividing both shifts by a factor of cos(30°) and comparing with the results presented in Fig. 5.6 (for the same experimental conditions), it is clear that the two peaks are the same two peaks of the 0° spectrum, representing the $H_{2/3}^+$ and H^+ species respectively (marked in the figure). This confirms that the blue-shifted

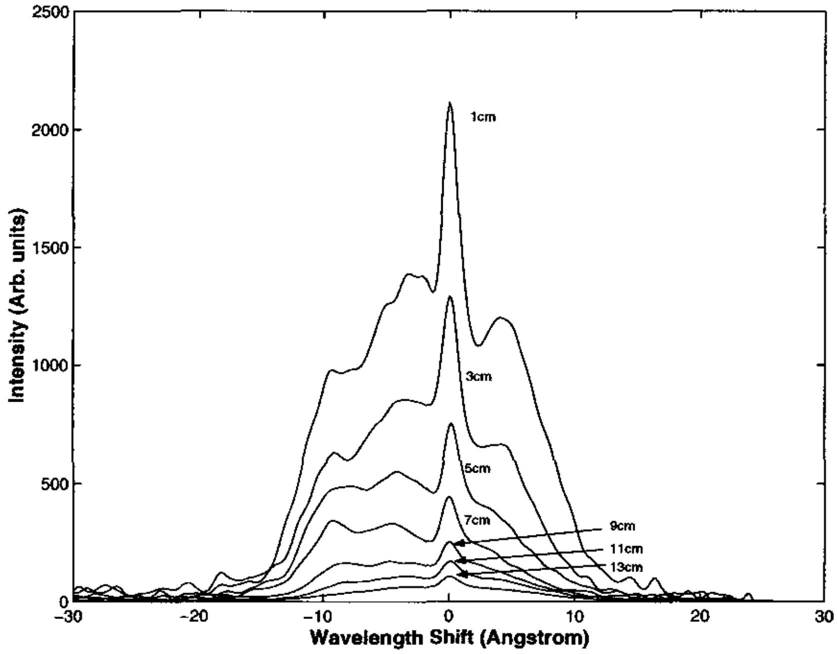

Figure 5.10: Spectra obtained for a pressure of 25 mTorr, for an applied cathode voltage of −6 kV and for observing positions along the beam measured from the cathode edge (marked in the figure). The spectra were normalized with respect to the experimental results presented in Fig. 4.13.

wings for the 30° spectra are the squashed image of the blue-shifted wings of the 0° spectra, and that the Gaussian fitting method of analysis is still valid.

However, the Gaussian approach presents a few difficulties: since the three peaks are squashed together they are not well resolved. Consequently, the fitting procedure has to be repeated several times until a reasonable fit to the experimental spectrum is found (a "reasonable fit" is when the three Gaussians are relatively narrow and the base of the Gaussians is at noise level). In many cases it is impossible to find a three Gaussian fit. Furthermore, the intensity reduces exponentially along the beam towards the anode and the wing shape changes due to de-excitation along the beam. This is shown in Figs. 5.10 and 5.11, where the same spectra were normalized once with respect to the experimental results presented in Fig. 4.13 (Fig. 5.10) and again with respect to the unshifted peak, where the spectra were lifted upwards in relation to one another (Fig. 5.11). The spectra was obtained for a pressure of 25 mTorr, an applied cathode voltage of −6 kV and at different positions along the beam. It is clear that for distances over 9 cm the peak representing the H^+ specie is nearly at noise level. For distances larger than 12 cm from the cathode the part of the wing that is dominated by the $H^+_{2/3}$ species lowers in intensity and it becomes impossible to resolve its associated peak.

Figures 5.12 and 5.13 present the same spectra measurements, taken along the beam for a cathode voltage of −6 kV and a pressure of 5 mTorr. The spectra were normalized once with respect to the experimental results presented in Fig. 4.13 (Fig. 5.12) and again with respect

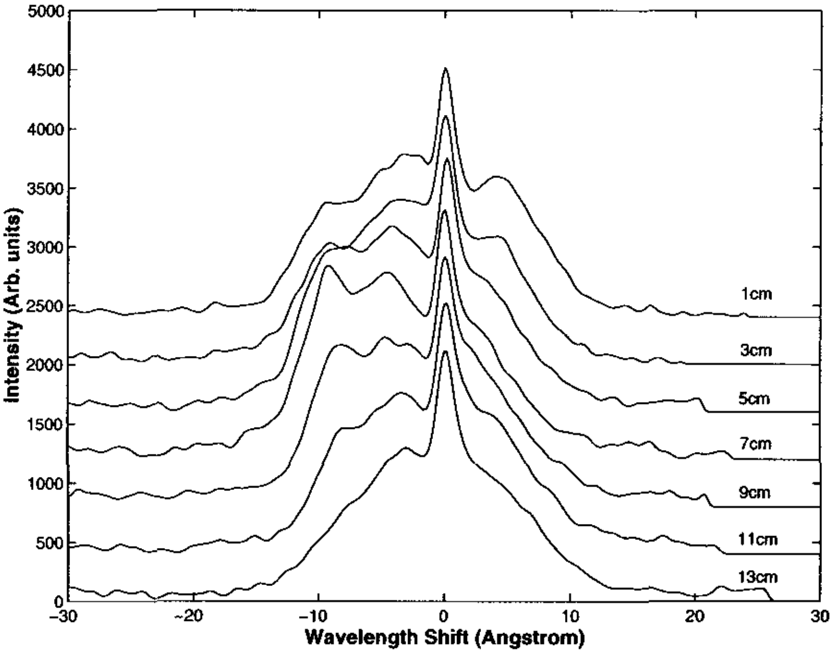

Figure 5.11: The same spectra presented in Fig. 5.10, normalized with respect to the unshifted peak. The spectra are lifted upwards in relation to one another.

to the unshifted peak, where the spectra were lifted upwards in relation to one another (Fig. 5.13). Notwithstanding the fact that the intensity of the emission decreases with pressure and with larger angles of observation while causing an increase in noise, the spectra in the figures show that the peaks, associated with the three species, are not resolvable. This results from de-excitation processes, where the most dominant are spontaneous de-excitation and inelastic collisions of H atoms with the H_2 background gas (quenching). Spectra taken at pressures lower than 5 mTorr were excluded from the analysis.

Consequently, an alternative method was used to approximate the energies associated with the $H^+_{2/3}$ species (referring to the second Gaussian peak). This enabled the inclusion of most spectra measurements with reasonable confidence. Referring to Fig. 5.9, the Gaussian peak representing the wavelength shift of the $H^+_{2/3}$ species is positioned near the second most significant peak in the spectrum (second peaks in the spectral line), and the energy associated with the Gaussian peak was found to be in good agreement with former analysis (presented in Fig. 5.6). Furthermore, the second peak of the spectral line falls nearly linearly until it merges with the H^+ distribution in the spectrum. Therefore, it is possible to define the point were the linear drop is established and estimate an associated maximum error for each spectrum. Using the spectrum presented in Fig. 5.9 for the error estimation, the linear drop is at ~ 8.8 Å and the Gaussian peak at ~ 9.7 Å resulting in maximum error of $\sim \pm 1$ Å. This method was applied while using the ORIGIN program to analyze spectra taken at pressures of 10, 15, 20 and 25 mTorr (see table 5.3).

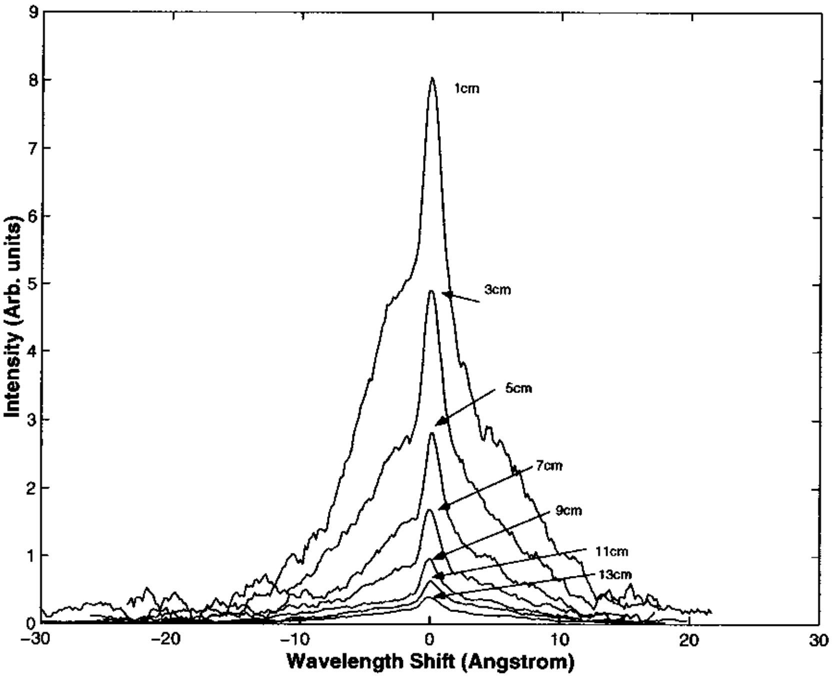

Figure 5.12: Spectra obtained for a pressure of 5 mTorr, for an applied cathode voltage of −6 kV and positions along the beam measured from the cathode edge (marked in the figure). The spectra were normalized with respect to the experimental results presented in Fig. 4.13.

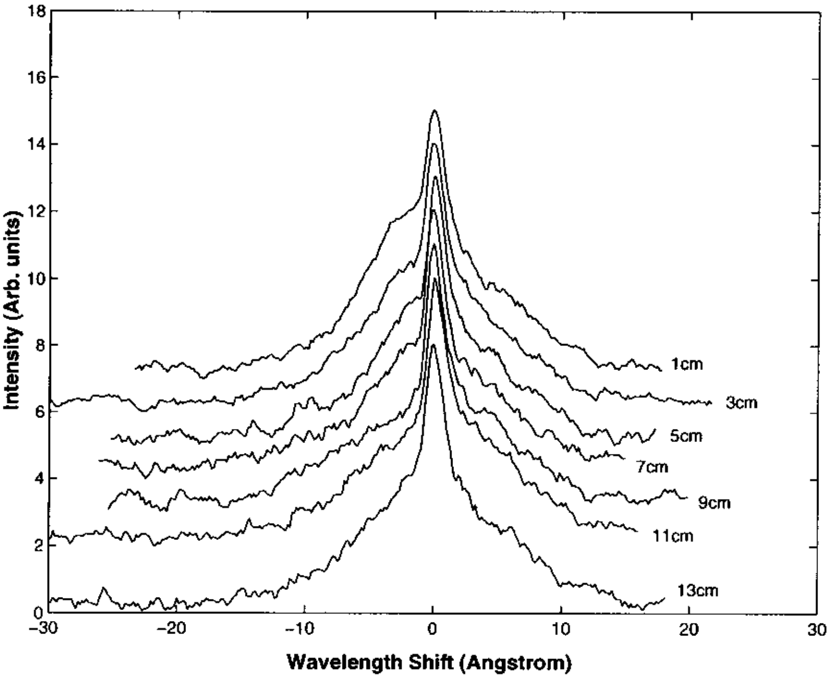

Figure 5.13: The same spectra presented in Fig. 5.12, normalized with respect to the unshifted peak. The spectra are lifted upwards in relation to one another.

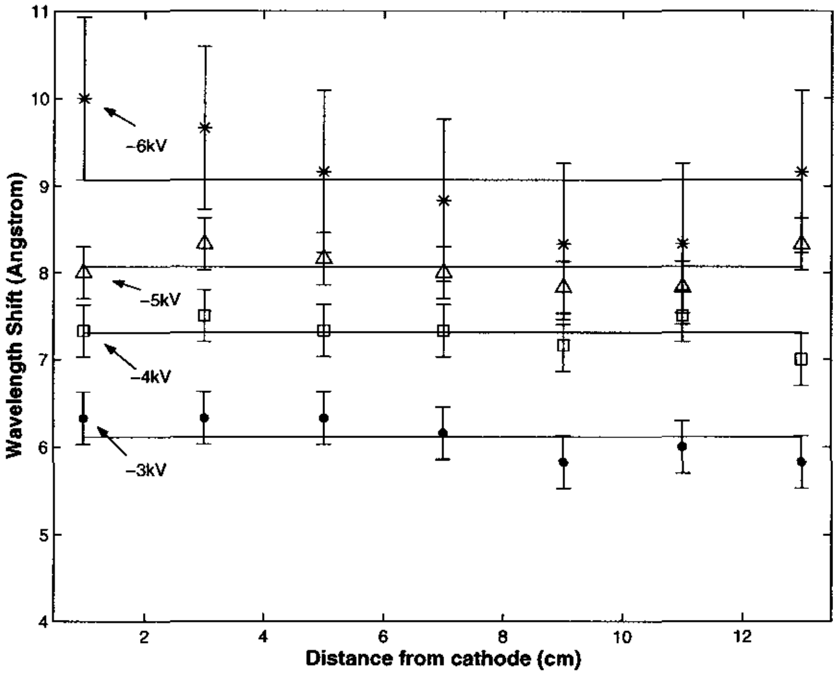

Figure 5.14: Results for 28 spectra, taken at 25 mTorr, for cathode voltages of −3, −4, −5 and −6 kV and for observation points along the beam. The wavelength shifts estimated for the $H^+_{2/3}$ Gaussian peak are plotted against the distance from the cathode edge. The 4 continuous lines represent the mean of the results for each voltage group.

5.3.3 Results and discussion

Figure 5.14 presents results of the analysis of 28 spectra, taken for a pressure of 25 mTorr, for cathode voltages of −3, −4, −5 and −6 kV, at 1, 3, 5, 7, 9, 11, 13 cm from the cathode edge. The figure shows the estimated wavelength shift of the $H^+_{2/3}$ peak plotted against the distance from the cathode edge. There are 4 distinct groups corresponding to each of the 4 cathode voltages (marked in the figure). Referring to the groups representing the −3, −4 and −5 kV, for each group the data points fluctuate around an average point in a spread smaller than 0.3 Å. For the −6 kV group the data points fluctuate around an average point in a spread smaller than 0.9 Å. These results are in the error range that was estimated for the approximation method that was used (maximum error of ∼ ±1 Å). Moreover, the fluctuation of the data points in each group do not follow the same trend for all groups. If the fluctuations in energy were caused by a fluctuating electric field, accelerating ions between the cathode and anode, the trend of the data points should have been the same for all groups.

Figure 5.15 presents the spectra that were analyzed in Fig. 5.14. The spectra were normalized with respect to the unshifted peak, where they were lifted upwards in relation to one another. There is a correlation between the data points in Fig. 5.14 and the spectra in Fig. 5.15. When the intensity of the second peak (in Fig. 5.15) is closer to noise level, the data point (in Fig. 5.14) has a higher value of wavelength shift and vice versa (e.g. the second

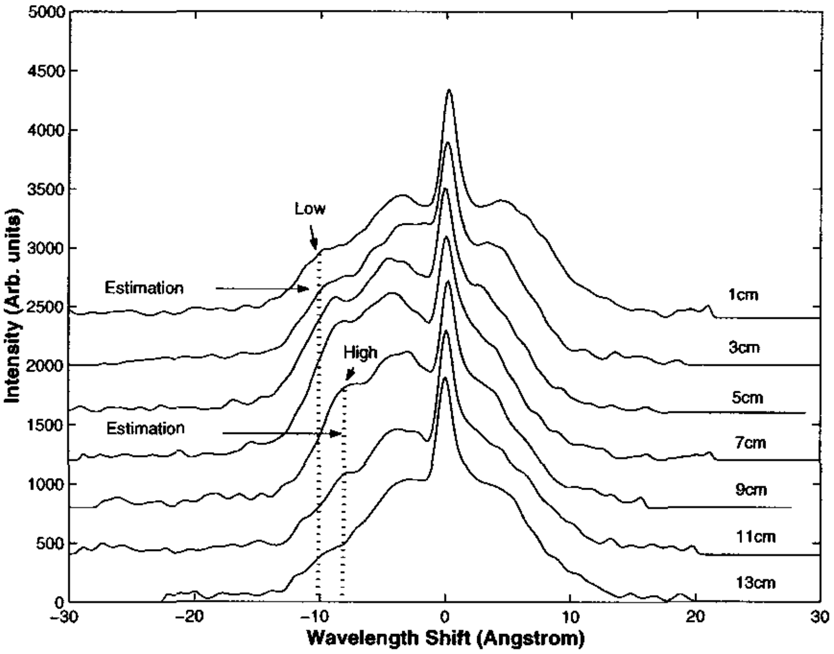

Figure 5.15: The spectra that were analyzed in Fig. 5.14 for −6 kV, normalized with respect to the unshifted peak. The spectra are lifted upwards in relation to one another.

peaks of the 1 and 13 cm spectra are closest to noise level and the associated wavelength shifts in Fig. 5.14 are relatively high). Since the approximation method is based on finding the top of the linear decline of the second peak, when the intensity of the peak is lower, the beginning of the decline is estimated to be closer to the base of the spectra where the spectra at that point is wider (this results in estimating a longer wavelength shift, as seen by the dotted lines of the 1 and 9 cm spectra in Fig. 5.15). This explains the fluctuation in the trend of the data points. Therefore, the results presented in Fig. 5.14 imply that the energy is independent of the distance from the cathode due to neutral atoms that move along the beam towards the anode.

The same approximation method was carried out for measurements taken at pressures of 10, 15 and 20 mTorr. The data points in each of the 4 groups, corresponding to voltages of −3, −4, −5 and −6 kV, were averaged. This resulted in 4 wavelength shifts data points for each of the 4 pressures. In previous work a linear relationship was found between the wavelength shift and the square-root of the voltage [1], and therefore, a linear fit was applied to the 4 data points of each of the pressures. The 3 short lines in Fig. 5.16.A are linear fits for experimental pressures of 15, 20 and 25 mTorr (marked in the figure), where the 2 average data points for the pressure of 10 mTorr are plotted without a linear fit (marked as "*").

Clearly the 3 lines are parallel, where the two data points of the 10 mTorr measurements are also placed on a line, representing the 25 mTorr measurements. This further confirms the linear relation between the square-root of the voltage and the wavelength shift and reinforces the validity of the approximation method (considering the statistical analysis, it is unlikely

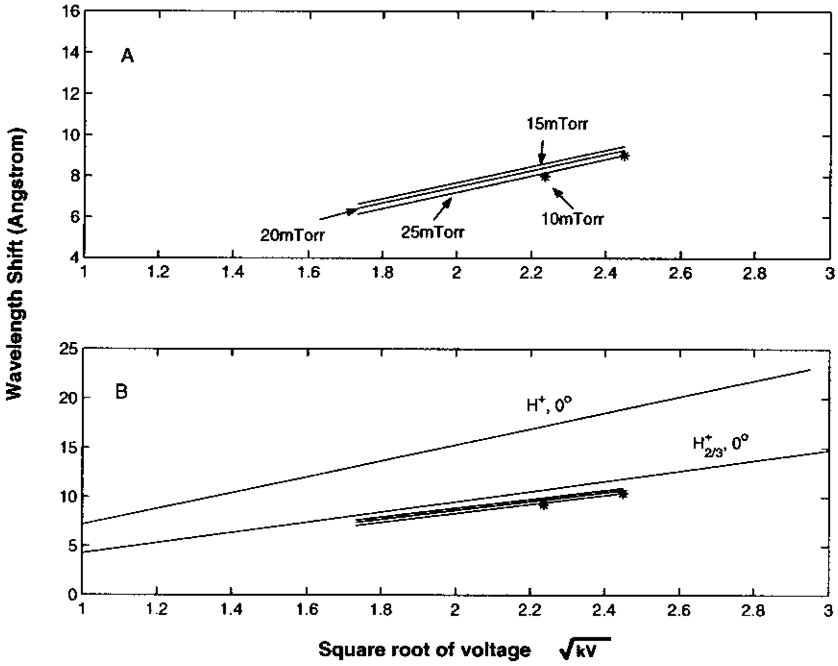

Figure 5.16: In plot A the 3 short lines present results of the linear fit for 15, 20 and 25 mTorr. The 2 average data points for the 10 mTorr are plotted without a linear fit (marked as "*"). In plot B the results are divided by a factor of cos(30°) and plotted over Fig. 5.6, where the two longer lines are the relations found for the $H^+_{2/3}$ and H^+ species analysis for the 0° measurements.

Distances (cm)	Voltages (-kV)	Pressure (mTorr)	No. of spectra
2, 4, 6	4	30	3
2, 4, 6	4	25	3
2, 4, 6	4	20	3

Table 5.4: 30 degrees measurements between the anode and wall.

that these results are coincidental). The three lines are separated by no more than ~ 0.5 Å, which is equivalent to a maximum energy spread of ~ 100 eV (see eq. 2.8 in chapter 2, or Fig. 2.5 for shifts in the range of $9.5 - 10$ Å). The experimental error of the voltage can reach a value of ± 100 V. Moreover, the error in the linear fit is larger and it can be assumed that the three lines overlap. This result implies that the energies of the neutrals are independent of pressure.

In Fig. 5.16.B the three short lines (presented in Fig. 5.16.A) were divided by a factor of cos(30°) and plotted over Fig. 5.6, which shows the two relations found for the $H^+_{2/3}$ and H^+ species analysis and for the 0° measurements. The lines are in the ± 1 Å error range and clearly in good agreement with the $H^+_{2/3}$ species line of the 0° measurements. In this section it was found that the neutral atom energies are constant along the path and that the energy for a given cathode voltage is independent of pressure. Moreover, the energies were found to be the same as in the cathode region (see Fig. 5.16). This strongly suggests that the spectra taken along the beam are an image of the energy distribution that is formed in the cathode region (for the same conditions).

5.4 Spectrum measurements in the anode-to-wall region

5.4.1 30° anode-to-wall measurements

Although the anode and wall of the chamber were both grounded, the beam extends from the anode to the wall (through the spacings of the anode mesh). If an electric field was established in this region, it was assumed to be negligible and any ions created in this region should have had low energies (units or tens of eV). However, since there were highly energetic blue-shifted neutral atoms comprising the beam, it was expected that these neutral atoms would drift through the anode-to-wall field free region and bombard the chamber wall. Measurements of spectra were taken along the 6 cm anode-to-wall distance at 2 cm, 4 cm and 6 cm from the anode. This was carried out for different pressures and an observation angle of 30° relative to the beam. The experimental conditions are detailed in table 5.4.

5.4.2 Wall reflection

Figure 5.17 presents three spectra obtained for distances of 2, 4, and 6 cm from the anode, for a pressure of 20 mTorr and for an applied cathode voltage of -4 kV. The blue shifted wing is a remaining of the distribution created in the cathode region (many of the neutral atoms have

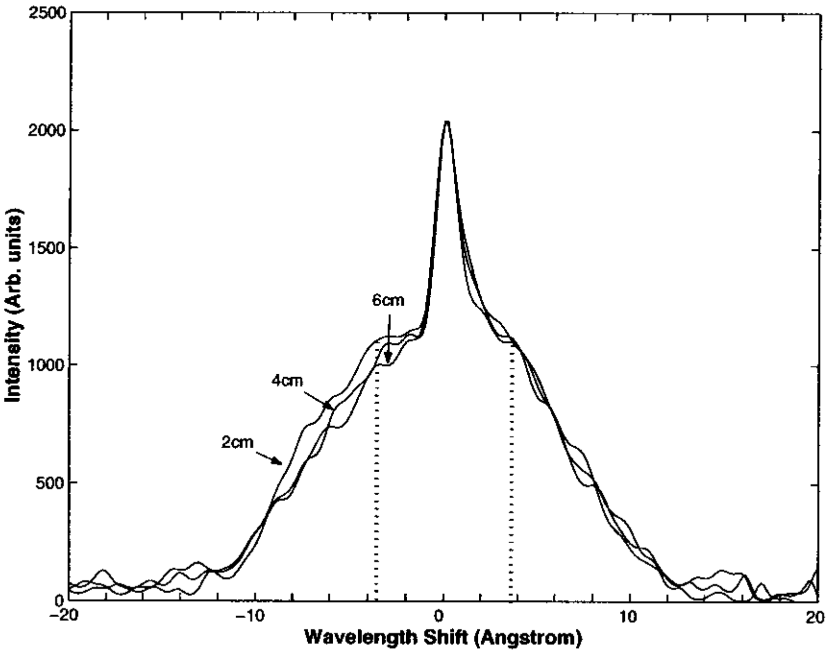

Figure 5.17: Three spectra for distances of 2, 4 and 6 cm from the anode, for pressure of 20 mTorr and an applied cathode voltage of −4 kV (the dashed lines show the beginning of the nearly linear decline of the spectral line).

de-excited and the blue-shifted wing has lost the resolution of the three peaks). However, the figure shows a nearly symmetric red-shifted wing that extends to ~ 14 Å. The three spectra overlap, which implies that the energy distribution is constant along the path in both blue-shifted and red-shifted directions. It is clear that the red-shifted wing of the spectrum that was taken near the glass (marked as "6 cm" in the figure) has a broad distribution extending to energies of more than 2.5 keV (see Fig. 2.5, chapter 2 for ~ 14 Å). Since there are highly energetic neutral atoms near the wall that are heading towards the anode (red-shifted) and since the red-shifted wing is relatively symmetric to the blue-shifted wing, it is suggested that the red-shifted wing of the spectrum consists of reflected blue-shifted neutral atoms from the chamber wall. From the symmetry of the spectrum it is suggested that the collisions of the neutrals with the wall are mostly elastic.

Since the blue-shifted wing profile along the cathode-to-anode path was found to be independent of pressure, it is expected that the red-shifted wing in this region is also independent of pressure. Figure 5.18 presents three spectra taken 6 cm from the anode (near the wall), for pressures of 20, 25 and 30 mTorr, and for an applied cathode voltages of −4 kV. It is clear that the three spectra overlap, where any small discrepancies can be accounted for in the fluctuations of the emission due to de-excitation mechanisms. These results clearly explain the red-shifted wing in the field free region and reinforce the former results (sections 5.2, 5.3).

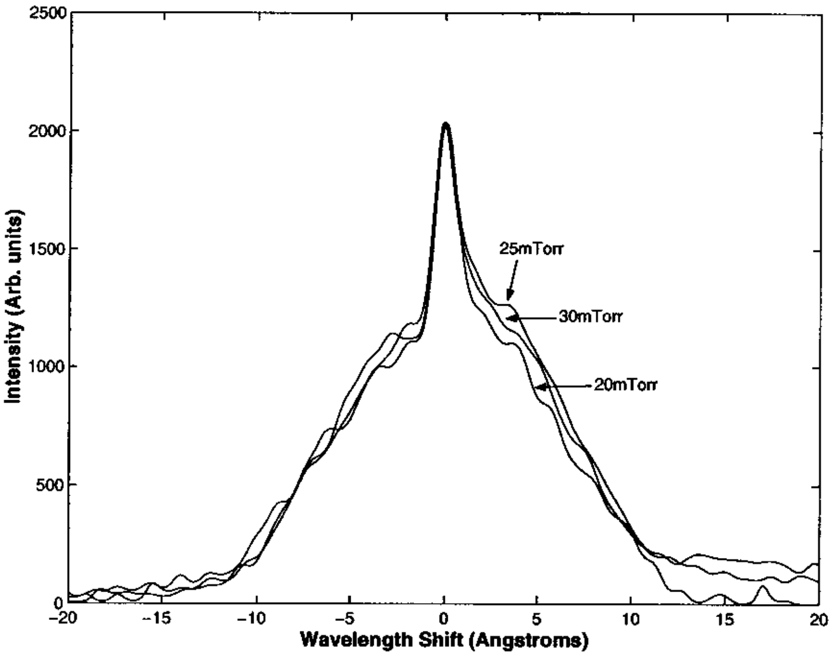

Figure 5.18: Three spectra taken 6 cm from the anode (near the wall), for an applied cathode voltages of −4 kV and for pressures of 20, 25 and 30 mTorr.

5.5 The radial component

5.5.1 90° cathode-to-anode measurements

The blue-shifted and red-shifted neutral atoms motion was assumed to be highly directional. If the beam is fully collimated in one direction, when observing at 90° angle relative to the beam (perpendicular to the beam) there should be no significant Doppler shifts registered. However, measurements taken at observation angles of 90° relative to the beam show a significant Doppler shift distribution. In this section the 90° spectrum profile is presented and explained with a relatively simple model.

Measurements were taken for an observation angle of 90° relative to the beam, where the experimental conditions presented in section 5.3 were repeated with some additional measurements. The experimental details are presented in table 5.5. Note that the distances of the points on the beam that are focused onto the monochromator's slit are measured from the cathode centre. "A-C" represents the distance between the cathode's centre and anode (the cathode half length is 2.75 cm).

5.5.2 Spectrum profile and results

Figure 5.19 presents three spectra obtained at angles of 0°, 30° and 90° relative to the beam, for a pressure of 20 mTorr and for an applied cathode voltage of −6 kV. The 30° and 90° measurements were taken 1 cm outside the cathode edge. In section 5.3 it was established that the 30° spectrum is a 30° component of the 0° spectrum. However, the 90° measurement

Distances (cm)	Voltages (−kV)	Pressure (mTorr)	A-C (cm)	No. of spectra
4, 6, ..., 16	7	5	16	7
4, 6, ..., 16	5, 6	10	16	14
4, 6, ..., 16	3.5, 4, 5, 6	15	16	28
4, 6, ..., 16	3, 4, 5, 6	20	16	28
4, 6, ..., 16	3, 4, 5, 6	25	16	28
4, 6, ..., 16	5, 6, 7	20	10	21
4, 15	5, 6, 7	20	12	6
4, 15	5, 6, 7	20	20	6

Table 5.5: 90 degrees measurements along the beam.

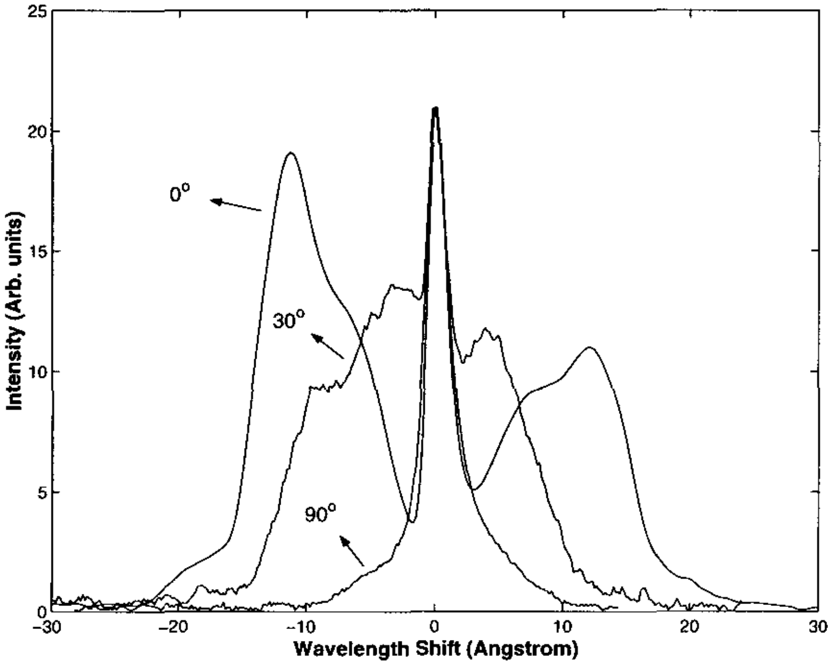

Figure 5.19: Spectra obtained at angles of 0°, 30° and 90° relative to the beam, for a pressure of 20 mTorr and an applied cathode voltage of −6 kV. The 30° and 90° measurements were taken 1 cm outside the cathode.

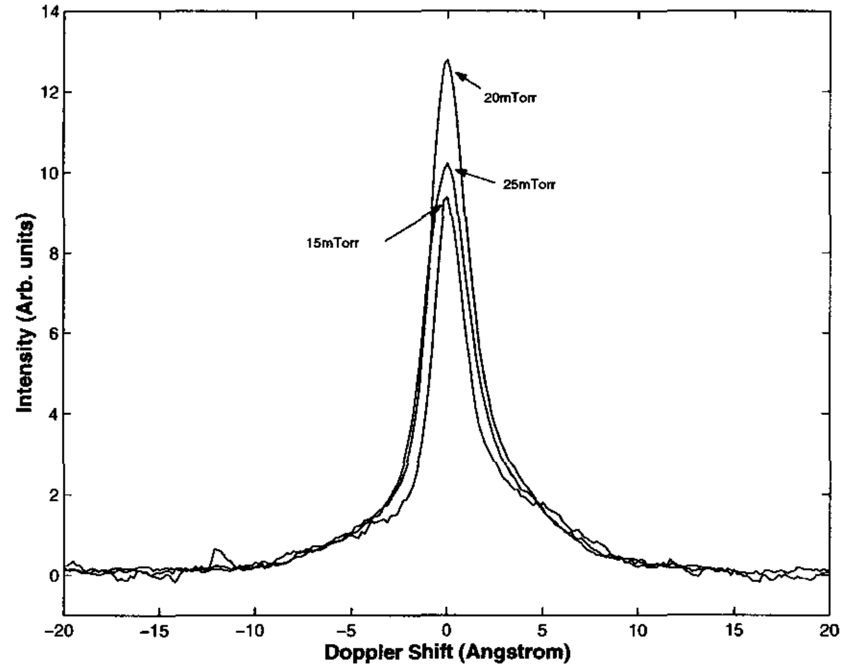

Figure 5.20: Spectra taken at an observation angle of 90° relative to the beam, 1 cm outside the cathode, for an applied cathode voltage of −5 kV and for pressures of 15, 20 and 25 mTorr.

shows a profile of a large broadening of the unshifted peak at its base (a shift of 10 Å at the base is equivalent to $\sim$ 1 keV). It is also evident that the spectrum is relatively symmetric around the unshifted peak, which implies that there is a radial component of the velocity of neutral atoms relative to the beam axis.

If it is assumed that the beam is entirely directional, there is an independent radial motion of neutral atoms towards the beam. This implies that a radial electric field is established along the beam, which causes ions to accelerate radially to the beam. However, if there is a slight scatter of the beam, the 90° profile will reflect the radial component of the scattered neutral atoms. The experimental results, supplemented with a model, suggest that the beam has some scatter (however, note that the model is valid for both hypotheses and can be implemented in both cases with simple changes in the programing).

In section 5.2 it was found that the energies of the neutral atoms in the beam are independent of pressure and anode-to-cathode distance. Figure 5.20 presents three spectra taken at an observation angle of 90° relative to the beam, 1 cm outside the cathode, for an applied cathode voltage of −5 kV and pressures of 15, 20 and 25 mTorr. Since we are concerned with comparing the broadened part of the spectra, the spectra were normalized to heights, where the broadening was found to overlap. This clearly suggests that the broadening is independent of pressures (measurements for 5 and 10 mTorr were noisy and are not shown in the figure however, when using the three point averaging method to smooth the spectra they showed the same profile as seen in Fig. 5.20).

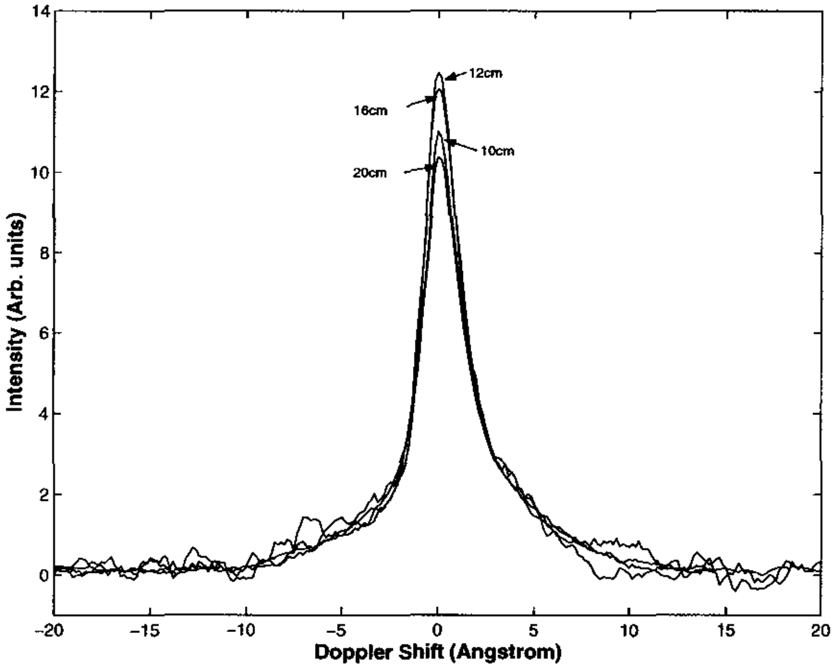

Figure 5.21: Spectra obtained for 10, 12, 16 and 20 cm anode-to-cathode distances. The measurements were taken for a pressure of 20 mTorr and for an applied cathode voltage of −6 kV.

Figure 5.21 presents 4 spectra obtained for 10, 12, 16 and 20 cm anode-to-cathode distances. The measurements were taken at an observation angle of 90° relative to the beam, for a pressure of 20 mTorr and for an applied cathode voltage of −6 kV (note that for lower pressures and shorter anode-to-cathode distances the noise increases, which limits the study range presented in this work). The spectra were normalized to heights, where the broadening of all spectra was found to overlap. Therefore, implying that the broadening is independent of anode-to-cathode distance.

The analysis of the 30° measurements in section 5.3 showed that the neutral atom energies were constant along the beam. Figure 5.22 presents 7 spectra obtained for distances of 1, 3, 5, 7, 9, 11 and 13 cm along the beam, where the distances are measured from the cathode edge. The spectra were taken at an observation angle of 90° relative to the beam, for a pressure of 20 mTorr and for an applied cathode voltage of −5 kV. The spectra were normalized with respect to the unshifted peak. Figure 5.23 presents the same spectra however, normalized by the base broadening. Clearly there is an overlap of the broadened part of the spectra, where the ratio of the unshifted peak to the broadened wing decreases with distance from the cathode. The broadening of the spectrum is independent of the distance from the cathode.

For all 138 measurements presented in table 5.5 the broadening of the spectrum was found to be independent of pressure, cathode-to-anode distance and position along the beam. This agrees with the experimental results presented in sections 5.2, 5.3 and therefore, suggest that the origin of these spectra might be in the scatter of the beam. Moreover, if it is assumed that

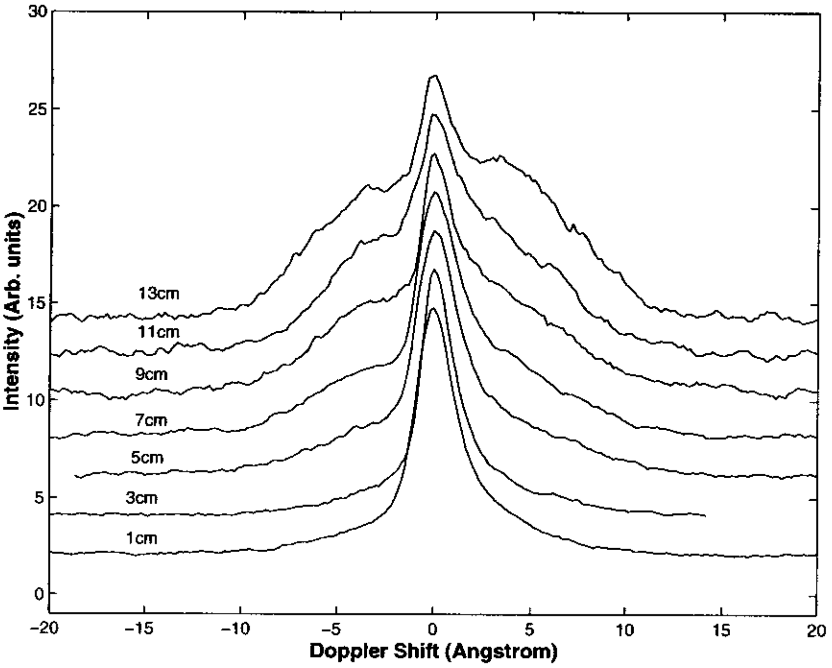

Figure 5.22: Spectra obtained for distances of 1, 3, 5, 7, 9, 11 and 13 cm along the beam, where the distances are measured from the cathode edge. The spectra were taken at an observation angle of 90° relative to the beam, for a pressure of 20 mTorr and for an applied cathode voltage of -5 kV. Moreover, the spectra were normalized with respect to the unshifted peak and lifted upwards in relation to one another.

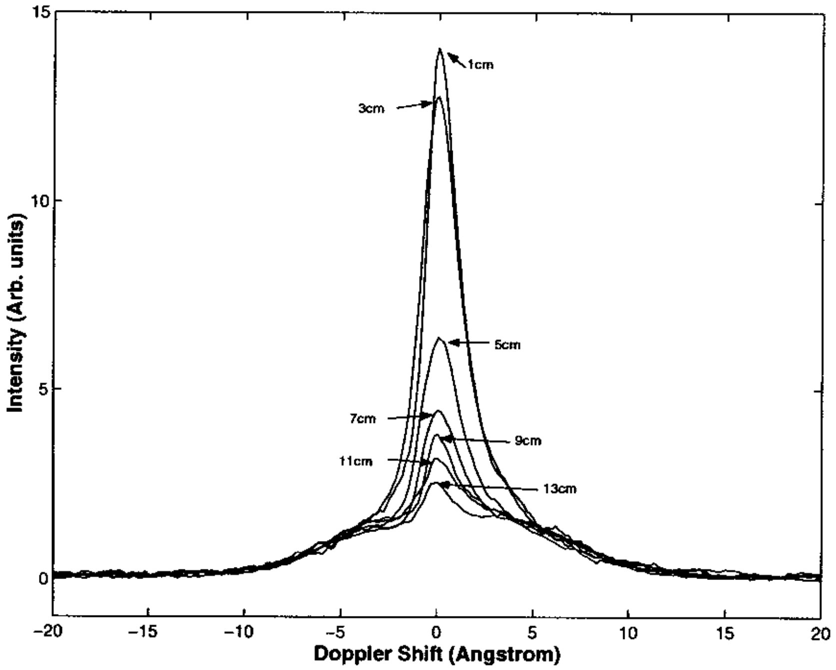

Figure 5.23: The same spectra presented in Fig. 5.22, where normalized by the base broadening.

the radial motion is caused by a radial field that is established by electron and ion currents in the beam, the experimental results in Fig. 5.23 suggest that the radial field is constant along the beam. This is unlikely since the current density changes along the beam.

The 90° spectrum profile can be explained by a simplified model, given in the next section.

5.5.3 The radial model

Spectra obtained at 0° relative to the beam show a wide distribution of H neutral atoms, which are moving out of the cathode towards the anode (e.g. see Fig. 5.19). The momentum transfer collision cross sections for H$-$H$_2$ are comparable to the charge exchange collision cross sections for energies in the range of 0.1 eV to $\sim$ 150 eV [9], and since the ions have energies in the range of kV relative to the background gas, these collisions are negligible. However, since the energy distribution of the H neutral atoms in the beam is continuous, the relative velocities of the neutral atoms span a broad range of relative velocities. Therefore, elastic momentum transfer collisions between H atoms in the beam might be significant. In fact, at low energies of $\sim$ 0.1 eV the cross sections are $\sim 55 \times 10^{-20}$ m^2 and exponentially decrease, where for energies of $\sim$ 10 keV the cross sections are $\sim 0.55 \times 10^{-20}$ m^2, which are compatible to the charge exchange cross sections for a wide range of energies [10]. It is likely that higher energetic neutral atoms "catch up" with lower energetic neutral atoms while colliding and deflecting some of the neutral atoms from the initial beam's direction (similar to a hot gas).

A model was constructed while considering the physics and the diagnostics (90° measurements), where the simplifying assumptions are as follows:

1. There is a uniform distribution of H–H collisions all along the beam, where the faster neutral atoms collide with the slower neutral atoms all along the beam creating the same energy distribution of scattered neutrals (this is implied in Fig. 5.23, where the 90° spectrum's profile does not change along the beam).

2. The neutrals can scatter from the beam's direction at any trajectory having an angle $\leq 90°$, measured from the beam (see Fig. 5.24: each angle forms a cone of possible trajectories surrounding the main beam).

3. Since the original direction of the neutral atoms is highly collimated in the beam's direction, it is possible that the probability for scatter at some angle decreases with increasing angle. Therefore, the model was constructed to account for a weighting function (can be exponential or other).

4. For a given trajectory, the energy profile is assumed to be the 0° energy distribution. Note that this is a crude first order approximation estimating the dynamics of the system (governed by momentum and energy conservation laws). The assumption enables each velocity component to be weighted on the cone according to its intensity in the original 0° spectrum. Also note that the amount of scattered atoms is assumed to be negligible in comparison with the amount of atoms that are moving in the direction of the anode or cathode (this is the reason that the scatter is observed at 90° to the beam but not at 30° to the beam, since the intensity of the emission received from the scatter is significantly less than the intensity received from the emission of the beam).

Figure 5.24 illustrates a cone of velocity trajectories, where each trajectory on the cone's surface is a component of a velocity from the 0° distribution. We consider at first one velocity out of the entire distribution on the cone's surface (e.g. the velocity v_1^0 in the figure). The v_i^0 velocity components at 90° to the beam are proportional to $\sin(\psi)$ such that $v_i = v_i^0 \sin(\psi)$. Note that ψ is the angle between v_i^0 and the X axis. This is illustrated in Fig. 5.24, where a "bicycle's wheel" is formed at the point of observation. The spikes of the wheel are the v_i velocity components of v_i^0 (the figure shows only half the wheel of the velocity trajectories).

The non-relativistic Doppler equation for the relation between the emitted and received wavelength is:

$$\lambda' = \lambda_0 \left(1 \mp \frac{v}{c}\right) \tag{5.1}$$

where λ_0 is the emitted wavelength in the rest frame (6563 Å), λ' is the detected wavelength, v is the velocity of the source and c is the speed of light in vacuum. Note that the "+" and "-" signs represent the receding and approaching sources, respectively. Therefore, the Doppler wavelength shift can be expressed as follows:

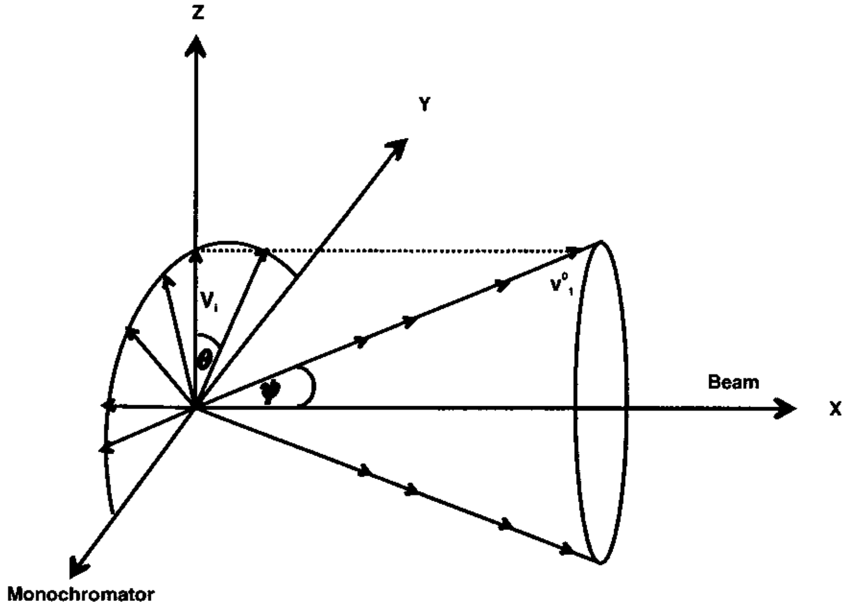

Figure 5.24: A cone of velocity trajectories, where each trajectory on the cone's surface is a velocity from the 0° distribution. The v_i^0 velocities components at 90° to the beam are proportional to $\sin(\psi)$ and are marked as v_i. These have a component in the monochromator direction, which is proportional to $\sin(\theta)$.

$$\Delta\lambda = \lambda_0 \left|\frac{v}{c}\right| \tag{5.2}$$

In this case we define $\Delta\lambda = \left(\lambda_i^{\prime} - \lambda_0\right)$ such that a positive result represents receding motion (red shifts) and a negative result represents approaching motion (blue shifts). The radial velocities v_i have to be further split into components that point in the direction of the monochromator (see Fig. 5.24). Defining the angle θ to be the angle between the v_i trajectories and the Z axis the Doppler shift equation takes the form:

$$\Delta\lambda_i = \lambda_0 \left|\frac{v_i \sin\theta}{c}\right| \tag{5.3}$$

From the symmetry of the problem it is clear that all trajectories coming from the half of the "wheel" closer to the monochromator ($\theta = 0°$ to $\theta = -180°$) will be blue-shifted and trajectories coming from the other half of the "wheel" further away from the monochromator ($\theta = 0°$ to $\theta = 180°$) will be red-shifted. Moreover, the distribution of the velocity components that point in the monochromator's line of observation is the same for all four quarters of the "wheel" (defined by $\theta = 0°$ to $\theta = 90°$, $\theta = 90°$ to $\theta = 180°$, $\theta = 180°$ to $\theta = 270°$, $\theta = 270°$ to $\theta = 360°$). Therefore, the problem is further simplified by considering one of the quarters only.

We now find the intensity distribution of the $\Delta\lambda_i$ wavelength shifts for one of the quarters. A constant interval of shifts $d\left(|\Delta\lambda|\right)$ is spanned in an interval $d\theta$, which is proportional to the probability of having a $d(|\Delta\lambda|)$ range of shifts. Therefore, it is also a measure of the observed relative intensity. From eq. 5.3 it follows that,

$$\theta = \arcsin\left[|\Delta\lambda_i|\,\frac{c}{\lambda_0 v_i}\right], \tag{5.4}$$

and the geometric weight function becomes,

$$I_i = \frac{d\theta}{d(|\Delta\lambda_i|)} = \left(\frac{c}{\lambda_0 v_i}\right)\left[1 - \left(|\Delta\lambda_i|\,\frac{c}{\lambda_0 v_i}\right)^2\right]^{-\frac{1}{2}}. \tag{5.5}$$

Note that $\Delta\lambda_i$ is dependent on the angle θ and has a range of values corresponding to the values of θ (see eq. 5.3). For computational reasons we choose a discrete approach and set an array of $\Delta\lambda_i$ ranging from $\Delta\lambda_i = 0$ to $\Delta\lambda_i = \Delta\lambda_{i\,\mathrm{max}}$ in constant intervals ($\Delta\lambda_{i\,\mathrm{max}}$ is the maximum shift corresponding to the maximum magnitude of the velocity component in the monochromator's direction, which is $v_i \sin 90°$). Consequently, the intensities I_i can be expressed as a vector $\mathbf{I}_i$ corresponding to the array of $\Delta\lambda_i$'s.

Symmetry suggests that we need only consider one red-shifted quarter and another blue-shifted quarter as our final solution. We now consider all v_i's corresponding to all v_i^0's on the surface of the cone (all the components of the 0° distribution at an angle ψ). The relative intensities f_i of the initial distribution (the intensities of the 0° spectrum's profile) are used to weight the v_i's corresponding to the v_i^0's (see fourth assumption). The intensity takes the following form:

$$\mathbf{I}' = \sum_{i=1}^{k} \mathbf{I}_i f_i \tag{5.6}$$

where k is the number of v_i^0's in the initial distribution (note that in this notation all vectors $\mathbf{I}_i$ are padded with zeros to have them all in the same length).

Last, we consider all cones of scatter spanning from $\psi = 0°$ to $\psi = 90°$. Once again, for computational reasons a discrete set of ψ_j angles is chosen. Therefore, each angle ψ_j has a corresponding intensity $\mathbf{I}'_j$ (this corresponds to the velocities of the 0° distribution in the ψ_j direction, where $v_i = v_i^0 \sin(\psi_j)$). A weighting function g_j is assigned to each angle of scatter (see third assumption) and the total intensity is expressed as,

$$\mathbf{I}_T = \sum_{j=1}^{p} \mathbf{I}'_j g_j, \tag{5.7}$$

where p is the number of angles ψ_j (note that in this notation all vectors $\mathbf{I}'_j$ are padded with zeros to have them all in the same length).

5.5.4 Results of the model and discussion

The model was programed using MATLAB, where its main structure is as follows:

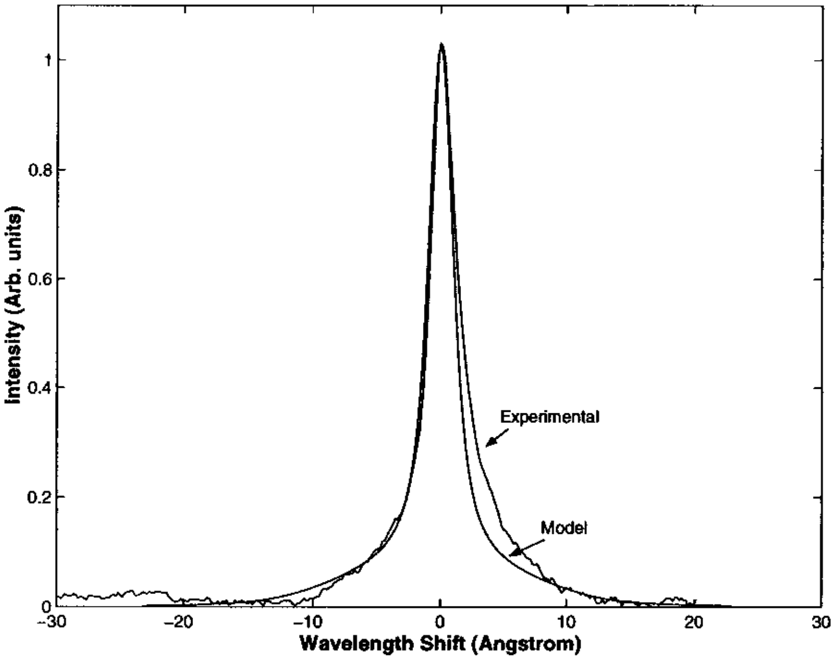

Figure 5.25: Comparison of the experimental spectrum that was obtained at an observation angle of 90° relative to the modelled spectrum.

1. Input: the experimental energy distribution (spectrum) that was taken at a 0° angle relative to the beam was inserted into the program, where the intensity was used as the weighting function f_i (see eq. 5.6). The weighting distribution function for the angles of scatter (the function g_i in eq. 5.7) was set to be uniform, which assumes that the scatter has the same probability for any angle (the results slightly improve for an exponential weighting function).

2. The main part of the program: the intensity versus the wavelength shift is calculated based on the model.

3. Adding a Lorentzian: the unshifted peak of 6563 Å is represented by a Lorentzian. The Lorentzian half-width was set by the experimental half-width of the same spectrum that is reconstructed.

4. Convolution: the program was made to convolve the response function of our instrument with the resulting theoretical spectrum. Note that this did not change the results significantly.

5. Scaling and plotting: both spectra were normalized with respect to the unshifted peak for comparison.

A comparison of the experimental spectrum to the modelled results is presented in Fig. 5.25. Since all spectra that were taken at an observation angle of 90° relative to the beam

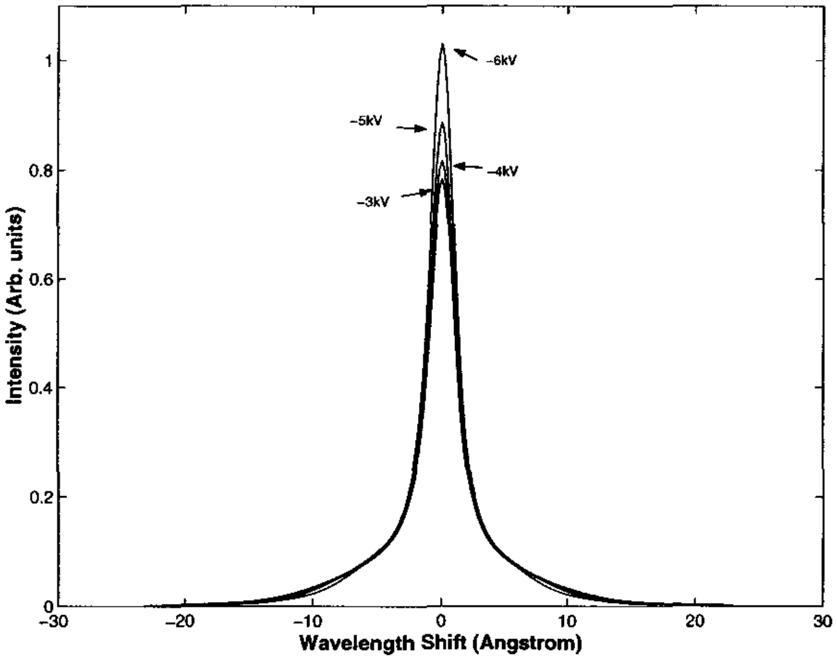

Figure 5.26: Results from the model for input voltages of −3, −4, −5 and −6 kV. The 4 reconstructed spectra overlap.

show the same profile, the choice of the experimental spectrum was arbitrary. In the figure the experimental spectrum was taken for a pressure of 20 mTorr, cathode voltage of −6 kV, anode-to-cathode distance of 20 cm and at 1 cm from the cathode edge. The experimental spectrum (energy distribution) that was used for the model calculation was taken for the same conditions, focussing on the cathode centre at an observation angle of 0° relative to the beam. Clearly, the model results agree with the experimental spectrum. However, there is a slight discrepancy, which is caused by the slight asymmetry of the experimental spectrum. Note that the blue-shifted wing cuts off at $\sim$ 10 Å whereas, the red-shifted wing cuts off at $\sim$ 12 Å. This might result from the experimental set-up, where the monochromator is aligned at an observation angle of 90° relative to a point on the beam at the centre of the cathode. When scanning along the beam the angle slightly exceeds 90°, therefore, a small component of the beam can cause a broadening of the red-shifted side.

In section 5.2, the spectra taken at an observation angle of 0° relative to the beam were found to be independent of pressure and anode-to-cathode distance. They were also found to maintain the same distribution along the beam (section 5.3). Since these energy distributions are inserted into the program as an initial starting point, the model results presented in Fig. 5.25 must agree with all 90° experimental findings that were presented in this section.

The experimental results presented in this section relate to variations in pressure, anode-to-cathode distance and position along the beam. Figure 5.26 presents the model results for 4 reconstructed spectra. The 4 spectra that were used in the model were taken for an observation angle of 0°, a pressure of 20 mTorr, anode-to-cathode distance of 20 cm and for

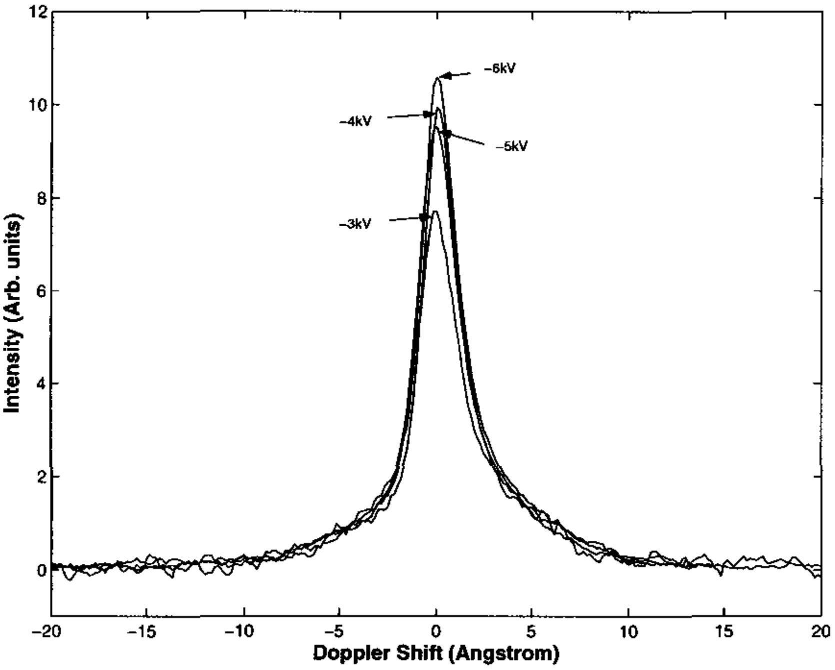

Figure 5.27: The experimental spectra taken for cathode voltages of −3, −4, −5 and −6 kV, showing that broadening is independent of the cathode voltage.

cathode voltages of −3, −4, −5 and −6 kV. Clearly the 4 reconstructed spectra overlap, implying that the broadening is independent of voltage. This is an unexpected result since that previous energy measurements showed a linear dependence on voltage (sections 5.2 and 5.3).

Figure 5.27 presents 4 spectra taken at an observation angle of 90° relative to the beam, 1 cm outside the cathode, for a pressure of 20 mTorr and cathode voltages of −3, −4, −5 and −6 kV. The spectra were normalized by the base broadening. Clearly, the broadening is independent of the applied voltage. This can be explained by considering the reduction of the intensity of the larger shifts. The 90° components, which become smaller with smaller angles of scatter, enhance the intensity of the lower shifts. The components pointing in the monochromator's direction further enhance the intensity of the lower shifts. Finally, the larger shifts in the initial energy distribution are less intense (the outer part of the spectrum representing the H^+ ion specie is significantly less intense). This also explains why the results of the model are not affected significantly when weighting the scatter angles (ψ_j) with a linear or exponential functions (g_j). These functions reduce the larger shifts intensities, which are small.

5.6 Summary and conclusions

The beam profile was systematically studied with spectroscopic measurements, obtained from the three regions: cathode, cathode edge-to-anode and anode-to-wall. Measurements in the cathode region confirm previous work [1], showing that the energy represented by the Gaussian peaks is the same for all three species. The distributions presented in Fig. 4.5 (chapter 4) suggest that this energy is close to the maximum energy gained by the potential depth, where this is further supported with previous experimental results of Khachan et al. [1,2].

The ion energy was also found to be independent of cathode-to-anode distance and of pressure for the experimental conditions presented in this work. Since the minimum in the potential is found at the cathode edge and is mostly dependent on the cathode geometry, material and bias, moving the anodes closer or further from the cathode does not affect the energy distribution, which is formed mostly in the cathode region. The energy independence of pressure can only be explained with a model including electronic and ionic processes in the cathode, which is out of the scope of this work. However, these results imply that the maximum potential depth is independent of pressure for the experimental conditions presented in this work (5 – 30 mTorr). Therefore, the ion energies (represented by the Gaussian peaks) are an estimate of the potential depth. In this work experimental results showed a neutral atom energy equivalent to $\sim$ 60% of the applied voltage, which implies that for the experimental set-up of this work the maximum potential depth of the well was $\sim$ 60% of the applied voltage.

Results for the asymmetric systems (placing the two anodes at different distances from the cathode) agree with the results presented for the symmetric systems, where the ion energy was found to be independent of asymmetry and was the same as in the symmetric case. This implies that each of the two potential wells, established on each side of the cathode, is identical to the wells established in the symmetric system for the same anode-to-cathode distance. This further supports the fact that the potential minimum and its position are mainly influenced by the cathode geometry and material (and bias).

Energy measurements taken at an observation angle of 30° relative to the beam and along the beam agree with the measurements in the cathode region. The energies were found to be independent of pressure, cathode-to-anode distance and were also found to be constant all along the beam. This implies that the spectra obtained at 30° angle to the beam are a component of the 0° spectra at that angle (the neutral atom trajectories are in the direction of the beam but the emission is collected at 30° angle to the beam). The results further support the fact that the energy distribution is created mainly before exiting the cathode, where at each point along the beam a sample of this distribution is found (energies are constant along the beam).

Energetic red-shifted neutral atoms were found next to the chamber wall. The broadening of the energy distribution reached $\sim$ 2.5 keV for a cathode voltage of -4 kV, which is $\sim$ 60% of the applied cathode voltage. This implies that neutral atoms are reflected from the wall, explaining the symmetry of the blue-shifted and red-shifted wings in the anode-to-wall region.

Energy measurements perpendicular to the beam agree with all previous results, showing that energy is independent of pressure, cathode-to-anode distance and position of observation along the beam. The spectra show a broadening of $\sim$ 11 Å at their base, which implies that there may be a radial component of the velocity of neutral atoms towards the beam. However, it was suggested that the broadening is caused by the emission perpendicular to the beam, which originates in neutral atoms scattered from the beam. The scattered neutral atoms are a small component of the directional beam, and therefore, the emission from the directional component of the beam is much more significant at an observation angle of 30° relative to the beam axis. A model was developed to predict the spectrum line profile, which was found to agree with the experimental results. Moreover, the model predicted that the profiles of the 90° spectra should be independent of voltage, which was confirmed experimentally.

Bibliography

[1] J. Khachan and S. Collis, Phys. of Plasmas, **8**(4), 1299 (2001).

[2] J. Khachan, D. Moore and S. Bosi, Phys. of Plasmas, **10**(3), 596 (2003).

[3] M. Fitzgerald, J. Khachan and S. Bosi, Phys. J., D **39**, 35-39 (2006).

[4] S. Steenstrup, Aust. J. Phys., **38**, 319-327 (1985).

[5] C. E. Shannon, The Bell System Technical Journal, **27**, 379-423, 623-653 (1948).

[6] E. T. Jaynes, The Physical Review, **106**(4), 620-630 (1957).

[7] R. Bevington Philip and D. Keith Robinson, "Data Reduction and Error Analysis for the Physical Science", Second Edition.

[8] T. A. Thorson, R. D. Durst, R. J. Fonck and L. P. Wainwright, Phys. Plasmas, **4**(1), 4 (1997).

[9] A. V. Phelps, J.Phys. Chem. Ref. Data, **19**, 3 (1990).

[10] P. S. Krstic and D. R. Schultz, Atomic and Plasma-Material Data for Fusion, **8**, 1 (1998).

Chapter 6

IEC Fusion Rate Estimates

This chapter presents fusion rate estimations for a conventional IEC device, which also demonstrates another application of the charge exchange model. The modelling is presented followed by results and discussion, which are compared to experimental results obtained by Thorson et al. [5].

6.1 Background and motivation

Although the main principles of operation of IEC devices are confinement by using a potential well and beam-beam fusion interactions in the cathode core, many experiments are carried out in the mTorr regime where the operation of the device does not strictly follow these principles. Hirsch [1] experimented with an IEC device while using ion guns to inject deuterium and deuterium/tritium ions into the chamber. He reported 10^{10} n/s neutron production rates (for D-T), but models based on a multi-electrode structure in the cathode could not account for these measurements. Baxter and Stuart [2] developed a model that was based on charge exchange, which took place in the ion guns (see chapter 3). They explained Hirsch's experimental results by showing that the total fusion reactivity was a consequence of the interaction of energetic ions and neutral atoms with the background gas. Miley et al. and Nadler et al. [3,4] measured fusion reactivity while operating their devices at pressures higher than 1 mTorr. If ions had to accelerate through a path of several cm between the anode and cathode, most ions would have undergone charge exchange before reaching the cathode. Considering that the charge exchange cross sections are orders of magnitude larger than the fusion cross sections, it is more probable for the resulting fast neutrals to fuse with the background gas rather than for the accelerating ions to fuse with ions in the cathode. This is strongly supported by the experimental work of Thorson et al. [5] showing that the neutron production rates are a result of beam-background interactions.

Theoretical modelling suggested the existence of a virtual anode at the cathode centre [1,6–8] where Khachan et al. [9] and Thorson et al. [10, 7] measurements show a potential well that extends from the cathode centre to the anode. The minimum of the potential was found near the cathode edge, and therefore, the potential well was found to be asymmetric around its minimum (see Fig. 4.4). This implies that the maximum ion energy is gained near the cathode edge and not at the centre of cathode. Moreover, in chapter 4 it was suggested that high fluxes of ions diverge from the cathode centre while undergoing charge exchange to become neutral atoms.

In this chapter it is shown that the "blue shift" phenomenon (see discussion in chapter 4) can account for measurements of fusion rates in IEC devices operating in the mTorr regime. D-D fusion neutron production rates were estimated for an IEC device with the use of the charge exchange programs (presented in chapter 3). These were compared with an experimental study of neutron production rates for D-D interactions carried out by Thorson et al. [5].

6.2 Modelling and numerical results

The fusion rate for two interacting species is given by the expression,

$$R = V n_i n_j v \sigma \tag{6.1}$$

where V is the volume of reactivity, n_i and n_j are the number densities of the two interacting species, v is the relative velocity of the two species and σ is the fusion cross section. Therefore, estimating fusion rates requires knowledge of the density distributions and their energies along the beam. Although it is possible to use Monte Carlo simulations [11] or numerically solve the Boltzmann equation [2], here the semi-analytical method [12] was used to find the density and energy distributions of neutral atoms along the beam (see model in chapter 3).

Neutron production rates measured by Thorson et al. [5] showed a linear relationship between the ion density and the rate. Moreover, the ion density was estimated to be 4 orders of magnitude lower than the background density. This suggests that the beam-beam interaction was negligible in comparison to the beam-background interaction. They also reported that most (90%) of the fusion reactions took place outside the cathode. This implies that either most of the ions have charge exchanged before reaching the cathode or that the "blue shift" phenomenon was responsible for the creation and divergence of neutral atoms from the cathode. Nevertheless, the virtual anode at the cathode centre prevents energetic beam-beam interactions to occur at the centre of the cathode. The model presented here assumes that charge exchange is dominant (for pressures above 0.5 mTorr) and that the neutral-background fusion interactions are more significant than the ion-background fusion interactions. It is also assumed that ions are trapped in the potential well (extending from the cathode centre to the anode) until they undergo charge exchange and exit the cathode region as neutral atoms.

The programs that were used to calculate the fusion rates are an extension of the programs for the potential well case presented in chapter 3. The experimental potential well measurements [9, 10] were used to estimate the potential that was used in the simulations (see Fig. 4.4). The charge exchange cross sections for D_i^+–D_2 (where i = 1, 2, 3) are similar to those of H_i^+–H_2 [13], and therefore, it is assumed that the charge exchange process is

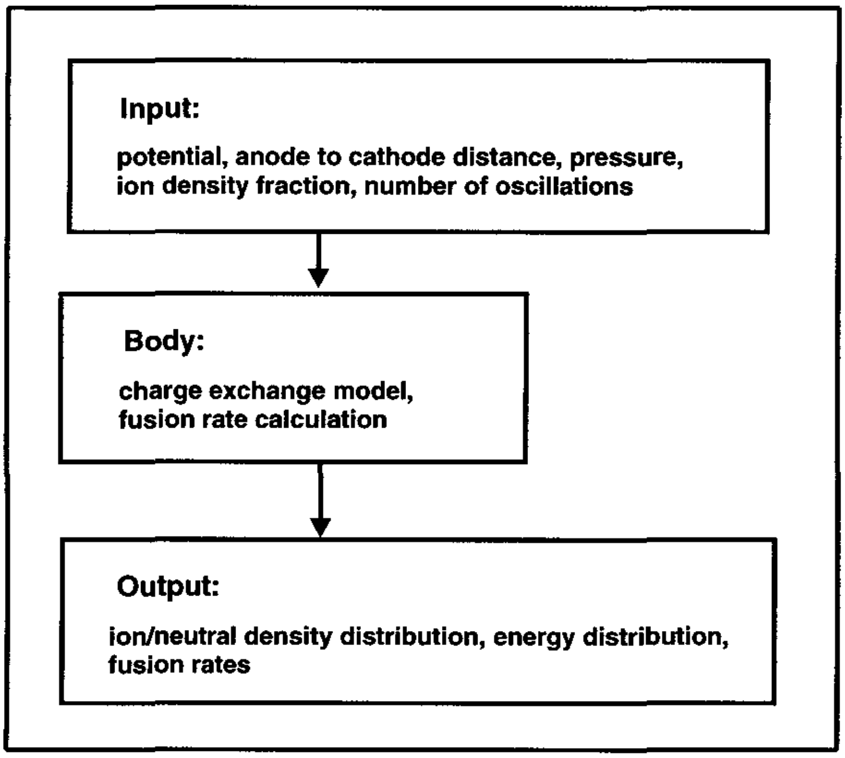

Figure 6.1: A schematic showing the three main parts of each program, which are based on the method and programs presented in chapter 3.

similar in both cases. As a first order approximation, initial densities of D^+, D_2^+ and D_3^+ ions were assumed to start the process at the centre of the cathode (the "blue shift" phenomenon presented in chapter 4). Although the D^+, D_3^+ species create more cold D_2^+ ions along the path, in this first order approximation the D_2^+, D_3^+ and D^+ programs remained separate from each other and the newly created D_2^+ ions were not fed back into the program of the D_2^+ specie. The fusion rate estimates were based on the distributions of the neutral atoms resulting from the 3 charge exchange programs.

Figure 6.1 presents a schematic of the three main parts of each program. The input includes the features of the potential, the distance between the cathode centre and anode, the gas pressure, the fraction of ionization of the gas and the number of oscillations of the ions in the well. For the number of oscillations, a number larger than 4 oscillations was found sufficient for the neutron production rate calculations. The charge exchange process reduces the ion energies and the fusion production rate does not change significantly for a larger number of oscillations. In the body of the programs the neutral atom density and energy distributions were calculated along the potential well. Experimental charge exchange cross sections [13, 14] were used in the calculations.

Once the densities and corresponding energies were determined, fusion rates, R, were calculated with

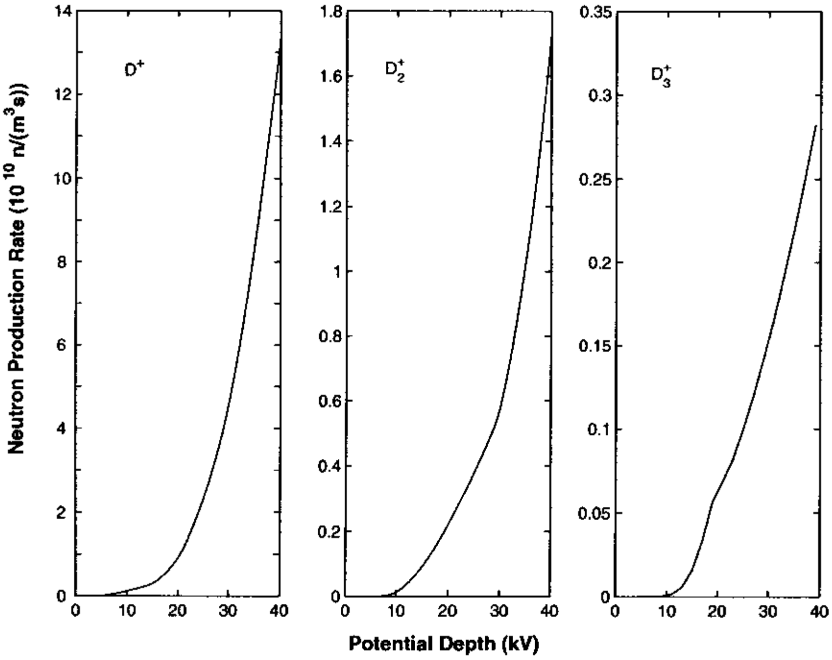

Figure 6.2: Modelled neutron production rate as a function of potential depth for the three ionic species (D^+, D_2^+, D_3^+).

$$R = \sum_{i=1}^{all} n^{(b)} \left(n_i^{(f)} v_i^{(f)} \sigma_i \right), \tag{6.2}$$

where $n^{(b)}$ is the background gas density, $n_i^{(f)}$ is the fast neutral atom densities resulting from charge exchange, $v_i^{(f)}$ is the absolute magnitudes of the velocities of the neutral atom densities $n_i^{(f)}$ and σ_i is the fusion cross section corresponding to $v_i^{(f)}$. The experimental fusion cross sections were taken from Kaye and Laby [15]. Note that in this expression the units of R are reactions per unit volume per unit time.

6.3 Results and discussion

6.3.1 Neutron production rate dependence on voltage

The model described in section 6.2 was used to reproduce the experimental neutron production rates of Thorson et al. [5], which their work was carried out on an IEC device at the University of Wisconsin in Madison. Fusion neutron production was carried out using D_2 gas for cathode voltages ranging from −20 to −60 kV and for background pressures of ~ 1.2 mTorr and ~ 1.8 mTorr. The neutron production rates were found to increase monotonically with voltage and were in the range of $0.2 \times 10^6 - 5 \times 10^6$ (n/s).

The neutron production rate estimates from the model, for the three ionic species, are presented in Fig. 6.2. Since the cathode radius was 0.05 m, the minimum in the potential was assumed to occur at 0.05 m. The potential depth was varied between -5 and -40 kV and the pressure was set to 2 mTorr. The density of ions was set to 10^{-4} of the background gas density, which is the density estimate of Thorson et al.

Using the D_2^+ specie, which is the most abundant, the estimated fusion rates were in the order of 10^9 and 10^{10} n/m^{3}s. In order to compare these with the experimental results, an estimate of the fusion reaction volume was made. Thorson et al. showed that most neutrons were produced outside the cathode region, and therefore, it is reasonable to estimate the active radius to be 3 or 4 times the cathode radius ($\sim 0.15 - 0.2$ m, which is the distance from the cathode to the anode mesh). Using the volume obtained from the reaction radius, it is found that the estimated fusion rates should be multiplied by a factor of 10^{-3}. Another consideration that affects the production rates is the depth of the potential. Previous measurements of the potential showed that the depth of the potential well varied between 25% and 60% of the applied cathode voltage [9,10]. By estimating the depth of the potential to be in the range of $\sim$ 30% to $\sim$ 50% of the applied cathode voltage, it was found that modelled and experimental fusion rate results were in good agreement.

The rates from the D^+ specie, however, were found to be an order of magnitude greater than the total measured rates (note that the experimental rates are given as the total neutron production rates with no distinction between the 3 ionic species). This is expected since the D^+ is the lightest specie hence the fastest, where the rates largely increase with increasing velocities. However, the D^+ is the least abundant among the three species and this can reduce the estimated rates by a factor of 10 or more (note that the initial density used in the simulation was the same for all 3 species). The D_3^+ specie is the heaviest and ,therefore, contributes the least to the total fusion rates.

6.3.2 The dependence of neutron production rates on pressure and ion density

Thorson et al. found that the neutron production rate is linearly dependent on the ion density, which implies that fusion occurred by beam-background interactions. Figure 6.3 presents the modelled neutron production rate as a function of the ion density (in the figure, the ion density is expressed as a fraction of the background density). Using the experimental conditions from Thorson, the minimum of the potential well was set at 0.1 m (the cathode radius is 0.1 m) and the potential well depth was set to -7 kV. Note that this is 35% of the applied voltage, which is closer to the lower limit of the potential depth and ,therefore, will set a lower limit for the estimated rates. The calculations were carried out for pressures of 4.5, 14 and 52 mTorr. From eq. 6.2 it is clear that the rate depends linearly on the ionization fraction and therefore, agrees with the experimental results.

Figure 6.3 implies that there is an optimum pressure for a maximum neutron production rate. Thorson set the pressures to $\sim$ 0.6, $\sim$ 2 and $\sim$ 7.5 mTorr, where the neutron counts were largest for $\sim$ 2 mTorr, second largest for $\sim$ 7.5 mTorr and lowest for $\sim$ 0.6 mTorr. These results can be explained qualitatively with the estimated neutron production rate as

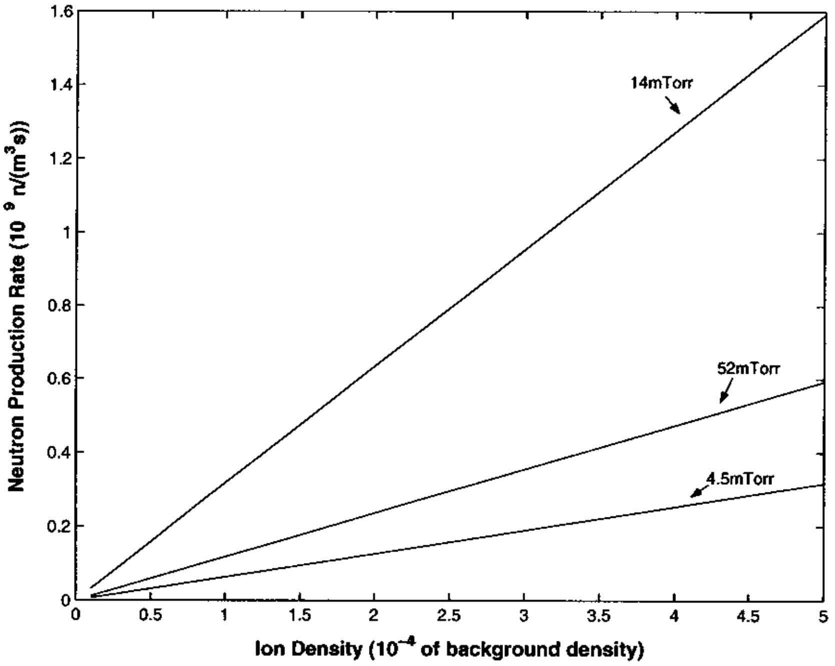

Figure 6.3: Modelled neutron production rate as a function of the ion density and for pressures of 4.5, 14 and 52 mTorr. Note that the ion density is expressed as 10^{-4} of the background density.

a function of pressure. The conditions were set to be the same as for Fig. 6.3, where the ion density was set to 10^{-4} of the background gas density. Figure 6.4 presents the modelled results, where it is evident that the neutron rate is a maximum at $\sim$ 21 mTorr and then is reduced for higher pressures. This is a consequence of beam-backround fusion interactions, where for pressures higher than the optimum pressure, charge exchange significantly reduces the energies, and for pressures below the optimum pressure there are not enough cold gas targets.

The shape of the curve is in agreement with a similar plot presented by Baxter and Stuart [2], however, their maximum production rate was found at $\sim$ 45 mTorr. In their model, ions were accelerated in ion guns for a distance of 0.05 m and the accelerating potential was set to more than 10 times the input potential depth that was used in our model (these were Hirsch's operational conditions). The position of the peak was found to be dependent on the input voltage. Using the same input voltage as in Hirsch's experiments the peak in Fig. 6.4 shifts to $\sim$ 45 mTorr (not shown here). Nevertheless, this curve explains Thorson's experimental results since it is evident that the rate corresponding to 14 mTorr is placed on one side of the peak and the rate corresponding to 52 mTorr is placed on the other. However, it seems that there is a quantitative discrepancy between the results presented in Fig. 6.4 and Thorson's experimental results. In their results the peak is found at $\sim$ 3 mTorr, whereas our results show a peak at $\sim$ 21 mTorr.

Thorson's results show that the neutron production rate is $\sim 0.2 \times 10^6$ n/s for a pressure

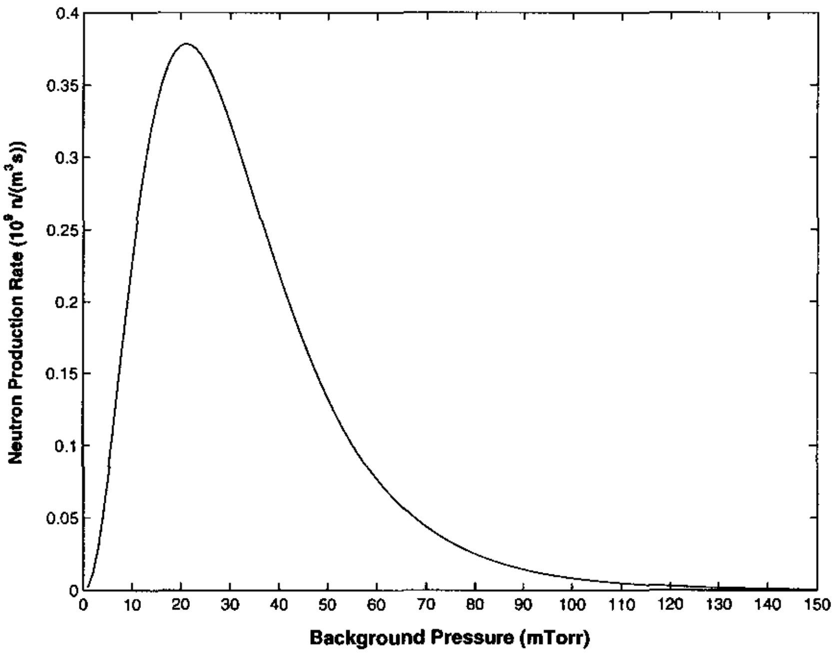

Figure 6.4: Modelled estimates for the neutron production rate as a function of pressure. The conditions were set to be the same as for Fig. 6.3, where the ion density was set to 10^{-4} of the background gas density.

of ~ 2 mTorr (this is for the same experimental conditions mentioned above: cathode current of 20 mA and cathode voltage of -20 kV, which is equivalent to a potential depth of ~ -7 kV). From Fig. 6.4 it can be seen that this is the same neutron production rate as for a modelled pressure that is 7 times larger, which is $\sim$ 14 mTorr. Note that the pressure ($\sim$ 21 mTorr) corresponding to the peak in Fig. 6.4 is also 7 times larger than the pressure ($\sim$ 3 mTorr) corresponding to the experimental peak. Figure 6.3 presents the modelled results for each of Thorson's pressures multiplied by a factor of 7. For these pressures, the rates in the figure are found to be in good agreement with the experimental neutron production rates.

This result might suggests that the ion density is greater in the cathode region (therefore the neutral atoms production is greater) than in other parts of the chamber. Thorson reports that the gas pressures was measured in the vacuum chamber but not specifically in the cathode. High densities of ions might be created in the cathode core due to significant secondary electron ionization (the "blue shift" phenomenon assumes the creation of a high density of ions in the cathode core [16]). The ions and the fast neutral atoms that are created via charge exchange increase the total density in the cathode region. Moreover, Thorson reports a local (not integrated on the entire cathode) high proton and neutron production rate in the cathode region. Considering that the major contribution to the neutron production rate is neutral-background interactions, this implies that there is a significant increase in density in the cathode region.

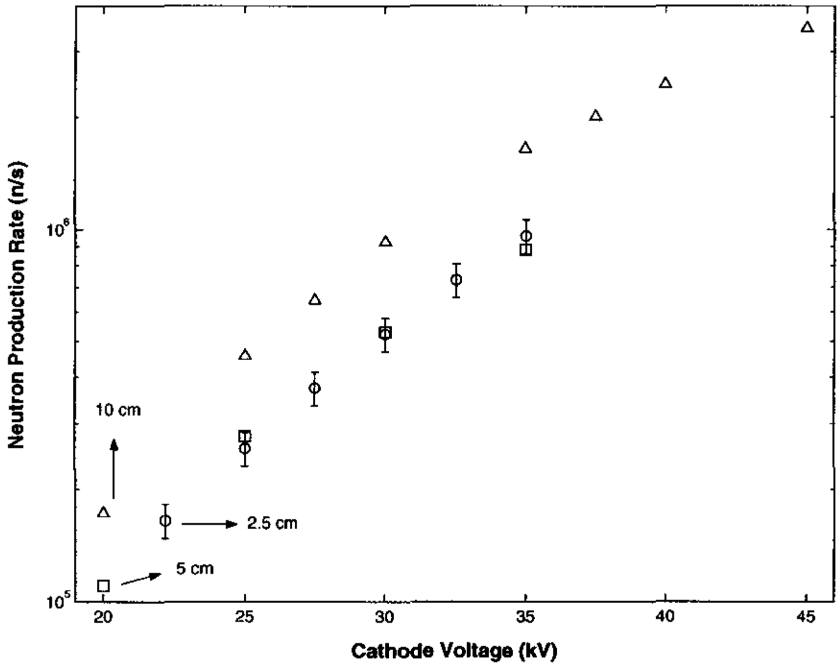

Figure 6.5: A reproduction of Thorson et. al. plot [5] of the neutron production rate as a function of voltage for the three cathode radii of 0.025, 0.05 and 0.1 m (marked in the figure).

6.3.3 Neutron production rate dependence on cathode size

The charge exchange model predicts that the energy distribution of the fast neutral atoms changes with the distance travelled by the ions. Since the minimum of the potential was found near the cathode edge, increasing the cathode radius will increase the ion path-length. It is expected that this will slightly affect the neutron production rates. Thorson measured neutron production rates for cathodes of different radii. They set the cathode current to 20 mA, pressure to ~ 2 mTorr and varied the cathode voltage between -20 and -45 kV for cathode radii of 0.025, 0.05 and 0.1 m. The neutron production rates were found to be in the range of 10^5 to $\sim 2 \times 10^6$ n/s, where the rates for the 0.1 m cathode were found to be the highest of the three measurements. A reproduction of the neutron produciton rates versus voltage, from Thorson et al., is given in Fig. 6.5 for the three cathodes they used.

Figure 6.6 presents the modelled results for the same experimental conditions and cathode sizes (the potential minimum was set at 0.025, 0.05 and 0.1 m). The modelled results were in good agreement with the experimental results. This is for the experimental range where: (1) the depth of the potential well was assumed to be 35%–50% of the applied voltage, which is equivalent to a depth of 10 - 20 kV in the simulations results presented in Fig. 6.6, and (2) the cathode current was ~ 20 mA, which equates to an ion density of $\sim 10^{-4}$ of the background gas density that was used in the simulations. The neutron rates were approximately in the same range and the shape of the curves agrees with the experimental shape. The model also predicts the same distance between the two curves representing the 0.025 m and 0.1 m

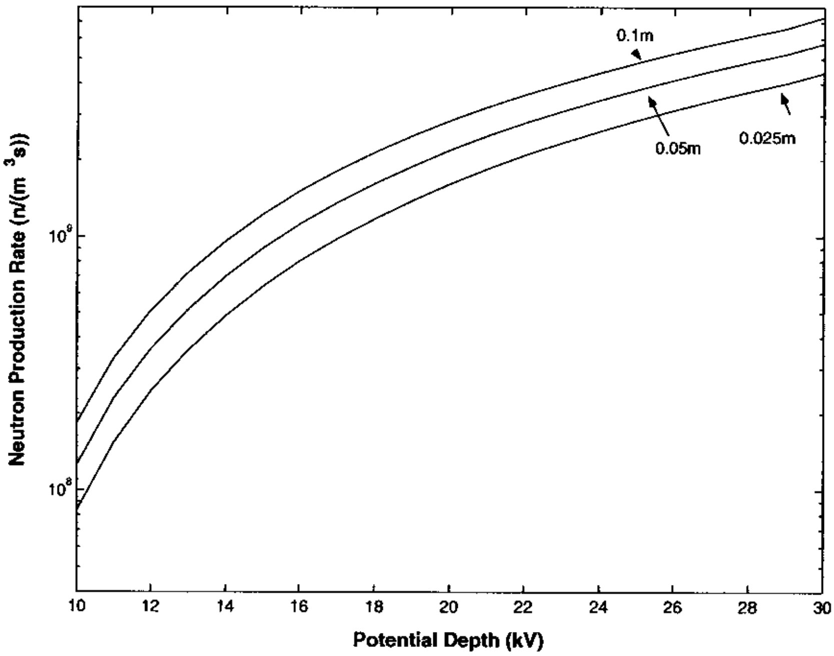

Figure 6.6: Modelled results for the neutron production rates as a function of voltage and for three cathode sizes. This follows Thorson's experimental conditions and cathode radii of 0.025, 0.05 and 0.1 m.

cathodes as in the experimental case. However, the experimental results show no significant difference between the rates of the 0.025 m cathode and the 0.05 m cathode, whereas the model does predict a difference.

6.4 Conclusions

Neutron production rates were estimated for an IEC device operating in the mTorr regime and compared with experimental measurements taken by Thorson et al. [5]. It was assumed that charge exchange is dominant and, therefore, the calculations were based on collisions of neutrals with the background gas. The modelled results were found to agree with the experimental range of rates and they further support the results of Baxter and Stuart [2], which showed that the neutron production rates in Hirsch's experiments [1] were mainly a product of neutral-background fusion interactions.

Referring to the "blue shift" phenomenon [16] presented in chapter 4, it was suggested that large densities of ions were created in the core of the cathode and exit the cathode due to a potential well structure that accelerates ions away from the centre, leading to a majority undergoing charge exchange and exiting the cathode as neutrals. In chapter 4 spectra were reconstructed that support this hypothesis further. In this chapter experimental neutron production rates were explained by using the same concepts. Furthermore, Thorson et al. found that the neutron production rate was independent of the transparency of the cathode for transparencies of 91% to 96% (this was done by varying the cathode wire thickness). If the ions were to converge to the cathode centre and fuse by beam-beam interactions, the fraction of the ions colliding with the surface of the cathode should increase with a decrease in transparency and as a result, the fusion rate should decrease. However, if we consider the suggested hypothesis, there should not be any rate dependence on transparency (in their experimental range); The ions striking the inner cathode surface will deflect, charge exchange and the resulting neutral atoms will still contribute to the total measured rate. The independence of the fusion rate from cathode transparency could also be explained if we consider ions converging to the cathode. These would undergo charge exchange and become neutral atoms that fuse with the background gas. However, this would not account for the high local measured fusion rates in the cathode region, which was reported by Thorson et al.

Thorson et al. also carried out experiments with different cathodes made from stainless steel, titanium and tungsten cathodes. The neutron production rates for the titanium and tungsten cathodes were found to be the same, whereas, there was a small increase in the neutron production rates for the stainless steel cathode. Since the ionization in the cathode core is greatly dependent on the secondary electron production, it is likely that different cathode materials will slightly influence the ion density in the cathode and the depth of the potential well. Considering the suggested hypothesis of diverging ions from the cathode, there should be a slight difference in the neutron production rates for different ion densities that are created in the cathode.

Bibliography

[1] R. L. Hirsch, J. Appl. Phys., **38**, 4522 (1967).

[2] D. C. Baxter and G. W. Stuart, J. Appl. Phys., **53** (7), 4597 (1982).

[3] G. H. Miley, J. Nadler, T. Hochberg, Y. Gu, O. Barnouin and J. Lovberg, Fusion Technol, **19**, 840 (1991).

[4] J. Nadler, G. H. Miley, Y. Gu and T. Hochberg, Fusion Technol, **20**, 850 (1991).

[5] T. A. Thorson, R. D. Durst, R. J. Fonck and A. C. Sontag, Nuclear Fusion, **38** (4), 495 (1998).

[6] D. A. Swanson, B. E. Cherrington and J. T. Verdeyen, Phys. Fluids, **16**, 1939 (1973).

[7] D. A. Swanson, B. E. Cherrington and J. T. Verdeyen, Appl. Phys. Lett., **23**, 125 (1973).

[8] T. J. Dolan, J. T. Verdeyen, D. J. Meeker and B. E. Cherrington, J. Appl. Phys., **43**, 1590 (1972).

[9] J. Khachan, D. Moore and S. Bosi, Phys. of Plasmas, **10** (3), 596 (2003).

[10] T. A. Thorson, R. D. Durst, R. J. Fonck and L. P. Wainwright, Phys. Plasmas, **4** (1), 4 (1997).

[11] S. Børve, H. L. Pécseli, J. Trulsen and S. Longo, Phys. Scr. T122, 125-128 (2006).

[12] O. Shrier, J. Khachan and S. Bosi, J. Phys. A: Math. Gen., **39**, 11119-11128 (2006).

[13] C. F. Barnett, J. A. Ray, E. Ricci, M. I. Wilker, E. W. McDaniel, E. W. Thomas, H. B. Gilbody, Atomic Data for Controlled Fusion Research Volume I., ORNL-5206 (1977).

[14] A. V. Phelps, J.Phys. Chem. Ref. Data, **19** (3), 653 (1990).

[15] G. W. C. Kaye and T. H. Laby, "Tables of Physical and Chemical Constants", (1989).

[16] O. Shrier, J. Chachan, S. Bosi, M. Fitzgerald and N. Evans, Phys. Plasmas, **13**, 012703 (2006).

Chapter 7

ICR Device: Physical Principles and Modelling

In this chapter the physical principles of operation of the ICR device are presented. A two dimensional charge exchange model is developed, extending the charge exchange model that was presented in chapter 3.

7.1 Introduction

Even though the original intention of inertial electrostatic confinement was for energy production, it has mostly been used as a compact neutron source (see chapter 1). In particular, this was found to occur due to energetic neutrals and ions undergoing fusion reactions with the background gas. Consequently, part of the aim of this thesis was to maximize the neutron production rate due to beam-background fusion. In this chapter, a device is presented that resonantly accelerates ions in the background gas using ion cyclotron resonance (ICR device). This device was designed to be an alternative compact neutron source and therefore, the ratio of input to output power is of less concern. However, the efficiency of the neutron production rate was estimated.

IEC devices have produced between $10^6 - 10^8$ n/s for D-D interactions and $2 - 3$ orders of magnitude more neutrons for D-T interactions (see chapters 1, 6). Considering the "ion divergence" phenomenon that was presented in chapter 4, the dominant neutral atoms distribution in the spectrum was suggested to result from ions created at the cathode centre, which diverged out of the cathode via a potential well (see chapters 5, 6). When measured from the cathode centre, the depth of the potential well in the IEC device was found to be in the range of 20% to 60% of the applied cathode voltage (see chapter 4). Consequently, the ions do not gain the maximum possible energy and, therefore, the fusion rate does not reach the maximum theoretical amount. Furthermore, the very high voltages required to reach commercially acceptable neutron rates may result in arcing and melting of the cathode. It has also been suggested that beam-beam interactions (for a solid cathode device) are small in comparison with beam-background interactions [1].

Experimental measurements show that the maximum neutron production rates are achieved at background gas pressures of ~ 3 mTorr (the pressure was not measured in the cathode) [1]. The charge exchange model also predicts an optimum pressure for a maximum neutron production rate but for gas pressures in the order of tens of mTorr in the cathode (depending on the cathode voltage) [2] (see chapters 6). This was found to be a consequence of beam-backround fusion interactions.

The ICR device is a cyclotron that was designed to be a gas target neutron source. This device is expected to accelerate the ions to high energies while applying a relatively small voltage on the electrodes. Moreover, the device can be made compact in size (for a D_2^+ ion energy of 100 keV and a magnetic field of 0.6 T the radius of the device is ~ 15 cm. For the same ion energy and for a magnetic field of 1 T, the radius of the device is ~ 9 cm). Since the targets are cold gas atoms, there is no deterioration of the targets. The aims in this work were to build a prototype of the device and obtain initial energy measurements. A two dimensional charge exchange model was developed and compared with the experimental results. The same model was used to estimate the optimum operating conditions and to calculate the expected fusion rates.

7.2 Physical principles of operation

The ICR device is a cyclotron, which is designed to produce neutrons from fusion interactions of hot neutral atoms with the background gas. The distribution of energetic neutral atom densities is created by charge exchange. The energies of the spiraling ions have a maximum value, which is bounded by the walls of the device or by the physical volume that the magnetic and electric fields occupy (the "active volume").

The charge exchange model (presented in chapter 3) was used to predict energy distributions and estimate the neutron production rates for the ICR device. Since the semi-analytical model requires explicit knowledge of the positions and velocities of the ions, we briefly derive the solutions of the equations of motion for ions in a cyclotron while also presenting the physics involved.

In a cyclotron, an alternating electric field accelerates the ions linearly, whereas an additional magnetic field that is applied perpendicular to the electric field bends the ion trajectory. If the electric field alternates with the ion's velocity component that is parallel to the electric field (resonance condition), the resulting ion motions becomes a spiral.

For a partially ionized plasma that is subject to an alternating electric field $\mathbf{E}$ and a perpendicular constant magnetic field $\mathbf{B}$, the Lorentz equation of motion describing the force working on the ions is,

$$m_j \ddot{\mathbf{r}}_j = e_j \left[\mathbf{E}(\mathbf{r}, t) + \dot{\mathbf{r}}_j \times \mathbf{B}(\mathbf{r}, t)\right] \tag{7.1}$$

where m_j and e_j are the ion mass and charge, respectively. When working with Cartesian coordinates eq. 7.1 can explicitly be written as two equations describing the acceleration of the ion in the $\hat{\mathbf{x}}$ and $\hat{\mathbf{y}}$ directions:

$$\ddot{x} = \alpha\dot{y} \tag{7.2}$$

$$\ddot{y} = \beta\cos(\omega t) - \alpha\dot{x} \tag{7.3}$$

where $\alpha = \frac{e|B|}{m}$, and $\beta = \frac{e|E|}{m}$. Note that **B** is applied in the $\hat{\mathbf{z}}$ direction and **E** alternates along the $\pm\hat{\mathbf{y}}$ direction with a constant angular frequency ω.

Differentiating eq. 7.2 with respect to t and substituting in eq. 7.3 gives:

$$\dddot{x} + \alpha^2\dot{x} = \alpha\beta\cos(\omega t) \tag{7.4}$$

Let

$$z = \dot{x}. \tag{7.5}$$

Equation 7.4 can be written as,

$$\ddot{z} + \alpha^2 z = \gamma\cos(\omega t) \tag{7.6}$$

Equation 7.6 is classified as a non-homogeneous second order differential equation, where $\gamma = \alpha\beta$. The general solution of eq. 7.6 can be constructed from the particular solution of eq. 7.6 and the general solution of the homogeneous equation (the homogeneous equation is the same as eq. 7.6, where the right side is made zero).

The particular solution has the following form:

$$z_s = At\cos(\omega t) + Bt\sin(\omega t) \tag{7.7}$$

Substituting the particular solution into eq. 7.6 results in 4 conditions. From these conditions we derive that $A = 0$, $B = \frac{\beta}{2}$ and $\alpha = \omega$. Substituting these into eq. 7.7, the particular solution becomes:

$$z_s = \frac{\beta}{2}t\sin(\alpha t) \tag{7.8}$$

The general solution of the homogeneous equation takes the form,

$$z_h = C_1\cos(\omega t) + C_2\sin(\omega t) \tag{7.9}$$

and therefore, the general solution of eq. 7.6 is:

$$z = z_h + z_s = C_1\cos(\omega t) + C_2\sin(\omega t) + \frac{\beta}{2}t\sin(\omega t) \tag{7.10}$$

Equation 7.10 describes the component of the ion's velocity in the $\hat{\mathbf{x}}$ direction. Imposing the condition that at $t = 0$ the ion's velocity is, $\dot{x} = 0$, from eq. 7.10 the constant C_1 is found to be: $C_1 = 0$. Differentiating eq. 7.10 results in the ion's acceleration in the $\hat{\mathbf{x}}$ direction:

$$\dot{z} = C_2\omega\cos(\omega t) + \frac{\beta}{2}\sin(\omega t) + \frac{\omega\beta}{2}t\cos(\omega t) \tag{7.11}$$

On resonance the ion's velocity component in the $\hat{\mathbf{y}}$ direction is constantly pointing in the direction of the alternating electric field. From eq. 7.3 it is clear that the electric field is at maximum magnitude when $t = 0$ whereas, the ion's velocity component in the $\hat{\mathbf{y}}$ direction should be zero because its direction of motion reverses at this point. Therefore, from eq. 7.2 it is clear that when $t = 0$ the ion's acceleration in the $\hat{\mathbf{x}}$ direction is zero. From this condition we find that $C_2 = 0$. Inserting, $C_2 = 0$, into eq. 7.10 and changing variables ($z = \dot{x}$), results in the solutions for the ion's velocity in the $\hat{\mathbf{x}}$ direction:

$$\dot{x} = \frac{\beta}{2} t \sin(\alpha t) \tag{7.12}$$

Integrating eq. 7.12 and imposing the condition that at $t = 0$ the ion is positioned at $x = 0$, the solution for the ion's position in the $\hat{\mathbf{x}}$ direction is,

$$x = \frac{\beta}{2\alpha^2} \sin(\alpha t) - \frac{\beta}{2\alpha} t \cos(\alpha t) \tag{7.13}$$

The velocity component in the $\hat{\mathbf{y}}$ direction is derived from eq. 7.2:

$$\dot{y} = \frac{\beta}{2\alpha} \sin(\alpha t) + \frac{\beta}{2} t \cos(\alpha t) \tag{7.14}$$

Integrating eq. 7.14 and imposing the condition that at $t = 0$ the ion is positioned at $y = 0$, the solution for the ion's position in the $\hat{\mathbf{y}}$ direction is,

$$y = \frac{\beta}{2\alpha} t \sin(\alpha t) \tag{7.15}$$

It is clear that the ion motion is spiral, where the sine and cosine functions in eqs. 7.13 and 7.15 are responsible for the back and forth oscillations, and the linearity in t is responsible for the increasing amplitude with respect to time.

Equations 7.12, 7.13, 7.14 and 7.15 are explicit solutions for the ion's path and velocity when subject to the stated physical conditions (additional information is found in references [3–6]). The resonance condition ($\omega = \alpha$) states that the angular frequency of the system is:

$$\omega = \frac{e\,|B|}{m} \tag{7.16}$$

Since the frequency is mass dependent, only a single specie of ions can be accelerated in the device for a given frequency. In this work the more abundant H_2^+ specie was chosen. Considering that the magnetic field in the device was set to 0.6 T, the device was made to operate at a resonant frequency of 4.57 MHz (see eq. 7.16).

In chapter 8 spectroscopic measurements were obtained from the ICR device. The experimental energy distribution of the neutral atoms depends on charge exchange taking place in the active volume of the device. Next, the energy distribution of neutral atoms is modeled for the physical constraints of our device.

7.3 Modelling the energy distribution of neutral atoms

7.3.1 The two dimensional charge exchange problem for spiral motion

The two hollow electrodes of the cyclotron enclosed an active region of 9 cm along the X axis, 9 cm along the Y axis and 0.5 cm along the Z axis, where the constant B field was applied in the Z direction and the alternating E field was applied in the Y direction (these definitions are as in section 7.2. A schematic of the system is presented in Fig. 8.1). The gas in the active volume was partially ionized and the ions spiraled in the X-Y plane. We simulated the physical conditions with a uniform distribution of ion sources placed on a surface perpendicular to the magnetic field and considered the ion motion in this plane (X-Y plane). In this approximation the distribution of ion sources in the entire active volume is restricted to a single X-Y plane and the solution is for all sources of ions spiraling on the surface (the separation of the parallel plates of each of the electrodes was $\sim$ 0.4 cm. This is in the range of the line integration of the emission, where a lens was used to image different regions of the active volume onto the slit of the monochromator). Although the electric field was assumed to act on the ions mostly in the gap between the two electrodes (along a 2 cm gap in the centre of the volume), we simplified the problem and assumed that the field was constantly acting on the ions.

The ions of each source on the surface accelerate in a spiral motion while some of the ions undergo charge exchange and produce new cold ions on the spiral path. The new cold ions (creating new sources) will spiral further and can undergo charge exchange while creating other new sources.

Figure 7.1 illustrates the problem, where the spirals are the plotted solutions of the equations of motion presented in eqs. 7.2 and 7.3. The calculations were carried out for the H_2^+ specie, for a magnetic field $B = 0.3$ T (although the experimental magnetic field was 0.6 T, the ion path-length is $\sim$ 1 m for both cases with a 0.04 m difference between the two path-lengths), for an electric field amplitude $E_{Amp} = \pm 20$ kV/m and for a maximum ion energy of 10 keV.

The figure presents ions spiraling from the centre of the device until they gain maximum energy, which is limited by the radius of the active volume. At the maximum chamber radius the ions hit the walls and neutralize. Otherwise, the ions simply escape to the field free part of the chamber since part of the chamber is outside the magnetic field region. Furthermore, the figure shows one of the newly created densities of ions on the main spiral, where the ions accelerate in a smaller spiral motion which branches off. The branching spiral is smaller since it is restricted by the radius of the active volume. New densities of cold ions will be created along the smaller spiral's path and become new sources for spirals, which will branch off the smaller spiral.

Mathematically there are an infinite number of spirals of various lengths to consider, however, in practice the system is open (ions are lost from the system) and the total density of new cold ions that is created (out of an initial density distribution starting the process) decreases with time and the process can be stopped when the newly created ion density

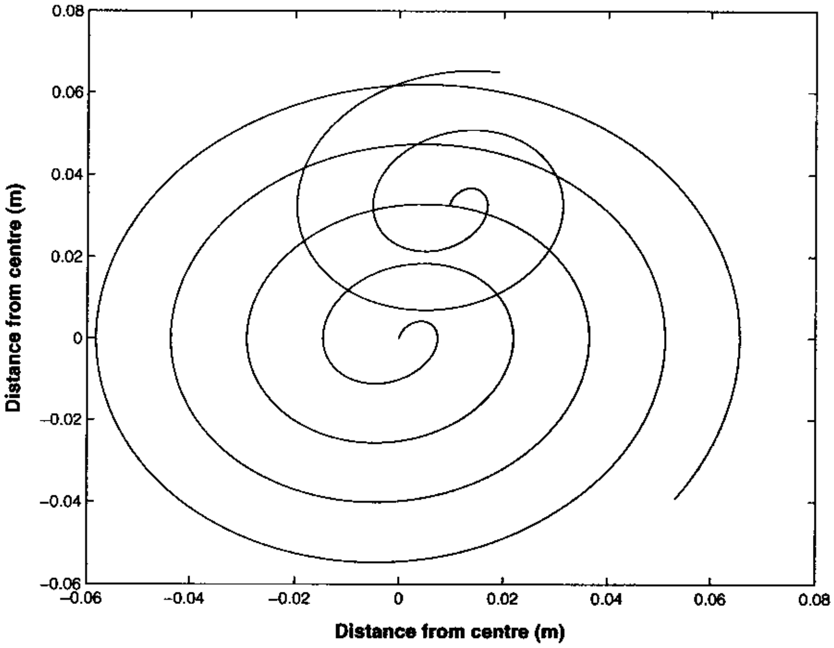

Figure 7.1: The figure illustrates a newly created source of ions branching off from the big spiral to a new smaller spiral.

becomes small in comparison to the initial density starting the process.

7.3.2 Modelling with a grid approximation method

The charge exchange modelling is based on the semi-analytical method presented in chapter 3. In chapter 3 the modelling was carried out for a one dimensional ion motion (along a straight path), where the ion path was divided into small segments. In this two dimensional problem the spiral path is divided into small segments but in addition, the surface is divided into a regular grid of points (see illustration in Fig. 7.2).

Starting with an initial surface ion density distribution $F^1_{i,j}$, each density is positioned on a grid point (i,j is the grid point index). From each grid point the ions accelerate along a spiral path while undergoing charge exchange. Each spiral length is restricted by the radius of the active volume of the device. If there are $T \times T$ grid points, the ions of T^2 densities will spiral to the edge of the active volume. Therefore, each spiral on a grid point will have a total of k^{IJ} segments, where the number of segments depends on the length of the spiral. I and J are equal to the starting values of i and j of a grid point. So I and J keep track of the grid point that an ion started from (k^{IJ} is the number of segments of a spiral path created by ions that started to accelerate from a grid point i, j).

For each spiral the fractions of ions charge exchanging in each segment and their associated energies are calculated with the semi-analytical method presented in chapter 3 (this is the motivation for section 7.2). The computation time was minimized by carrying out the calculation only for the largest spiral (for the density starting at the centre of the device).

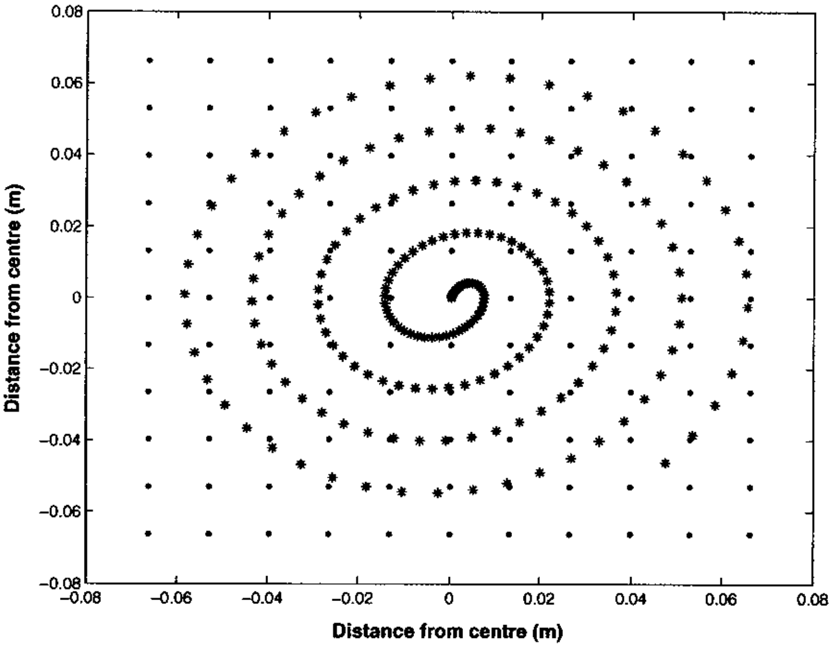

Figure 7.2: An illustration of the grid points (dots) representing the surface of the active cyclotron volume and the spiral motion of the ions from the centre (stars). The number of grid points on the surface and number of segments on the spiral are the two free parameters in the simulations (note that a segment on the spiral extends between two stars).

It was unnecessary to carry out the same calculations for all other spirals since the results would be the same as those of the longest spiral but truncated at a point that depends on the length of the spiral.

A simplifying approximation is made whereby each newly created ion source on each spiral is placed on its closest grid point. This approximation states that new ion densities are created only at grid points, and therefore, new spirals always originate from grid points. It is clear that the approximation improves with increasing number of grid points (see Fig. 7.2).

More formally, an energy cubic matrix $\mathbf{E}^{IJ}$ (a matrix that has a third dimension into and out of the page) is assigned to a spiral starting at a grid point i, j. The ions spiral from this grid point while passing through or close to other grid points on the surface (see Fig. 7.2). Therefore, we can register the energy of the ions accelerating from the beginning of the first segment to the end of the n segment on the spiral as the element $E^{IJ}_{i,j,n}$ in the cubic matrix $\mathbf{E}^{IJ}$, where i, j are the coordinates of the closest grid point to the n segment (note that n is also the index of the third dimension of the cubic matrix). As an example, let us refer to ions spiraling from a grid point positioned at the centre of the device, for 25 grid points (5×5 grid) and for 8 segments on the spiral. The energy cubic matrix $\mathbf{E}^{33}$ can take the form,

$$\mathbf{E}^{33}_{i,j,1} = \begin{bmatrix} 0 & 0 & 0 & 0 & 0 \\ 0 & 0 & 0 & 0 & 0 \\ 0 & 0 & E_{3,3,n=1} & 0 & 0 \\ 0 & 0 & 0 & 0 & 0 \\ 0 & 0 & 0 & 0 & 0 \end{bmatrix}, \mathbf{E}^{33}_{i,j,2} = \begin{bmatrix} 0 & 0 & 0 & 0 & 0 \\ 0 & 0 & 0 & E_{2,4,n=2} & 0 \\ 0 & 0 & 0 & 0 & 0 \\ 0 & 0 & 0 & 0 & 0 \\ 0 & 0 & 0 & 0 & 0 \end{bmatrix}, \tag{7.17}$$

$$\mathbf{E}^{33}_{i,j,3} = \begin{bmatrix} 0 & 0 & 0 & 0 & 0 \\ 0 & 0 & 0 & 0 & 0 \\ 0 & 0 & 0 & 0 & E_{3,5,n=3} \\ 0 & 0 & 0 & 0 & 0 \\ 0 & 0 & 0 & 0 & 0 \end{bmatrix}, \mathbf{E}^{33}_{i,j,4} = \begin{bmatrix} 0 & 0 & 0 & 0 & 0 \\ 0 & 0 & 0 & 0 & 0 \\ 0 & 0 & 0 & 0 & 0 \\ 0 & 0 & 0 & E_{4,4,n=4} & 0 \\ 0 & 0 & 0 & 0 & 0 \end{bmatrix},$$

$$\mathbf{E}^{33}_{i,j,5} = \begin{bmatrix} 0 & 0 & 0 & 0 & 0 \\ 0 & 0 & 0 & 0 & 0 \\ 0 & 0 & 0 & 0 & 0 \\ 0 & E_{4,2,n=5} & 0 & 0 & 0 \\ 0 & 0 & 0 & 0 & 0 \end{bmatrix}, \mathbf{E}^{33}_{i,j,6} = \begin{bmatrix} 0 & 0 & 0 & 0 & 0 \\ 0 & 0 & 0 & 0 & 0 \\ E_{3,1,n=6} & 0 & 0 & 0 & 0 \\ 0 & 0 & 0 & 0 & 0 \\ 0 & 0 & 0 & 0 & 0 \end{bmatrix},$$

$$\mathbf{E}^{33}_{i,j,7} = \begin{bmatrix} 0 & 0 & 0 & 0 & 0 \\ 0 & E_{2,2,n=7} & 0 & 0 & 0 \\ 0 & 0 & 0 & 0 & 0 \\ 0 & 0 & 0 & 0 & 0 \\ 0 & 0 & 0 & 0 & 0 \end{bmatrix}, \mathbf{E}^{33}_{i,j,8} = \begin{bmatrix} 0 & 0 & E_{1,3,n=k^{33}=8} & 0 & 0 \\ 0 & 0 & 0 & 0 & 0 \\ 0 & 0 & 0 & 0 & 0 \\ 0 & 0 & 0 & 0 & 0 \\ 0 & 0 & 0 & 0 & 0 \end{bmatrix}.$$

Referring to the element $E_{2,4,n=2}$, it states that the density of ions charge exchanging in the second segment was found to be placed closest to the $i = 2, j = 4$ grid point and with an energy that was gained while accelerating from the first segment to the end of the second segment. The next element $E_{3,5,n=3}$ suggests that the density of ions charge exchanging in the third segment was found to be placed closest to the $i = 3, j = 5$ grid point and with an energy that was gained while accelerating from the first segment to the end of the third segment. The element $E_{4,4,n=4}$ suggests that the density of ions charge exchanging in the fourth segment was found to be placed closest to the $i = 4, j = 4$ grid point and with an energy that was gained while accelerating from the first segment to the end of the fourth segment etc. If we insert all the non-zero i, j elements of the cubic matrix $\mathbf{E}^{33}$ into a two dimensional matrix, the spiral path of the ions becomes clear,

$$\mathbf{E}'^{33} = \begin{bmatrix} 0 & 0 & E_{1,3,n=k^{33}=8} & 0 & 0 \\ 0 & E_{2,2,n=7} & 0 & E_{2,4,n=2} & 0 \\ E_{3,1,n=6} & 0 & E_{3,3,n=1} & 0 & E_{3,5,n=3} \\ 0 & E_{4,2,n=5} & 0 & E_{4,4n=4} & 0 \\ 0 & 0 & 0 & 0 & 0 \end{bmatrix}. \tag{7.18}$$

Following the index n of the elements in the matrix, starting with $n = 1$ to $n = 8$ (which is also the last k^{33} segment), the ions spiral from the centre outwards.

Each energy element in matrix $\mathbf{E}^{IJ}$ is associated with a fraction of newly created ions in the n'th segment (equivalent to the fraction of ions charge exchanging in the n'th segment). Therefore, the newly created ion density can be inserted into a cubic matrix $\mathbf{P}^{IJ}$, which has the same structure as cubic matrix $\mathbf{E}^{IJ}$. Referring to the same example of the matrix in eq. 7.17, the cubic matrix takes the following form,

$$\begin{aligned}
\mathbf{P}^{33}_{i,j,1} &= \begin{bmatrix} 0 & 0 & 0 & 0 & 0 \\ 0 & 0 & 0 & 0 & 0 \\ 0 & 0 & P_{3,3,n=1} & 0 & 0 \\ 0 & 0 & 0 & 0 & 0 \\ 0 & 0 & 0 & 0 & 0 \end{bmatrix}, \mathbf{P}^{33}_{i,j,2} = \begin{bmatrix} 0 & 0 & 0 & 0 & 0 \\ 0 & 0 & 0 & P_{2,4,n=2} & 0 \\ 0 & 0 & 0 & 0 & 0 \\ 0 & 0 & 0 & 0 & 0 \\ 0 & 0 & 0 & 0 & 0 \end{bmatrix}, \\
\mathbf{P}^{33}_{i,j,3} &= \begin{bmatrix} 0 & 0 & 0 & 0 & 0 \\ 0 & 0 & 0 & 0 & 0 \\ 0 & 0 & 0 & 0 & P_{3,5,n=3} \\ 0 & 0 & 0 & 0 & 0 \\ 0 & 0 & 0 & 0 & 0 \end{bmatrix}, \mathbf{P}^{33}_{i,j,4} = \begin{bmatrix} 0 & 0 & 0 & 0 & 0 \\ 0 & 0 & 0 & 0 & 0 \\ 0 & 0 & 0 & 0 & 0 \\ 0 & 0 & 0 & P_{4,4,n=4} & 0 \\ 0 & 0 & 0 & 0 & 0 \end{bmatrix}, \\
\mathbf{P}^{33}_{i,j,5} &= \begin{bmatrix} 0 & 0 & 0 & 0 & 0 \\ 0 & 0 & 0 & 0 & 0 \\ 0 & 0 & 0 & 0 & 0 \\ 0 & P_{4,2,n=5} & 0 & 0 & 0 \\ 0 & 0 & 0 & 0 & 0 \end{bmatrix}, \mathbf{P}^{33}_{i,j,6} = \begin{bmatrix} 0 & 0 & 0 & 0 & 0 \\ 0 & 0 & 0 & 0 & 0 \\ P_{3,1,n=6} & 0 & 0 & 0 & 0 \\ 0 & 0 & 0 & 0 & 0 \\ 0 & 0 & 0 & 0 & 0 \end{bmatrix}, \\
\mathbf{P}^{33}_{i,j,7} &= \begin{bmatrix} 0 & 0 & 0 & 0 & 0 \\ 0 & P_{2,2,n=7} & 0 & 0 & 0 \\ 0 & 0 & 0 & 0 & 0 \\ 0 & 0 & 0 & 0 & 0 \\ 0 & 0 & 0 & 0 & 0 \end{bmatrix}, \mathbf{P}^{33}_{i,j,8} = \begin{bmatrix} 0 & 0 & P_{1,3,n=k^{33}=8} & 0 & 0 \\ 0 & 0 & 0 & 0 & 0 \\ 0 & 0 & 0 & 0 & 0 \\ 0 & 0 & 0 & 0 & 0 \\ 0 & 0 & 0 & 0 & 0 \end{bmatrix}.
\end{aligned} \tag{7.19}$$

Referring to the element $P_{2,4,n=2}$ that corresponds to the element $E_{2,4,n=2}$, it states that the fraction of ions charge exchanging in the second segment has created the same fraction of cold ions closest to the $i = 2, j = 4$ grid point. The element $P_{3,5,n=3}$ that corresponds to the element $E_{3,5,n=3}$ states that the fraction of ions charge exchanging in the third segment has created the same fraction of cold ions closest to the $i = 3, j = 5$ grid point etc.

There are T^2 cubic matrices $\mathbf{P}^{IJ}$, which hold the information of the fraction of cold ions created at each grid point due to T^2 densities of ions spiraling from each grid point. There are also T^2 cubic matrices $\mathbf{E}^{IJ}$, which hold the information of the energies of the neutral atoms associated with the densities in cubic matrices $\mathbf{P}^{IJ}$. Next, an iterative process takes place. The first generation of cold ions that are created at each grid point is,

$$\mathbf{D}^{IJ1} = F^1_{I,J}\mathbf{P}^{IJ} \tag{7.20}$$

where $F^1_{I,J}$ is the initial surface ion density distribution starting the process and I, J get the values of the indexes i, j respectively. This states that each element $F^1_{I,J}$ in the initial ion sources distribution multiplies the corresponding $\mathbf{P}^{IJ}$ cubic matrix associated with the same grid point. Therefore, T^2 cubic matrices $\mathbf{D}^{IJ1}$ are formed. Before proceeding to the next iteration, we use cubic matrices $\mathbf{D}^{IJ1}$ to find the new surface ion density distribution. This is generated as follows,

$$F^2_{i,j} = \sum^{IJ} \sum_{n=1}^{k^{IJ}} D^{IJ1}_{i,j,n} \tag{7.21}$$

where the inner summation is on the k^{IJ} elements of the i, j coordinate in a cubic matrix $\mathbf{D}^{IJ1}$, and the outer summation is on the resulting element of the first summation for all T^2 cubic matrices $\mathbf{D}^{IJ1}$ (summing the k^{IJ} elements for the i, j coordinate of a cubic matrix, and summing the results of all cubic matrices for the same i, j coordinate).

The newly created distribution $F^2_{i,j}$ is inserted into eq. 7.20 and a new set of $\mathbf{D}^{IJ2}$ cubic matrices is created. Inserting the $\mathbf{D}^{IJ2}$ cubic matrices in eq. 7.21 results in a new generation of a surface ion density distribution $F^3_{i,j}$, which is inserted into eq. 7.20 for the next iteration (this results in the set of $\mathbf{D}^{IJ3}$ cubic matrices). The iteration continues for an S number of generations and is stopped when the total sum of the resulting new ion densities in eq. 7.21 is small in relation to the total sum of the initial ion densities starting the process $(\sum_{j=1}^{T} \sum_{i=1}^{T} F^{S+1}_{i,j} \ll \sum_{j=1}^{T} \sum_{i=1}^{T} F^1_{i,j})$.

The total neutral atoms density distribution for an S number of iterations, having the corresponding energies stated in eq. 7.17, is,

$$\mathbf{G}^{IJ} = \sum^{S} \mathbf{D}^{IJS} \tag{7.22}$$

7.3.3 Programing

The major advantage of the grid approximation method of modelling is that it is relatively easy to compute. However, since it is a two dimensional spatial problem, computer operation time drastically increases in comparison to the programs presented in chapter 3. Figure 7.3 presents the general flow-chart of the program that was constructed to calculate energy distributions and fusion rates for the ICR device. The program was computed in MATLAB.

The inputs (box (1)) for the program include the magnitude of the magnetic field, the electric field amplitude, the maximum possible ion energy (equivalent to the maximum radius of the active volume) and the initial distribution of ion sources on the surface. All other inputs are the same as for the charge exchange programs that were presented in chapter 3. The semi-analytical charge exchange model is used to calculate the fraction of neutral atom densities that are created along the longest spiral (the spiral starting from the centre of the device) and their associated energies (box (2)).

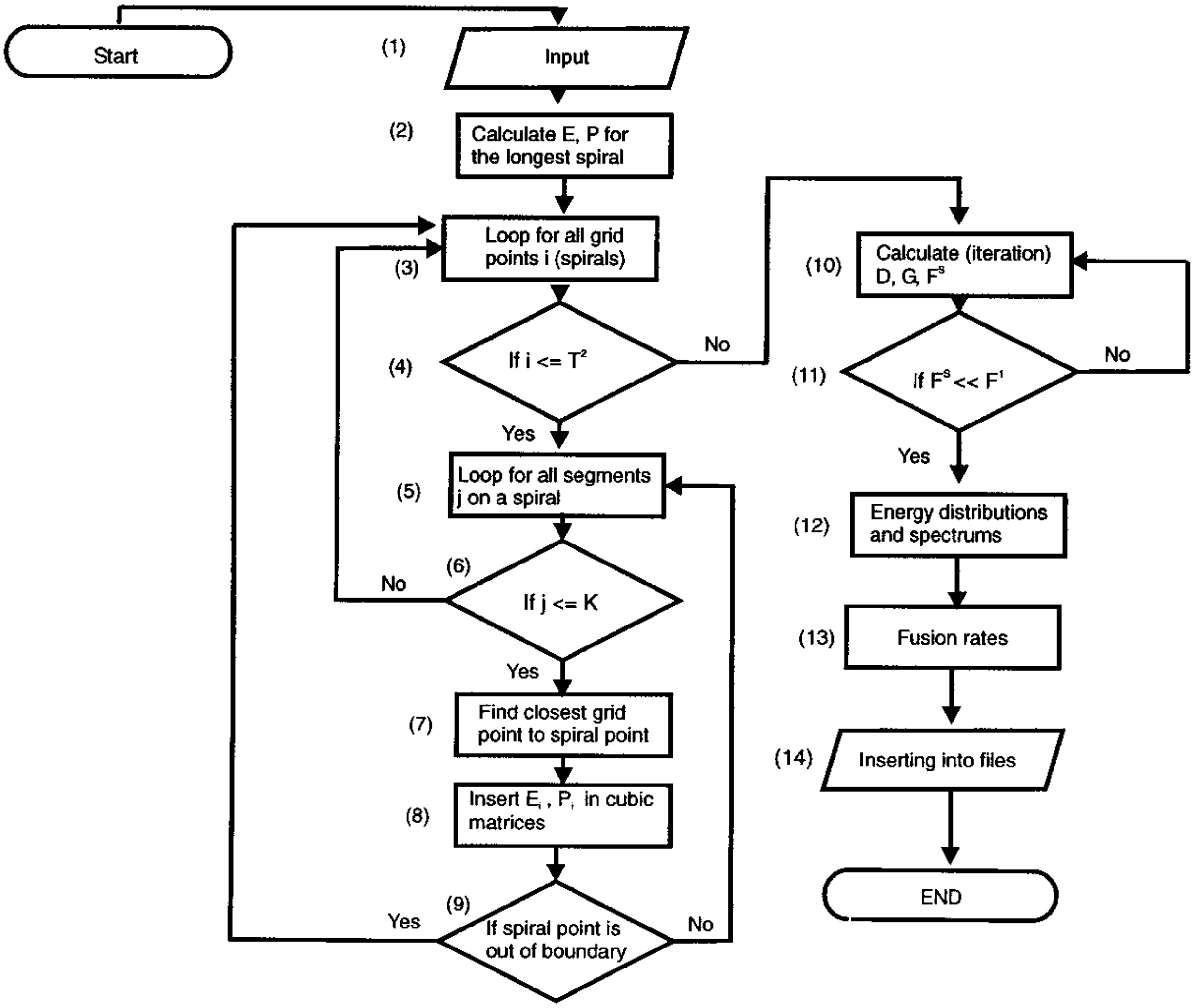

Figure 7.3: The flow-chart of the program that calculates energy distributions and fusion rates in the active volume of the ICR device. The program was computed in MATLAB.

The program loops for all spirals at each grid point and for all segments on each spiral (Boxes (3) and (5)). For each segment of a spiral the closest grid point is found, where the fraction of neutral atoms created in the segment and its associated energy are inserted into two cubic matrices ($\mathbf{P}^{IJ}$ and $\mathbf{E}^{IJ}$) at indexes corresponding to the grid point. This procedure is relatively simple to compute since each spiral is a truncated part of the longest spiral and the information that was calculated in box (2) is sufficient to construct the cubic matrices $\mathbf{E}^{IJ}$ and $\mathbf{P}^{IJ}$ (Boxes (5) to (9)). The cubic matrices $\mathbf{D}^{IJ}$, $\mathbf{G}^{IJ}$ and the next distribution of ion sources $F_{i,j}^{S+1}$ are calculated with eqs. 7.20, 7.21 and 7.22 (box (10)). The program stops the iteration when the total density of the newly created ions is a $q\%$ of the initial total density of ions starting the process (box (11)).

Once the $\mathbf{G}^{IJ}$ cubic matrices were constructed, various energy distributions could be obtained (e.g. the energy distribution along the plane at different points on the plane or the total energy distribution for the entire plane etc.). We refer to boxes (12) and (13) in chapter 8, where the model is used to explain spectrum measurements and to estimate fusion rates.

7.4 Summary

The ICR device is an alternative neutron producing device based on hot neutral and cold gas target fusion interactions. It is a cyclotron, which is designed to accelerate ions in a partially ionized gas to high energies. The distribution of hot neutrals results from densities of ions spiraling in the active volume of the device while undergoing charge exchange and creating more ion sources that further spiral and charge exchange. This process was modeled with a two dimensional charge exchange model, which not only considers segments along the spiral path but also the distribution of ion sources on a surface.

This design has several advantages: it is expected to operate at relatively low voltages, solving the problem of arcing and cathode melting. The ICR device is a compact portable neutron source, where it can accelerate D^+ ions to energies of 100 keV in a radius of ~ 10 cm for a magnetic field of 0.6 T. This corresponds approximately to the maximum fusion cross section for D-T interactions, where the tritium could be the target (see chapter 1). In solid target neutron producing devices there is a deterioration of the target, which is a problem that does not exist in gaseous target systems such as ICR.

Next, spectroscopic measurements of energy distributions of the neutral atoms are presented. These measurements were obtained with an experimental prototype. The model presented in this chapter was used to explain the experimental findings and to predict the efficiency of the device.

Bibliography

[1] T. A. Thorson, R. D. Durst, R. J. Fonck and A. C. Sontag, Nuclear Fusion, **38** (4), 495 (1998).

[2] D. C. Baxter and G. W. Stuart, J. Appl. Phys., **53** (7), 4597 (1982).

[3] T. J. M. Boyd and J. J. Sanderson, "The Physics of Plasmas", Cambridge University Press (2003).

[4] F. F. Chen, "Introduction to Plasma Physics and Controlled Fusion", 2*nd* Ed., Vol. 1. Plenum Press (1984).

[5] W. B. Mann, "The Cyclotron", Printed in Great Britain by Butler & Tanner Ltd., Frome and London (first bublished in 1940).

[6] T. L. Grimm, C. T. Ramsell, and R. C. York, National Superconducting Cyclotron Laboratory, Michigan State University, East Lansing, MI 48824, IEEE (1998).

Chapter 8

ICR Device: Energy Distribution and Fusion Rate Estimates

This chapter opens with a detailed report of the experimental apparatus, which enabled spectrum measurements to be carried out. These are compared with model simulations. Last, fusion rates are estimated with two models: the first is a one dimensional linear potential approximation and the second is a two dimensional grid approximation.

An experimental prototype of the ICR device was built with the aim of verifying the principles of operation and efficiency expectations. Measurements taken with the IEC device (see chapter 6, Fig. 6.4) show that gas target fusion is based on optimum pressures corresponding to maximum neutron production rates. In the ICR device ions are expected to gain high energies, however, for these optimum pressures charge exchange might reduce the energies thus, lowering the fusion rates in comparison with the fusion rates of the IEC device. In this chapter, energy measurements of neutral atoms and their dependence on background gas pressure and applied frequency are presented. In addition, the spatial dependence of the energies was found by obtaining spectra along the accelerating plane (following the definitions in section 7.2, along the Y axis). The "grid approximation" model presented in chapter 7 was used to simulate the experimental conditions. The optimum conditions for neutron production rates were estimated with the "grid approximation" and "linear potential approximation" (presented in chapter 3) models. The advantage of the calculations carried out for the one dimensional model ("linear potential approximation"), is the relatively short computer time required for a large variety of input conditions. Although the two dimensional grid approximation is supposedly a more accurate estimation for the physical process, it requires longer computer times.

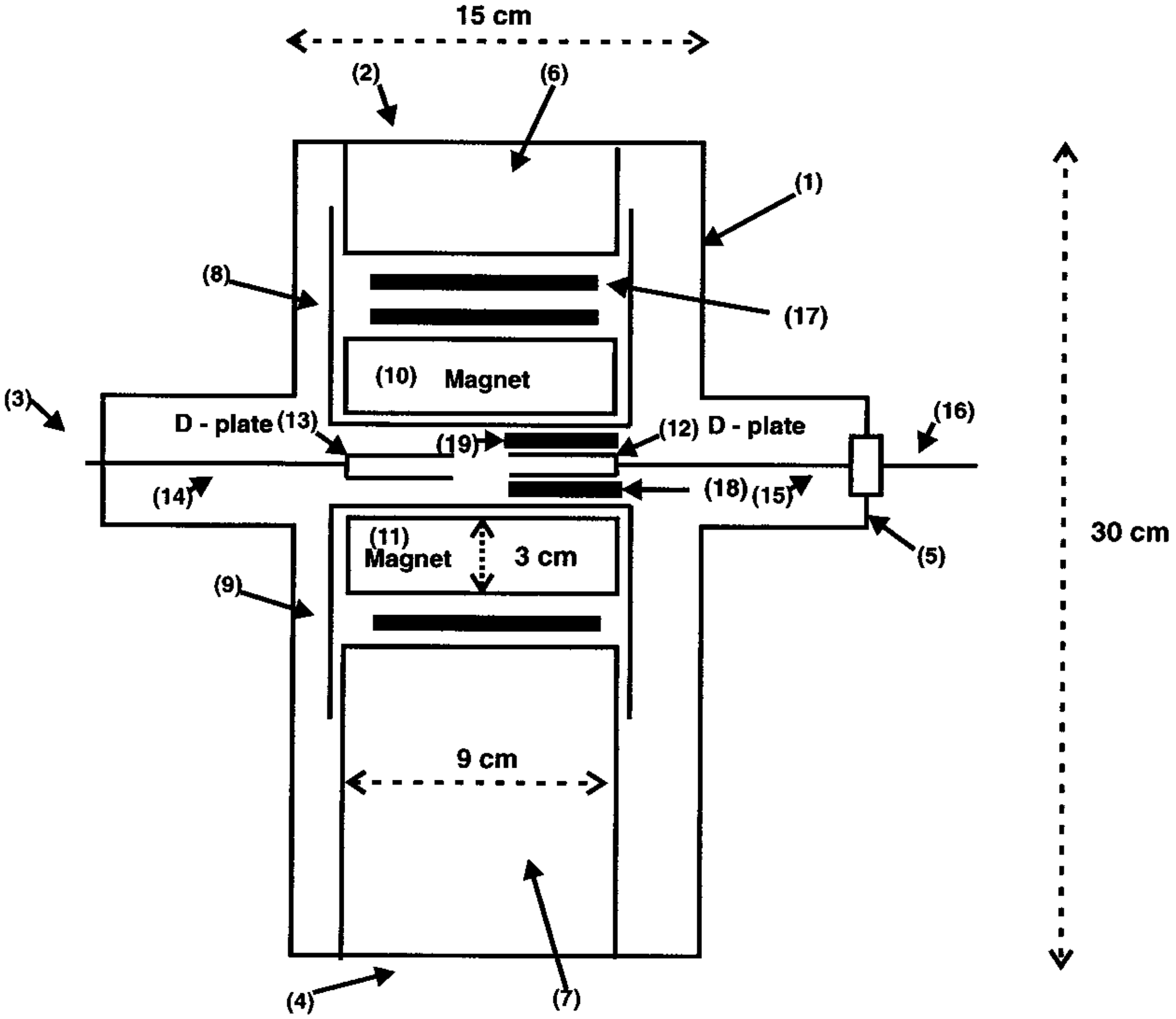

Figure 8.1: A cross section of the ICR device, which cuts through a cylindrical vacuum chamber containing the assembly.

8.1 Prototype and experimental set-up

8.1.1 The vacuum chamber

Figure 8.1 presents a cross-section of the cylindrically vacuum chamber that housed the ICR assembly. Referring to the figure, (1) is the aluminium cylindrical vacuum chamber, which is 30 cm long and has a 15 cm diameter. The chamber had a 15 cm diameter window that enabled emission spectroscopy to be carried out. Parts (2), (3), (4) and (5) are ports with diameters 10 cm, 3.4 cm, 10 cm, and 6.3 cm, respectively.

Two cylindrical Neodymium-Iron-Boron magnets (9 cm diam., 3 cm thick) were designed to fit through the top and bottom ports of the device (labelled (2) and (4)). Each magnet had a surface magnetic field of $\sim$ 0.3 T. The top magnet (part (10)) was held in place with an assembly of cylinders shown as parts (6) and (8). Part (6) is an aluminium cylinder, which is also used as the lid of the top port. Part (8) is a hollow aluminium cylinder cap, which screws on to part (6). The magnet rests in the cylindrical cap, where it is possible to raise and lower the magnet by screwing the cylinder cap. In order to keep the magnet firmly in place aluminium slabs were placed in the space between the magnet and the full cylinder (part (17)). A small hole was made in the hollow cylindrical cap for evacuation. This same arrangement was used for the bottom magnet (part (11)), where part (7) is the full aluminium cylinder and part (9) is the hollow aluminium cylindrical cap.

Since the magnetic field has to be relatively uniform, it is necessary to have the magnets placed as close as possible to one another. However, the distance between the magnets is limited by the thickness of the cylindrical casing (0.5 cm) and the width of the electrodes (the width of the active volume was 0.4 cm). A gap of 0.2 cm was left between the electrodes and cylinders so that the active electrode did not short to earth. Two slabs of ceramics of 0.2 cm thickness each were inserted in the gap (these are parts (18) and (19)). This set ~ 2 cm minimum limit on the distance between the magnets.

The two "D's" (parts (13) and (12)) were designed to be two rectangular boxes, each closed from three sides. The separation of the larger surfaces (D-plates) of the box was made 0.4 cm, where each surface was made 9 cm long and 3.5 cm wide. The alternating electric field was assumed to be uniform in the gap between the two electrodes. However, sheath effects change the uniformity of the applied electric field and the field also "leaks" into the inner volume of the electrodes [1]. This can affect the resonance condition and the ion energy distribution. Therefore, the accelerating gap between the two electrodes was made relatively small (~ 2 cm). The active volume is a short cylinder formed between the D-plates and magnet area, which is $\pi \times 9^2 \times 0.4$ cm^3. The electrodes were held by posts that were connected to the side ports (parts (14) and (15) in the figure). The posts could be shortened or lengthened for fine adjustment. One electrode was grounded to the chamber, while the other was connected to an RF source through an impedance matching box (the RF feed through is part (16) in the figure).

Any $\mathbf{E} \times \mathbf{B}$ drifts in the device were ignored since we were only interested in neutron production and not confinement, which is needed for energy generation [2,3].

8.1.2 The apparatus

Figure 8.2 presents the apparatus that was used to obtain spectroscopic measurements. The signal from an RF generator (Trio-Kenwood, SG-402) was amplified with a linear amplifier (Kenwood TL-922) and an RF power amplifier (ENI 3100L) connected in series. Although this allowed a power transfer of ~ 100 W, the power was limited to 50 W by arcing, mainly in the matching box, but was sufficient to produce energetic ions and neutrals, as will be seen by the Doppler spectrum. The matching box was built in-house with only 5% of reflected power. Although the match was carried out for 4.57 MHz, it was possible to operate the device in the range of $4.5 - 5$ MHz.

The gas pressure was regulated with a mass flow controller. A rotary pump and a

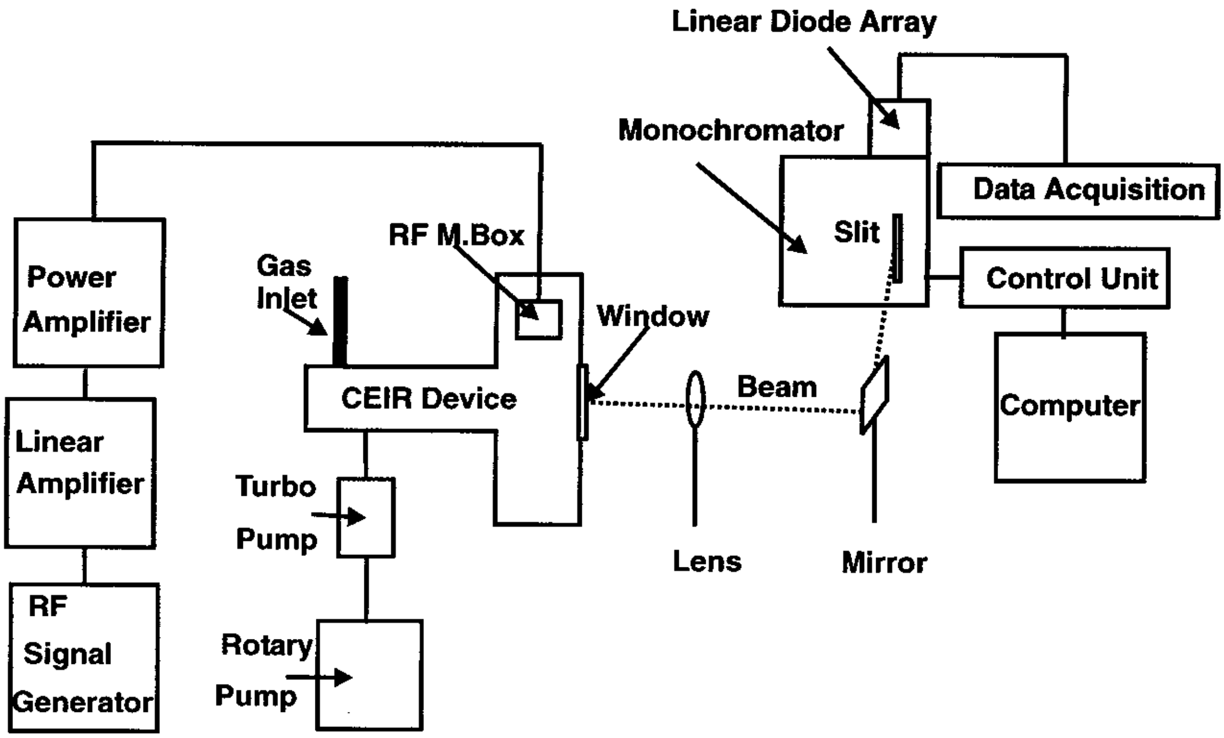

Figure 8.2: Schematic of the experimental apparatus that was used to obtain spectroscopic measurements. Note that the active volume shown in Fig. 8.1 is exposed to the monochromator through the window, where a line integration of emission is collected as seen in Fig. 8.4.

turbomolecular pump (170 l/s) were used. Considering the relatively small volume of the vacuum chamber, this enabled a base pressure well below 1 mTorr to be reached. However, at 50 W the breakdown of the plasma was found to occur for pressures higher than $\sim$ 25 mTorr and in the steady state it was possible to lower the pressure to a minimum of $\sim$ 10 mTorr. For pressures lower than 10 mTorr the plasma switched off.

A linear diode array (Princeton Applied Research 1421G linear diode array (LDA)) was mounted on a 0.5 m focal length monochromator (Spex 500M), having a resolution of $\sim$ 0.04 nm. The pixels of the detector had a wavelength spacing of 0.015 nm.

The hydrogen plasma produced in the apparatus was found to be most intense near the active electrode. Nevertheless, there was also a discharge throughout the active volume. The position from which the spectra were obtained was located by using a glass lens to project a real image of the regions of interest onto the entrance slit of the monochromator. Spectra were obtained for the hydrogen H_α line.

8.2 Spectrum measurements

8.2.1 Energy distribution and resonance

In this section we present measurements of Doppler shift distributions of neutral atoms resulting from H_2^+ charge exchange, which are compared to the results of the model.

Figure 8.3 presents spectra obtained at 20 mTorr and power input of 50 W. The spectra in plot A were normalized with respect to their base broadening, whereas in plot B the same spectra were normalized with respect to the unshifted peak and were shifted upwards in relation to one another. Since greater energies are expected to be found further away from the centre of the active volume, the spectra were obtained closer to the edge of the active volume.

Although the theoretical resonance condition for the motion of a single particle in a cyclotron was found to be 4.57 MHz, the behavior of a relatively dense and partially ionized gas might differ. The tunable RF matching box allowed an operating range between 4.5 and 5 MHz. Figure 8.3 shows 4 spectra for 4.5, 4.57, 4.6 and 5 MHz. It is clear that there is no significant differences in the spectrum shape between 4.5 and 4.6 MHz.

The Doppler shift is asymmetric around the unshifted peak and shows a maximum wavelength shift of $\sim$ 9 Å (this is for the blue-shifted motion and is equivalent to $\sim$ 1 keV for the charge exchanging H_2^+ ion). The root mean square voltage between the electrodes can be roughly estimated assuming that $P = \frac{V^2}{R}$, $R = 50\ \Omega$ and $P = 50$ W, which results in $\sim$ 50 V. Therefore, the maximum voltage is estimated to be $\sqrt{2} \times 50 \simeq 70$ V. In order to gain a maximum energy of $\sim$ 1 keV in the IEC device, it was necessary to bias the cathode with ~ -4 kV. The cathode current for this voltage and for a pressure of 20 mTorr is $\sim 6-8$ mA. This suggests that $\sim 25-30$ W were invested for an energy gain of $\sim$ 1 keV. It is clear that the ICR device can accelerate ions to the same energies with significantly lower voltages however, it requires nearly twice the power that the IEC device requires. Note that this does

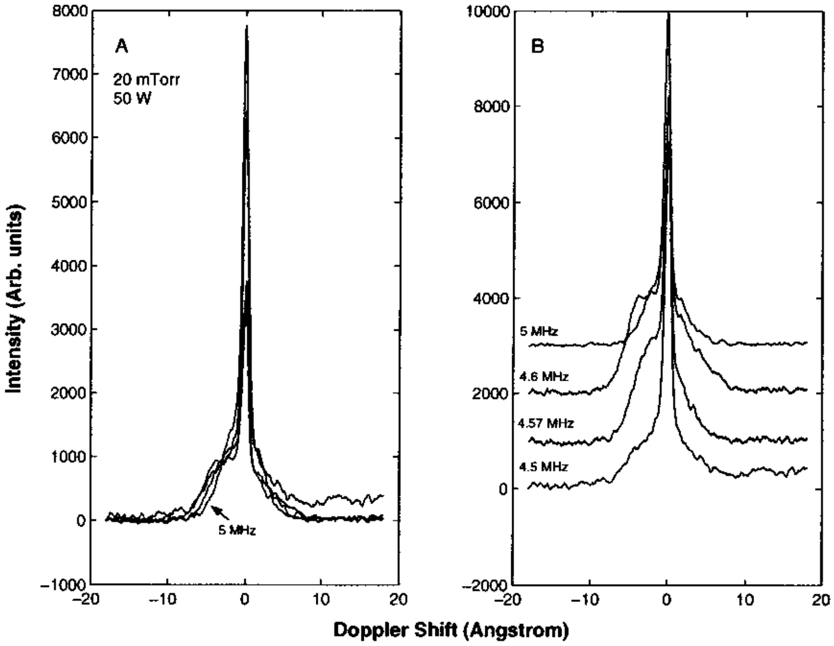

Figure 8.3: Spectra obtained at 20 mTorr, for a power input of 50 W and for 4.5, 4.57, 4.6 and 5 MHz. In plot A the spectra are normalized with respect to their base broadening and in plot B they are normalized with respect to the unshifted peak and are lifted upwards in relation to one another.

not take into account the density in the ICR device, which may have been greater than that of IEC.

Since the spectroscopy was carried out near the edge of the active volume (see Fig. 8.4), the energies in the spectrum should include components of the most energetic neutrals (the vector "v" in Fig. 8.4 is the velocity of a neutral atom that was created at the base of the arrow). The spectra in Fig 8.3 show that the intensity declines with increasing energies. The intensity of the distributions resulting from the IEC device peaked at maximum energies. Nevertheless, the distribution in Fig 8.3 is broad and the tail of the distribution might still be sufficient to produce significant fusion rates relative to the IEC device.

8.2.2 Energy distribution along the active volume and pressure dependence

Measurements along the plane axis (defined in Fig. 8.4) were taken, starting from the edge of the active volume to the centre of the device in intervals of ~ 1 cm. The measurements were taken for the grounded electrode.

Figure 8.5 presents 5 spectra obtained at a pressure of 20 mTorr, for a power input of 40 W, at 4.57 MHz and for distances of 0, 1, 2, 3, 4 cm, measured from the centre of the active volume. The spectra in plot A were normalized with respect to their base broadening, whereas in plot B the same spectra were normalized with respect to the unshifted peak and

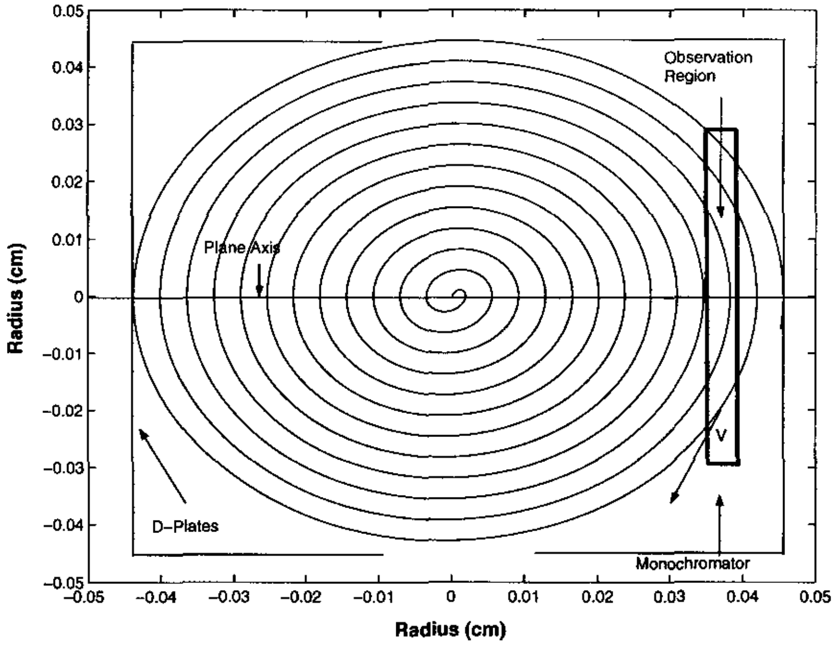

Figure 8.4: A schematic of the observed plane of spiraling ions. The rectangular region shown is focussed onto the slit of the monochromator. This region moves as the lens scans along the plane axis.

were lifted upwards in relation to one another.

Clearly the broadened bases of the spectra overlap, showing the same spectral line shape. This suggests that the spiraling ion sources are distributed in the entire active volume or equivalently, the gas is ionized in the entire active volume. The shorter spirals are much more numerous than longer ones (the long spirals result from the density in the centre where the shorter spirals result from all other sources in the volume) and therefore, the intensity of the lower energies is enhanced and is approximately the same all over the device. Moreover, the charge exchange significantly reduces the energies. For the same experimental conditions but in vacuum, an H_2^+ ion should gain an energy of 18 keV where the maximum energy in the spectrum is $\sim 5\%$ of that energy. The experimental result shown in Fig. 8.5 implies that the neutron production rate will be uniformly distributed in the active volume (neglecting the edge of the active volume).

It is evident that the spectrum is asymmetric around the unshifted peak. That is, the red-shifted side drops faster than the blue-shifted side of the spectrum (this will be further discussed in section 8.3). Note that the IEC spectra were also found to be asymmetric ("blue shift" phenomenon, chapter 3) but for different reasons. In both cases we are concerned with the more energetic distribution in the spectrum, since that is an optimal measure of the efficiency of the devices.

Figure 8.6 presents 3 spectra obtained for an input power of 40 W, for a frequency of 4.57 MHz and pressures of 10, 20 and 47 mTorr. The spectra in plot A were normalized

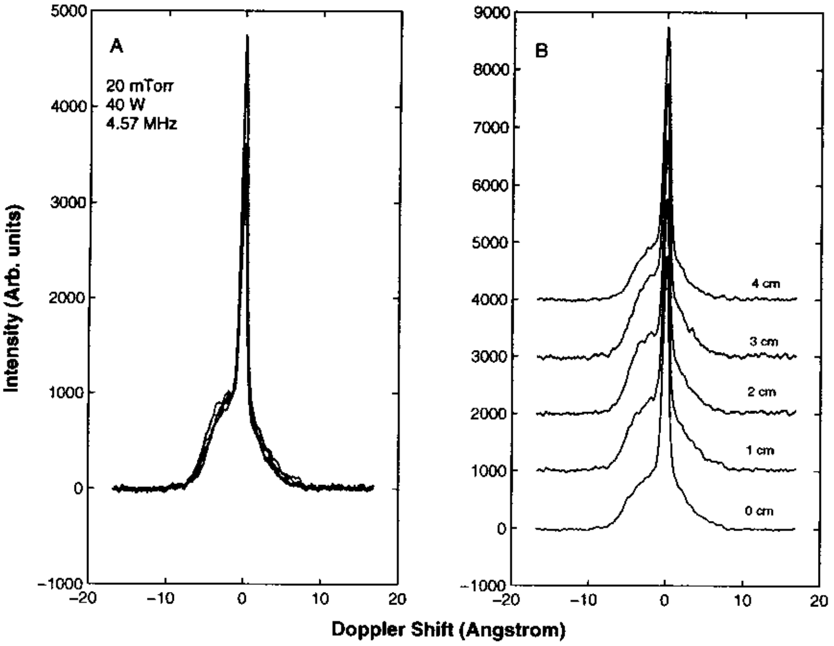

Figure 8.5: Spectra obtained for distances of 0, 1, 2, 3 and 4 cm, measured from the centre of the active volume. The pressure was 20 mTorr, where the power input was 40 W at 4.57 MHz. In plot A the spectra are normalized with respect to their base broadening and in plot B they are normalized with respect to the unshifted peak and are lifted upwards in relation to one another.

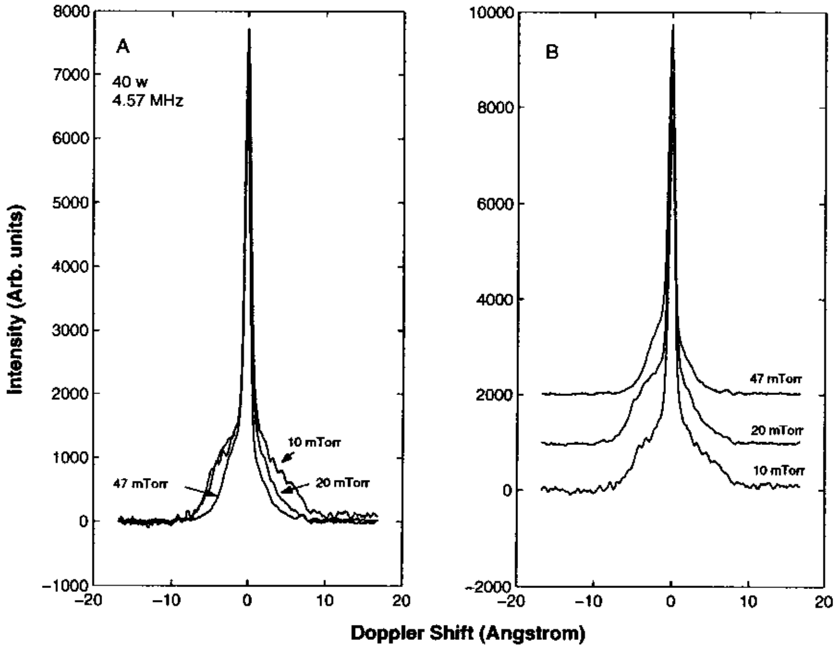

Figure 8.6: Spectra obtained for pressures of 10, 20 and 47 mTorr. The input power was 40 W at 4.57 MHz. In plot A the spectra are normalized with respect to their base broadening and in plot B they are normalized with respect to the unshifted peak and are lifted upwards in relation to one another.

with respect to their base broadening, whereas in plot B the same spectra were normalized with respect to the unshifted peak and were lifted upwards in relation to one another. It is clear that the blue shifted side of the spectrum does not change for the 10 and 20 mTorr measurements, however, the 10 mTorr spectrum is more symmetric around the unshifted peak. The distribution drops for the 47 mTorr measurement. This implies that the energy distribution does depend on pressure. At relatively high pressures, charge exchange becomes dominant and the energies are reduced. This is expected to lower the neutron production rates.

8.3 Simulations of the model for the energy distributions

The model and program described in chapter 7 were used to estimate energy distributions in the range of the experimental conditions (box (12) in Fig. 7.3). The spectra were obtained from a line integrated emission, while scanning transverse to the plane axis (see illustration in Fig. 8.4). Therefore, in each region of observation (see rectangle in Fig. 8.4) only the components of velocities that are perpendicular to the plane axis are registered as Doppler shifts in the spectra. The program was made to calculate these velocity components along the line integral. Moreover, a simplifying assumption was made, where a region of observation is equivalent to a column of grid points (perpendicular to the plane axis). The total energy

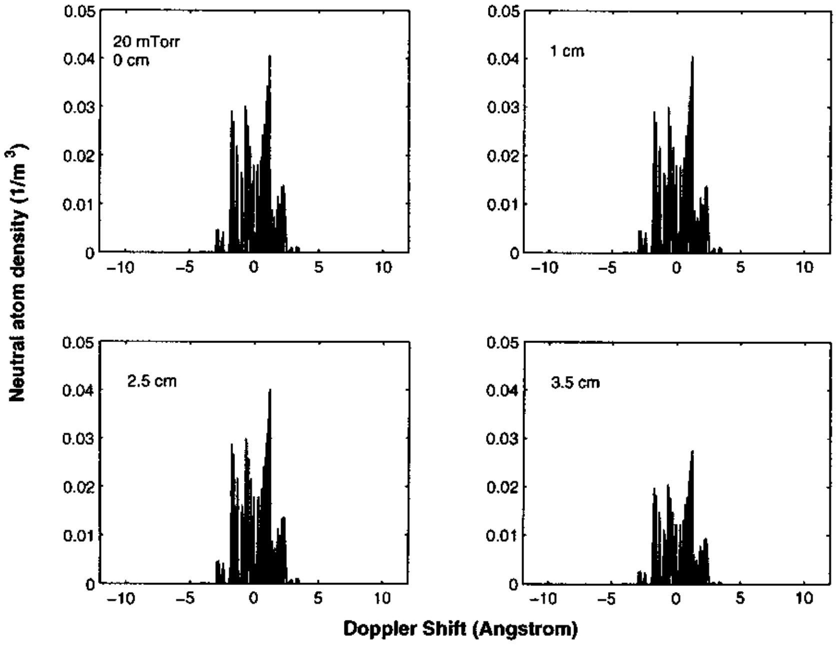

Figure 8.7: Results for the simulations for distances of 0, 1, 2.5 and 3.5 cm, from the centre of the active volume (the distances are marked in the figure). The input peak voltage was set to 100 V (for a 2 cm separation of the electrodes) at a pressure of 20 mTorr.

distribution was calculated by summing the densities of the distributions (created at each grid point of the column), which have the same energy. Neutral atoms that enter the observation region from outside the region of observation, were ignored.

A spatially uniform initial ion density distribution, spread throughout the active volume, was used in the simulations. Each source was placed at each grid point on the surface (the densities were normalized). The calculations were for 81 grid points and ~ 550 segments (this is for the largest spiral). The maximum possible ion energy was set to 18 keV, which for a magnetic field of 0.6 T corresponds to the radius of the active volume (4.5 cm). The program was made to stop when the total sum of the newly created ions was 1% of the total fraction of ions starting the process.

8.3.1 Energy distribution dependence on position along the surface and the estimated spectrum line shape

Figure 8.7 presents the results from the simulation for an input peak voltage of 100 V (for a 2 cm separation of the electrodes), for a pressures of 20 mTorr and distances of 0, 1, 2.5 and 3.5 cm from the centre of the active volume.

The initial ion sources distribution is not continuous on the surface (the sources are placed on the grid points), which is partially the reason for the non-smooth spectrum shown in the figure. However, the average difference of the wavelength shifts in the figure is ~ 0.1 Å, which is smaller than the monochromator resolution. It is possible to reconstruct a spectrum

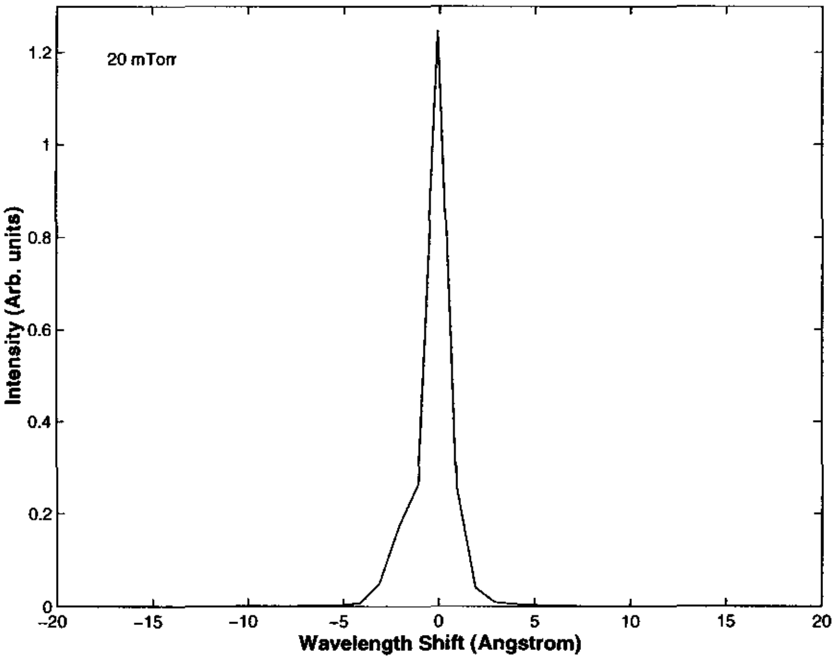

Figure 8.8: A spectrum reconstruction using the results of the upper left plot of Fig. 8.7, where the Doppler shifts were placed in bins with a width that was twice the resolution of the monochromator (0.8 Å). A Lorentzian with a half-width of 0.5 Å was superimposed, representing the unshifted peak.

by binning the wavelength shifts and adding a Lorentzian to represent the unshifted peak. Figure 8.8 presents the results of the simulation for the upper left plot of Fig 8.7, where the Doppler shifts were placed in bins with a width that was twice the resolution of the monochromator (0.8 Å) and a Lorentzian with a half-width of 0.5 Å was superimposed.

Clearly the reconstructed line shape agrees with the experimental line shape presented in Fig. 8.5. In particular, the reconstruction predicts the asymmetry around the zero unshited peak. However, there is a discrepancy in the maximum energy range, where the maximum energy predicted by the model is a factor of $\sim$ 0.5 of the maximum energy in the spectrum. This can be explained if the electric field between the electrodes was greater than estimated. Nevertheless, the model can be used to predict lower limits of energies, and therefore, lower limits of neutron production rates (the rate calculations are shown in section 8.5).

The shapes of the distributions in Fig. 8.7 are the same for all positions along the device, implying that there is no spatial dependence. This agrees with the experimental findings presented in Fig. 8.5. The calculations for 10 and 45 mTorr showed the same spatial independence (not presented here).

8.3.2 Energy distribution dependence on pressure and voltage

Figure 8.9 presents the results from the simulation for an input peak voltage of 100 V and pressures of 1, 10, 20 and 45 mTorr (since the energy distribution was found to be spatially

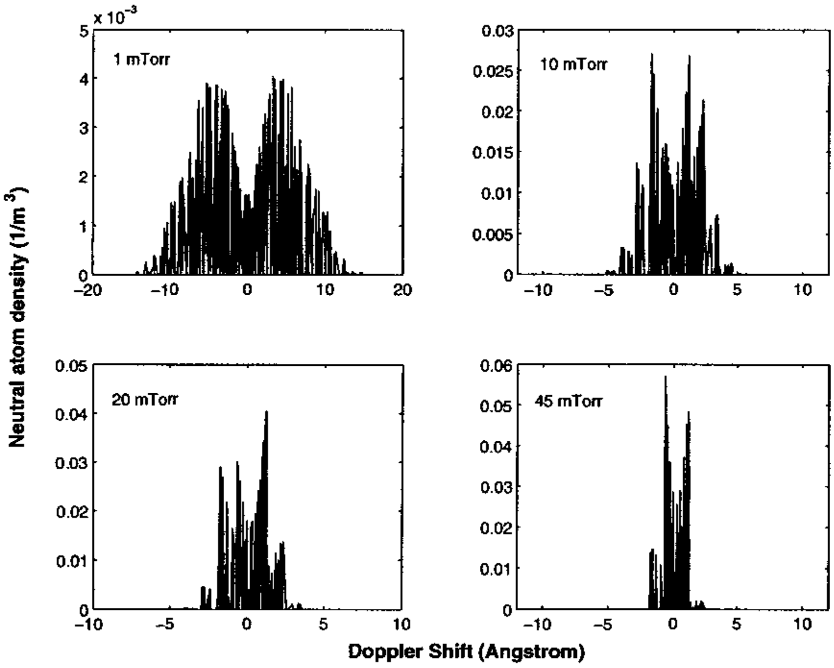

Figure 8.9: Results from the simulations for pressures of 1, 10, 20 and 45 mTorr. The input peak voltage was set to a 100 V and the calculations were done for the column of grid points at the centre of the device.

independent, the column of grid points at the centre of the device was arbitrarily chosen for the calculations).

The reconstructed spectral line shape for the 20 mTorr pressure in Fig. 8.8 (lower left plot in Figure 8.9) was shown to agree with the experimental results that were presented in Fig. 8.6. The results from the simulation for a pressure of 45 mTorr (lower right plot in Fig. 8.9) show that the distribution has shifted closer to the unshifted peak and is also asymmetric around the unshifted peak. The results of the simulation for a pressure of 10 mTorr (upper right plot in Fig. 8.9) show that the distribution has shifted further away from the unshifted peak and is nearly symmetric around the unshifted peak. These results agree with the experimental results presented in Fig. 8.6. Placing the Doppler shifts of the 45 and 10 mTorr distributions in bins, with width twice the resolution of the monochromator, and superimposing a Lorentzian with a half-width of 0.5 Å results in the reconstructed spectra shown in Figs. 8.10 and 8.11, respectively. The left plots in the figures show the simulation results, whereas the right plots show the experimental results presented in Fig. 8.6.

The simulations show similar spectral line shapes to the experimental line shapes, however, the maximum energy predicted by the model is a factor of ~ 0.5 of the maximum energy in the spectra. Generally, Fig. 8.9 predicts that with a decrease in pressure the energy distribution broadens and becomes more symmetric around the unshifted peak, which largely agrees with the experimental results.

Although the dependence of the energy distribution on voltage was not measured (the

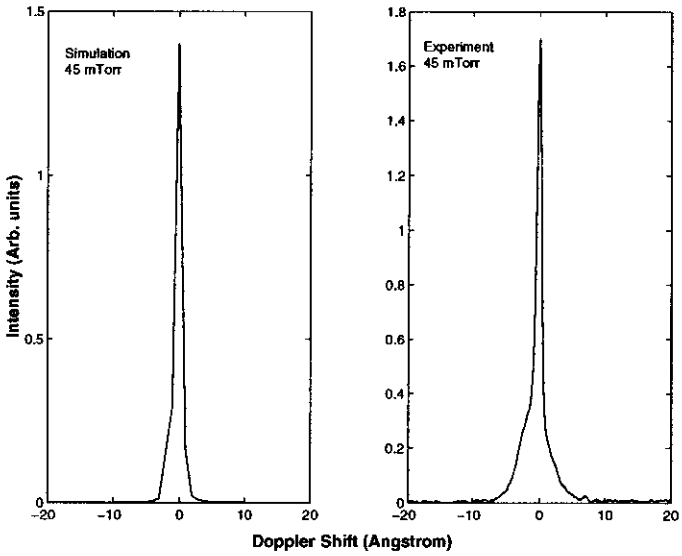

Figure 8.10: The left plot is a reconstruction of the spectrum in the right plot that was presented in Fig. 8.6. For the reconstruction the Doppler shifts of the 45 mTorr distribution in Fig. 8.9 were placed in bins with a width that was twice the resolution of the monochromator (0.8 Å). A Lorentzian with a half-width of 0.5 Å was superimposed, representing the unshifted peak.

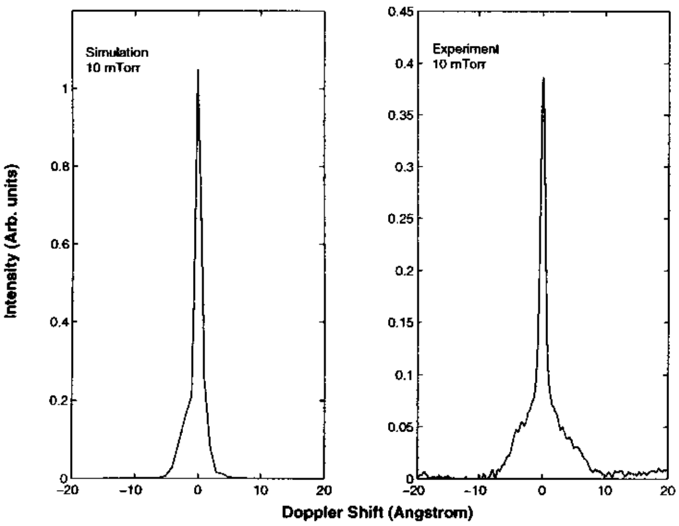

Figure 8.11: The left plot is a reconstruction of the spectrum in the right plot that was presented in Fig. 8.6. For the reconstruction the Doppler shifts of the 10 mTorr distribution in Fig. 8.9 were placed in bins with a width that was twice the resolution of the monochromator (0.8 Å). A Lorentzian with a half-width of 0.5 Å was superimposed, representing the unshifted peak.

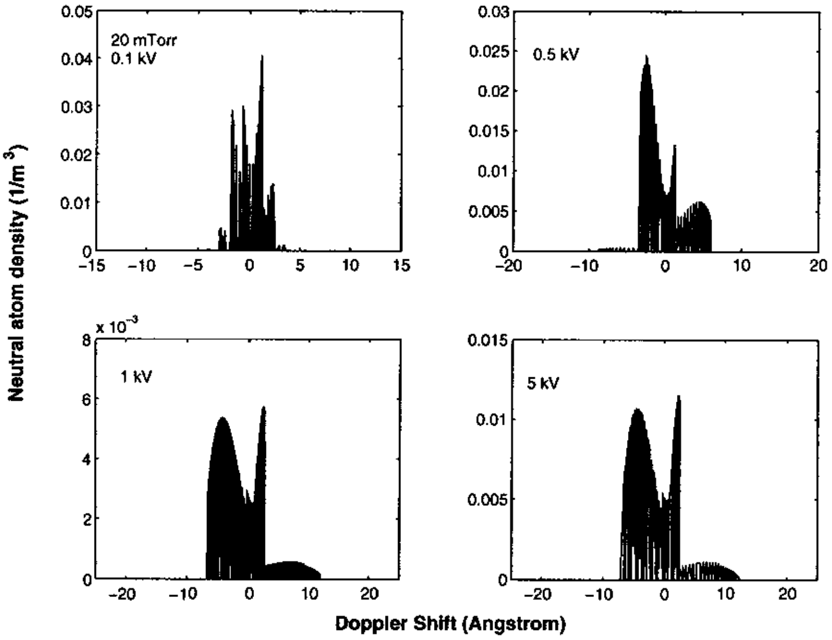

Figure 8.12: Predictions from the simulations of the variation in the energy distribution for voltage amplitudes of 0.1, 0.5, 1 and 5 kV (marked in the figure). The pressure was 20 mTorr.

device was made to operate at a maximum input power of 50 W, limiting the voltage between the electrodes to a few tens of volts), the predictions from the simulation for the variation in the energy distribution for different voltages is presented in Fig. 8.12. The calculation was for a pressure of 20 mTorr and voltage amplitudes of 0.1, 0.5, 1 and 5 kV. The distributions show a broadening of both the blue-shifted and red-shifted sides with increasing voltage. However, the distributions of the 1 and 5 kV calculations are similar in shape, which might suggests that in this range the energy distribution does not change much.

The ICR device allows a maximum ion energy of 18 keV. Figure 8.13 presents the simulation results for an input voltage of 500 V and for a pressures of 20 mTorr, where it is evident that the distribution extends in this range of energies. The densities for the Doppler shifts in the range of 10 – 28 Å (equivalent to 1 – 18 keV for the H_2^+ charge exchanging ion) were summed and stated in the figure. The total density is found to be 2 – 3 orders of magnitude smaller than the densities in the 0 – 1 keV range. However, since the fusion rates are energy dependent, these densities might significantly contribute to the neutron production rates.

8.4 Fusion rate estimates: a one dimensional linear potential approximation

The two dimensional physical process taking place in the ICR device was simulated as a one dimensional problem, where the largest spiral was stretched to become a straight line and the electric field was estimated to be the half-cycle average of the alternating field. This allowed

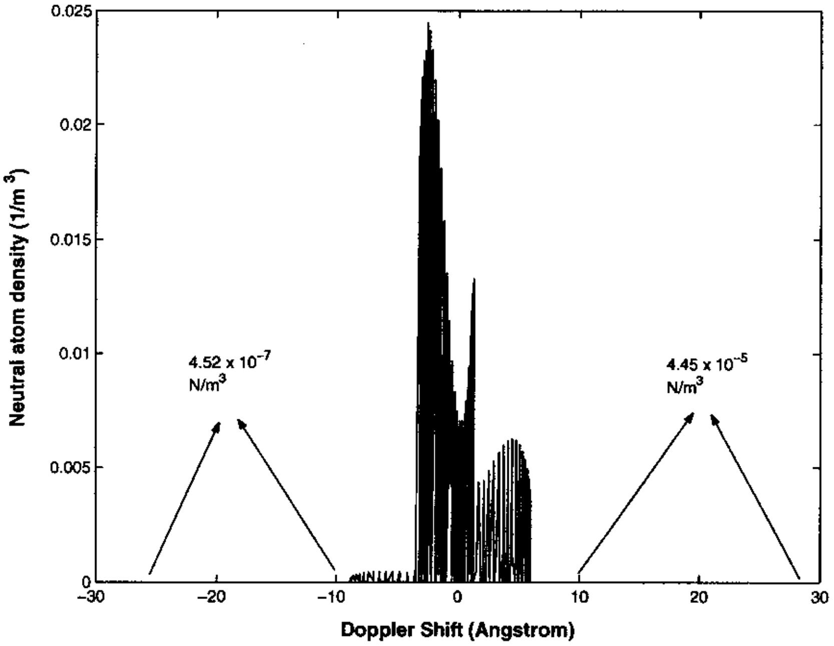

Figure 8.13: Simulation results for an input peak voltage of 500 V and for a pressures of 20 mTorr. The densities in the Doppler shift range of 10 – 28 Å (equivalent to 1 – 18 keV) were summed and are stated in the figure (the base of the arrows bound the 10 – 28 Å range, where the arrows point to the total density in this range).

for the use of the linear potential model (presented in chapter 3) to calculate the neutral atom energy distribution. The initial ion sources that were placed on the grid points (in the two dimensional case) were estimated with an initial uniform distribution of ion sources placed at the beginning of each segment along the stretched spiral. The expected neutral atom energy distributions for the three H^+, H_2^+ and H_3^+species are shown in Fig. 4.11. The main advantage of this approximation is the large number of calculations for many different physical conditions that could be processed in a relatively short computer operating time.

8.4.1 Programing

The calculations presented in this chapter were carried out using the H_2 charge exchange program presented in chapter 3 for the linear potential case. The program was modified to account for the D_2 mass and charge exchange cross sections. An additional section was added to calculate the fusion rates (see section 6.2). The variable inputs of the program were the maximum ion energy (which is restricted by the radius of the device), the accelerating electric field, the fraction of gas ionization and the gas pressure (the program was made to loop for various values of each of these inputs).

In the IEC device the ions accelerate along a path of few cm between the anode and cathode, whereas, in the ICR device the ions accelerate along a path of meters and tens of meters. The results of the calculations depend on the size of the segments, which have to be made small enough for the results to converge. For a longer ion path there are more segments and the computer processing time increases exponentially (a "long path" is in the order of meters). This problem was partially solved by having the program find the place along the path where the newly created densities of ion sources were insignificant in comparison to the initial density of ions. The program calculated the density and energy distributions to that point along the path (this is a minimum limit for the neutron production rate estimations).

However, for a combination of low pressures, small electric fields and large maximum ion energies, charge exchange is significant along large distances and relatively long segments have to be chosen. The program was made to account for the error in the average energy resulting from the chosen segment size. For the error calculation an extrapolation error function was estimated to be,

$$U_i^{error} = f_{(p)} a_{(E)} e^{-b_{(E)} k_i} \tag{8.1}$$

where the function f is pressure dependent, the constants $a_{(E)}$ and $b_{(E)}$ are electric field dependent, and k is the ratio of the sufficient segment size to the chosen segment size. The sufficient segment size was estimated to be $\sim \frac{1}{1000}$ m (note that the error becomes smaller as the chosen segment size approaches the sufficient segment size). The evaluation of the constants $a_{(E)}$ and $b_{(E)}$ and the function $f_{(p)}$ was carried out by fitting the error function to experimental data. Specifically, the pressure was varied for each value of the electric field, and the k parameter was varied for each pressure. An experimental error was calculated using,

$$U_i^{error} = \frac{\overline{U}_{k=1} - \overline{U}_{k_i}}{\overline{U}_{k=1}} \tag{8.2}$$

where $\overline{U}_{k=1}$ is the average energy of all segments for each calculation with $k = 1$ and $\overline{U}_{k_i}$ is the average energy of all segments for the same calculation conditions but for various k_i. Inserting the results of the calculated error and the input conditions for k and p (pressure) into eq. 8.1 enabled $f_{(p)}$, a and b to be found for each value of electric field (the function $f_{(p)}$ was found to be $f = p$ for all electric field values). This experimental error approximation does not hold for $k = 1$ (where the error is zero) and was used in the program only for cases where $k < 1$.

The fusion rate was calculated while following a similar procedure to that described in section 6.2, where eq.6.2 was used.

8.4.2 Fusion rate estimates and discussion

This study concerns tuning the device to achieve maximum fusion rates. The fusion rate estimates were calculated for variations in pressure, maximum ion energy and magnitude of electric field.

For a maximum ion energy, $U_{\max}$, and an applied electric field, E, the maximum distance the ions travel is: $x = \frac{U_{\max}}{E}$ (in this expression $U_{\max}$ is in eV and E is in V/m). When pressure

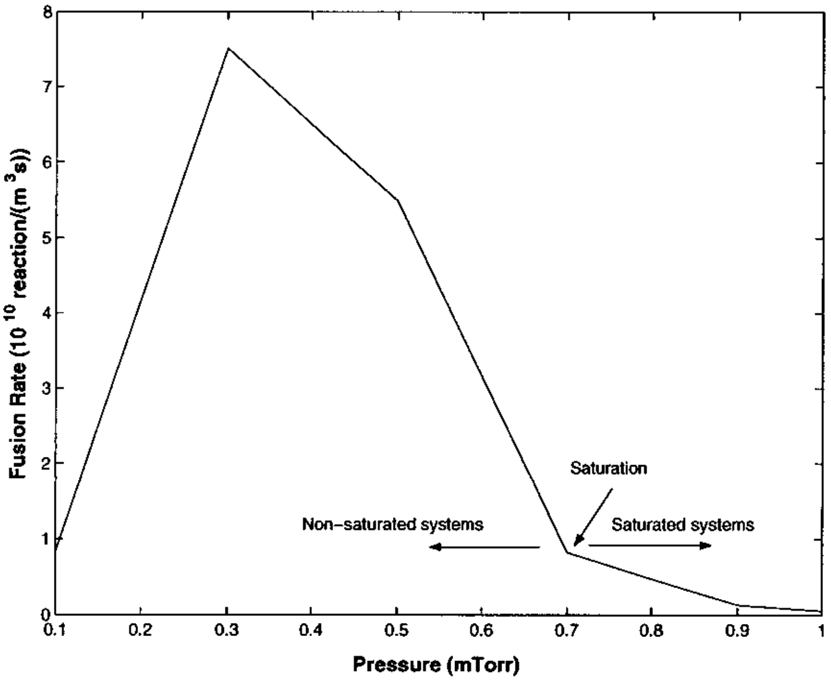

Figure 8.14: Simulated fusion rate versus pressure. The ion density was set to 10% of the background gas density, the maximum ion energy was 50 keV and electric field was 10 kV/m. This corresponds to a maximum ion path-length of 5 m.

is high (above 10 mTorr), after a relatively short distance (distance in the range of mm and cm) the density of newly created ions can become small relative to the initial density starting the charge exchange process. Systems, where the density of the newly created ions along the path becomes small (relative to the initial density) before the ions reach the end of the path, will be referred to as "saturated" systems. However, when pressure is low the newly created densities of ions might be significant all along the ions path. In this case the systems will be referred to as "non-saturated" systems. Note that in the "saturated" case, although the newly created ion density becomes small (relative to the initial density) after a relatively short distance, the total amount of ions that have charge exchanged might be larger than in the "non-saturated" case. An analysis of the saturated and non-saturated systems shows a higher fusion rate for the non-saturated systems. Figure 8.14 presents a fusion rate versus pressure curve.

In these calculations the ion density was set to 10% of the background gas density, the maximum ion energy was 50 keV and the electric field was 10 kV/m (equivalent to a cathode voltage ~ -1 kV in the IEC device) and therefore, the maximum ion path was 5 m. For pressures higher than 0.7 mTorr the systems become saturated (e.g. for a pressure of 5 mTorr the newly created density of ions become insignificant at ~ 0.5 m). For pressures lower than 0.7 mTorr all systems are non-saturated and the fusion rate reaches a peak at an optimum pressure. The same results were found for other combinations of maximum ion energies and

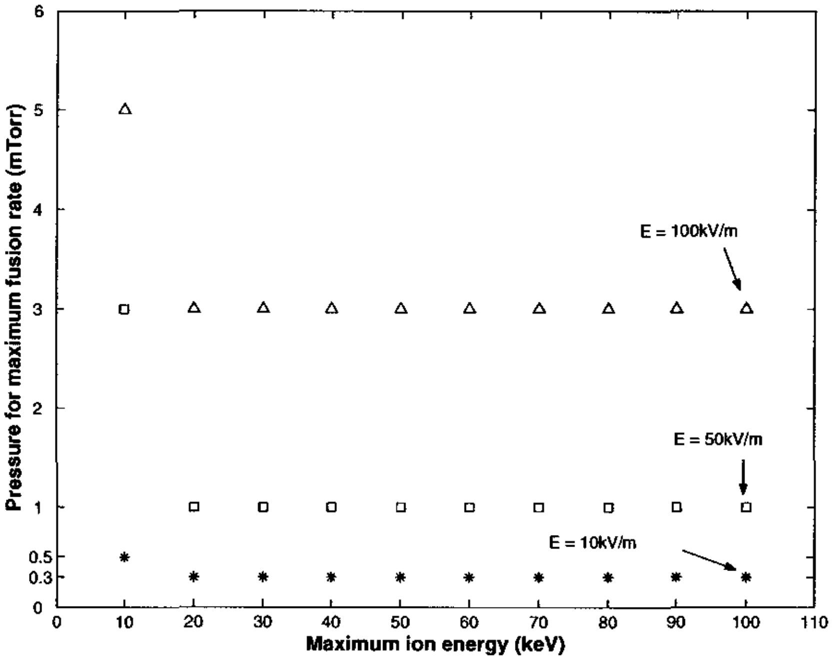

Figure 8.15: Simulation results of the dependence of optimal pressure on maximum ion energies and accelerating fields. The horizontal axis represents the maximum energy the ions gain, and the vertical axis shows the pressure for the maximum fusion rate. Accelerating electric fields of 10 kV/m, 50 kV/m and 100 kV/m were used.

electric fields inputs.

The dependence of the optimal pressure on maximum ion energies and accelerating fields is presented in Fig. 8.15. The horizontal axis represents the maximum energy the ions gain (this also depends on the size of the device), and the vertical axis shows the pressure for the maximum fusion rate. This was carried out for accelerating electric fields of 10 kV/m, 50 kV/m and 100 kV/m. Note that the optimal pressure is constant above a maximum ion energy of 10 keV and is independent of the maximum ion energy. The optimal pressure increases with increasing electric field. For example, the optimal pressure at 100 kV/m is 10 times greater than that at 10 kV/m. The optimal pressure changes for maximum ion energies less than 10 keV. However, the maximum ion energies of these systems have small fusion cross sections and are of no concern.

Figure 8.16 presents the corresponding fusion rates of the optimal pressures that were presented in Fig. 8.15, and for the same three accelerating fields. Note that the fusion rates increase with an increase in the maximum possible ion energy. This can be explained if we consider that the maximum fusion rates are achieved in the non-saturating systems (many ions acquire high energies) and that the fusion cross sections increase with increasing energies. It is also evident that the fusion rate increases with an increase in the accelerating field. For an accelerating field 10 time larger than the 10 kV/m field the fusion rates increase by a factor of 100. This can be explained if we consider that for higher accelerating fields the

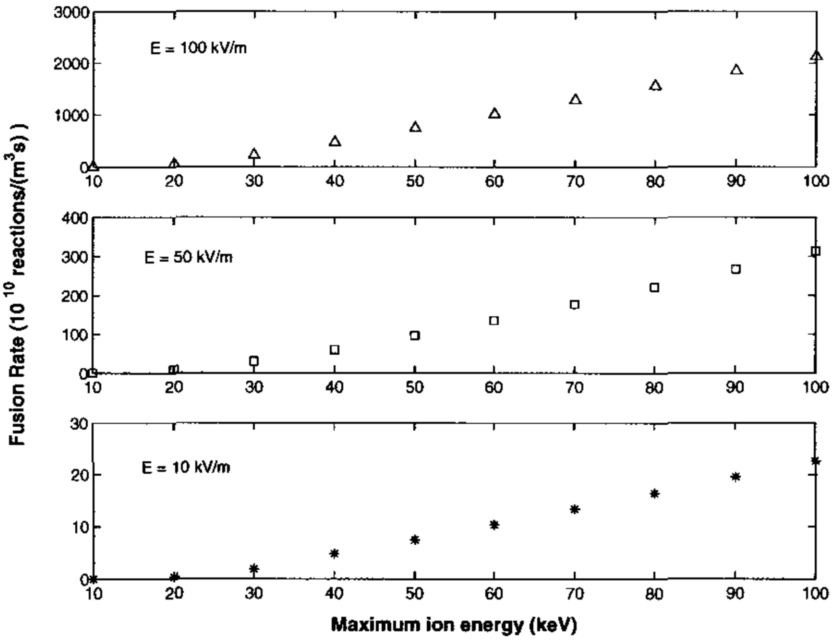

Figure 8.16: Simulated fusion rates at the optimal pressures that were presented in Fig. 8.15 and for the same three accelerating fields (marked in the figure).

ion path-length is shorter (for the same maximum ion energy) and more ions reach higher energies before charge exchanging.

The dependence of fusion rate on electric field for a maximum ion energy of 50 keV is presented in Fig. 8.17. Note that the fusion rate and optimal pressure increase with increasing accelerating electric fields. Moreover, the optimal pressure and fusion rate increase by a factor of $\sim$ 10 and $\sim$ 100, respectively, for a ten times in increase in the electric field. Figures 8.15, 8.16 suggest that these relations hold for all devices with maximum ion energies greater than 10 keV.

8.5 Fusion rate estimates: a two dimensional grid approximation

8.5.1 Programing

A second method of estimating the fusion rates for the ICR device was used. The calculations were carried out with the "grid approximation" model and program presented in chapter 6. The fusion rates were calculated using eq. 6.2, (this was indicated in box (13) in the flow-chart presented in Fig. 7.3).

The spiral length and the number of grid points on the surface affected the accuracy of the calculation. The spiral length was divided into small non-equal segments, where each segment length is set by the acceleration in a time interval Δt (the segments become larger with distance). Through trial and error, it was found that segments smaller than 1 mm are

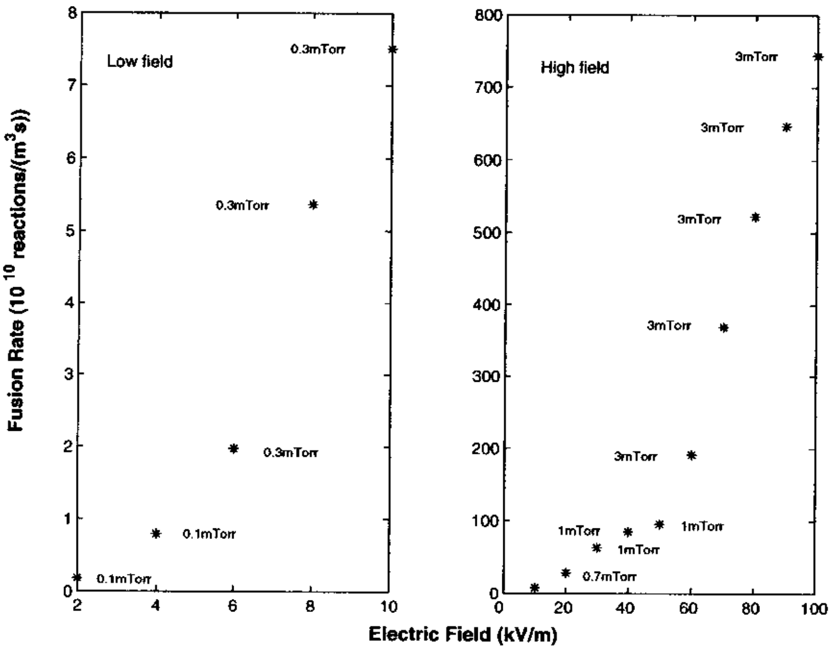

Figure 8.17: The dependence of fusion rate on the electric field for a maximum ion energy of 50 keV. The left plot shows the estimated fusion rate dependence on low accelerating electric fields (less than 10 kV/m) and the right plot shows the estimated fusion rates dependence on high accelerating electric fields (greater than 10 kV/m). Each data point represents the maximum fusion rate, where the optimal pressure is noted next to the data point.

sufficient. When the accelerating field is relatively small (below 6 kV/m, equivalent to a cathode voltage ~ -600 V in an IEC device) and the maximum ion energy is high (above 50 keV) the intervals can extend to ~ 2 cm for ~ 2000 spiral points. In this case, and when pressure is below 3 mTorr, the results were found to be larger by a factor of ~ 2 at most. A reduction in the number of spiral points to ~ 500 does not change the results significantly, where the factor increases to ~ 2.2. However, when pressures are in the range of few mTorr and higher, a large fraction of ions undergo charge exchange at relatively short distances. The intervals are relatively short for these distances (less than 1 cm) and the results are found to sufficiently converge. The computing time significantly increases with increasing number of grid points. Trial and error was used to estimate the maximum error for a given number of grid points. It has been found that for ~ 49 grid points spread on an area of $\sim 30 \times 30$ cm^2 the results are at most larger by a factor of ~ 5, although in most cases not larger than by a factor of ~ 2.

A uniform initial spatial ion density distribution was used in the simulation because ionization takes place uniformly throughout the active volume. The iteration of the calculation was stopped when the total fraction of newly created neutral atoms (summing the densities of neutral atoms of all grid points) was 1% of the total initial starting density.

Most of the initial ions undergo charge exchange for pressures above ~ 3 mTorr and pathlength in the order of tens of cm. At lower pressures and shorter ion paths the amount of ions surviving charge exchange can be significant. These ions reach the walls of the device, recombine with electrons at the surface and become energetic neutral atoms, consequently increasing the fusion rates. The main program was extended to account for this process.

8.5.2 Fusion rate estimates and discussion

Simulations of fusion rates were carried out for a device with a radius of ~ 20 cm and a magnetic field of 0.3 T, which restricts the D_2^+ ion energies to a maximum of 50 keV (note that although the experimental magnetic field used in this work was 0.6 T, for the simulated conditions the total pathlength of the ions is similar in length for the 0.3 T and 0.6 T magnetic fields. Therefore, the results are relevant to the experimental apparatus as well). The fusion rate estimates were calculated for a 10% gas ionization and for variations in pressure and magnitude of electric field. Spirals with 1000 segments and 81 grid points were used for each simulation (computer operation time was significantly longer for this method of approximation).

A typical fusion rate versus pressure curve, for a relatively small accelerating field of 5 kV/m (equivalent to a cathode voltage of ~ -500 V in an IEC device) is presented in Fig. 8.18. The shape of the curve agrees with the results presented in Fig. 8.14 and shows a peak at ~ 0.1 mTorr. For pressures higher than ~ 0.1 mTorr, charge exchange reduces the energies in the distribution, consequently lowering the fusion rate. For pressures lower than ~ 0.1 mTorr, the density of targets is low, which also decreases the fusion rates. Other fusion rate versus pressure curves, which resulted from the program for different accelerating fields,

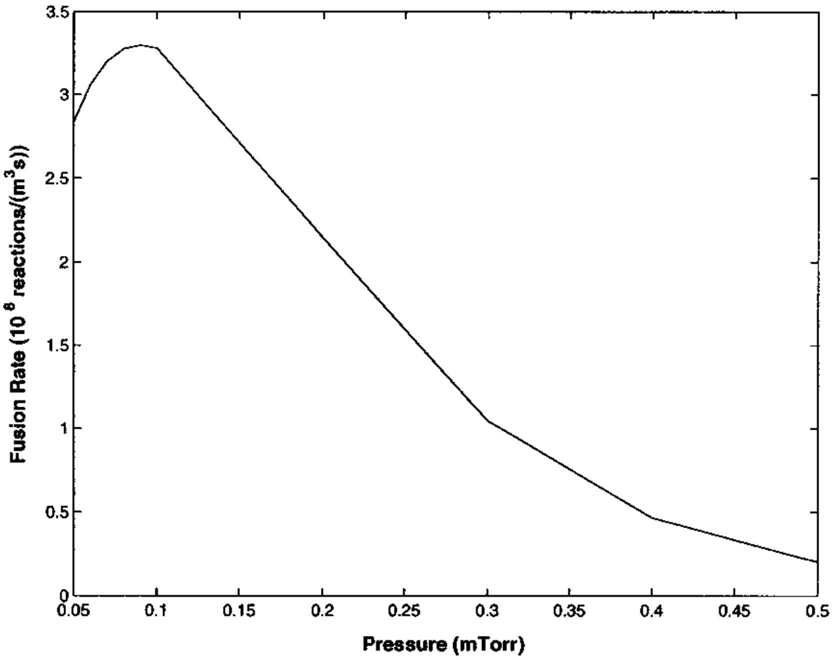

Figure 8.18: Simulated typical fusion rate versus pressure curve. The calculations were for a relatively small accelerating field of 5 kV/m (equivalent to a cathode voltage of ~ −500 V in an IEC device).

showed the same curve shape. However, for some conditions the peak of the curve slightly changes position.

A major technical advantage of the ICR device is the ability to operate it at low voltages. The fusion rates presented in Fig. 8.19 show an increase with increasing electric field strength. In particular, the optimum pressure increases by a factor of 10 by increasing the electric field by a factor of 10, with an accompanying 100 times increase in the fusion rate. These results largely agree with the linear potential approximation results (shown in Fig. 8.17) however, the rate approximations are ~ 30 times smaller on average and the optimal pressure is estimated to be slightly lower.

8.6 Summary and conclusions

The ICR apparatus is basically a cyclotron, which accelerates ions in a partially ionized gas with the aim of fusing with the background gas. A first experimental prototype of the device was built and energy measurements were taken using Doppler shift spectroscopy.

The energy distribution was found to be asymmetrically broadened around the unshifted H_α line for an input power of 50 W (estimated electrode voltage of ~ 50−100 V). The Doppler shift extended to ~ 1 keV on one side of the unshifted peak. Although this is a factor of 10−20 times the equivalent energy of the potential, the invested power is twice that in the IEC device for the same ion energy gain. The energy distribution was found to be independent of the

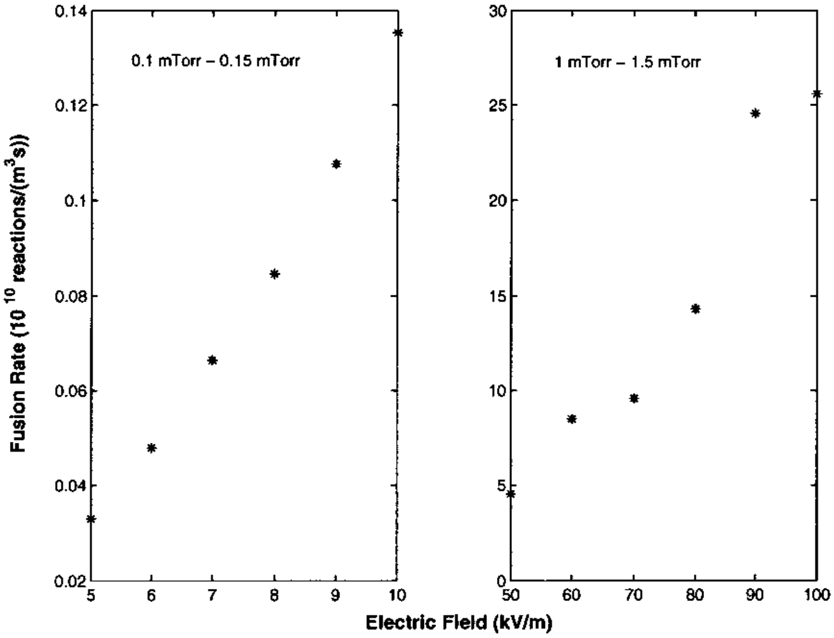

Figure 8.19: Simulated maximum fusion rate as a function of accelerating electric fields for less than 10 kv/m (left plot) and greater than 10 kV/m (right plot). The pressure ranges are indicated in the figure (the optimal pressure range is stated at the top of each plot).

location along the device (neglecting the edges of the device) but dependent on pressure. For decreasing pressures the energy distribution broadens and becomes more symmetric around the unshifted peak.

The model presented in chapter 7 was found to agree with the experimental results. However, there was a discrepancy in the maximum broadening, where the experimental results show a larger broadening. This suggests that the results from the model give a lower limit for energy and fusion rate estimates. The model also shows that the low intensity part of the Doppler shift distribution, extending to the maximum possible ion energy, might significantly contribute to the fusion rate. Although the densities in this part of the distribution are negligible in comparison to the densities in the central broadening, the fusion rate is energy dependent and for a one order of magnitude increase in energy the fusion rate can increase between 2 – 3 orders of magnitude.

Two different approximations were used to estimate the fusion rates resulting from the device. A typical IEC device is about 20 – 30 cm in radius, where for an applied voltage of $\sim$ 50 kV the neutron counts are of the order of 10^9 n/m^3s (for D-D interactions, see chapter 6). The linear potential approximation shows that the fusion rates of the ICR device are comparable to the fusion rates of the IEC device but for much smaller applied voltages and for a more compact device. For an ICR device of $\sim$ 20 cm radius, where a magnetic field of 0.3 T and an accelerating field of 50 kV/m are applied (equivalent to an applied cathode voltage of ~ -5 kV in an IEC device), 10^{12} n/m^3s are estimated. Considering

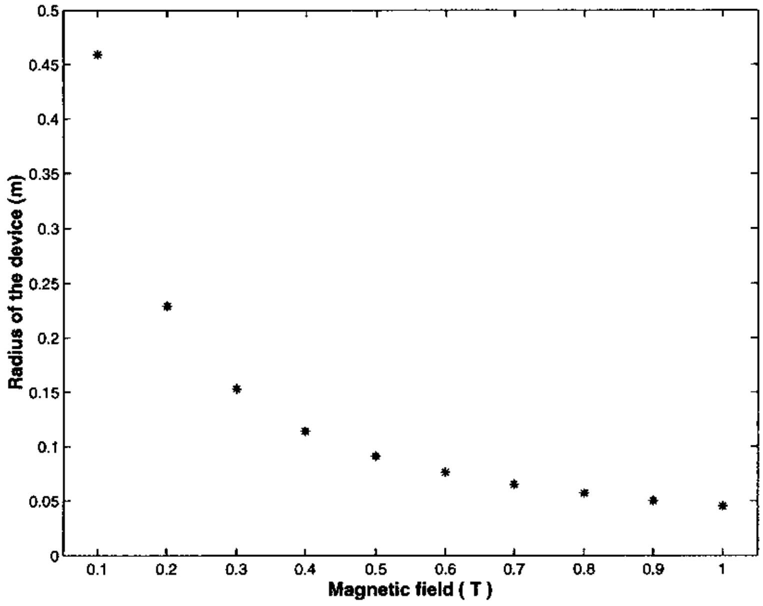

Figure 8.20: The radius of the device as a function of the magnetic field for a maximum D^+ ion energy of 50 keV.

that in these calculations the ion density was 3 orders of magnitude larger, the results are comparable with the rates presented in chapter 6. The fusion rates estimated with the grid approximation model are about an order of magnitude smaller than in the linear potential approximation case. However, in both cases it is shown that an increase of the accelerating field by a factor of 10 leads to a fusion rate increase by a factor of 100. Consequently, from the grid approximation, a smaller electric field is required to achieve the same fusion rates as in the IEC device. Moreover, it has been suggested that for the grid approximation model the fusion rate calculations are a lower limit.

The optimal operating pressures were found to be in the range of 0.1 to 3 mTorr, depending on the accelerating field, which affects the fusion rate (there is a factor of 100 increase in the fusion rate for a 10 fold in increase in the electric field). The size of the device is determined by the maximum ion energy, for a chosen magnetic field. Naturally, the radius of the devices must be larger for greater maximum ion energy. As a result, there is an increase in fusion rate since fusion cross-sections increase with energy. It is possible to make the device more compact by increasing the magnetic field for a given maximum ion energy. Figure 8.20 shows the radius of the device as a function of the magnetic field for a maximum D^+ ion energy of 50 keV. However, this is limited due to the dependence of the fusion rates on the volume of the device.

The success of the IEC device is in the strong potential drop, which is established in the short distance between the cathode centre and edge. In this relatively short distance a significant density of ions gain high energies before charge exchanging. This can be achieved in the ICR device by increasing the accelerating electric field, where for a given magnetic field and maximum ion energy, this shortens the ion path-length but does not affect the radius of the device.

Bibliography

[1] W. B. Mann, "The Cyclotron", Printed in Great Britain by Butler & Tanner Ltd., Frome and London (first bublished in 1940).

[2] F. F. Chen, "Introduction to Plasma Physics and Controlled Fusion", *2nd* Ed., Vol. 1. Plenum Press (1984).

[3] T. J. M. Boyd and J. J. Sanderson, "The Physics of Plasmas", Cambridge University Press (2003).

Chapter 9

Conclusions and Suggestions for Further Work

For the first time, an explanation of the optical emission spectrum was given for an Inertial Electrostatic Confinement (IEC) device. Moreover, the model that was developed enabled the accurate prediction of fusion rates and confinement times. As a result of the spectroscopy and the modelling, a new type of compact neutron source, based on ion cyclotron resonance, was modelled and constructed. This was shown to have the potential to equal or exceed the neutron rates for spherically symmetric IEC devices but without the high voltage arcing problems.

In detail, the spectrum from an IEC was simplified by making a one dimensional IEC discharge that consisted of a linear optical emission channel, which extended from the cathode to the anode, and through the anode mesh to the chamber wall. This arrangement enabled the channel to be rotated in order to obtain spatial resolution of the spectrum at different points on the channel. The operating conditions were restricted to a DC cathode bias of -1 to -10 kV and a pressure range of $5 - 30$ mTorr. At this range of pressures charge exchange was found to be dominant, which enabled the use of Doppler shift spectroscopy. The diagnostic method is based on charge exchange collisions of energetic H^+, H_2^+ and H_3^+ with the background hydrogen gas, H_2. These three collisions result in energetic and excited atomic hydrogen, H^*, which have energies that depend on the incident ion energy. As a result, there is a convolution of peaks that can be deconvolved by fitting three Gaussians to the spectra. This enabled the energy distributions of the incident ions and the resulting neutral atoms to be obtained.

Charge exchange of hydrogen ion beams was modelled by developing an intuitive method ("semi-analytical") as an alternative to a Monte Carlo method. This was shown to agree with a Markov chain approach to the problem. The modelling was carried out for the general cases of monotonic increasing (or decreasing) potentials, which include the linear potential and potential well. The semi-analytical method was applied to hydrogen ions accelerating in a linear potential in a background H_2 gas and compared with a Monte Carlo simulation. It was found that the advantage of the semi-analytical method was the rapid computing time without any numerical noise. The method can easily be applied to many systems where charge exchange is dominant, and further applied to other processes providing they have similar chain properties.

The charge exchange model was found to explain the physical interpretation of the Gaussian method of analysis for obtaining the energies of the three ionic species. For the conditions specified in this work, the Gaussian peaks were found to represent the maximum energy the ions gain in the potential well.

It was experimentally found that high fluxes of energetic neutral atoms emerge from within the cathode. It was suggested that the neutral atoms originate within the two potential wells and are created by ions that are diverging from the cathode centre while undergoing charge exchange. Not only was this found to be supported by other work [1–3], it was further supported with the charge exchange models. Energy distributions, calculated based on this hypothesis, were found to be in good agreement with previous experimental findings, where the energy of the neutral atoms of the three species (represented by the Gaussian peaks) were found to be equal and gained the maximum possible energy. Furthermore, it was possible to reconstruct the blue-shifted wing of the spectrum with these distributions. The fainter red-shifted wing was simulated with the energy distributions of H^+, H_2^+ and H_3^+ ion species, obtained for discharge conditions between the anode and cathode. This implies that the blue-shifted wing does not result solely from neutral atoms drifting from the other side of the cathode (the conventional view). If that had been the case, the blue-shifted wing should have resembled the red-shifted wing (at least near the cathode). These results suggest that ions created in the cathode centre were responsible for the formation of the blue-shifted wing, whereas, the discharge along the anode-to-cathode path was responsible for the formation of the fainter red-shifted wing.

Further applications of the charge exchange model were carried out for a higher pressure (hundreds of mTorr) discharge system and for estimates of IEC confinement time. Spectra resulting from a high pressure discharge system were simulated for an approximation of the discharge conditions. This further validated the reliability of the modelling method and showed the generality of the model, where it can be applied to various systems. The confinement time for IEC devices operating in the mTorr regime was estimated to be 7-8 orders of magnitude smaller than the Lawson criterion for D-D confinement. This implies that at units of mTorr confinement is largely affected by the loss of ions from the system.

Spectroscopic measurements were carried out on the beam. The energy represented by the Gaussian peaks was found to be the same for all three species in the cathode region. The simulated energy distributions suggest that this energy is equivalent to the potential difference between the cathode centre and the bottom of the potential well (This potential difference was referred to as the maximum possible potential depth). This finding is also supported by previous experimental results [4, 5]. The experimental results showed a neutral atom energy equivalent to $\sim 60\%$ of the applied voltage, which implies that for the experimental set-up of this work the maximum potential depth of the well was $\sim 60\%$ of the applied voltage. The ion energy was also found to be independent of cathode-to-anode distance and pressure, for the experimental conditions presented in this work. The minimum in the potential was found at the cathode edge and is mostly dependent on the cathode geometry, material and bias. Therefore, assuming that the ions diverge from the cathode centre outwards, moving the anodes closer or further from the cathode did not affect the energy distribution, which is formed mostly in the cathode region. The results also imply that the maximum potential depth is independent of pressure for the experimental conditions presented in this work ($5-30$ mTorr). Measurements, where the two anodes were placed at different distances from the cathode (asymmetric systems) agreed with the results presented for the symmetric systems. The ion energy was found to be independent of asymmetry and was the same as in the symmetric case. This implies that each of the two potential wells, established on each side of the cathode, is identical to the wells established in the symmetric system for the same anode-to-cathode distance. This further supports the fact that the potential minimum and its position are mainly influenced by the cathode geometry and material (and bias).

Energy measurements taken at an observation angle of 30° relative to the beam and along the beam agree with the measurements in the cathode region. The energies were found to be independent of pressure, cathode-to-anode distance and were also found to be constant all along the beam. This implies that the spectra obtained at 30° angle to the beam are a component of the 0° spectra at that angle. The results further support the fact that the energy distribution is created mainly before exiting the cathode, where at each point along the beam a sample of this distribution is found (energies are constant along the beam). Energetic red-shifted neutral atoms were found next to the chamber wall. The broadening of the energy distribution reached ~ 2.5 keV for a cathode voltage of -4 kV. This implies that neutral atoms were reflected from the wall, which explained the symmetry of the blue-shifted and red-shifted wings in the anode-to-wall region.

Energy measurements taken perpendicular to the beam agree with all previous results, showing that energy is independent of pressure, cathode-to-anode distance and position of observation along the beam. The spectra showed a broadening of ~ 11 Å at their base, which implies that there may be a radial component of the velocity of neutral atoms in the beam. However, it was suggested that the broadening is caused by the emission perpendicular to the beam, which originates in neutral atoms scattered from the beam. The scattered neutral atoms are a small component of the directional beam, and therefore, the emission from the directional component of the beam is much more significant at an observation angle of 30° relative to the beam axis. A model was developed to predict the spectrum line profile, where the simulations agree with the experimental results.

The charge exchange model was used to estimate neutron production rates for an IEC device operating in the mTorr regime. Results were compared with experimental measurements taken by Thorson et al. [6]. It was assumed that charge exchange is dominant, and therefore, the calculations were based on collisions of neutrals with the background gas. The modelled results were found to agree with the experimental range of rates and they further support the results of Baxter and Stuart [7], which showed that the neutron production rates in Hirsch's experiments [8] were mainly a product of neutral-background fusion interactions.

Since the simulations were based on the hypothesis that ions diverge from the cathode centre outwards, this further supports the hypothesis. Furthermore, Thorson et al. found that the neutron production rate was independent of the cathode transparency, for transparencies of 91% to 96%, and slightly increased when using a stainless steel cathode instead of titanium and tungsten cathodes. The independence of fusion rate of cathode transparency can be explained, assuming that neutral atoms scattered from the cathode surface also undergo fusion. The dependence of fusion rate on cathode material might result from a change in the secondary electron production with different cathode materials. A higher secondary electron production will result in a larger density of ions at the cathode centre.

An alternative neutron producing device, based on hot neutral and cold gas target fusion interactions, was built and studied by Doppler shift spectroscopy and modelling. The operation is based on ion cyclotron resonance (ICR) and was designed to accelerate ions in a partially ionized gas to high energies. The distribution of hot neutrals results from densities of ions spiraling in the active volume of the device while undergoing charge exchange and creating more ions that further spiral and undergo charge exchange. This process was modeled with a two dimensional charge exchange model.

The experimental energy distribution was found to be asymmetrically broadened around the unshifted H_α line for an input power of 50 W (estimated electrode voltage of $\sim 50-100$ V). The Doppler shift extended to ~ 1 keV on the blue-shifted side of the unshifted peak. Although this is a factor of $10-20$ times the equivalent energy of the potential, the invested power was twice that in the IEC device for the same ion energy gain. The energy distribution was found to be independent of the location along the device (neglecting the edges of the device) but dependent on pressure. For decreasing pressures the energy distribution broadens and becomes more symmetric around the unshifted peak. The simulations were found to agree with the experimental results. However, there was a discrepancy in the maximum broadening, where the experimental results showed a larger broadening. Therefore, the simulations could give a lower limit for energy and fusion rate estimates. The model also showed that the low intensity part of the Doppler shift distribution, extending to the possible maximum ion energy, might significantly contribute to the fusion rate. Although the densities in this part of the distribution are negligible in comparison to the densities in the central broadening, the fusion rate is energy dependent and for a one order of magnitude increase in energy the fusion rate can increase between $2-3$ orders of magnitude.

Two different approximations were used to estimate the fusion rates resulting from the device. The fusion rates estimated with the grid approximation model were found to be an order of magnitude smaller than in the linear potential approximation case. However, the grid approximation simulations were shown to be a lower limit for the fusion rates. A typical IEC device is about $20-30$ cm in radius, where for an applied voltage of ~ 50 kV the neutron counts are of the order of 10^9 n/m^{3}s (for D-D interactions). The simulated fusion rates of the ICR device were found to be comparable to the fusion rates of the IEC device but for much smaller applied voltages and for a more compact device. This is for an ICR device of ~ 20 cm radius, where a magnetic field of 0.3 T and an accelerating field of 50 kV/m are applied (equivalent to an applied cathode voltage of ~ -5 kV in an IEC device). It was shown that an increase of the accelerating field by a factor of 10 leads to a fusion rate increase by a factor of 100. Consequently, a smaller electric field is required to achieve the same fusion rates as in the IEC device. The optimal operating pressures were found to be in the range of 0.1 to 3 mTorr, depending on the accelerating field.

The fusion rate increases with increasing ion energies since fusion cross-sections increase with energy. It is possible to decrease the radius of the device for a given maximum ion energy by increasing the magnetic field. However, this is limited due to the dependence of the fusion rates on the volume of the device. In the IEC device there is a strong potential drop, which is established in the short distance between the cathode centre and edge. In this relatively short distance a significant density of ions gain high energies before charge exchanging. However, the potential difference is limited to a fraction of the applied voltage, where the latter is limited due to arcing and melting of the cathode. In the ICR device the ion energy can be increased by increasing the accelerating electric field, where for a given magnetic field and maximum ion energy, this shortens the ion path-length but does not affect the radius of the device.

The ICR device is expected to operate at relatively low voltages, solving the problem of arcing and cathode melting. It is a compact portable neutron source, where it can accelerate D^+ ions to energies of 100 keV in a radius of $\sim$ 10 cm for a magnetic field of 0.6 T. This corresponds approximately to the maximum fusion cross section for D-T interactions, where the tritium could be the target. In solid target neutron producing devices there is a deterioration of the target, which is a problem that does not exist in gaseous target systems such as ICR.

Naturally, the work presented in this thesis could be extended: the semi-analytical and Markov chain methods of modelling charge exchange were developed for the two cases of monotonic decreasing (or increasing) potentials and potential wells. These could be mathematically generalized to include any given spatial potential and could be applied to complex systems. For example, simulating the oscillations of ions in the two wells (simultaneously), which are established in the cathode of the IEC device presented in this work (the potential is lower at the centre of cathode, allowing ions moving towards the cathode in one well to enter the other).

In other work on IEC devices, a potential well was measured and was found to extend from the cathode centre to anode, where a minimum in the potential was found near the cathode edge. In this work neutral atoms were found to diverge from the cathode outwards. This was attributed to ions, created in the cathode centre, which accelerate in the potential well and undergo charge exchange. This can be further established with a model that includes electronic and ionic processes in the cathode region. The model should explain the potential shape and the creation of ions in the cathode centre. Furthermore, energy measurements taken for the cathode region showed that the ion energy was independent of pressure. This can only be explained with a model that considers electronic and ionic processes in the cathode region.

The phenomenon of diverging ions from the cathode suggests that beams of neutral atoms are established between the cathode and anodes. This gives rise for new designs of alternative neutron sources, which are based on beam-beam interactions. These could include the study of systems with linear arrays of cathodes or circular arrangements, where the beams are made to converge to the centre of the circle. Cathode materials could be studied (having different secondary electron emission coefficients) together with cathode geometry (width of the hollow space, length and shape). Naturally, neutron production rates could be measured and compared with the conventional IEC device.

Fusion rate estimates for the ICR device were found to be comparable with IEC fusion rates. However, the neutron production rate for the ICR device was not measured. A second model of the ICR device could be built, having a larger volume and allowing for an increase in input power. Energy measurements and neutron production rates could be carried out, to be compared with other existing neutron producing devices.

Bibliography

[1] O. Shrier, J. Khachan, S. Bosi, M. Fitzgerald and N. Evans, Phys. of Plasmas, **13**, 12703 (2006).

[2] J. Khachan and A. Samarian, Physics Letters A 363, 297–301 (2007).

[3] L. Blackhall and J. Khachan, J. Phys. D: Appl. Phys., **40**, 2491–2494 (2007).

[4] J. Khachan and S. Collis, Phys. of Plasmas, **8**(4), 1299 (2001).

[5] J. Khachan, D. Moore and S. Bosi, Phys. of Plasmas, **10**(3), 596 (2003).

[6] T. A. Thorson, R. D. Durst, R. J. Fonck and A. C. Sontag, Nuclear Fusion, **38** (4), 495 (1998).

[7] D. C. Baxter and G. W. Stuart, J. Appl. Phys., **53** (7), 4597 (1982).

[8] R. L. Hirsch, J. Appl. Phys., **38**, 4522 (1967).